

Aerodynamic Interaction between Propeller and Vortex

Yang, Yannian

DOI

[10.4233/uuid:9efb571c-0441-4690-84ca-7c5d5e8bfea6](https://doi.org/10.4233/uuid:9efb571c-0441-4690-84ca-7c5d5e8bfea6)

Publication date

2017

Document Version

Final published version

Citation (APA)

Yang, Y. (2017). *Aerodynamic Interaction between Propeller and Vortex*. [Dissertation (TU Delft), Delft University of Technology]. <https://doi.org/10.4233/uuid:9efb571c-0441-4690-84ca-7c5d5e8bfea6>

Important note

To cite this publication, please use the final published version (if applicable).
Please check the document version above.

Copyright

Other than for strictly personal use, it is not permitted to download, forward or distribute the text or part of it, without the consent of the author(s) and/or copyright holder(s), unless the work is under an open content license such as Creative Commons.

Takedown policy

Please contact us and provide details if you believe this document breaches copyrights.
We will remove access to the work immediately and investigate your claim.

Aerodynamic Interaction between Propeller and Vortex

Proefschrift

ter verkrijging van de graad van doctor
aan de Technische Universiteit Delft,
op gezag van de Rector Magnificus prof.ir. K.C.A.M. Luyben;
voorzitter van het College voor Promoties,
in het openbaar te verdedigen op
donderdag 16 Maart 2017 om 10.00 uur

door

Yannian YANG
Master of Engineering, School of Aeronautics
Northwestern Polytechnical University, China
geboren te Hubei province, China

This dissertation has been approved by the

promotor: Prof.dr.ir. L.L.M. Veldhuis

promotor: Prof.Dr.-Ing. G. Eitelberg

Composition of the doctoral committee:

Rector Magnificus	Chairman
Prof.Dr.-Ing. G. Eitelberg	Delft University of Technology
Prof.dr.ir. L.L.M. Veldhuis	Delft University of Technology

Independent members:

Prof. Fulvio Scarano	Delft University of Technology
Prof. Yangang Wang	Northwestern Polytechnical University
Prof. Rolf Radespiel	Braunschweig University of Technology
Prof. Markus Raffel	German Aerospace Center (DLR)
Dr. Gustavo Trapp	Embraer
Prof. Gerard van Bussel	Delft University of Technology, reserve



ISBN 978-94-6233-580-6

Copyright © 2017 by Y. Yang

This work is supported by the scholarship under the State Scholarship Fund of China (File No. 2011629079).

Summary

In many situations, aircraft propellers are operated at non-uniform inflow conditions due to inherent installation effects. Compared to a uniform inflow, the non-uniform inflow may influence the aerodynamic performance of the propeller; cause additional structural fatigue; and generate additional aero-acoustic noise. Various situations of propeller being operated at a non-uniform inflow, which are caused by concentrated vorticity, are frequently encountered but still lack a systematic description. Therefore, the current research focuses on the aerodynamic interaction between a propeller and an inflow vortex (or multiple vortices).

The situations with concentrated vorticity in the propeller inflow can be divided into two sub-categories based on the formation mechanism of the vortex (vortices). One situation occurs when vortices are generated by the propeller itself, e.g. ground vortices. The other situation occurs when the vortex is generated by upstream parts of the airframe, e.g. the tip vortex from a canard and the vortex shed from a control surface.

In category one which is about the interaction between a propeller and ground vortices, one part of the effort undertaken is to resolve the flow field involving ground vortices, i.e. the occurrence of the ground vortices, the generation mechanism of the vortices, and the fluctuation characteristics of the vortices. Investigation methods to resolve the flow field are Particle Image Velocimetry (*PIV*) measurements and Large Eddy Simulations (*LES*). Firstly, the relation between the occurrence of ground vortices on the operating conditions of the propeller is investigated, i.e. the thrust of the propeller and the elevation of the propeller from the ground. Secondly, the vorticity source of ground vortices induced by the pressure gradient on the ground due to the propeller suction effect is investigated. The results confirm the vorticity generation equation which is based on the theory first developed by Lighthill. Thirdly, the unsteady and turbulent flow involving ground vortices is investigated by spectral analysis and Proper Orthogonal Decomposition (*POD*).

The other part of the effort undertaken in category one is to quantify the influence of the vortices upon the propeller. The variation of the angle of attack of the blade in the circumferential direction is observed, which is analysed by investigating the velocities in the plane upstream of the propeller. The time-averaged loading of the propeller is found to be independent of ground vortices within the resolution of the measurements performed with the help of a rotating shaft balance.

In category two, about the interaction between an externally generated vortex and a propeller, the effect of the propeller on the vortex is focused on the flow field in

the vicinity of the blades. Investigations were performed at two planes upstream and downstream of the propeller. By varying the propeller thrust and maintaining the settings of the vortex generator, the dependence of vortex properties on the propeller are investigated in these two planes. The stretching of the vortex is observed both upstream and downstream of the propeller at conditions with the relatively highly loaded propeller. The vortex downstream of the propeller is significantly interfered with by the propeller slipstream, and its structure depends on the relative distance between the vortex and blade wakes. The propeller has a negligible effect on the total circulation of the vortex upstream of the propeller, as well as the circulation in the inner region of the vortex downstream of the propeller. This implies that the downstream vortex still has the potential to influence the further downstream parts of the airframe. To visualize the interaction between the impinging vortex and the propeller slipstream, the three-dimensional flow topology is built from the numerical results, which greatly enhance the understanding of this complex phenomenon.

The effect of the externally generated vortex on the propeller in category two is investigated systematically by varying the vortex strength, the vortex sign, and the off-axis radial position of the impinging vortex. The time-averaged performance of the propeller is obtained by both the rotating shaft balance and numerical simulations. Firstly, the time-averaged loading of the propeller shows an increase due to the contra-rotating vortex, and the opposite is true for a co-rotating vortex. Secondly, the change of the time-averaged loading is proportional to the circulation of the vortex. Thirdly, as the impinging vortex moves outward in the propeller radial direction, its effect on the propeller loading decreases. For all the above situations, the efficiency of the propeller exhibits a negligible change at a given advance ratio.

The time dependent characteristic of the propeller loading influenced by the externally generated vortex in category two is analysed from the numerical results. Firstly, due to a contra-rotating vortex, the blade thrust has its minimum value at the phase angle around that of the impinging position; and the opposite for the case of a co-rotating vortex. Secondly, a strong variation of the thrust on the blade during the rotation is observed and needs to be taken into account for dynamic structural stress analysis during the blade design. Thirdly, the pressure fluctuation on the blade due to the vortex impingement increases and it is mainly observed at the leading edge of the blade.

Samenvatting

In veel situaties opereren vliegtuigpropellers onder niet-uniforme instromingscondities ten gevolge van inherente installatie-effecten. Ten opzichte van uniforme instromingscondities, kan de niet-uniforme instroming invloed hebben op de aerodynamische karakteristieken van de propeller, structurele vermoeiing veroorzaken, en aeroakoestisch geluid genereren. Diverse gevallen van propellers die opereren in non-uniforme instroming, veroorzaakt door geconcentreerde vorticeiteit, komen frequent voor, maar zijn tot op heden niet systematisch beschreven. Om deze reden is het huidige onderzoek verricht, waarbij de focus lag op de aerodynamische interactie tussen de propeller en een inkomende wervel of wervels.

De situaties met geconcentreerde vorticeiteit in de propellerinstroom kunnen verdeeld worden in twee subcategorieën, gebaseerd op de ontstaanswijze van de wervel(s). In de ene situatie genereert de propeller de wervels zelf, zoals het geval voor bijvoorbeeld grondwervels. In de andere situatie wordt de wervel gegenereerd door stroomopwaartse delen van het vliegtuig, bijvoorbeeld een tipwervel van een canard of een wervel afgestroomd van een stuurvlak.

In de eerste categorie, de interactie tussen een propeller en grondwervels, is een onderdeel van het verrichte werk gericht op het in kaart brengen van het stromingsveld met de grondwervels en hun aanwezigheid, de ontstaanswijze van de wervels, en de tijdsafhankelijke werveleigenschappen. Onderzoeksmethoden om het stromingsveld in kaart te brengen zijn metingen met Particle Image Velocimetry (*PIV*) en numerieke simulaties op basis van Large Eddy Simulations (*LES*). Allereerst is het verband onderzocht tussen de aanwezigheid van de grondwervels en de operationele condities van de propeller, dat wil zeggen de stuwkracht van de propeller en de afstand van de propeller tot de grond. Ten tweede is de bron onderzocht van de vorticeiteit van de grondwervels geïnduceerd door de drukgradiënt op de grond door de zuiging van de propeller. De resultaten bevestigen de vorticeiteitsproductievergelijking welke is gebaseerd op de theorie oorspronkelijk afgeleid door Lighthill. Ten derde zijn de tijdsafhankelijke en turbulente stromingen met grondwervels onderzocht gebruikmakende van spectrumanalyse en Proper Orthogonal Decomposition (*POD*).

Het andere deel van het werk in de eerste categorie omvat het kwantificeren van de invloed van wervels op de propeller. Analyses van het snelheidsveld in een vlak stroomopwaarts van de propeller hebben een variatie in omtreksrichting aangetoond van de invalshoek van het blad. Door middel van metingen met een roterende balans is vastgesteld dat de tijdsgemiddelde propellerbelasting niet wordt beïnvloed door grondwervels.

In de tweede categorie, de interactie tussen een extern gegenereerde wervel en een propeller, is het effect van de propeller op de wervel geconcentreerd in het stromingsveld in de nabijheid van de bladen. Het onderzoek is gedaan in twee vlakken stroomop- en stroomafwaarts van de propeller. De afhankelijkheid van de werveleigenschappen ten opzichte van de propeller zijn onderzocht in deze twee vlakken door de stuwkracht van de propeller te variëren en de instellingen van de wervelgenerator gelijk te houden. De uitrekking van de wervel is zowel stroomopwaarts als stroomafwaarts van de propeller waargenomen in omstandigheden met een relatief zwaar belaste propeller. Stroomafwaarts van de propeller wordt de wervel significant beïnvloed door de propellerslipstroom, en is de wervelstructuur afhankelijk van de relatieve afstand tussen de wervel en het zog van het blad. De propeller heeft een verwaarloosbaar effect op de totale circulatie van de wervel stroomopwaarts van de propeller, als mede op de circulatie van de binnenste regio van de wervel stroomafwaarts van de propeller. Dit betekent dat de stroomafwaartse wervel nog altijd de potentie heeft verder stroomafwaarts gelegen onderdelen van het vliegtuig te beïnvloeden. Om de interactie tussen de botsende wervel en de propellerslipstroom te visualiseren, is de driedimensionale stromingstopologie in kaart gebracht met behulp van numerieke resultaten, welke het begrip van dit complexe fenomeen sterk vergroten.

De invloed van de externe wervel op de propeller, categorie twee, is systematisch onderzocht door het variëren van de wervelsterkte, de wervelrichting, en de radiale positie van de inkomende wervel in de richting weg van de propelleras. De tijdsgemiddelde propellerprestaties zijn verkregen door zowel de roterende balans alsmede numerieke simulaties. Allereerst neemt de tijdsgemiddelde propellerbelasting toe ten gevolge van de contra-roterende wervel, terwijl het tegenovergestelde waar is voor een co-roterende wervel. Ten tweede is de verandering van de tijdsgemiddelde propellerbelasting evenredig aan de circulatie van de wervel. Ten derde neemt het effect van de botsende wervel op de propellerbelasting af als de wervel naar buiten verplaatst in de radiale richting van de propeller. Bij een gegeven voortgangscoefficiënt is het effect op het propellerrendement verwaarloosbaar voor alle voorgaande situaties.

Het tijdsafhankelijke karakter van de propellerprestaties onder invloed van de externe wervel is onderzocht in categorie twee met behulp van de numerieke resultaten. Ten eerste vertoont de stuwkracht van het blad een minimale waarde bij een fasehoek rond die van de positie van de botsing met een contra-roterende wervel, en vice versa voor het geval van een co-roterende wervel. Ten tweede is een sterke variatie van de stuwkracht op het blad geobserveerd gedurende de rotatie, welke in acht genomen dient te worden tijdens het bladontwerp door middel van analyses van de dynamische mechanische spanningen. Ten derde nemen de drukvariaties op het blad toe door de botsing met de wervel, wat voornamelijk waargenomen is rondom de voorlijst van het blad.

Contents

Nomenclature	xi
Part I Prologue	
Chapter 1 Introduction	3
1.1 Propulsion by propellers in aviation.....	3
1.2 Challenges for the integration of propeller and aircraft	3
1.3 Past efforts and research questions.....	5
1.3.1 Past efforts and research questions for the interaction between ground vortices and a propeller	6
1.3.2 Past efforts and research questions for the interaction between an external vortex and a propeller	6
1.4 Outline of the thesis.....	8
Chapter 2 Theoretical description of propeller and vortex	11
2.1 Theoretical description of propeller characteristics.....	11
2.1.1 Momentum theory	11
2.1.2 Blade element method	14
2.1.3 Aerodynamic parameters of propeller performance	16
2.2 Description of a vortex	17
2.2.1 Vorticity.....	17
2.2.2 Circulation and Kelvin's theorem	18
2.2.3 Source of vorticity	20
2.2.4 Vorticity transport equation.....	22

2.2.5	Profile of vortex.....	22
2.3	Interaction between propeller and vortex by analytical models	25
2.3.1	Propeller induced flow field on the ground	25
2.3.2	Impact of a streamwise vortex on the propeller inflow	28
2.4	Conclusions	31
2.5	Discussion	31
Part II Interaction between propeller and its self-induced vortices		
Chapter 3 Tools and methods for the investigation of interaction between propeller and its self-induced vortices.....		
3.1	Wind tunnel and propeller rigs	35
3.1.1	Open jet facility	35
3.1.2	Experimental setup	36
3.1.3	Rotating shaft balance and air motor.....	38
3.2	<i>PIV</i> arrangement.....	39
3.2.1	Low frequency <i>PIV</i> arrangement.....	39
3.2.2	High frequency <i>PIV</i> arrangement	41
3.3	Error analysis of the experimental measurements	42
3.4	Numerical simulations.....	43
3.4.1	Numerical methods.....	43
3.4.2	Mesh for the computation.....	45
3.4.3	Solver.....	47
Chapter 4 Results and discussion of interaction between propeller and its self-induced vortices		
4.1	Flow fields of ground vortices.....	49

4.1.1	Flow fields in the wall parallel plane	49
4.1.2	Flow fields upstream of the propeller.....	52
4.1.3	Three dimensional flow field.....	53
4.1.4	Domain boundary of the occurrence of ground vortices	55
4.2	Source of vorticity for the ground vortices.....	58
4.2.1	Development of the lateral-component of the vorticity.....	58
4.2.2	Development of the streamwise-component of the vorticity.....	62
4.2.3	Development of the wall-normal component of the vorticity	65
4.3	Unsteadiness and coherent turbulent structures of ground vortices	66
4.3.1	Time resolved analysis of flow fields.....	66
4.3.2	Unsteadiness of ground vortices.....	69
4.3.3	Proper Orthogonal Decomposition of flow fields in the wall parallel plane	72
4.3.4	Proper Orthogonal Decomposition of the flow fields in the plane upstream of the propeller.....	76
4.4	Impact of vortices on the propeller inflow	80
4.4.1	Non-uniform inflow of propeller due to the impact of ground vortices	80
4.4.2	The effect of the thrust coefficient on the non-uniformity of the propeller inflow	84
4.4.3	The effect of the height ratio on the non-uniformity of the propeller inflow	86
4.4.4	Impact of ground vortices on the time averaged performance of propeller	86
4.5	Conclusions	87
4.6	Discussion	89

Part III Interaction between an externally generated vortex and a propeller

Chapter 5	Tools and methods for the investigation of interaction between an externally generated vortex and a propeller	93
5.1	Experimental arrangements	93
5.1.1	Vortex generator	93
5.1.2	Experimental setup	94
5.1.3	Test matrix	95
5.1.4	<i>PIV</i> setup	96
5.1.5	Bin method for the phase lock analysis	97
5.1.6	Error analysis of the experimental measurements	98
5.2	Numerical methods	100
5.2.1	Methodology of the numerical simulation	100
5.2.2	Computational domain and boundary conditions	101
5.2.3	Mesh of the model	101
5.2.4	Turbulence model	103
5.2.5	Solver	103
Chapter 6	Results and discussion of the response of an externally generated vortex to a propeller	105
6.1	Typical flow fields and three-dimensional vortex topology	105
6.1.1	Flow fields upstream of the propeller	105
6.1.2	Flow fields downstream of the propeller	108
6.1.3	Three dimensional flow topology	110
6.2	Impact of the propeller on the vortex upstream of the propeller	112

6.2.1	Impact of the propeller on the vortex meandering upstream of the propeller	112
6.2.2	Impact of the propeller on the tangential velocity and the radius of the vortex upstream of the propeller.....	113
6.2.3	Impact of the propeller on the circulation of the vortex upstream of the propeller.....	114
6.3	Impact of the propeller on the vortex downstream of the propeller	117
6.3.1	Impact of the propeller on the vortex meandering downstream of the propeller	117
6.3.2	Impact of the propeller on the vortex shape downstream of the propeller	119
6.3.3	Impact of the propeller on the tangential velocity and radius of the vortex downstream of the propeller.....	120
6.3.4	Impact of the propeller on the circulation of the vortex downstream of the propeller.....	121
6.4	Conclusions	123
6.5	Discussion	125
Chapter 7	Impact of an externally generated vortex on a propeller	127
7.1	Impact of the vortex on the propeller performance	127
7.1.1	Effects of the strength and the direction of the rotation of the vortex on the performance of the propeller	127
7.1.2	Effect of the radial position of the impinging vortex on the propeller performance.....	132
7.1.3	Impact of the vortex on the propeller at different advance ratios....	134
7.2	Impact of the vortex on the additional fluctuating pressure of the blade	136
7.3	Conclusions	139
Part IV Conclusions and recommendations		

Chapter 8	Conclusions and recommendations	143
8.1	Conclusions about the interaction between a propeller and its self-induced vortices	143
8.2	Conclusions about the interaction between a propeller and an externally generated vortex	144
8.3	Recommendations	146
Appendix A	Particle Image Velocimetry	147
Appendix B	Boundary layer profile near the ground table	149
Appendix C	Proper Orthogonal Decomposition	151
Appendix D	Determination of the vortex centre	153
Appendix E	Flow fields downstream of the propeller at high loading condition	155
Appendix F	Flow fields downstream of the propeller at different impinging radial positions of the vortex	157
Appendix G	Flow fields downstream of the propeller with different rotating directions of the vortex	159
Appendix H	Loading and pressure distribution on the blade	161
Bibliography	163
Acknowledgements	173
Publications	175
Curriculum Vitae	177

Nomenclature

Abbreviations

<i>AOA</i>	Angle of attack
<i>BLA</i>	Blade
<i>BVI</i>	Blade vortex interaction
<i>CFD</i>	Computational Fluid Dynamics
<i>FOD</i>	Foreign object damage
<i>FOV</i>	Field of view
<i>GC</i>	Geometric centre
<i>LE</i>	Leading edge
<i>LES</i>	Large Eddy Simulation
<i>OFAT</i>	One factor at a time
<i>OJF</i>	Open jet facility
<i>PIV</i>	Particle Image Velocimetry
<i>POD</i>	Proper Orthogonal Decomposition
<i>RSB</i>	Rotating shaft balance
<i>SF</i>	Shape factor
<i>TE</i>	Trailing edge
<i>TKE</i>	Turbulent kinetic energy
<i>TVs</i>	Tip vortices
<i>VS</i>	Vortex section chopped by the blade
<i>rms</i>	Root mean square

English Symbols

a	Coefficient of velocity increment upstream of the actuator disk
b	Coefficient of velocity increment far downstream of the actuator disk
c	Chord length of the blade element
c_n	Time coefficient of the spatial mode of POD analysis
dr	Infinitesimal radial length of the blade element
dL	Lift on the blade element
dD	Drag on the blade element
dF	Tangential force on the blade element
dT	Thrust on the blade element
dQ	Torque on the blade element
D	Diameter of the propeller
h	The distance between the propeller centre line and the ground
J	Advance ratio of the propeller
L	Length of the propeller model
l	The integral path on the material curve
M	Mach number
n	Rotating speed of the propeller (round per second)
O	Order of magnitude
p	Static pressure
p_1	Pressure immediately upstream of the actuator disk
p_∞	Ambient pressure
Q	Torque of the propeller

Q_c	Torque coefficient of the propeller
R	Radius of the propeller
r_c	The core radius of the vortex
r_{imp}	The radial position of the impinging vortex
\bar{r}	Radial distance from the vortex centre normalized by the vortex-core radius
S_{disk}	Area of the propeller disk
T	Thrust of the propeller
T_c	Thrust coefficient of the propeller
U_a	The resultant velocity in the axial direction of the propeller
$U_{a,i0}$	The induced axial velocity upstream of the isolated propeller
U_e	Effective velocity of the blade element
U_{eq}	Equivalent axial velocity in the slipstream of the propeller
U_t	The resultant velocity in the tangential direction of the propeller
$U_{t,i0}$	The induced tangential velocity upstream of the isolated propeller
U_∞	Free stream velocity

Greek and mathematic symbols

α	Angle of attack
β	Geometry pitch angle of the propeller blade
Γ	Circulation
Γ_{imp}	The circulation of the externally-generated impinging vortex
Γ_∞	The total circulation of the vortex

δ_{BL}	Boundary layer thickness
δ_l	The distance of the laser sheet from a reference position
η	Efficiency of the propeller
κ	The strength of the doublet flow
μ	Dynamic viscosity
ν	Kinematic viscosity
ρ	The density of the air
σ	Standard deviation
Φ	Spatial mode of the flow field
Ψ	Phase angle of the blade
Ω	Rotational speed of a fluid element
ω	Vorticity

Subscripts

a	Axial direction
avg	Average
imp	Impinging
cor	Core
max	Maximum
t	Tangential direction
v	Vortex
X, Y, Z	Coordinates in the reference frame of the fixed propeller
∞	Infinity

Part I

Prologue

Chapter 1 Introduction

1.1 Propulsion by propellers in aviation

From the first manned flight by Wright brothers on, propellers have been chosen as the propulsor of aircraft for more than one century. In the aviation market nowadays, aircraft with propeller propulsion still constitute a large part of the market. The number of propeller aircraft was 40% of the 7,200 aircraft in the regional fleet of the world in 2014 [1]. In general aviation, propeller aircraft are predominant and amounted to 81% of worldwide deliveries in 2014 [2]. Military transport aircraft are also dominated by the ones with propellers, and the number of propeller aircraft was approximately 80% among the top ten military transport aircraft in 2015 [3]. In addition, the majority of unmanned vehicles adopt propellers as the propulsor [4].

Among the many reasons for choosing propellers as the propulsion system of aircraft, e.g. the shorter range of taking off, the higher climbing rate, and the lower weight penalty of thrust reversal compared with turbofans [5], etc. the most significant reason is the relatively high propulsive efficiency of propellers. The ideal propulsive efficiency (theoretical upper limit neglecting the installation effects) of an aircraft propulsor is defined as,

$$\eta_{ideal} = \frac{2}{1 + \frac{U_{jet}}{U_{\infty}}}. \quad \text{Eq.(1.1)}$$

U_{∞} is the velocity of the aircraft, and U_{jet} is the jet speed of the propulsor in the aircraft frame of reference. Because the jet speed of a propeller is relatively lower than that of a turbofan, its propulsive efficiency is higher. The propulsive efficiency of the installed propeller is 10~30% higher than the turbofan at a cruise speed of Mach number below 0.7 [5].

1.2 Challenges for the integration of propeller and aircraft

In an effort to further increase the propulsive efficiency of propellers over a wider range of operating conditions, two major activities can be identified. Firstly, effort is put into the performance enhancement of the uninstalled propeller, e.g. advanced airfoil sections, the application of blade sweep, and the technique of counter-rotating rotors [6]. Secondly, the performance improvement is sought through the optimization of the interaction between propellers and airframe (as well as the runway), which is the interest of the current research and summarized as,

1. Interaction between a propeller and downstream parts of the airframe, e.g. inlet, cowl, nacelle, wing, fuselage, etc. for a tractor configuration [7-9].
2. Interaction between a propeller and upstream parts of the airframe, e.g. nacelle, pylon, wing, fuselage for a pusher configuration [10-12].
3. Interaction between a propeller and ground/fuselage, no matter whether the aircraft is a tractor or a pusher configuration.

Interactions of these types cause a non-uniform inflow into the propeller plane. They may have an impact on the efficiency of the propeller [7, 9, 13]; induce excessive cyclic stress on the blade [7, 10, 12-14]; and increase the noise level of the propulsive devices [7, 12, 15-17]. For the many situations of the propeller operating at a non-uniform inflow, the non-uniform inflow caused by concentrated vorticity still lacks a systematic description and analytical predictive models, which defines the topic of the current research. Two cases of this type of vortical flow are introduced below.

One situation of the non-uniform inflow with concentrated vorticity entering a propeller plane is classified as the interaction between a propeller and ground vortices (or fuselage vortices). When the aircraft operates on the runway with a highly loaded propeller, a system of ground vortices is generated and enter the propeller as shown in Figure 1.1 (although there is one major vortex observed in this figure, there are other weak vortices which are not observable as they are dependent on the visualization methods [18]). Ground vortices can be observed when rain droplets are present or air condensation occurs in the vortex core region. A similar phenomenon with a vortex shed from the fuselage and ingested into the propulsor was reported in [19] as well. In the thesis, the fuselage vortices are not investigated, but results from ground vortices can be applied to the understanding of the interaction between vortices and any solid boundary, which includes ground vortices and fuselage vortices.

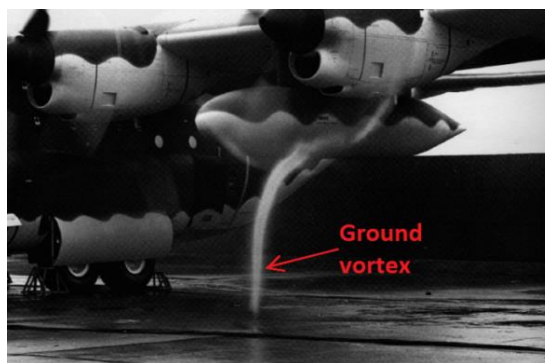


Figure 1.1 Occurrence of a ground vortex on the outboard propeller of aircraft C130 [20].

The other situation of a non-uniform inflow with concentrated vorticity can be induced by upstream lifting surfaces. Examples of such vortical flow entering the propeller are shown in Figure 1.2. The vortex from the tip of the canard entering the propeller is shown in the left of Figure 1.2; the potential vortex from the root of the control surfaces entering the propeller is shown in the right of Figure 1.2. Not only the propellers in the fixed wing aircraft, but also the tail rotor of a helicopter experiences such vortical flow from the upstream lifting surfaces. The vortex shed from the main rotor of Bell OH-58 Kiowa helicopter impinging onto the tail rotor as it operated at a side slip condition was reported in [21], and the vortex shed from the flaperon of the Piasecki compound helicopter has the potential to impinge onto the ducted tail rotor [22].

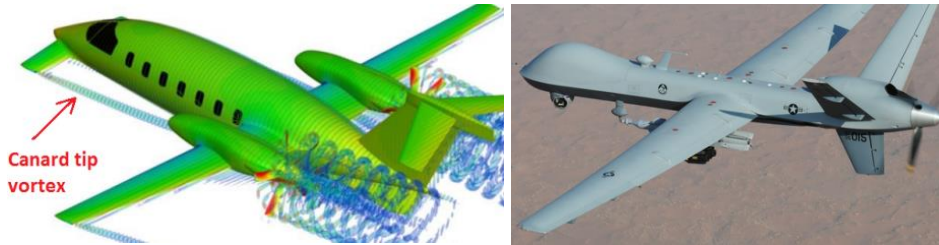


Figure 1.2 Occurrence and potential occurrence of external vortex impinging onto a propeller. Left: Piaggio P.180 Avanti aircraft [14]; right: Predator B UAV.

These phenomena of vortices entering propellers, like other types of non-uniform inflow mentioned above, may have impact on the performance of the propeller, the structural fatigue related to the dynamic loading, pressure fluctuation on the blade, etc. Furthermore, the propeller may also have impact on the inflow vortex, i.e. the generation of the vortex, the transport of the vortex, etc. According to these concerns, literature review is conducted, and research questions are defined in the following sections.

1.3 Past efforts and research questions

It can be found from a preliminary analysis that the vortical flow entering a propeller has two sub-categories. Firstly, if the propeller is not positioned close to the ground as shown in Figure 1.1, it is obvious that there is no vortical flow entering the propeller, so the ground vortices are also termed as propeller self-induced vortices in this thesis. Secondly, for the vortices as shown in Figure 1.2, the vortex is always there independently of the existence of the propeller. This type of vortex is denoted as an external vortex. As these two types of interactions between the vortex and the propeller are intrinsically different, the thesis treats these two types of flow separately, and the literature review and objectives are elaborated in two subcategories.

1.3.1 Past efforts and research questions for the interaction between ground vortices and a propeller

Ground vortices were first investigated during the 1950s because of concerns of foreign object damage (*FOD*) to engines [23]. It was reported that 40~50% of engine repairs was due to *FOD* when aircraft operated near the ground [24, 25]. A distortion of the propulsor inflow caused by vortices was also reported in [26] for a suction tube model intended to represent a turbofan propulsor.

In order to find ways to alleviate these detrimental effects of ground vortices, it is a prerequisite to model the source of the vorticity entering ground vortices, but inconsistency in approach is observed in open literature. In the early publications treating this phenomenon it was stated that the vorticity transported in the far field boundary layer was the sole source of the vorticity of ground vortices at headwind conditions [27, 28]. This view has prevailed in subsequent research, e.g. [29, 30]. However, the model based on the boundary layer convected vorticity is not sufficient for the headwind condition and especially does not describe the takeoff condition. In fact, the source of vorticity as explained by Lighthill in 1963 in the “Fluid motion memoirs: Laminar boundary layers” showed that, for the production of vorticity, a pressure gradient on the wall is required [31], which certainly exist on the ground due to the suction effect of the propulsor.

Therefore, the first objective of this research is to evaluate this inconsistency of vorticity source. Specifically,

1. To gain understanding on the fundamentals of the vorticity source required for the forming of ground vortices.

For the vortices generated during ground operations by aircraft propulsors, extensive research has been conducted by utilizing a simplified suction tube model [26, 28-30, 32, 33] to represent a turbofan. This model does not take the rotor effect into account, e.g. the characteristic of intermittency of the propulsor inflow due to the blade passing. In addition, this model was not able to generate understanding of the influence of the vortices on the rotor performance. Therefore, two other objectives of the present research are to:

2. Gain insight into the propeller inflow due to the interaction between the propeller and ground vortices.
3. Investigate the impact of ground vortices on the propeller performance.

1.3.2 Past efforts and research questions for the interaction between an external vortex and a propeller

For a vortex originating from upstream components of the airframe (e.g. the canard and control surfaces, as shown in Figure 1.2), its axial velocity can be assumed to be aligned with the free stream velocity. This type of vortex impinging

onto the propeller is regarded as a streamwise-vortex/blade interaction (or perpendicular-vortex/blade interaction) as defined in [34].

Only limited open literature is available for the cases of streamwise-vortex/blade interaction, where the investigations utilize a real propeller model. The blade tip vortex shed from the main rotor of a helicopter impinging onto a tail rotor, as the helicopter was operated at a side slip condition, was reported in [35]. As the tail rotor contra-rotated with the blade tip vortex, the thrust of the tail rotor increased, and a reverse trend was observed as the tail rotor was operated at the opposite rotating direction [35]. The vortex generated by a separate wing upstream of the propeller impinging onto the propeller tip region ($0.9 R$ and $0.975 R$ radial positions, where R is the propeller radius) was investigated for the concern of the aero-acoustic impact of the vortex/blade interaction in [36]. Cyclic pressure on the blade suction and pressure sides was observed, resulting in an increase in far field noise by 5 to 15 dB [36]. Although the aero-acoustic effect of the interaction between a propeller and a vortex is not quantified in the current thesis, this observation indicates the significance to quantify the cyclic pressure on the blade from aerodynamic investigations.

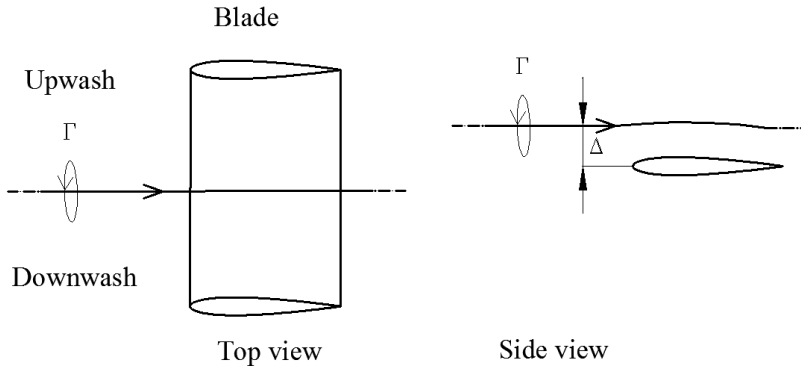


Figure 1.3 The effect of the vortex on the blade (wing).

Research of vortex/propeller interaction was extensively conducted on the simplified model of a vortex impinging onto a steady wing [37-45], as shown in Figure 1.3. It was found in [45] that, as the vortex impinged at the mid-span and above the wing, the wake of the wing triggered the turbulent decay of the vortex core and this resulted in a decrease of the vortex circulation. However, as the vortex impinged at the tip region of the wing, the incident vortex was paired and even merged with the wing tip vortex and the merged vortex featured a higher circulation than the incident vortex [37, 38, 42] (this process was dependent on the rotation direction of the particular vortices). The phase angle effect of the blade was represented by the distance between the wing and the impinging vortex [44, 46] in the vertical direction, Δ , as shown in the right hand side of Figure 1.3. It was found that the interaction had little influence on the vortex as the distance between the

wing and the vortex was beyond 0.3 chord length of the wing; and as the distance decreased, the interaction substantially weakened the vortex core and increased its size downstream of the wing [44].

The pressure distribution on the wing indicated a downwash at one side of the impinging position, and an upwash on the other side [38, 41], as sketched in Figure 1.3. This resulted in a variation of loading in the spanwise direction, and shifted the separation region aft or forward on the airfoil depending on the downwash or upwash effects [41]. The blade vortex interaction (*BVI*) has an effect of increasing the lift-to-drag ratio when a vortex impinged on a steady wing as reported in [41, 47]

In open literature (as mentioned above), extensive descriptions were presented on the main flow features associated with the vortex-wing interaction. However, the blade dynamic loading has received limited attention. The overall effect of the vortex on the propeller was obtained during the study of the vortex/propeller interaction, but not so much flow detail of the impinging vortex as well as that on the blade is available. Therefore, the objectives of the research in this part are to fill this gap by obtaining both flow details, and at the same time obtaining the impact of the vortex on the blade dynamic loading and the overall propeller performance. The details of these objectives are:

4. To generate a well-defined vortex upstream of the propeller, and build a map of propeller performance versus vortex quantities, i.e. the sign of the vortex, the strength of the vortex and the radial positions of the impinging vortex.
5. Investigate the flow topology and strength of the vortex under the impact of the propeller, especially the vortex in the slipstream of the propeller.

1.4 Outline of the thesis

Based on the objectives of the research, the thesis is divided into four parts. Part I is the introduction and the theoretical background of the propeller and the vortical flow, and it includes Chapter 1 and Chapter 2. Chapter 1 has been read already; Chapter 2 explains the thrust generating mechanism of the propeller, the vortex aerodynamics, the analytical model for the interaction of a propeller and a ground plane, and the analytical model for the interaction of a propeller and a streamwise vortex.

Part II is about the interaction between a propeller and ground vortices, and it includes Chapter 3 and Chapter 4. Chapter 3 describes the tools and methodologies for the investigation of propeller induced ground vortices. It introduces the experimental setup in the wind tunnel and the numerical methodology. The experiments are conducted on an eight-blade propeller operating at a highly loaded condition. Particle Image Velocimetry (*PIV*) measurements are conducted to resolve

the flow involving ground vortices. The propeller performance is measured by a rotating shaft balance (*RSB*). The numerical studies are conducted on an actuator disk model, which is intended to represent the effect of the propeller thrust and mainly utilized to investigate the vorticity source of ground vortices.

Chapter 4 presents experimental and numerical results. The numerical results are validated by the experimental results in terms of flow topologies. The map of the domain boundary that represents the occurrence of ground vortices is obtained by utilizing both the experimental and numerical methods. The formation mechanism of the ground vortices is studied by the numerical results, and is compared to Lighthill's vorticity source theory. The coherent flow structures upstream of the propeller are revolved by the Proper Orthogonal Decomposition (*POD*) analysis from the *PIV* results. The impact of vortices on the inflow and performance of the propeller are investigated by evaluating the blade angle of attack (*AOA*) and balance measurement results.

Part III is about the interaction between a propeller and an external vortex, and it includes Chapters 5, 6, and 7. Chapter 5 introduces the experimental and numerical tools for the study of this topic. The impinging vortex is generated by a wing with finite span upstream of the propeller, and the propeller model is the same as that for studying the ground vortices. Numerical simulation is intended to represent the experimental condition by solving the unsteady Reynolds Averaged Navier-Stokes equations (*uRANS*).

Chapter 6 discusses the vortex topology interacting with the blade and its subsequent structure. For a vortex generated by the wing, the impact of the propeller on this vortex is evaluated by varying the propeller loading. The properties of the vortex, i.e. the position, the maximum tangential velocity, the core radius and the circulation are analysed both upstream and downstream of the propeller.

Chapter 7 discusses the impact of the vortex on the propeller, in terms of time dependent loading on the blade and time averaged performance of the propeller. For a propeller operating at a constant free stream velocity and a constant rotating speed, the propeller performance for variable vortex strengths is evaluated. In addition, the effects of the vortex impinging position, as well as the propeller operating condition are investigated. Furthermore, the pressure fluctuation on the blade due to the vortex impingement is analysed from the numerical results.

In Part IV which includes Chapter 8, conclusions of the thesis are drawn and recommendations of the research are presented.

Chapter 2 Theoretical description of propeller and vortex

The aerodynamics of propellers and vortices, as well as the interaction with each other is reviewed and analysed in this chapter. The momentum theory and the blade element method are introduced to explain the mechanism of the thrust generation of propellers. Generation and transport of vorticity, the Kelvin's theorem, and the Lamb-Oseen vortex model are reviewed for the aerodynamics of vortex behaviour. Analytical models are introduced to explain the interaction between a propeller and a vortex. In particular, the mechanism of vorticity generation from a flat wall due to the effect of the propeller suction which is represented by a doublet flow, and the non-uniform inflow of the propeller due to the impact of the vortex are analysed.

2.1 Theoretical description of propeller characteristics

2.1.1 Momentum theory

For the study of ground vortices induced by a propeller, the actuator disk model (by adding an axial momentum in the flow at the position of the propeller disk plane) is chosen for numerical simulations. The reasons to choose this model are as follows. Firstly, the ground vortices were assumed to be mostly determined by the axial force (thrust) of the propeller and the torque of the propeller has a negligible influence, because ground vortices are mostly located upstream of the propulsor [26, 29, 33] and the induced velocities (tangential component) by the torque are negligible upstream of the propeller [48]. Secondly, the model of the actuator disk can be simply implemented in the *CFD* code. The limitation of the actuator disk model is the exclusion of the blade passing effect. However, as will be described in Section 4.3.2, although the blade passing effect is significant in the region close to the blades, the effect on the flow field near the ground is negligible. Therefore, it is assumed that the flow field near the ground induced by the actuator disk model represents the real situation for the purposes of this study.

The actuator disk theory is also known as one dimensional momentum theory, and it is the oldest mathematical model of propellers [49]. It was first applied on marine propellers by Rankine [50] and developed by Froude [51]. The idea of the momentum theory is that the momenta of the flow far upstream and far downstream of the propeller are not equal, the difference of which is the momentum added to the flow by the propeller. In order to explain this model, the propeller is considered as a stationary disk in a moving fluid. This conceptual model for the flow going through the propeller is shown in Figure 2.1.

The streamlines going through the disk from the far upstream position to the far downstream position define the stream tube. The flow is analysed at three planes in the stream tube, the plane far upstream, the plane of the actuator disk, and the plane far downstream. The plane far upstream of the propeller has the velocity of U_∞ and pressure p_∞ . The pressure decreases to p_1 and the velocity increases to $U_\infty + aU_\infty$ at the front surface of the disk. After passing through the disk, the pressure has an increment Δp and the velocity remains $U_\infty + aU_\infty$ due to the mass conservation. At the plane far downstream, the pressure decreases to ambient pressure p_∞ , and the velocity increases to $U_\infty + bU_\infty$.

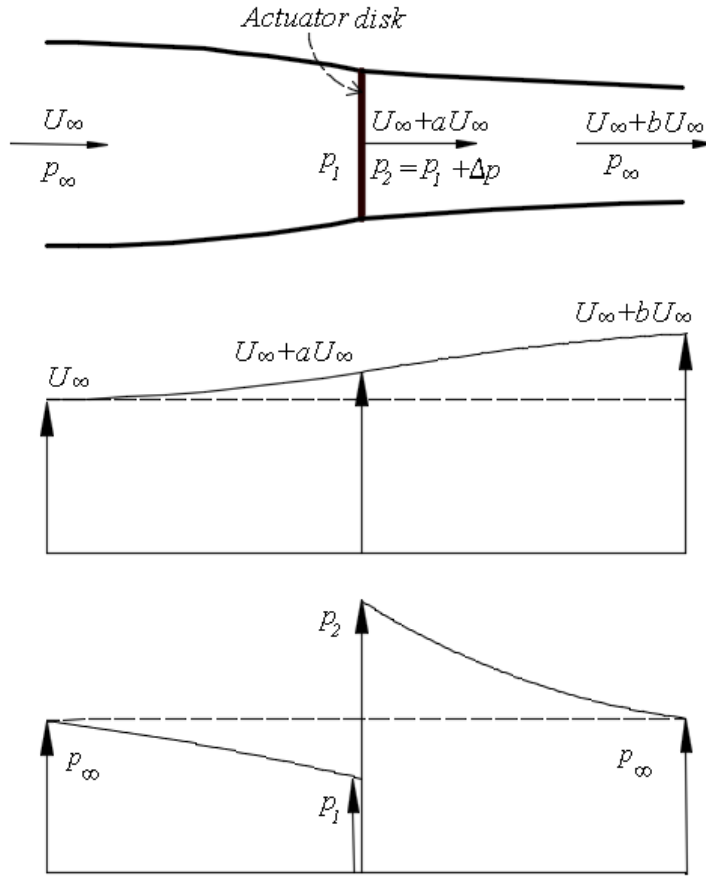


Figure 2.1 Top: schematic of the actuator disk model; middle: distribution of the axial velocity in the axial direction; bottom: distribution of the static pressure in the axial direction.

In the stream tube, the mass conservation and momentum equations are applied following the methods introduced in [48]. The flow is regarded as inviscid flow except in passing through the disk, and Bernoulli's equation is applied separately to

the flow upstream and downstream of the disk. The equation for the total pressure upstream of the disk is,

$$p_{\infty} + \frac{1}{2}\rho U_{\infty}^2 = p_1 + \frac{1}{2}\rho(U_{\infty} + aU_{\infty})^2, \quad \text{Eq. (2.1)}$$

where ρ is the density of the air.

The equation for the total pressure downstream of the disk is,

$$p_1 + \Delta p + \frac{1}{2}\rho(U_{\infty} + aU_{\infty})^2 = p_{\infty} + \frac{1}{2}\rho(U_{\infty} + bU_{\infty})^2. \quad \text{Eq. (2.2)}$$

The subtraction of Eq. (2.2) from Eq. (2.1) yields,

$$\Delta p = \frac{1}{2}\rho(U_{\infty} + bU_{\infty})^2 - \frac{1}{2}\rho U_{\infty}^2 = \rho U_{\infty}^2 b(1 + \frac{1}{2}b). \quad \text{Eq. (2.3)}$$

The thrust is determined by the pressure jump multiplied by the area of the disk,

$$T = \Delta p \cdot S_{disk} = \rho U_{\infty}^2 b(1 + \frac{1}{2}b) S_{disk}. \quad \text{Eq. (2.4)}$$

Also, since the thrust is equal to the rate of change of the axial momentum between the planes far upstream and far downstream, the thrust is then given by,

$$T = \rho S_{disk} (U_{\infty} + aU_{\infty}) b U_{\infty}. \quad \text{Eq. (2.5)}$$

Equating the two equations of the thrust from Eq. (2.4) and Eq. (2.5) leads to,

$$\rho U_{\infty}^2 b \left(1 + \frac{1}{2}b\right) S_{disk} = \rho S_{disk} (U_{\infty} + aU_{\infty}) b U_{\infty}, \quad \text{Eq. (2.6)}$$

and it yields,

$$a = \frac{1}{2}b. \quad \text{Eq. (2.7)}$$

Thus, according to the momentum theory, half of the total velocity increase far downstream of the disk is found at the location of the disk.

The static pressure directly upstream of the disk, p_1 , is reformulated as,

$$p_1 = p_{\infty} - \frac{1}{2}\rho U_{\infty}^2 \left(\frac{1}{4}b^2 + b\right). \quad \text{Eq. (2.8)}$$

The static pressure directly downstream of the disk p_2 is,

$$p_2 = p_1 + \Delta p = p_{\infty} + \frac{1}{2}\rho U_{\infty}^2 \left(\frac{3}{4}b^2 + b\right). \quad \text{Eq. (2.9)}$$

It is shown in Eq. (2.8) and Eq. (2.9) that the pressure upstream and downstream of the propeller is dependent on the increase of the axial velocity in the stream tube, which is determined by the operating condition of the propeller. The pressure on the two sides of the actuator disk model as implemented in the *CFD* code follows that described in Eq. (2.8) and Eq. (2.9).

Froude's momentum theory (actuator disk model) is widely applied for research of the propeller action, not propellers themselves, because of its simplicity and good approximation. It is applied to determine the propeller loading when it is utilized together with the blade element method (this method is introduced in the next section), which gives good results compared with experimental results [52]. It was also implemented to study the effect of the propeller slipstream on the wing loading in analytical descriptions [5, 53] and numerical simulations [5, 54]. This simple model indeed has limitations. There is no torque on the disk, so there is no rotation imparted to the flow going through the disk. This model also ignores the vorticity shed from the blades. The efforts to improve the actuator disk model for application in wider conditions are manifold. The tangential and radial velocities in the slipstream of the propeller, as well as the loading distribution in the radial direction, are implemented by introducing vortex rings and vortex lines in the slipstream of the propeller [55, 56]. Side forces resulting from the vortical flow around the edge of the disk is implemented in an improved model [57]. As mentioned at the beginning of this section, the original actuator disk model is still chosen for its good approximation for our study to generate ground vortices and its simplicity.

2.1.2 Blade element method

The blade element method introduced here is prepared for the explanation of the effect of the non-uniform inflow upon the propeller loading in a qualitative way. This method is useful for dealing with both the cases of ground vortices and the externally induced vortex.

The idea of the blade element method is introduced by Froude [51], and generally referred to as Drzewiecki theory [48], because Drzewiecki explained it in a practical form independently and he was the first to use airfoil data to find the force on the blade element. The blade element theory investigates the propeller in a greater detail compared with the momentum theory, e.g. the torque of the propeller is introduced to the model.

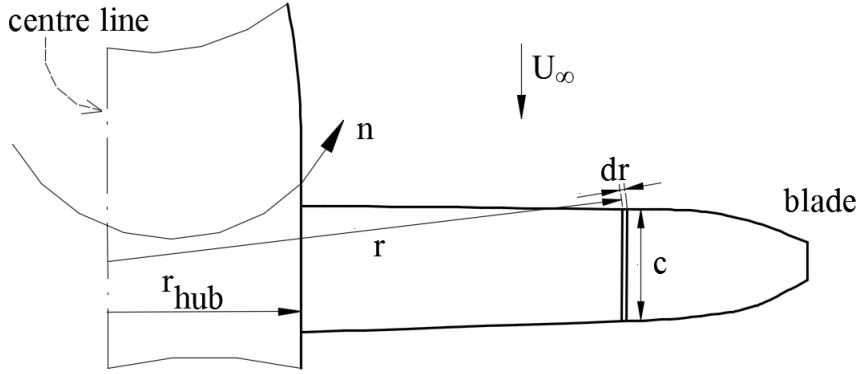


Figure 2.2 The section of an element on the blade.

A propeller model with a rotation speed of n (revolutions per second) is positioned in the free stream with a velocity of U_∞ . The blade is divided into elements in the radial direction, as shown in Figure 2.2. Consider the element located at the radius r , which has an infinitesimal length dr , a chord length c , and a geometrical pitch angle β .

The flow around the element is assumed to be two dimensional (later on this 2D flow is corrected by the Prandtl tip loss factor) and not affected by adjacent blades and there is no radial flow. Each element is treated as a two dimensional wing, and the cross section of the blade element is shown in Figure 2.3. The tangential velocity is the combination of the tangential velocity due to the blade rotation, $2\pi nr$, and the induced tangential velocity at the propeller plane, $U_{t,i0}$ (this tangential velocity is induced by the vortex system in the propeller plane and in the propeller slipstream, and the detail is reported in [5]). The axial velocity is the combination of the free stream velocity U_∞ and the induced axial velocity $U_{a,i0}$ (this axial velocity can be determined from the actuator disk model). The resultant velocity is defined as the effective velocity represented by U_e . The angle between the effective velocity and the chord line of the blade element defines the geometrical angle of attack α . The lift and the drag on the element are defined by following the definition of a wing model,

$$dL = \frac{1}{2} \rho U_\infty^2 C_l c dr, \quad \text{Eq. (2.10)}$$

$$dD = \frac{1}{2} \rho U_\infty^2 C_d c dr. \quad \text{Eq. (2.11)}$$

Here, C_l and C_d are the lift and the drag coefficients of the of the blade element. The thrust is defined in the opposite direction of the free stream. The angle between the thrust and the lift is $(\beta - \alpha)$, and the lift has a positive contribution to the thrust, while the drag has a negative contribution to the thrust. The thrust is defined in Eq. (2.12). The force perpendicular to the thrust, dF , induces a torque on the blade which is defined in Eq. (2.13).

$$dT = dL \cos(\beta - \alpha) - dD \sin(\beta - \alpha), \quad \text{Eq. (2.12)}$$

$$dQ = dF \cdot r = r(dL \sin(\beta - \alpha) + dD \cos(\beta - \alpha)). \quad \text{Eq. (2.13)}$$

The lift and the drag coefficients can be obtained from a database (obtained from calculations or experiments). After the induced velocities on the blade are known, the thrust and torque of the blade can be obtained. The determination of the induced velocities can be obtained from Froude's momentum theory, Prandtl's lifting line theory and Theodorsen's vortex model [52]. In our analysis as shown in Chapters 4 and 7, the induced velocities in addition to the free stream velocity are obtained from *PIV* measurements and *CFD* simulations, so these methods to determine the induced velocities are not explained in detail here.

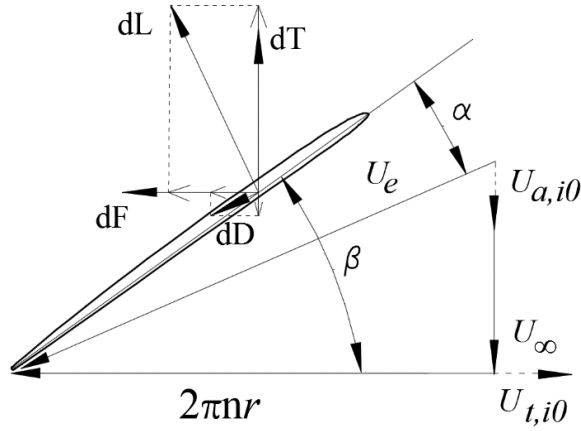


Figure 2.3 The velocities and forces on the blade element.

2.1.3 Aerodynamic parameters of propeller performance

The incidence angle of the blade is dependent on the free stream velocity and the rotating speed as shown in Figure 2.3. Hence, the local blade angle of attack, represented by the advance ratio becomes,

$$J = \frac{U_\infty}{nD}. \quad \text{Eq. (2.14)}$$

The thrust of the propeller is normalized by two times of the dynamic pressure of the free stream and the square of the propeller diameter,

$$T_C = \frac{T}{\rho U_\infty^2 D^2}. \quad \text{Eq. (2.15)}$$

The torque of the propeller is non-dimensionalized as,

$$Q_C = \frac{Q}{\rho U_\infty^2 D^3}. \quad \text{Eq. (2.16)}$$

The efficiency of the propeller represents the work in the forward direction of the propeller divided by the shaft power,

$$\eta = \frac{T U_\infty}{Q 2\pi n} = \frac{T_C}{2\pi Q_C} J. \quad \text{Eq. (2.17)}$$

When there is an unsteady force on the blade, e.g. the propeller is operated at a non-uniform inflow, it is necessary to define the phase angle of the blade, which represents the circumferential position of the blade as shown in Figure 2.4. The phase angle Ψ is defined by the angle between the OZ axis and the dashed line, which is the blade pivot axis for the blade to change the pitch angle. The coordinate system, with its origin located at the intersection of the propeller centre line and the leading edge of the blade root, is shown in the right hand side of Figure 2.4.

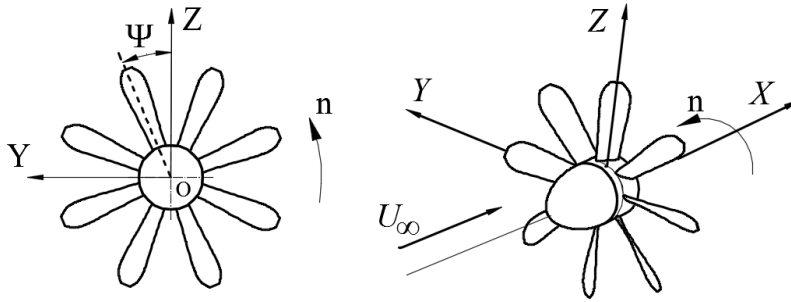


Figure 2.4 Left: definition of the phase angle of the blade; right: coordinate system of the propeller.

2.2 Description of a vortex

In order to investigate the interaction between a vortex and a propeller, the aerodynamics of the vortex needs to be elaborated. The aerodynamics of the vortex introduced in this section includes definitions and fundamentals about a vortex, i.e. definitions of vorticity and circulation, fundamentals of vorticity generation and transport, as well as a vortex model to represent typical vortical flow in aeronautics.

2.2.1 Vorticity

In order to quantify the strength of the flow spinning at each point, vorticity is defined. A spherical fluid particle is considered as shown in Figure 2.5. The mass centre is located at O , and the rotation speed around the mass centre is Ω .

Due to the rotation of the fluid (assumed to be a rigid rotation), the velocities are not constant along the X and Y axes. Applying the mathematical operation of taking curl of the velocity in the X - Y plane is,

$$\omega_z = \frac{\partial u_y}{\partial x} - \frac{\partial u_x}{\partial y} = 2\Omega. \quad \text{Eq. (2.18)}$$

It is found in Eq. (2.18) that the curl of the velocity is twice the angular velocity of the fluid particle. Therefore, in order to characterize the rotation of the fluid, the curl of the velocity is chosen and formulated in a three dimensional flow as,

$$\vec{\omega} = \nabla \times \vec{U} = (\omega_x, \omega_y, \omega_z) = \left(\frac{\partial u_z}{\partial y} - \frac{\partial u_y}{\partial z}, \frac{\partial u_x}{\partial z} - \frac{\partial u_z}{\partial x}, \frac{\partial u_y}{\partial x} - \frac{\partial u_x}{\partial y} \right). \quad \text{Eq. (2.19)}$$

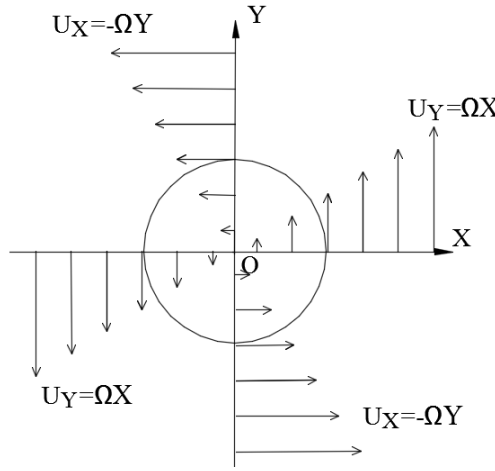


Figure 2.5 Velocity of a fluid particle at rotation speed of Ω (reproduced from [31]).

It is noticed that the vorticity satisfies the divergence free condition,

$$\begin{aligned} \nabla \cdot \vec{\omega} &= \frac{\partial \omega_x}{\partial x} + \frac{\partial \omega_y}{\partial y} + \frac{\partial \omega_z}{\partial z} \\ &= \frac{\partial^2 u_z}{\partial y \partial x} - \frac{\partial^2 u_y}{\partial z \partial x} + \frac{\partial^2 u_x}{\partial z \partial y} - \frac{\partial^2 u_z}{\partial x \partial y} + \frac{\partial^2 u_y}{\partial x \partial z} - \frac{\partial^2 u_x}{\partial y \partial z} = 0. \end{aligned} \quad \text{Eq. (2.20)}$$

This solenoidal feature of vorticity in 3D flow will be utilized to derive the generation rate of the wall-normal component of the vorticity in Section 2.2.3.

2.2.2 Circulation and Kelvin's theorem

Vorticity describes the angular velocity of a fluid particle as introduced in the previous section, and the circulation is a macroscopic measure of the rotation of a

finite area of fluid. It is defined on a closed path of the material curve (shown by the blue circle in Figure 2.6) as,

$$\Gamma = \oint \vec{U} d\vec{l}, \quad \text{Eq. (2.21)}$$

where \vec{U} is the velocity vector, \vec{l} is the integral path on the material curve.

The closed curve defined for the calculation of the circulation bounds a cluster of vortex lines. A vortex line is a line whose tangent is parallel to the vorticity vector. The vortex lines drawn through each point inside a closed curve form a tube and it is termed as a vortex tube, as shown in Figure 2.6.

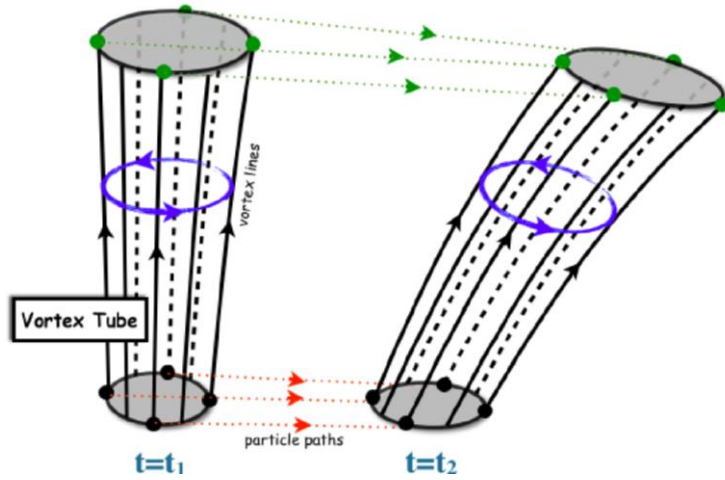


Figure 2.6 Schematic showing vortex tube which is tilted and stretched observed at two instants [58].

A case of a vortex tube which is stretched and tilted from t_1 to t_2 (the stretching and the tilting can also occur in the space domain, but it is not treated here) is shown in Figure 2.6. In order to investigate the circulation along the material curve as time advances, the Kelvin's theorem is introduced with assumptions of no body force and inviscid flow conditions. The substantial derivative of the circulation is,

$$\frac{D\Gamma}{Dt} = \frac{D}{Dt} \oint \vec{U} d\vec{l} = \oint \frac{D\vec{U}}{Dt} dl + \oint \vec{U} \frac{Ddl}{Dt} = \oint \frac{D\vec{U}}{Dt} dl + \oint \vec{U} D\vec{U}. \quad \text{Eq. (2.22)}$$

The integral of a scalar field on a closed curve is zero, and it yields the second term on the right hand side of Eq. (2.22) to be zero,

$$\oint \vec{U} D\vec{U} = \oint D \frac{1}{2} U^2 = 0. \quad \text{Eq. (2.23)}$$

For the inviscid flow assumption, the momentum equation is,

$$\frac{D\vec{U}}{Dt} = -\frac{1}{\rho}\nabla p. \quad \text{Eq. (2.24)}$$

Substituting Eq. (2.24) into Eq. (2.22), and considering the fluid as incompressible flow with a constant density, we obtain:

$$\frac{D\Gamma}{Dt} = -\oint \frac{1}{\rho}\nabla p dl = -\frac{1}{\rho}\oint dp = 0. \quad \text{Eq. (2.25)}$$

The preservation of the circulation along a material curve, as shown in Eq. (2.25), is known as Kelvin's theorem at conditions of no body force and inviscid flow. As a vortex is transported in the flow which is influenced by the propeller, Kelvin's theorem will be utilized in the following chapters.

2.2.3 Source of vorticity

The generation of vorticity from a flat surface in incompressible flow is introduced by following the work of Lighthill [31] and Morton [59]. A fluid element adjacent to the wall is shown in Figure 2.7. The wall is represented by the plane of $Z = 0$, and the wall parallel velocities adjacent to the wall are U_X and U_Y respectively (the distributions of the velocity presented here are along the wall parallel directions).

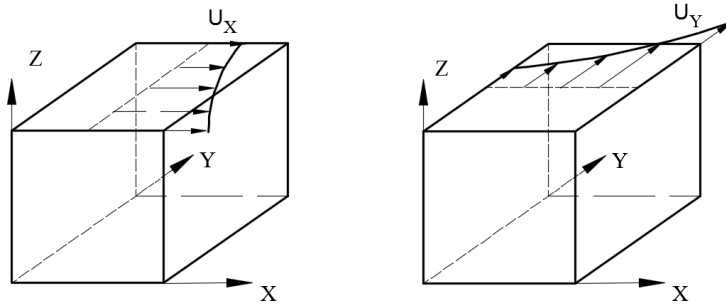


Figure 2.7 Fluid element adjacent to the wall (the wall is represented by the plane $Z = 0$).

The Navier-Stokes equation for a location on the wall ($Z = 0$) is,

$$\frac{\partial \vec{U}_{Z=0}}{\partial t} + (\vec{U}_{Z=0} \cdot \nabla) \vec{U}_{Z=0} = -\frac{1}{\rho} \nabla p_{Z=0} + \nu (\nabla^2 \vec{U})_{Z=0}, \quad \text{Eq. (2.26)}$$

where ν is kinematic viscosity.

On the left hand side of Eq. (2.26), because the velocity on the wall $\vec{U}_{Z=0}$ is the same everywhere (either zero or the same velocity as the movement of the wall)),

the term $\nabla \vec{U}_{Z=0}$ is zero; On the right hand side of Eq. (2.26), the terms of $\frac{\partial^2 U_X}{\partial X^2}$, $\frac{\partial^2 U_Y}{\partial Y^2}$, $\frac{\partial^2 U_X}{\partial Y^2}$, $\frac{\partial^2 U_Y}{\partial X^2}$, $\frac{\partial^2 U_Z}{\partial X^2}$, $\frac{\partial^2 U_Z}{\partial Y^2}$ inside the second term are all zeros (the second derivatives in the wall parallel directions are zeros because the velocities in the wall parallel components are all the same (zero or a constant)). Combining the analysis on the left and the right hand sides of Eq. (2.26) gives,

$$\frac{\partial \vec{U}_{Z=0}}{\partial t} = -\frac{1}{\rho} \nabla p_{Z=0} + \nu \left[\frac{\partial^2 U_X}{\partial Z^2} \vec{i} + \frac{\partial^2 U_Y}{\partial Z^2} \vec{j} + \frac{\partial^2 U_Z}{\partial Z^2} \vec{k} \right]_{Z=0}. \quad \text{Eq. (2.27)}$$

Forming the cross product of Eq. (2.27) with wall-normal vector \vec{k} gives,

$$\vec{k} \times \frac{\partial \vec{U}_{Z=0}}{\partial t} = -\vec{k} \times \frac{1}{\rho} \nabla p_{Z=0} + \nu \left[-\frac{\partial^2 U_Y}{\partial Z^2} \vec{i} + \frac{\partial^2 U_X}{\partial Z^2} \vec{j} + 0 \right] \quad \text{Eq. (2.28)}$$

The gradient of vorticity in the wall normal direction is,

$$\frac{\partial \omega_X}{\partial Z} = \frac{\partial}{\partial Z} \left(\frac{\partial U_Z}{\partial Y} - \frac{\partial U_Y}{\partial Z} \right) = \frac{\partial^2 U_Z}{\partial Y \partial Z} - \frac{\partial^2 U_Y}{\partial Z^2} \cong -\frac{\partial^2 U_Y}{\partial Z^2}, \quad \text{Eq. (2.29)}$$

$$\frac{\partial \omega_Y}{\partial Z} = \frac{\partial}{\partial Z} \left(\frac{\partial U_X}{\partial Z} - \frac{\partial U_Z}{\partial X} \right) = \frac{\partial^2 U_X}{\partial Z^2} - \frac{\partial^2 U_Z}{\partial X \partial Z} \cong \frac{\partial^2 U_X}{\partial Z^2}. \quad \text{Eq. (2.30)}$$

The velocity of the wall normal component is zero on the wall and assumed to be negligible next to the wall, therefore the terms of $\frac{\partial^2 U_Z}{\partial Y \partial Z}$ and $\frac{\partial^2 U_Z}{\partial X \partial Z}$ are both neglected.

Eq. (2.29) and Eq. (2.30) are the two terms in the square bracket of Eq. (2.28). Now Eq. (2.28) can be written as,

$$\nu \left[\frac{\partial \omega_X}{\partial Z} \vec{i} + \frac{\partial \omega_Y}{\partial Z} \vec{j} \right] = \vec{k} \times \left[\frac{\partial \vec{U}_{Z=0}}{\partial t} + \frac{1}{\rho} \nabla p_{Z=0} \right]. \quad \text{Eq. (2.31)}$$

Equation Eq. (2.31) is the well-known equation of the vorticity production rate from the wall. The terms $\nu \frac{\partial \omega_X}{\partial Z}$ and $\nu \frac{\partial \omega_Y}{\partial Z}$ represent the ‘total vorticity flux out of the solid surface per unit area per unit time’ [31]. It shows that the production of wall-parallel components of the vorticity is due to the acceleration of the wall and the pressure gradient on the wall. The vorticity production in the wall-normal direction can be derived from the solenoidal feature of the vorticity:

$$\nu \frac{\partial \omega_Z}{\partial Z} = -\nu \left(\frac{\partial \omega_X}{\partial X} + \frac{\partial \omega_Y}{\partial Y} \right). \quad \text{Eq. (2.32)}$$

Eq. (2.32) shows that the vorticity in the wall normal direction is due to the divergence of vorticity in the wall tangential directions. The vorticity in the wall normal direction can also be termed as the curl of shear stress,

$$\begin{aligned}
\nu \frac{\partial \omega_z}{\partial z} &= -\nu \left(\frac{\partial \omega_x}{\partial x} + \frac{\partial \omega_y}{\partial y} \right) = -\frac{\mu}{\rho} \left(-\frac{\partial U_y}{\partial x \partial z} + \frac{\partial U_x}{\partial y \partial z} \right) = \frac{1}{\rho} \left(\frac{\partial \tau_y}{\partial x} - \frac{\partial \tau_x}{\partial y} \right) \\
&= \frac{1}{\rho} \nabla \times (\tau_x \vec{i} + \tau_y \vec{j}),
\end{aligned} \tag{2.33}$$

where μ is the dynamic viscosity.

For a uniform flow along a flat surface, the wall parallel velocities are uniform, and the vorticity in the wall normal component is of orders of magnitude lower than the wall parallel components [31]. If the wall parallel velocities adjacent to the wall are not uniform, as shown in Figure 2.7, and the terms $\frac{\partial U_y}{\partial x \partial z}$ and $\frac{\partial U_x}{\partial y \partial z}$ are not equal, the vorticity in the wall normal component is generated. This mechanism of vorticity generation from a flat wall will be further discussed in Section 4.2 together with numerical results to show the vorticity source of ground vortices.

2.2.4 Vorticity transport equation

The derivation of the vorticity transport equation starts from the momentum conservation of Navier-Stokes equations with conditions of incompressible, Newtonian fluid and without a body force,

$$\frac{\partial \vec{U}}{\partial t} + (\vec{U} \cdot \nabla) \vec{U} = -\frac{1}{\rho} \nabla p + \nu \nabla^2 \vec{U}. \tag{2.34}$$

By taking curl on the momentum equation the vorticity transport equation is obtained (the detail of the derivation is shown in many textbooks of vorticity dynamics, e.g. [60]),

$$\frac{D \vec{\omega}}{Dt} = \vec{\omega} \cdot \nabla \vec{U} + \nu \nabla^2 \vec{\omega}. \tag{2.35}$$

The first term on the right hand side of vorticity transport equation represents the stretching and tilting of a vortex. The second term represents the rate of change of vorticity due to molecular diffusion.

2.2.5 Profile of vortex

The concentrated vorticity is present in tornados [61], wing tip vortices [62, 63] and ground vortices [26, 33] among others, and ideally they feature an axisymmetric profile. The velocity components as expressed in a cylindrical coordinate system are the tangential velocity, the radial velocity and the axial velocity. The magnitude of the tangential velocity is found to be of orders higher than the axial velocity and radial velocity for an intense vortex [64], so the majority of the vortex models concentrate on the description of the profile of the tangential velocity. Examples of well-known vortex models are the Rankine model [65], the Kaufman-Scully model [66], the Lamb-Oseen model [67] among others. The Lamb-Oseen vortex model is

extensively applied for the simulation of the vortex generated from a wing tip. A generic flow field for the far wake generated by an airplane was simulated by superposing Lamb-Oseen vortices as reported in [68]. A single vortex generated by a wing was studied in [69] and it was found that the vortex decay in the vortex core follows the characteristic of the Lamb-Oseen vortex, even though external turbulence was added. Therefore, in order to simulate the vortex that shed from upstream parts of lifting surfaces to impinge onto the propeller, the model of Lamb-Oseen vortex is chosen and its profile is elaborated as below.

The derivation of the velocity profile of the Lamb-Oseen vortex starts from vorticity transport equation of Eq. (2.35). Considering the two dimensional flow, the term $\vec{\omega} \cdot \nabla \vec{U}$ becomes zero (no tilting and no stretching). The velocity component is always perpendicular to the vorticity vector, so the term of $(\vec{U} \cdot \nabla) \vec{\omega}$ becomes zero. The detail of the derivation is not elaborated here, and the distribution of the circulation in the vortex is directly given as [70],

$$\Gamma(r, t) = \Gamma_{\infty} (1 - e^{-\frac{r^2}{4\nu t}}). \quad \text{Eq. (2.36)}$$

The circulation defined in the form of the path integral is,

$$\Gamma(r, t) = 2\pi r U_t. \quad \text{Eq. (2.37)}$$

Substitute Eq. (2.37) into Eq. (2.36) yields,

$$U_t = \frac{\Gamma_{\infty}}{2\pi r} (1 - e^{-\frac{r^2}{4\nu t}}). \quad \text{Eq. (2.38)}$$

One further step taken is to eliminate the term of time, which makes this formula applicable for a given strength and a given dimension of a vortex core. A definition introduced here is the vortex core radius, where the maximum tangential velocity of the vortex is located. By taking a partial differentiation of r and the result to be zero which is the necessary condition of a peak value, we obtain,

$$\frac{1}{4\nu t} = \frac{1.25643}{r_c^2}. \quad \text{Eq. (2.39)}$$

Substituting Eq. (2.39) into Eq. (2.38) yields,

$$U_t = \frac{\Gamma_{\infty}}{2\pi r} (1 - e^{-1.25643 \frac{r^2}{r_c^2}}). \quad \text{Eq. (2.40)}$$

The profile of the tangential velocity is obtained now. This profile will be applied for the study of the interaction between an externally induced vortex and the propeller (Section 2.3.2, Chapters 5, 6, and 7).

The pressure distribution in the vortex can also be deduced from the distribution of the tangential velocity. By the strategy of order analysis, the continuity and momentum equations of Navier-Stokes equations are simplified, and the detail of the derivation is given in [62]. The formula of the momentum equation in the radial direction is then formulated as,

$$\frac{dp}{d\bar{r}} = \rho \frac{U_t^2}{\bar{r}}. \quad \text{Eq. (2.41)}$$

The pressure far beyond the centre of the vortex is assumed to be the ambient pressure p_∞ , and the pressure in the centre of the vortex is,

$$p_0 = p_\infty - \rho \int_0^\infty \frac{U_t^2}{\bar{r}} d\bar{r}. \quad \text{Eq. (2.42)}$$

As shown in Eq. (2.42), the pressure in the centre of the vortex can be calculated after the tangential velocity is already known, and it is lower than the ambient pressure. The pressure in an arbitrary radial position is retrieved after the pressure in the vortex centre is known,

$$p(r_1) = p_0 + \rho \int_0^{r_1} \frac{U_t^2}{\bar{r}} d\bar{r}. \quad \text{Eq. (2.43)}$$

Based on the above equations, the profiles of the vorticity, the circulation, the tangential velocity, and the pressure along the radial direction of the Lamb-Oseen vortex are plotted in Figure 2.8, and these values at the vortex centre are also highlighted. The vorticity decreases monotonically as the radius increases, and the magnitude of vorticity at the vortex core radius is 28% of that in the vortex centre. The circulation which is a cumulative quantity of vorticity increases monotonically as the radius increases. It has 72% of the total circulation located in the core region of the vortex. The tangential velocity reaches its maximum at the position where it is defined as the vortex core radius. There is a pressure decrease toward the vortex centre. The pressure magnitude relative to the ambient pressure at the vortex core radius is 47% of that at the vortex centre.

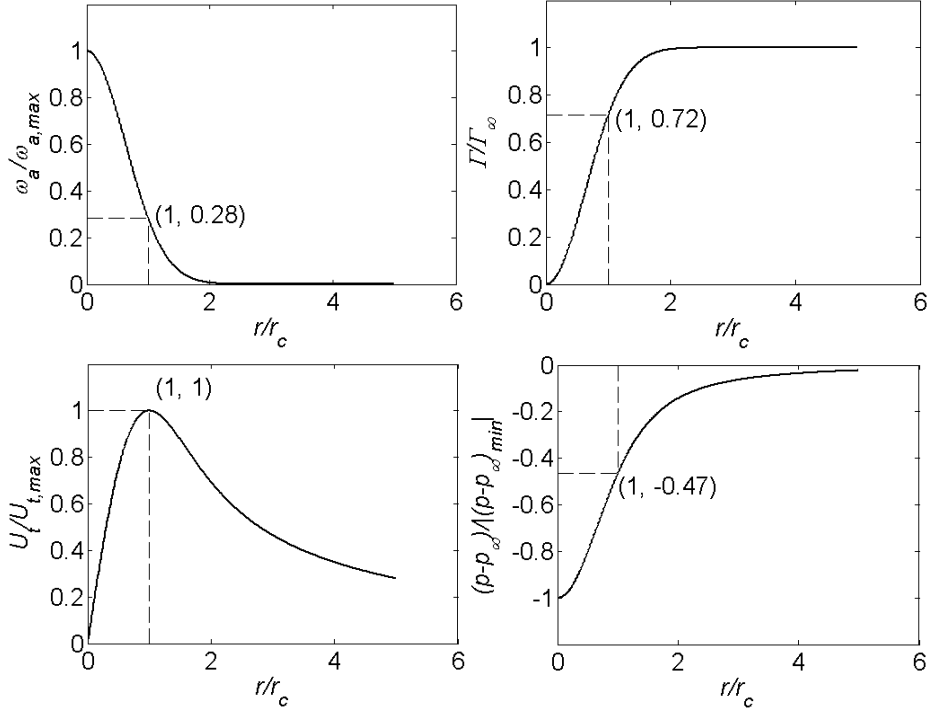


Figure 2.8 Profiles of the Lamb-Oseen vortex model. Top left; the axial vorticity; Top right: the circulation; bottom left: the tangential velocity; bottom right: the pressure.

2.3 Interaction between propeller and vortex by analytical models

After introductions of aerodynamics of propellers and vortices separately, aerodynamic interactions with each other are analysed as below.

2.3.1 Propeller induced flow field on the ground

An analytical model to represent the influence of the propeller on the ground is built in this section. The flow around the propeller can be represented by a doublet flow in an abstract sense (more complex model than this doublet model can be utilized, but for a simple description of the thrust of the propeller this model is assumed to be enough). The image method is employed to represent the induced flow of the doublet near the ground [71]. The analytical model with a pair of doublet flow models on the two sides of the ground is shown in Figure 2.9.

The stream function of the flow induced by a doublet of the strength κ is

$$\phi = \frac{\kappa}{2\pi} \frac{\cos\theta}{r} = \frac{\kappa}{2\pi} \frac{X/r}{r} = \frac{\kappa}{2\pi} \frac{X}{r^2} = \frac{\kappa}{2\pi} \frac{X}{X^2 + Z^2}. \quad \text{Eq. (2.44)}$$

The velocity field of the doublet flow is

$$U_X(X, Z) = \frac{\kappa}{2\pi} \frac{(X^2 + Z^2) - X(2X)}{(X^2 + Z^2)^2} = \frac{\kappa}{2\pi} \frac{(Z^2 - X^2)}{(X^2 + Z^2)^2}, \quad \text{Eq. (2.45)}$$

$$U_Z(X, Z) = \frac{\kappa}{2\pi} \frac{0 - X(2Z)}{(X^2 + Z^2)^2} = \frac{\kappa}{2\pi} \frac{-2XZ}{(X^2 + Z^2)^2}. \quad \text{Eq. (2.46)}$$

Applying the image method, the velocity at the position of the wall ($Z = -h$) is doubled for the X component, and zero for the wall normal component,

$$U_X(X, -h) = \frac{\kappa}{\pi} \frac{(h^2 - X^2)}{(X^2 + h^2)^2}, \quad \text{Eq. (2.47)}$$

$$U_Z(X, -h) = 0. \quad \text{Eq. (2.48)}$$

The surface pressure is then obtained by the Bernoulli's equation,

$$p(X, -h) = p_\infty - \frac{1}{2} \rho (U_X^2) = p_\infty - \frac{1}{2} \rho \left(\frac{\kappa}{\pi} \right)^2 \left(\frac{(h^2 - X^2)}{(X^2 + h^2)^2} \right)^2. \quad \text{Eq. (2.49)}$$

The pressure gradient on the ground is,

$$\frac{\partial p}{\partial X} = -\rho \left(\frac{\kappa}{\pi} \right)^2 * \frac{(h^2 - X^2) * (2X^5 - 4h^2 X^3 - 6h^4 X)}{(X^2 + h^2)^6}. \quad \text{Eq. (2.50)}$$

Due to the pressure gradient on the ground, vorticity generation rate can be determined from Eq. (2.31), and its two dimensional form is formulated as,

$$\nu \frac{\partial \omega_Y}{\partial Z} = (\partial p / \partial X) / \rho = - \left(\frac{\kappa}{\pi} \right)^2 * \frac{(h^2 - X^2) * (2X^5 - 4h^2 X^3 - 6h^4 X)}{(X^2 + h^2)^6}. \quad \text{Eq. (2.51)}$$

The profiles of the pressure and vorticity generation rate on the wall are plotted in Figure 2.10 for a doublet flow with the elevation of $h = 1.5 R$, where R represents the radius of the propeller. The magnitudes of Y component in the figures are scaled by $\frac{1}{2} \rho \left(\frac{\kappa}{\pi} \right)^2 \frac{1}{R^4}$, $\rho \left(\frac{\kappa}{\pi} \right)^2 \frac{1}{R^5}$ and $\left(\frac{\kappa}{\pi} \right)^2 \frac{1}{R^5}$ respectively.

The doublet flow induces a pressure decrease on the ground in the proximity to it as shown in the left hand side of Figure 2.10, and it reaches the minimum value at the position of $X/R = 0$. Due to the non-uniform pressure distribution, there is a negative pressure gradient. As formulated in Eq. (2.31), the pressure gradient on the ground is the source of vorticity. Therefore, the propeller, in this case simply represented by the doublet, generates the self-induced vorticity from the ground, as shown in the right hand side of Figure 2.10.

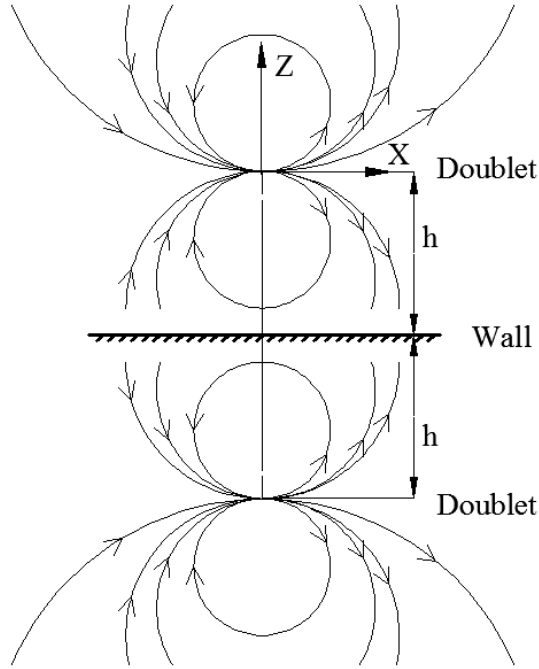


Figure 2.9 Image method on the doublet flow near the wall to represent the propeller induced flow near the ground.

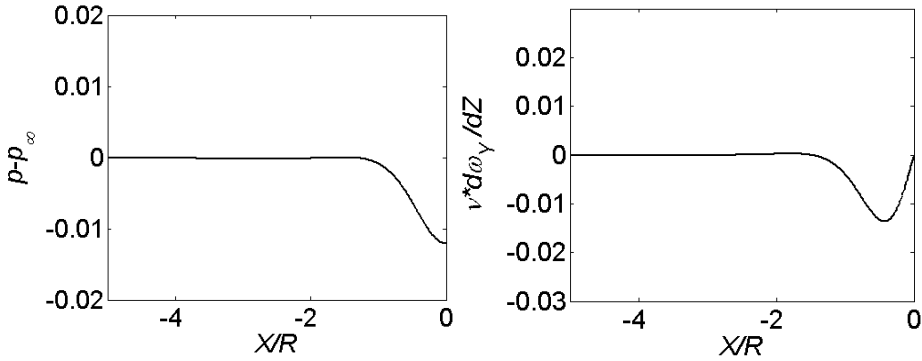


Figure 2.10 Distributions of pressure and production rate of vorticity on the wall due to the doublet flow.

It is found in Eq. (2.51) that the magnitude of the pressure gradient on the ground depends on the strength of the doublet, κ , and the height of the propeller above the ground, h . As the strength of the doublet increases and the height decreases, the vorticity generated from the ground is supposed to increase. This analysis helps us to determine parameters governing the strength of ground vortices, which is further discussed by a more complex model (actuator disk model) in Chapter 3 and 4. Next,

another simplified model is utilized to determine the parameters governing the impact of an externally generated vortex on a propeller, which is intended for the determination of the parameters governing this phenomenon and prepared for the studies in Chapter 5, 6 and 7.

2.3.2 Impact of a streamwise vortex on the propeller inflow

In this simplified model, the incoming vortex and the propeller are represented by the red dashed circle and the blue circle respectively, as shown in Figure 2.11. The vortex centre is located at C ; the tangential velocity of the vortex is $U_{t,C}$; and the circulation is Γ_∞ . The centre of the propeller is located at O ; the rotation speed is n ; the induced velocities of the vortex projected in the tangential and radial directions of the propeller are represented by $U_{t,i}$ and $U_{r,i}$. The rotation direction of the vortex is the same as that of the propeller, so the vortex is denoted as a co-rotating vortex as shown in Figure 2.11. Because the induced radial velocity has a negligible effect on the blade loading, it is ignored.

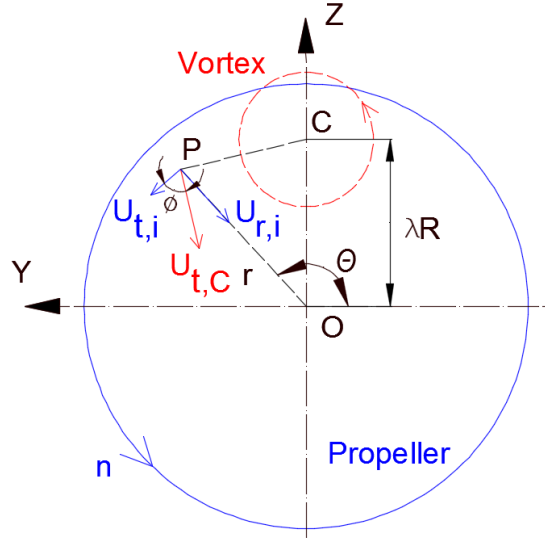


Figure 2.11 Induced velocities on the propeller inflow due to a vortex. All parameters associated to the vortex are represented by the red colour, and all parameters associated to the propeller are represented by the blue colour. Viewed from the front.

The induced tangential velocity on the blade is formulated as,

$$U_{t,i} = U_{t,C} \cdot \cos(\phi). \quad \text{Eq. (2.52)}$$

ϕ has the same value as $\angle CPO$, so

$$\cos(\phi) = \cos(\angle CPO) = \left(\frac{PC^2 + PO^2 - CO^2}{2 \cdot PC \cdot PO} \right). \quad \text{Eq. (2.53)}$$

The parameters in Eq. (2.53) are defined by,

$$PC = \sqrt{(r \cdot \cos\theta)^2 + (r \cdot \sin\theta - \lambda R)^2}, \quad \text{Eq. (2.54)}$$

$$PO = \sqrt{(r \cdot \cos\theta)^2 + (r \cdot \sin\theta)^2}, \quad \text{Eq. (2.55)}$$

$$CO = \lambda R, \quad \text{Eq. (2.56)}$$

where, r and θ are defined in Figure 2.11, λR is the radial distance from the impinging position to the centre of the propeller.

By employing the Lamb-Oseen vortex model from Eq. (2.40) as the impinging vortex,

$$U_{t,c} = \frac{\Gamma_\infty}{2\pi r_c} \left(\frac{1 - e^{-1.25643(PC/r_c)^2}}{PC/r_c} \right), \quad \text{Eq. (2.57)}$$

the induced tangential velocity on the propeller inflow can be calculated.

When the impinging radial position is $\lambda = 0.7$, the contour of the induced tangential velocity scaled by $\Gamma_\infty/2\pi$ is plotted in Figure 2.12. It features a disk region with negative induced tangential velocity, and the rest has positive induced tangential velocity. The dividing curve for the positive and negative value is the circle of $PC^2 + PO^2 - CO^2 = 0$, with a diameter of CO . The summation of the positive values of the induced tangential velocity is 2.14 times of the negative values at the current setting, so the combined effect is consistent with positive tangential velocity. The effect of induced tangential velocity on the propeller is analysed as below.

For an isolated propeller, the tangential velocity of the blade is $2\pi nr + U_{t,i0}$ as shown in Figure 2.3. As there is a vortex in the inflow of the propeller, there is an additional tangential velocity on the blade, $U_{t,i}$, which is shown in Figure 2.13. The induced positive tangential velocity decreases the angle of attack of the blade cross section; and vice versa for the negative induced tangential velocity. Consequently, the local loading decreases for the positive tangential velocity; and vice versa for the negative tangential velocity. The additional axial velocity involved in the vortex is neglected, because its magnitude is much lower than the tangential velocity for a strong vortex as reported in [64], and its influenced area is relatively small compared with the induced tangential velocity.

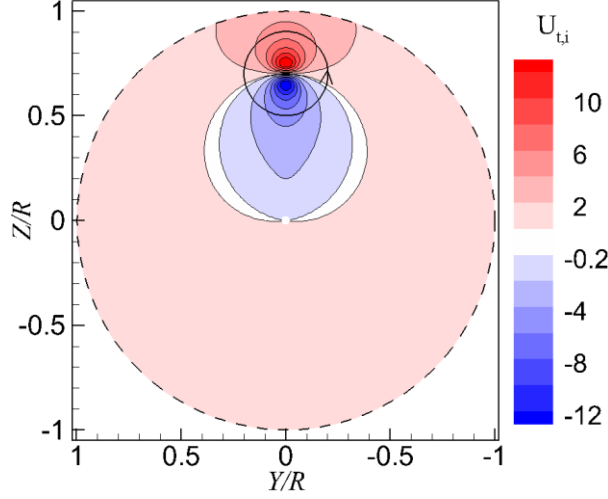


Figure 2.12 Example of the induced tangential velocity on the propeller disk due to the co-rotating vortex located at $\lambda = 0.7$. Viewed from the front. $U_{t,i}$ is scaled by $\Gamma_\infty/2\pi$.

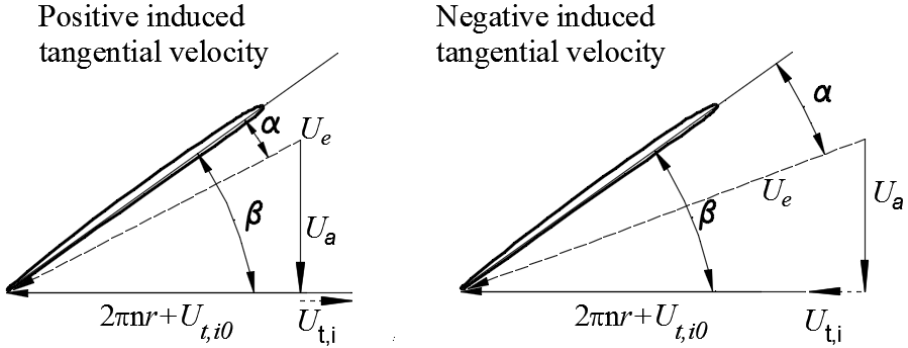


Figure 2.13 The effect of the induced tangential velocity on the incidence angle of the blade cross section. Left: positive induced tangential velocity; right: negative induced tangential velocity.

As mentioned before, the overall effect of the co-rotating vortex impingement on the propeller has a positive induced tangential velocity, so the loading on the propeller decreases. The opposite is true for the counter-rotating vortex impingement.

There are several parameters determining the distribution of the induced tangential velocity $U_{t,i}$ as shown in Eq. (2.52). First, the induced tangential velocity at the disk depends on the position, i.e., (r, θ) ; when the blade is rotating, the blade has a cyclic force due to the change of the induced tangential velocity. Second, the induced tangential velocity depends on the tangential velocity of the vortex, in terms of the magnitude and the rotation direction. Furthermore, the induced tangential

velocity also depends on the impinging position of the vortex on the propeller, which is represented by λ .

2.4 Conclusions

The momentum theory and blade element method are introduced to explain the working mechanism of propellers. The momentum theory was prepared for the study of ground vortices induced by the propeller in Part II of the thesis, in which it is implemented to the *CFD* calculations. The blade element method was prepared for the analysis of the impact of the vortex on the angle of attack of the blade, which determines the loading of the propeller, which will be discussed both in Part II and III.

The generation rate of vorticity from a flat wall is derived from the Navier-Stokes equations by following the work of Lighthill. From a simplified case by regarding a propeller as a doublet, the generation of vorticity is explicitly shown to be originated from the pressure gradient on the ground. The generation rate of vorticity is dependent on the strength of the doublet and the height of the doublet above the ground.

The Lamb-Oseen vortex is found to well represent the wing tip vortex from literature. The distribution of the tangential velocity of such a vortex model is derived which is the solution of Navier-Stokes equations. By applying the Lamb-Oseen vortex to impinge onto a propeller, an analytical investigation is performed to investigate the inflow of the propeller. Additional tangential velocity is observed in the inflow of the propeller due to the impinging vortex, which changes the local angle of attack of the blade. It is deduced that the parameters, i.e. the strength of the impinging vortex, the rotation direction of the vortex relative to the propeller, and the impinging radial position, determine the impact of the vortex on the performance of the propeller. In addition, the distribution of the tangential velocity of the wing tip vortex is prepared to be implemented in the *CFD* simulations during the study of the interaction between an externally induced vortex and the propeller in Part III.

The impact of the propeller on the vortex is not investigated analytically in this chapter, but the Kelvin's theorem and vorticity transport equation are prepared for this purpose, which will be analysed on the experimental and numerical results in the following chapters.

2.5 Discussion

From the theoretical background of propellers, the vortex, and analytical models to estimate the interaction between each other, the parameters governing the physics of the phenomena are found. For the ground vortices, the strength and the height of the doublet representing the flow around the propeller determine the generation of vorticity. For the interaction of an external vortex with a propeller, the induced

tangential velocity of the vortex determines the effective angle of attack of the propeller blades. The vorticity transport equation implicitly showed that the vortex could be tilted, stretched and diffused during the interaction with the propeller. For the study of the above parameters, methods and results are going to be discussed in the following chapters.

In Chapter 2, the vorticity production rate by a doublet near the ground is analysed in a two dimensional flow. In order to check the validity of this approximate model for a three dimensional flow, the flow fields will be resolved by means of numerical simulations with the help of the actuator disk model. In addition, the numerical simulations will be validated by the experimental measurements with the help of Particle Image Velocimetry (*PIV*) measurements. At the same time, the velocities, which characterise the flow field including the ground vortices, are also utilized for the temporal and the modal analysis of ground vortices. As found in Chapter 2, the vortex has an impact on the propeller inflow, therefore the vortex has an impact on the propeller performance from the blade element method. In order to quantify this impact, experimental measurements are conducted with the help of the rotating shaft balance (*RSB*). The details of the analysis methods and results will be presented in Chapter 3 and Chapter 4 which form Part II of the thesis.

From the qualitative analysis of the impact of the externally generated vortex on the propeller as shown in Chapter 2, it is found that this impact depends on several parameters, i.e. the strength, the off-axis distance with respect to the propeller centre line, the phase angle of the blade, etc. In order to quantify the impact of these parameters of the vortex on the propeller, the vortex is quantified by the *PIV* measurements, and the propeller performance is obtained with the help of *RSB* measurements and *CFD* simulations. In addition, in order to investigate the response of the vortex to the propeller, which was analysed theoretically by the vorticity transport equation in Chapter 2, the flow fields including the vortex are resolved with the help of *PIV* measurements and *CFD* simulations. The detail of the analysis methods and results will be presented in Chapter 5, 6 and 7, as well as Appendix E, F, G, and H.

Part II

Interaction between propeller and its self-induced vortices

Chapter 3 Tools and methods for the investigation of interaction between propeller and its self-induced vortices

In order to investigate the generation and behaviour of ground vortices in interaction with a propeller, the characteristics of ground vortices expressed through the distribution of velocities need to be obtained. The measurements of the velocities are conducted by utilizing the technique of Particle Image Velocimetry (*PIV*) in wind tunnel tests. The application of Lighthill's vorticity generation equation requires the pressure gradient and vorticity gradient on the ground; these are obtained from numerical analyses of Large Eddy Simulations (*LES*). The performance of the propeller influenced by the ground vortices is measured by a rotating shaft balance. A detailed discussion on the applied techniques is provided in the following sections.

3.1 Wind tunnel and propeller rigs

3.1.1 Open jet facility

The experimental tests were carried out in a low-speed, closed-loop open-jet wind tunnel in Delft University of Technology, as shown in Figure 3.1. The tunnel has an octagonal test section, and the maximum height and width is $2.85\text{ m} \times 2.85\text{ m}$ ($18 R \times 18 R$, where R is the propeller radius).

The inflow velocity was set at a relatively low speed of 2.7 m/s , which is chosen to achieve high thrust coefficients needed to generate ground vortices. This determination is based on the research reported in [29, 33] which showed that the occurrence and strength of ground vortices were related to the ratio between the inlet velocity of the turbofan and the free stream velocity. The measurement and analysis of the turbulence intensity of the flow at such a free stream velocity is reported in Appendix B. It is 0.5% in the region outside the boundary layer. In the current study only the head wind condition is chosen. This condition is obtained by setting the axis of the propeller aligned with the free stream direction, but findings from this case, especially the analysis of the vorticity source, can also be applied for other situations, e.g. the cross wind condition, the quiescent condition and the take-off condition.

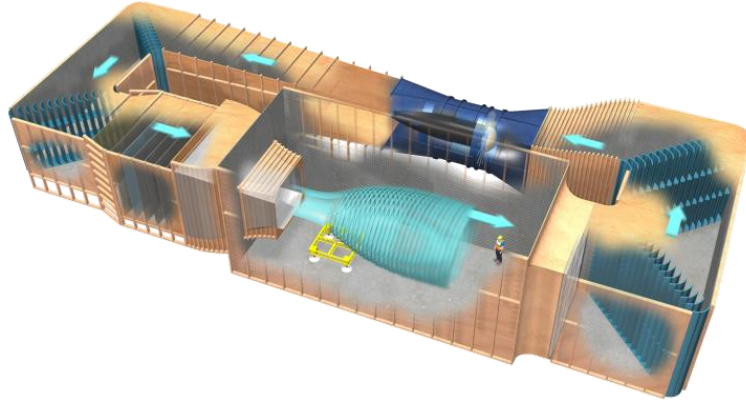


Figure 3.1 General layout of Open Jet Facility (*OJF*) in Delft University of Technology.

3.1.2 Experimental setup

The radius of the propeller, R , is 0.152 m . The selection was based on the availability of this propeller. The propeller size was originally selected to fit into the infrastructure of the *LSL* wind tunnel ($1.80\text{ m} \times 1.25\text{ m}$) of Delft University of Technology. The availability of the propeller for use in the *OJF* has the benefit, that even at high thrust conditions, the wind tunnel effects are relatively small. The correction of the free stream velocity for the highest thrust setting during the study of ground vortices is -2.80% , and that during the study of the interaction between an external vortex and the propeller is -0.38% . The detail of the correction method was reported in [72] by considering that the propeller entrains the still air outside the tunnel into the main stream. In addition, the PIV measurements become convenient if the field of view is relatively small. In order to resolve the flow field which involves ground vortices, and the flow field which captures the interaction between the impinging vortex and the propeller slipstream, the field of view is limited due to the required spatial resolution. Therefore, the propeller model cannot be so big.

The blade geometric pitch angle (β as shown in Figure 2.3) varies from 53° to 32° from the root to the tip of the blade as shown by the black curve in Figure 3.2, and it is set to 40 degrees at $0.7 R$ which corresponds to a typical high loading condition. One profile of the cross section of the blade was already shown in Figure 2.3 ($0.7 R$ radial position). The chord length distribution along the radial direction is shown by the red curve in Figure 3.2, and the chord length at 0.7 radial position is $0.25 R$.

The maximum rotating speed of the propeller in our test was 6000 rpm , which corresponds to a Mach number at the blade tip of 0.28 , and a Reynolds number of $113,000$. Because the propeller was designed for the Fokker F29 conceptual aircraft, the scaling effects compared to the full scale propeller cannot be provided. However,

an estimate can be made by considering a similar aircraft of Fokker F27 (with engine PW127B of rotating speed 1200 *rpm* [73]). This corresponds to a tip Mach number of approximately 0.67. It can be found that the Mach number of the scaled model is lower than the real propeller. Although the chord length of the blade tip of Fokker F27 is not available for us, the size of the real propeller is definitely several times of our model; the tip speed is also shown to be 2.4 times as high as our model. Therefore, the Reynolds number of the real propeller is approximately one order of magnitude higher than our model.

Although the Mach number and the Reynolds number are not achieved to be the same as the real situation, the non-dimensional parameter, i.e. the advance ratio J , is set at realistic values in our measurements. The advance ratio is one of the important parameters for propeller operations. It is set in the range corresponding to the taking off condition for studying ground vortices, and in the range corresponding to the cruise condition for studying the interaction between an external vortex and the propeller.

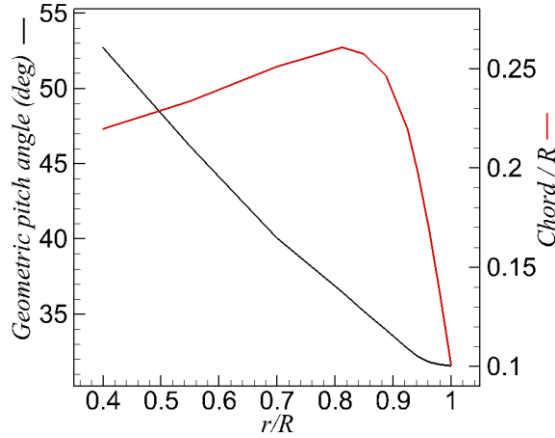


Figure 3.2 Distributions of the geometric pitch angle and chord length along the radial direction of the blade.

The set up with an eight bladed propeller, which is installed near a flat table to represent the ground operation of the propeller, is shown in Figure 3.3. The total length of the propeller model is $6R$, involving the spinner, the hub (with diameter of 0.084 m) and the nacelle. The width of the ground table is $18R$, and the radius of the propeller inflow stream tube (stream tube upstream of the propeller describes a virtual domain in which the flow enters the propeller, as shown in Figure 2.1) is $3.0R$ at $T_c = 63.3$, which is the highest propeller thrust setting of our tests. The width of the table is enough to avoid any influence from the table side edges. The distance from the leading edge of the table to the projection of the blade leading edge on the ground is $6R$. The propeller suction induces a pressure gradient on the ground table, and it is found that the pressure gradient at $6R$ upstream of the

propeller on the ground is negligible, which is shown in the next chapter. It can be concluded that the propeller influence on the table leading edge is negligible.

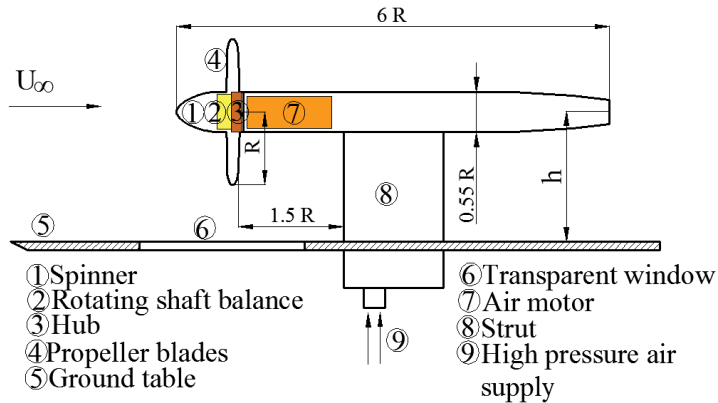


Figure 3.3 Schematic overview of the propeller model and experimental arrangement.

The ground table is raised 0.3 m ($2R$) above the bottom of the exit of the wind tunnel, and its leading edge has a triangle shape with a sharp edge toward the free stream (as shown in Figure 3.3). Such an arrangement of the ground table avoids the boundary layer of the wind tunnel wall and generates a new boundary layer. The analysis of the boundary layer is described in Appendix B. Because one main concern of this research is to evaluate the vorticity source of ground vortices from pressure gradient on the wall, the factors from interference of the leading edge are not systematically studied, for example, different shapes of the leading edge of the ground table.

The ground table has a transparent window insert (part 6 as shown in Figure 3.3), which allows optical access for *PIV* cameras. The height of the propeller from the ground table is defined by the distance from the propeller centreline to the ground, denoted as h . By moving the ground table vertically, the elevation of the propeller model is changed.

3.1.3 Rotating shaft balance and air motor

The propeller is driven by a *TDI* 1999 air motor, which is represented by part 7 in Figure 3.3 and is shown in detail on the right hand side of Figure 3.4. The maximum power of the engine is 98 HP (73.09 KW) when operated at air supply of 34.47 Bar and mass flow of 0.907 kg/sec . The temperature of the air is required to be between 15°C and 65.5°C upstream of the inlet of the motor, which is achieved by heating the air through the water tank with temperature of 65.5°C . The lubrication and cooling of the bearings are accomplished by an external two channel pulse oiler, which is pumped through an oil tank and ejected through the exit of the engine. The lubrication and cooling for the slip ring is through the static oil.

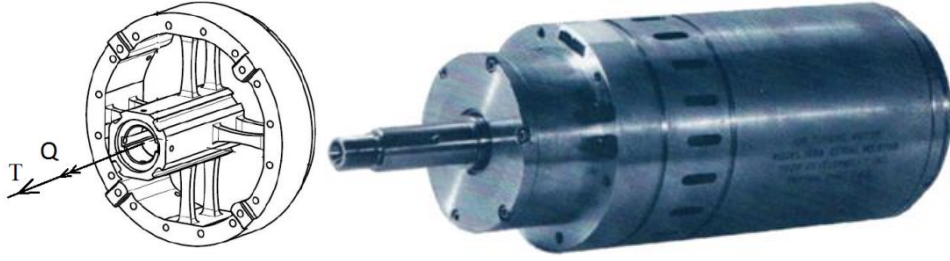


Figure 3.4 Left: Rotating shaft balance (*RSB*); right: air motor.

The propeller is directly coupled to a rotating shaft balance (*RSB*, represented by part 2 in Figure 3.3) that measures the isolated thrust and torque produced by the propeller, and the detail of the schematic of *RSB* is shown on the left hand side of Figure 3.4. The balance is mounted in front of the hub. The range of the balance is $\pm 350 \text{ N}$ for the axial force, and $\pm 30 \text{ Nm}$ for the axial torque.

3.2 *PIV* arrangement

3.2.1 Low frequency *PIV* arrangement

Planar *PIV* measurements were conducted at the wall parallel plane, whilst stereoscopic-*PIV* tests were carried out at the wall normal plane. These arrangements are chosen because the out of plane component of the velocity in the wall parallel plane is low and that in the wall normal plane is high. If the out of plane component of the velocity in the *PIV* measurement plane is large, the error of in-plane components of the velocity is high for a planar *PIV* measurement [74]. The measurement system was composed by two LaVision Imager Pro LX 16M cameras (*CCD* sensor of $4,870 \text{ pixels} \times 3,246 \text{ pixels}$, 12 bit resolution, $7.4 \mu\text{m}$ pixel pitch) and a Quantel Evergreen 200 laser (dual pulsed Nd:YAG laser, 200 mJ energy per pulse). The flow was seeded with micron-sized water-glycol particles produced by a SAFEX Twin Fog Double Power smoke generator inserted in the settling chamber.

The flow fields were captured using two different arrangements of the *PIV* system. For the *PIV* arrangement 1, measurements were conducted at the plane which is $\delta_{l,1} = 0.046 R$ ($0.1 \delta_{BL}$) above the ground, where δ_{BL} is the local thickness of the boundary layer tested during propeller absence (Appendix B), as shown in Figure 3.5 (a) and (b). The imaging system is based on a 35 mm Nikkor objective set at $f\# = 4$ and the magnification factor is 0.0735. The processing was conducted with the interrogation window size $128 \text{ pixels} \times 128 \text{ pixels}$, 75% overlap, the Gaussian-weighting function, and the vector pitch is 3.22 mm ($0.0212 R$).

For the second *PIV* arrangement, measurements were carried out at $\delta_{l,2} = 0.08 R$, which is 12 mm upstream of the leading edge of the root of the propeller blades, as shown in Figure 3.5 (c) and (d). In this case, the two cameras were

positioned with 45 degrees viewing angles, one in forward scatter and the other in backward scatter. The forward and backward scattering cameras are based on 200 mm Nikkor objectives set at $f\# = 5.6$ and $f\# = 4$ respectively. The magnification factor is 0.1076. The processing is conducted with interrogation window size of $128 \text{ pixels} \times 128 \text{ pixels}$, 75% overlap, Gaussian-weighting function, and the vector pitch is 2.21 mm ($0.0145 R$). In both arrangements, the number of image pairs recorded is 250 per testing condition.

The window size of $128 \times 128 \text{ pixels}$ corresponds to $12.9 \times 12.9 \text{ mm}$ in physical space. The choice of such a window size is due to the quality of the *PIV* images, which are poor due to the low seeding density and large illuminated region (low light intensity). Hence, a smaller interrogation window would cause many spurious velocity vectors.

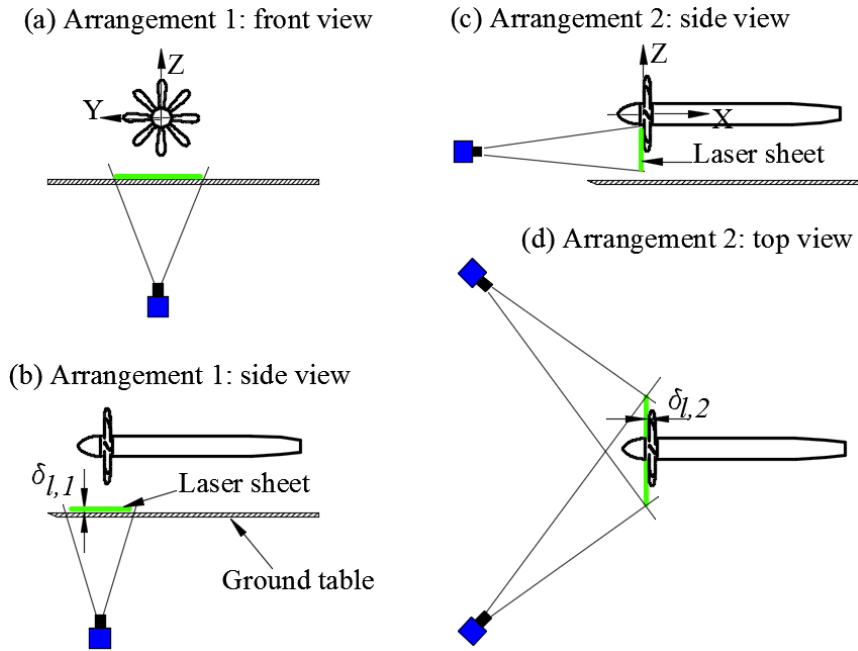


Figure 3.5 Setups of low frequency *PIV* measurements for the flow field near the ground and the flow field upstream of the propeller

The frame separation time is within the range of $10\text{-}100 \mu\text{s}$ for both the low and high frequency *PIV* measurements in the plane which is parallel to the ground; in the plane upstream of the propeller, it is within the range of $1\text{-}10 \mu\text{s}$. They are different between the two planes because the velocities in the two plane are different. The frame separation time was also changed for each loading condition of the propeller (the induced velocity by the propeller changes), in order to make sure that the particle movement is approximately 10 pixels .

The movement of the ground vortices is relatively slow, with period of 100-1000 *ms*, which is deduced from the analysis in Section 4.3.2. The period of the vortex movement is at least 1000 times larger than the frame separation time. Therefore, within the frame separation time, the vortex can be regarded as “frozen”.

In the plane upstream of the propeller, the blade movement was taken into account due to the blade reflection, which has an impact on the processing of *PIV* results. On the one hand, efforts were made to decrease the reflection. One technique is to paint the blade with a special material which is obtained from LaVision; the other technique is to move the measurement plane far away from the blade (but the plane can still capture the vortices). On the other hand, the time of the frame separation is set a relatively low value, i.e. 1-10 μs . For example, if the time of the frame separation is 5 μs and the *rpm* of the propeller is 6000, the movement of the blade tip is 0.14 *mm*. Hence, spurious vectors due to the blade movement may appear only in a small region in proximity of the light reflection on the blade.

3.2.2 High frequency *PIV* arrangement

The *PIV* measurements conducted at a low frequency with a relatively large field of view were utilized to cover the flow field as large as possible which involves ground vortices; and it is also utilized to analyse the impact of ground vortices on the propeller inflow. For the investigation of unsteady characteristics of ground vortices, high frequency *PIV* measurements are conducted. The field of view of the high frequency *PIV* measurement decreases with respect to the low frequency *PIV* measurements. The field of view of high frequency *PIV* measurement is located in the region where ground vortices have the most possibility to occur. This region is determined by analysing the results of low frequency *PIV* measurements, e.g. the positions of the dominant vortices in the measurement plane and the results are reported in [75].

For the *PIV* measurement at a high frequency, the seeding is still the same as that of low frequency *PIV* measurements. A Quantronix Darwin Duo Nd-YLF double pulse laser was used for illumination. The particle images are recorded by Photron FastCAM SA1.1 CMOS cameras (1024 \times 1024 *pixels* at 5400 *fps*, 12 *bits*, 20 μm pixel pitch). The processing was conducted with the interrogation window size 64 *pixels* \times 64 *pixels*, 50% overlap, the Gaussian-weighting function.

The setup of high frequency Stereoscopic-*PIV* measurements conducted at the wall parallel plane is shown in Figure 3.6 (a) and (b). The distance between the measurement plane and the ground is the same as that of low frequency *PIV* tests. The magnification factor is 0.2207. The measurement is conducted at a frequency of 1500 *Hz* for a trial, and then it is found that the flow features low frequency characteristics. Therefore, the measurements at this plane were conducted at a frequency of 500 *Hz* and sequences of 2000 image pairs were acquired.

Stereoscopic-*PIV* tests are carried out at the wall normal plane upstream of the propeller at $X/R = -0.16$, which was twice as far as that shown in Figure 3.5 (c) and (d) ($\delta_{l,3} = 2\delta_{l,2}$), because it is found that the reflection from the blade is strong when the measurement plane is too close to the blade. The forward and backward scattering cameras are based on 200 mm Nikkor objectives set at $f\# = 11$ and $f\# = 8$ respectively. The magnification factor is 0.1821. The flow field in this plane is dominated by the blade passing induced flow and features the frequency related to the propeller rotating speed. Therefore, the measurements at this plane were conducted at the frequency of 1500 HZ and sequences of 2500 image pairs were acquired.

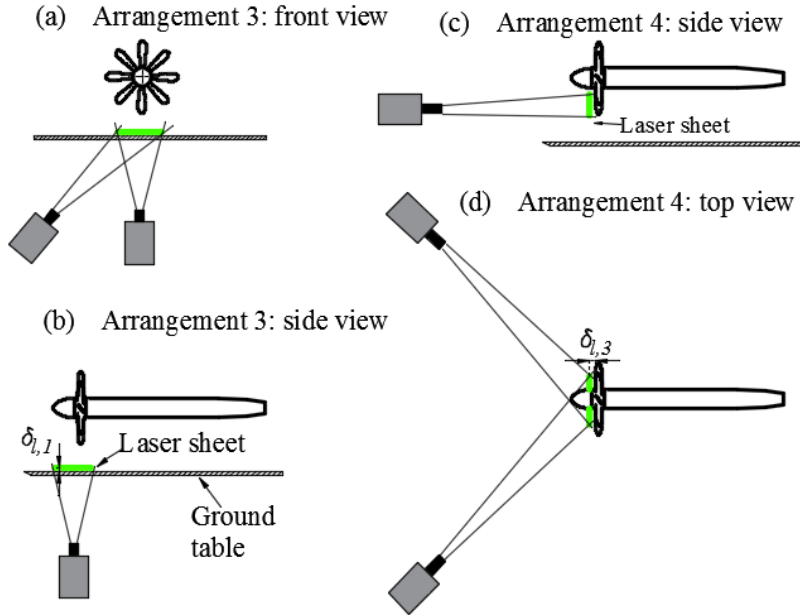


Figure 3.6 Setups of high frequency *PIV* measurements. Left column: arrangement for the measurement in the wall parallel plane; right column: arrangement for the measurement in the wall normal plane.

3.3 Error analysis of the experimental measurements

The propeller height is measured by a ruler with marks every 1 mm. Because of the difficulty in lining up the ruler mark with the tip point of the hub, the scatter of the propeller height measurement is about 2 mm, yielding a relative error of 1.3% of the propeller radius. The scatter of the time-averaged thrust (determined from repeated measurements, the same for the following quantities) is 0.36 N at a high value of the thrust of 66.33 N (relative error of 0.5%), and the scatter of the torque is 0.04 Nm at a high value of the torque of 5.46 Nm (relative error of 0.7%), both

with the confidence level of 95%. The scatter of rpm is 40 at 6250 rpm, and the relative error is 0.6%.

The uncertainties of *PIV* measurements are estimated by the image matching method [76]. The image matching method uses the measured velocity field to match the particle images of the recordings based on the processing algorithm (for example by window deformation or window shift). The approach detects particle images in each interrogation window. In case of exact velocity measurements, the particle images of the two recordings would match perfectly. In real experiments, the paired particle images do not match exactly and feature a positional disparity between them. The positional disparity is computed as the distance between the centroids of the particle images. The measurement uncertainty is determined within each interrogation window from the mean value and the statistical dispersion of the positional disparity vector.

For the low frequency *PIV* testes, the uncertainty of the instantaneous velocity fields at 95% confidence level is 0.02 m/s in the wall parallel plane. For the wall normal plane, the uncertainty is 0.18 m/s for the in-plane velocity components and 0.17 m/s for the out-of-plane velocity component.

For high frequency *PIV* tests, the uncertainty of instantaneous velocity fields at 95% confidence level is 0.04 m/s in the wall parallel plane. For the *PIV* measurement in the wall normal plane, the uncertainty is 0.04 m/s for the in-plane velocity components and 0.09 m/s for the out-of-plane velocity component.

For the error analyses of the *PIV* measurements as show above from conventional methods, it should be mentioned that they are underestimated. Firstly, the interrogation window size for the low frequency *PIV* measurements of ground vortices is as big as 128×128 pixels. Although the conventional methods correctly get the random part of the error, the systematic error due to the averaging over a large region is underestimated (the averaging area is 16 times as large as that of a good averaging window of 32× 32 pixels). In addition, some error sources are not accounted for the current analysis, e.g. particle velocity lag in the vortex centre where the swirl velocity is high. Furthermore, there is also an issue of high particle density and low intensity of the laser light (a large field of view is required during the tests), which introduces problems of multi-scattering and leads to inhomogeneities of the particle density.

3.4 Numerical simulations

3.4.1 Numerical methods

To obtain a detailed analysis of the propeller induced flow field a numerical study was performed based on the Large Eddy Simulations (*LES*). *LES* is a numerical approach to divide the variables (e.g. velocities) into resolved and

unresolved parts. The resolved parts or large-scale quantities are computed directly. The unresolved or sub-grid scale quantities are modelled, such as the dynamic Smagorinsky-Lilly subgrid model adopted in the thesis. The detail description of the *LES* method is elaborated in [77]. The main advantage of choosing *LES* for the simulation of ground vortices is that it is capable of capturing the unsteady effects much better than unsteady Reynold Averaged Navier-Stokes (*uRANS*) approach, and does not require such extensive computational power as Direct Numerical Simulation (*DNS*) [78]. In addition, the ground vortices induced by a suction tube model reported by using the *LES* approach are consistent with the experimental measurements as reported in [79].

The computational domain is a semi-cylindrical domain where the actuator disk model is inserted, as shown in Figure 3.7. The dimension of the domain is $[-13.1 R, 20.0 R]$ in the X component, and $[-13.1 R, 13.1 R]$ in the Y component on the ground plane. The dimension and the elevation of the actuator disk model are according to the experimental test conducted on the propeller model. The front and back boundaries of the semi-cylinder are prescribed as the velocity inlet and pressure outlet boundary conditions respectively, to allow the free stream to represent the headwind condition. The circular surface of the semi-cylinder is an outlet boundary condition as well, which is consistent with the flow condition in the open jet facility.

The velocity profile that is prescribed at the position of the velocity inlet is not available from experimental data, and it is approximated by the experimental data at the position which is aligned with the leading edge of the propeller blade (the experimental data is shown in Appendix B). This approximation would induce a thicker free-stream boundary layer in the *CFD* simulation than the experiment. The *CFD* simulations are mainly utilized to verify the vorticity source for the forming of ground vortices, and it is not intended to compare with experimental results in terms of the vorticity source. However, the *CFD* results are verified by Lighthill's equation. In fact, because the vorticity in the far field boundary layer is kept constant during the tuning of the thrust coefficient, the trend found in the *CFD* simulation should be the same as that found in the experiment. The fluctuation velocity at the velocity-inlet boundary is modelled by the vortex method, which is applied by adding "vortex points" on the velocity inlet via a fluctuating vorticity field. The magnitude of each vortex point is determined by the turbulent intensity and its distribution is assumed to be a Gaussian like profile (the detail of this vortex points method is reported in [80]). The turbulence intensity selected in the current study is 0.5% which is determined from the experimental measurement (Appendix B). No-slip wall boundary condition is prescribed on the ground. The pressure jump prescribed on the actuator disk model is according to that defined in section 2.1.2, and it is not repeated here again.

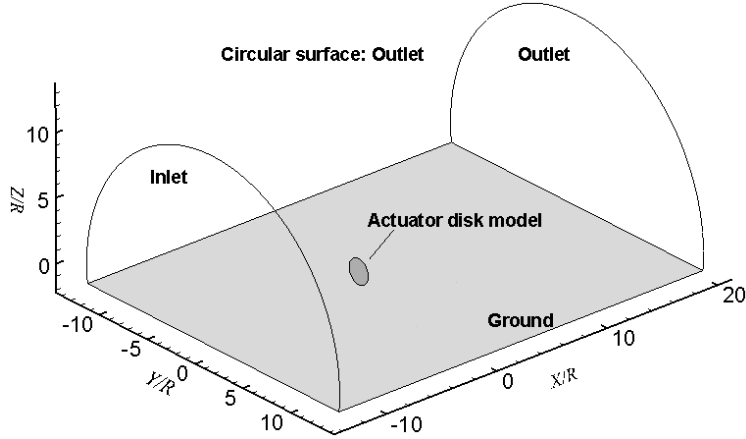


Figure 3.7 Overview of the computational domain and boundary conditions.

3.4.2 Mesh for the computation

The structured mesh is generated by *ANSYS ICEM* and shown in Figure 3.8. The thickness of the first layer next to the ground is $6.6 \times 10^{-4} R$, which achieves $Y^+ = 1$. The increase ratio of the mesh above the ground is 1.05. The dependence of the mesh size is studied by evaluating the convergence of the pressure distribution on the ground and the spectrum of the turbulent kinetic energy. The mesh sizes in the streamwise and the lateral directions are adapted by changing the number of nodes, whereas the mesh size in the wall normal direction is maintained constant ($Y^+ = 1$ is enough to resolve the turbulent boundary layer). The fine mesh, the medium mesh, and the coarse mesh have the numbers of nodes in the streamwise and lateral directions of 577×349 , 325×293 , 251×157 respectively. For the medium mesh which is considered to be enough for resolving our problem, the minimum size of the mesh in the lateral and the streamwise directions is $9.2 \times 10^{-3} R$.

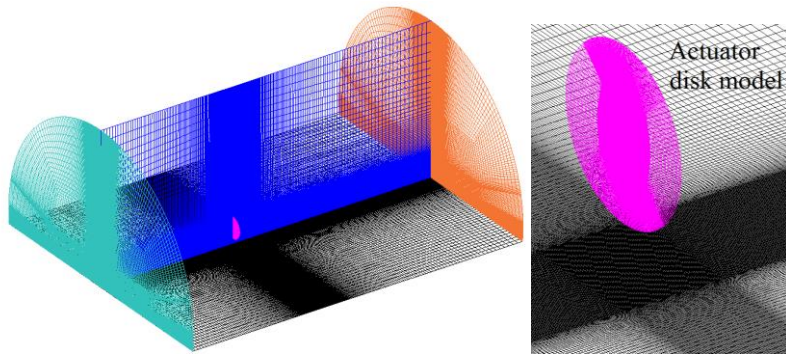


Figure 3.8 Left: structured mesh of the computational domain; right: detail of the mesh on the disk and below the disk.

The distribution of the pressure on the symmetric line on the ground is shown in Figure 3.9. According to this figure, the value of pressure at the node number of 20 million is approximately 2% lower than that at the node number of 39 million, and it is considered that the mesh converges at the node number of 20 million from the perspective of the numerical discretization. The velocity utilized for the normalization as shown in the label of Figure 3.9, U_{eq} , is the velocity in the slipstream of the propeller.

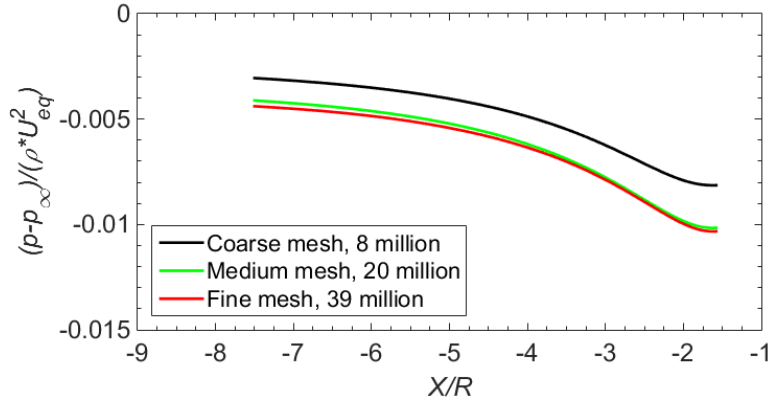


Figure 3.9 Study of mesh convergence by investigating the pressure distribution on the ground along the symmetrical line. Data are extracted from the intersection line between the meridional plane and the wall.

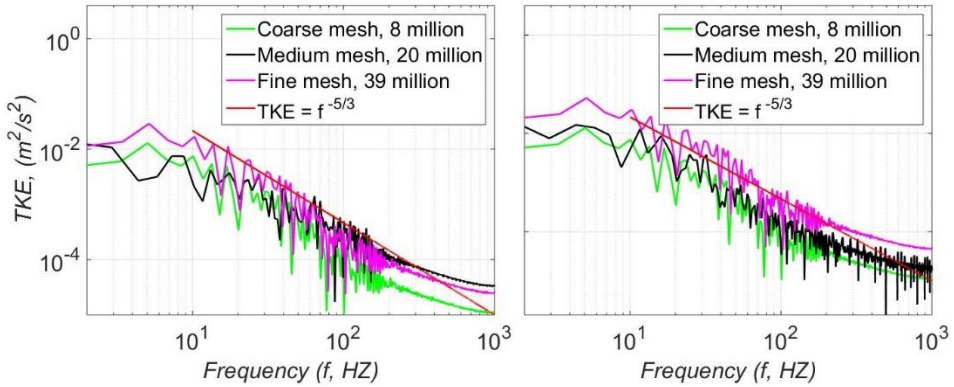


Figure 3.10 Spectra of the turbulent kinetic energy (TKE) from LES simulations. Left: $(X, Y, Z) = (-1 R, 0, -1.63 R)$; Right: $(X, Y, Z) = (-1 R, 0, -1.32 R)$. $h/R = 1.67$.

At the monitoring points of $(X, Y, Z) = (-1 R, 0, -1.63 R)$ and $(-1 R, 0, -1.32 R)$, the spectra of the turbulent kinetic energy from coarse to fine mesh are plotted in Figure 3.10. All the three sizes of mesh follow the classical characteristic trend of the Kolmogorov's theory for the spectral behaviour of the

turbulent kinetic energy. Indeed, the fine mesh provides a better representation of the turbulent flow, but the medium mesh is still chosen as it can already display sufficiently the correct behaviour of the turbulent kinetic energy.

3.4.3 Solver

The parallel computation is conducted by the commercial software of *ANSYS FLUENT*. It runs on a cluster with 48 processors. *FLUENT* uses a control volume based technique to solve the control equations numerically. The pressure based solver is adopted because the problem is incompressible (based on the velocity in the slipstream of the actuator disk model). Spatial discretization uses the Bounded Central-Differencing Scheme which is a second-order-accurate central differencing method. Velocity and pressure coupling is achieved by the *SIMPLE* algorithm in *FLUENT* [81].

The temporal discretization of the transient derivatives uses the second order implicit schemes. The time step is set at a constant value of 0.0005 second which is determined by Courant-Friedrichs-Lewy (*CFL*) condition ($CFL = 0.9$) and the frequency of the flow field (Strouhal number of the ground vortices induced by a suction tube model [33]). The computation starts from the steady calculation for 3000 steps until the residuals of pressure and velocities converge; the calculation is then switched to the *LES* simulation for 2 seconds, which corresponds to a time of $138 R/U_{eq}$ for a moderate loading condition ($T_c = 27.3$). The calculation continues for another 1 second which corresponds to a time of $69 R/U_{eq}$ and is utilized for the sample averaging.

Chapter 4 Results and discussion of interaction between propeller and its self-induced vortices

It is known that ground vortices have detrimental effects on propulsors [23, 26]. Therefore, it is helpful to understand when the ground vortices might occur. By visualization of the flow field with the help of *PIV* measurements and *CFD* simulations, a map is built that indicates three cases denoted as: a) no vortex, b) failed vortices, and c) vortices entering the propeller.

Although modelling the source of vorticity is a prerequisite to describe the mechanism governing the phenomenon, there are still inconsistencies in the previously published research. In previous research about ground vortices, it was stated that the vorticity transported from the far field boundary layer was the sole vorticity source at the headwind condition [27-30]. However, the vorticity generation equation as shown in Eq. (2.31) which was first derived by Lighthill [31] clearly indicated that the vorticity source had a contribution from the pressure gradient on the ground. By numerical simulations, the sources of vorticity entering ground vortices under the headwind condition are investigated.

The flow fields near the ground and upstream of the propeller feature highly unsteady flow, and the statistical method of Proper Orthogonal Decomposition (*POD*) is used to help understand this complex flow behaviour. The fluctuation of ground vortices has a quasi-periodic feature, and energetic frequencies are studied by spectral analysis.

After vortices are formed near the ground, they are transported toward the propeller. The propeller inflow is influenced by these vortices; consequently, the propeller performance has the potential to be influenced as well. The propeller inflow is investigated by *PIV* measurements conducted in the plane directly upstream of the propeller. The time averaged performance of the propeller is investigated by *RSB* measurements.

4.1 Flow fields of ground vortices

4.1.1 Flow fields in the wall parallel plane

The instantaneous flow fields from low-frequency *PIV* measurements shown in Sections 4.1.1 and 4.1.2 are intended to present typical flow topologies of ground vortices, and validate *CFD* results which will be utilized to analyse the vorticity source in Section 4.2. The evolution of flow fields in the time domain (high frequency *PIV* measurements) is discussed in detail in Section 4.3 and not shown here.

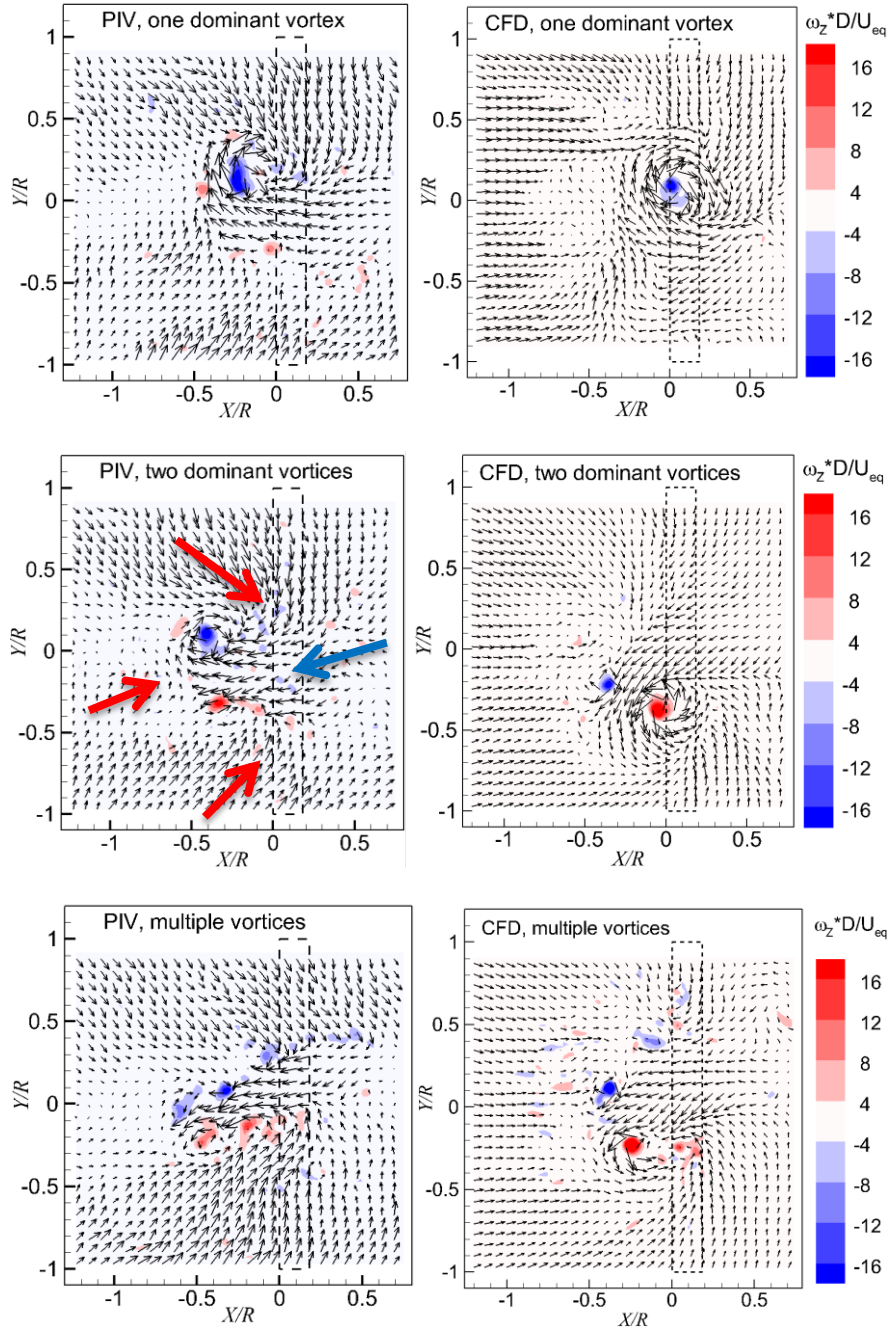


Figure 4.1 Instantaneous flow fields above the ground ($T_c = 27.3$, $h/R = 1.46$).
Top: one dominant vortex; middle: two dominant vortices; bottom: multiple dominant vortices. The dashed lines show the location of the propeller. The red arrows are indicators of the flow moving downstream, and the blue arrow is that of the flow moving upstream.

Figure 4.1 shows the typical instantaneous flow fields in the wall parallel plane (7 mm above the ground as defined in Figure 3.5) under conditions of $T_c = 27.3$ (this corresponds to $J = 0.18$, which is a highly loaded condition) and $h/R = 1.46$ (the lowest height ratio during the measurements). The figures on the left hand side are from the *PIV* measurements and the figures on the right hand side are from the *CFD* simulations. These instantaneous flow fields, selected at random instants, are intended to show the different flow topologies near the ground, specifically different number of dominant vortices in the flow fields.

The free stream direction is from the left to the right, and the projection of the propeller on the measurement plane is represented by the dashed rectangle. The figures are color-coded with non-dimensional vorticity in the wall normal component. The velocity utilized for normalization, $U_{eq} = (1 + b)U_\infty$, is the velocity in the slipstream of the actuator disk as shown in Figure 2.1, which represents the pressure jump across the propeller (Eq. (2.4)).

The flow upstream of the propeller is dominated by its downstream component (represented by red arrows in the middle row of Figure 4.1), while an upstream flow can be observed in the region underneath the propeller projection (blue arrow), which is mainly due to the suction effect of the propeller. This non-uniform flow near the ground induces positive velocity gradient $\partial U_x / \partial Y$ (clockwise vortex, blue contour region) and negative velocity gradient $\partial U_x / \partial Y$ (counter-clockwise vortex, red contour region). Both *PIV* measurements and *CFD* results show the similar flow topologies in the same plane.

The location of vortices is identified by the local maximum of vorticity magnitude. There is one dominant peak of the vorticity value shown in the top row of Figure 4.1, therefore the flow field is interpreted as representing one dominant ground vortex. In a similar manner, the flow field in the middle row of Figure 4.1 is interpreted as having two dominant ground vortices, and the flow field in the bottom row of Figure 4.1 is interpreted as having multiple vortices.

Variation of the number of ground vortices was reported in [82] as well which was studied by a suction tube model. The reason given in [82] stated that the vertical vortex lines (i.e. the velocity gradient in the lateral direction of the free stream) played a significant role in this process. Due to the fluctuation of the free stream, the velocity gradient in the lateral direction varies in the time domain, and the incoming vertical vortex lines become unstable. When the free stream velocity is set to be zero, the ground vortices (a pair of vortices) become stable again. This explanation also satisfies our situation, as shown by U' in Figure 4.2. In our case, one more source of vertical vortex line(s) is in the flow downstream of the propeller near the ground, which is not involved in the suction tube model. These vertical vortex lines are ascribed to the vortex system in the propeller slipstream, which can be decomposed into vortex rings and longitudinal vortex lines [55, 56] (the effect of longitudinal vortex lines in the propeller slipstream is not considered here and it is assumed to

follow the same mechanism as the vortex rings). Herein, the effect of the vortex rings have induced flow moving toward the upstream direction, as shown in Figure 4.2. This upstream flow and the free stream generate shear layers involving vertical vortex lines. These vortex lines are transported to the region where ground vortices occur. Due to the turbulent feature of the vortex system in the propeller slipstream, these vertical vortex lines become unstable, so do the ground vortices. This vortex ring system also exists in the *CFD* simulations which is generated by the shear layer between the slipstream and the free stream (as shown in Figure 4.4), so the *CFD* simulations can simulate this effect qualitatively as well.

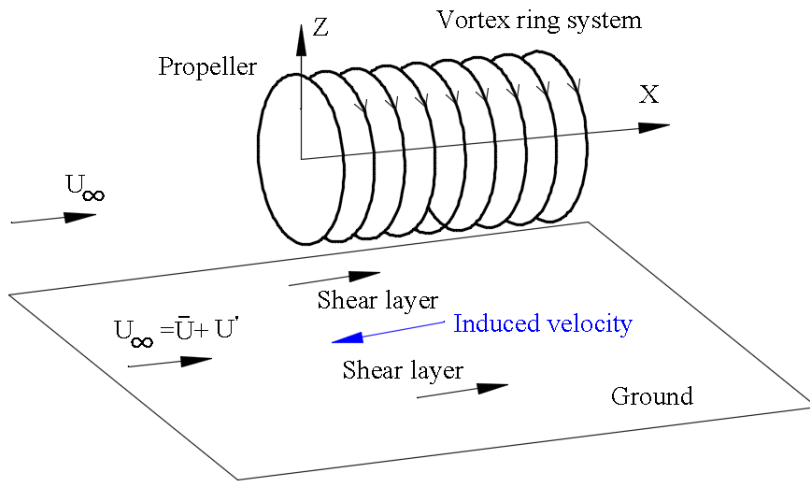


Figure 4.2 Two factors assumed to account for the unsteadiness of ground vortices: the fluctuation of the free stream, and shear layers near the ground induced by the vortex system in the propeller slipstream [55, 56]).

The other observation of the ground vortices is the meandering, which is reported to be a common characteristic of the vortices shed from a solid surface, like the wing tip vortex [33]. A small disturbance in the free stream would cause the vortex to wander in space [83].

4.1.2 Flow fields upstream of the propeller

The instantaneous flow fields in the wall normal plane just upstream of the propeller ($X = -0.08 R$, *PIV* arrangement 2) are presented in Figure 4.3, where the color-coded contour of vorticity in the axial component is superimposed on the velocity vector field. The vortices entering the propeller can be identified by the peak values of vorticity. There is one dominant vortex shown in the top row of Figure 4.3, whereas there are two dominant vortices in the bottom row of Figure 4.3.

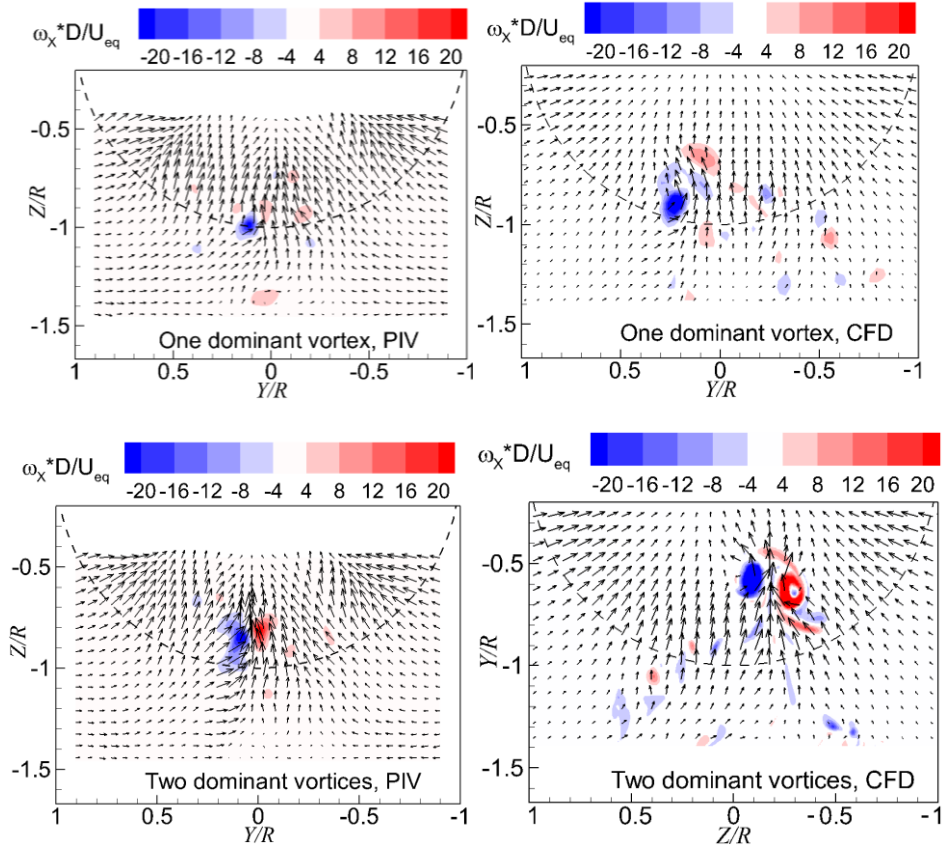


Figure 4.3 Instantaneous flow fields in the wall normal plane. Top: one dominant vortex; bottom: two dominant vortices. $T_c = 27.3$, $h/R = 1.46$.

4.1.3 Three dimensional flow field

Based on the flow fields in the planes near the ground and upstream of the propeller, the *CFD* results are shown to have good agreements with the *PIV* measurement results. This implies that the flow field induced by the actuator disk model can represent that induced by a propeller. Therefore, the three dimensional flow fields represented by displaying the iso-surface of the vorticity magnitude as shown in Figure 4.4, can be considered as representing the propeller induced flow.

The 3D flow fields are shown at a sequence of instants to represent the time evolution of the flow field. The flow field at the selected starting instant, $t = t_{co} + 0 \text{ ms}$, features a pair of dominant vortices. It is also noted that there are a set of concentrated vortices transported from the downstream field and sucked into the propeller plane. Furthermore, there are wall-parallel vortices surrounding the dominant wall-normal vortices. At the subsequent time, $t = t_{co} + 20 \text{ ms}$, one noticeable change is that another dominant vortex is formed on the right hand side of

the figure (it can also be interpreted as two but the other one is relatively weak). This new vortex becomes relatively stronger at the instant $t = t_{c0} + 40 \text{ ms}$. At the same time, the vortex in the middle of the figure moves toward the left vortex. At $t = t_{c0} + 60 \text{ ms}$, the foot of the middle vortex surrounds the left vortex, and only two dominant vortices exist in the flow field again. Here, a sequence of example flow fields in 60 ms and the time interval of 20 ms are chosen to show a typical process of the flow development. The characteristics of the flow field in the whole time domain will be evaluated by the spectral analysis in Section 4.3.2.

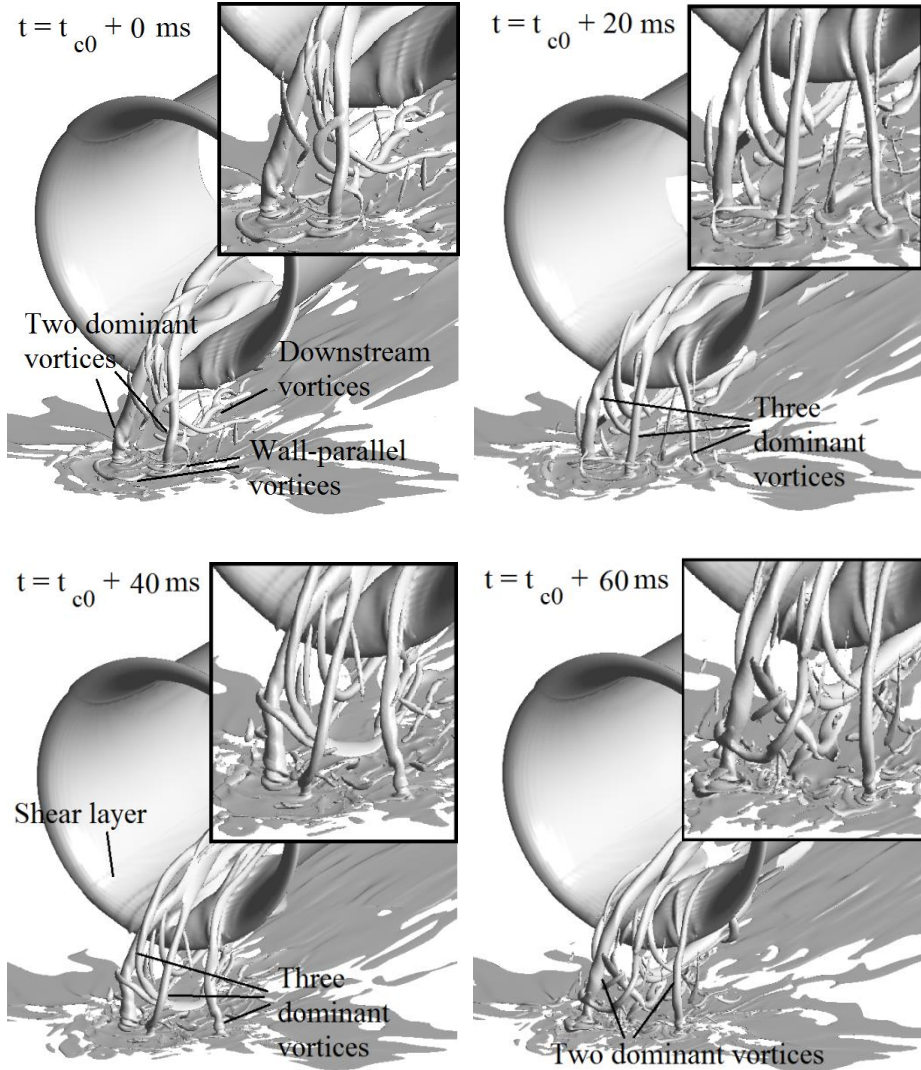


Figure 4.4 Three-dimensional flow fields in a sequence of time, represented by iso-surface of vorticity magnitude of $|\omega| * D/U_{eq} = 17$. $T_c = 27.3$, $h/R = 1.46$.

4.1.4 Domain boundary of the occurrence of ground vortices

The occurrence of ground vortices entering a propeller can cause several detrimental effects as mentioned in Chapter 1. Therefore, to establish a domain boundary of the occurrence of ground vortices is important, e.g. for determining the installation position of propellers on aircraft (probably not the most important factor, but it is still a good reference), and for the experimental design of propeller tests in wind tunnels [84].

For both the *PIV* and *CFD* results, the determination method for the occurrence of vortices is by detecting the concentrated vorticity region in the time-averaged flow field. The concentrated vorticity in the wall-parallel plane and the wall-normal plane are shown in the left and right hand sides of Figure 4.5 respectively from experimental results; and that of *CFD* results are shown in Figure 4.6. The time-averaged flow fields show a pair of vortices and the results from the two methods are generally consistent. Discrepancies of the results between the two methods are also observed. The *CFD* results show a more concentrated region of vorticity than the experimental results, which is ascribed to the impact of the unsteadiness in the free stream, blades rotation, and slipstream in the experiments. In addition, the vorticity in the time averaged flow field (in the range of -2 to 2) is an order of magnitude lower than the instantaneous flow field (in the range of -20 to 20), which is due to the smearing effect.

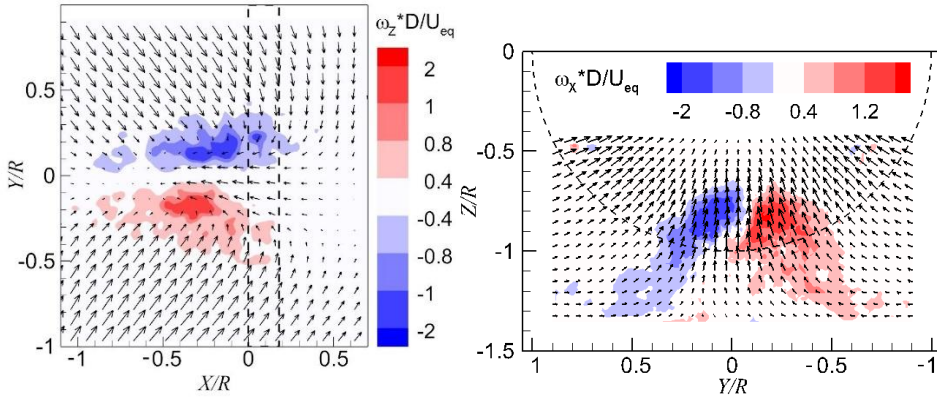


Figure 4.5 Distributions of vorticity in the time-averaged flow field (experimental results). Left: wall-parallel plane; right: wall-normal plane directly upstream of the propeller. $T_c = 27.3$, $h/R = 1.46$.

A parameter is defined here to evaluate the concentration of vorticity, which is the ratio between the maximum magnitude of vorticity in the time-averaged flow field and the value in the region assumed to be unaffected by the ground vortices. These unaffected regions chosen at a 3×3 kernel centred at $[X/R, Y/R] = [-1, 0.7]$ in the wall parallel plane, and $[Y/R, Z/R] = [-0.8, -1]$ in the wall normal plane. The criterion applied in the thesis is that if the ratio is larger than 10 (this

value is determined by considering the concentrated vorticity should be one order of magnitude larger than the vorticity from turbulence), it is considered to be concentrated vorticity; otherwise there is no concentrated vorticity in the flow field.

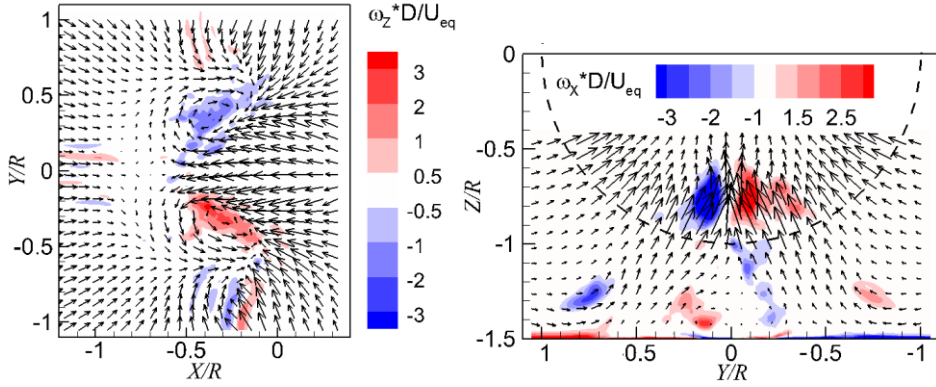


Figure 4.6 Distributions of vorticity in the time-averaged flow field (*CFD* results). Left: wall-parallel plane; right: wall-normal plane directly upstream of the propeller. $T_c = 27.3$, $h/R = 1.46$.

If there is no concentrated vorticity in the flow field either near the ground or upstream of the propeller, it is defined as the case ‘no vortex’. If there is concentrated vorticity in the flow field both near the ground and upstream of the propeller, it is defined as the case ‘vortices entering the propeller (vortices)’. If there is concentrated vorticity in the flow field near the ground but not existing directly upstream of the propeller, it is defined as the case ‘failed vortices’ (a three dimensional flow representing this type of flow is shown in Figure 4.7). A map of ‘no vortex’ (symbol ‘x’), ‘failed vortices’ (symbol ‘+’) and ‘vortices entering propeller’ (symbol ‘o’) from both the *PIV* results and *CFD* simulations is shown in Figure 4.8.

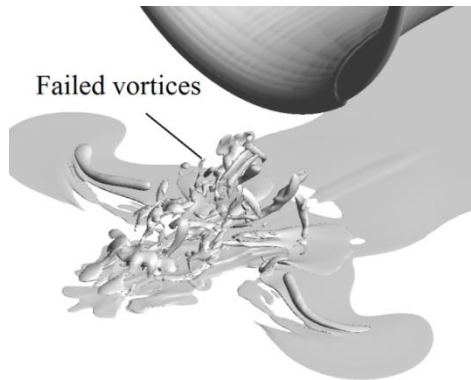


Figure 4.7 Three-dimensional flow field with failed vortices, $|\omega| * D/U_{eq} = 8$.
 $T_c = 14$, $h/R = 1.85$.

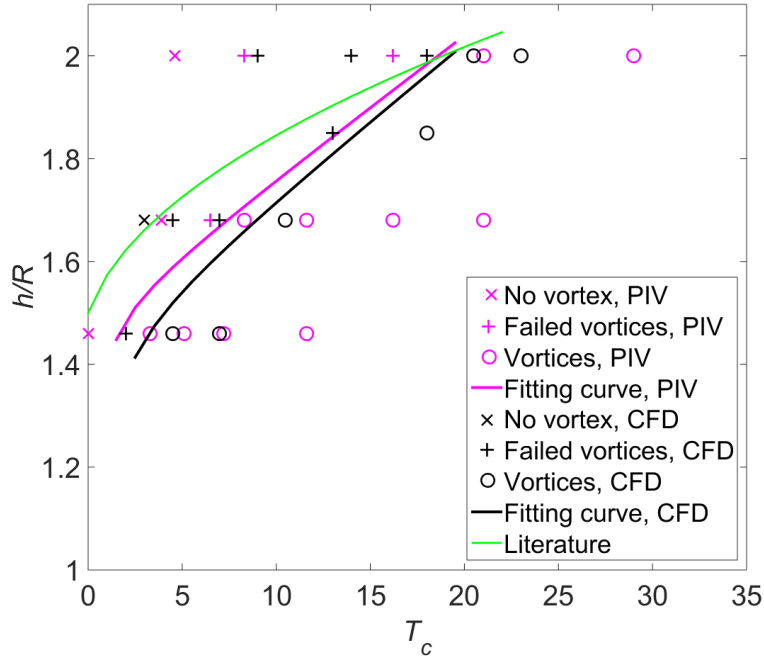


Figure 4.8 Domain boundary of occurrence of ground vortices induced by the propeller. The data from literature (green curve) is reported in [85] .

The fitting curves by connecting the midpoints between the vortices and failed vortices or no vortex at $h/R = 1.46, 1.7$, and 2.0 are shown by the solid purple and black curves in Figure 4.8. The fitting curve divides the domain into two sub-domains: the upper left domain represents no vortex entering the propeller, while the bottom right domain represents vortices entering the propeller. In other words, as the height ratio decreases and the thrust coefficient increases, the ground vortices occur.

As found in Figure 4.8, both the fitting curves from the *PIV* results and the *CFD* results agree quite well. Because the number of blades is assumed to be infinity, and the loading in the radial direction is assumed to be constant for the actuator disk model, the consistency with the experimental results implies that the occurrence of ground vortices is not sensitive to these parameters and it is mainly determined by the total thrust generated by the propeller.

It should be noted that only the parameters of T_c and h/R are taken into account when predicting the occurrence of ground vortices, and the parameter of the free stream velocity is kept constant. The vorticity transported from the free stream velocity is also one source of vorticity to form ground vortices as will be discussed in Section 4.2. The free stream velocity is very likely one factor determining the occurrence of ground vortices. Although different free stream velocities are not investigated in the current research, the mechanism of the free stream in the formation of the ground vortices is discussed in Section 4.2 together with the

mechanism due to the pressure gradient on the ground which is related to T_c and h/R .

In addition, the green curve is the domain boundary of occurrence of ground vortices for turbofans which is reported in [85]; it shows that the ground vortices induced by turbofans occur at lower thrust coefficients than that induced by the propeller for the same height ratio. This discrepancy is perhaps due to the different free stream velocities and fluctuating characteristics, which play a role in the forming of ground vortices [82].

4.2 Source of vorticity for the ground vortices

After the description of the occurrence of ground vortices by *PIV* measurements and *CFD* simulations, one further step taken is to investigate the vorticity source of these vortices. In Section 2.2.3, the 3D vorticity generation equation derived from Lighthill's work was explicitly presented. In Section 2.3.1, a simplified model of image doublet flow to predict the vorticity source on the ground was built. Both the two methods showed that the pressure gradient on the ground should be one source of wall-parallel components of the vorticity when there is a propulsor in proximity to the ground. The wall-normal component of the vorticity is also explicitly shown in Eq. 2.32 as a result of the divergence of wall-parallel components of the vorticity. Herein, the *CFD* results from the simulations of the actuator disk model are analysed for the vorticity source entering ground vortices, which is performed at the condition of $T_c = 27.3$, $h/R = 1.46$.

4.2.1 Development of the lateral-component of the vorticity

The ground vortices are ascending from the ground, and the vorticity source is certainly on the ground (even if it is convected downstream in the far field boundary layer). Therefore, the flow field near the ground wall will be investigated. The component of vorticity in the lateral direction (Y component) in the domain close to the wall is analysed in this section in the meridional (geometrical symmetry) plane $Y = 0$ as defined Figure 4.9. The component of the vorticity in the X component will be discussed in Section 4.2.2.

One instantaneous flow field is investigated to analyse the vorticity source on the ground. This flow field corresponds to the one displayed in the top left of Figure 4.4. The mechanism found in this instant can also be applied to other instants and the time averaged flow field.

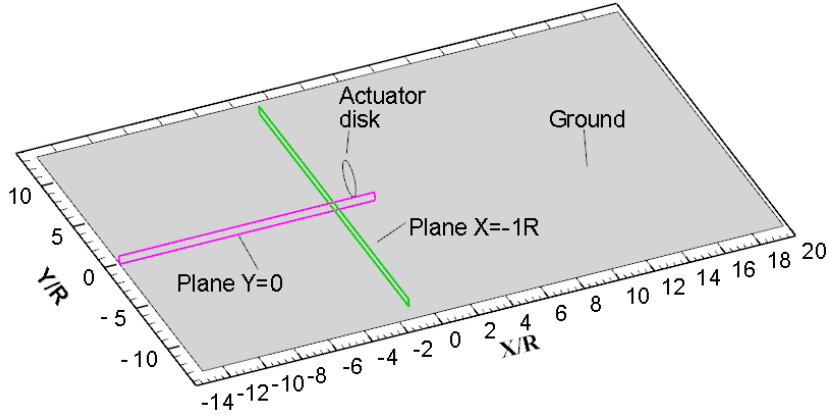


Figure 4.9 Definitions of planes for analysis of vorticity source. Plane $Y = 0$ is utilized to analyse the production of the Y -component of the vorticity, and plane $X = -1 R$ is utilized to analyse the production of the X -component of the vorticity.

The profile of the X -component of the velocity in the plane of $Y = 0$ is shown in the left hand side of Figure 4.10. At the position of $X = -13.1 R$ (velocity inlet), the velocity has the profile as that prescribed at the velocity inlet. The boundary layer has a thickness of $0.45 R$ at the velocity inlet. As the flow progresses downstream, the X -component of the velocity has a trend of increasing both inside and outside the boundary layer, and the velocity outside the boundary layer reaches $1.3 U_\infty$ at the position of $X = -2.0 R$.

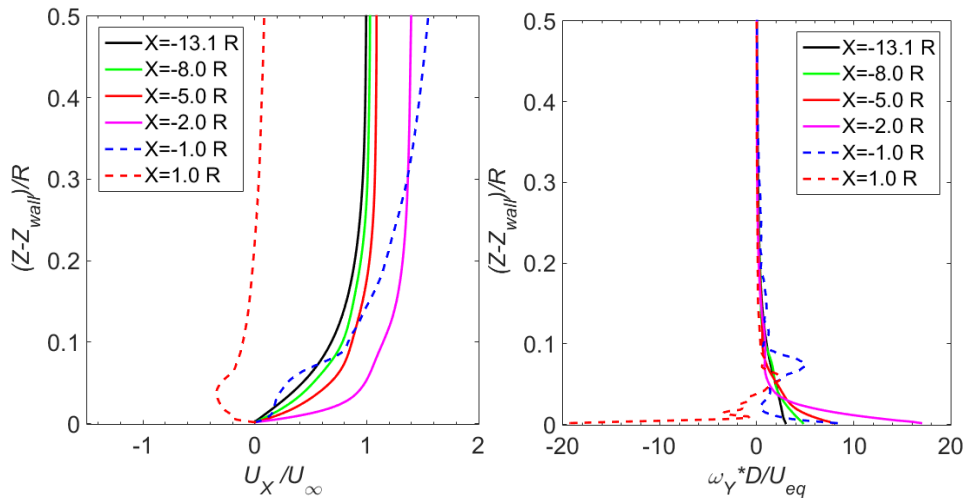


Figure 4.10 Left: profile of the X -component of the velocity in the boundary layer; right: distribution of the Y -component of the vorticity in the boundary layer. The data are extracted from the plane $Y = 0$.

At the position of $X = -1.0 R$, flow becomes obviously three dimensional and the X -component of the velocity changes dramatically in the wall normal direction. At the position of $X = 1.0 R$, an adverse flow with negative value of X -component of the velocity near the wall is observed.

The distribution of vorticity close to the wall in the meridional plane $Y = 0$ is shown in the right hand side of Figure 4.10. At positions from $X = -13.1 R$ to $X = -2 R$, the magnitude of vorticity on the wall increases monotonically from $\omega_Y * D/U_{eq} = 3.0$ to 16.9 . The vorticity at the wall at the position $X = -2 R$ is 5 times as large as that at $X = -13.1 R$. Downstream of the propeller, i.e. $X = 1 R$ in the current analysis, the vorticity on the ground is $\omega_Y * D/U_{eq} = -19.2$, the magnitude of which is beyond 6 times as large as that at $X = -13.1 R$.

One parameter defined to evaluate the vorticity in the boundary layer is the integration of vorticity in the wall normal direction, i.e. $\int_0^\delta \omega_Y dY$. This integration represents the total vorticity in the boundary layer. The vorticity integration along the wall-normal direction is mathematically the velocity magnitude outside the boundary layer for a free stream over a flat plate. At the position $X = -13.1 R$, the vorticity integration in the boundary layer is $\int_0^\delta \omega_Y dY = 2.70 \text{ m/s}$. At the position $X = -2.0 R$, the vorticity integration in the boundary layer is 3.51 m/s , which is 0.3 times larger than that at the position $X = -13.1 R$. The integral of vorticity is $\int_0^\delta \omega_Y dY = -0.30 \text{ m/s}$ at $X = 1 R$, and its magnitude is 0.1 times of the vorticity integral in the boundary layer. This negative value of vorticity integral at $X = 1 R$ represents the vorticity production with the opposite sign as that upstream of the propeller.

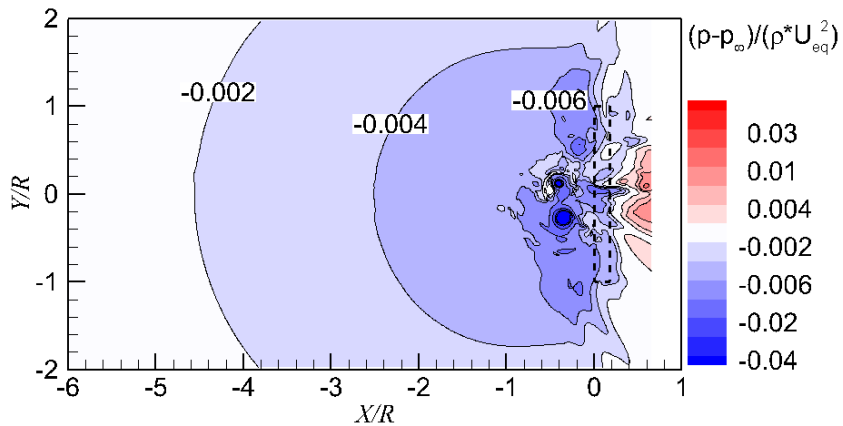


Figure 4.11 Pressure distribution on part of the ground.

The cause for the increment of vorticity magnitude upstream of the propeller and the negative vorticity downstream of the propeller is investigated by analysing the

pressure distribution on the ground. This pressure distribution is shown for the upstream and downstream vicinity of the propeller in Figure 4.11. Generally, the pressure decreases upstream of the propeller and increases downstream of the propeller in the streamwise direction, and the pressure decreases toward the propeller in the lateral direction. The two local minimum values of pressure occur at the centres of the dominant vortices, which is due to the centrifugal force of the swirling flow and it is already explained in Eq. (2.42).

The pressure on the ground features a notably non-uniform distribution. As already elaborated in Chapter 2, the pressure gradient in the X direction accounts for the production of the Y -component of the vorticity. The production rate of the Y -component of the vorticity is obtained from the equation Eq. (2.31) as,

$$\nu \frac{\partial \omega_Y}{\partial z} = (\partial p / \partial X) / \rho. \quad \text{Eq.(4.1)}$$

In order to use this equation to verify the numerical results, a comparison between the terms on the left and right hand sides of Eq. (4.1) is shown in Figure 4.12, which is extracted from the intersection line between the ground and the meridional plane. The two terms agree with each other very well. In the region close to the actuator disk, discrepancies are observed between the two terms, which is due to the Y component of the vorticity being depleted in feeding the other components (e.g. it is shown that the wall-parallel components of the vorticity are turned into the wall-normal component in Section 4.2.3). However, as found in Figure 4.12, the trends of the two terms are consistent in most of the domain.

After the validation of the vorticity source on a line, the production of the Y -component of vorticity induced by the pressure gradient on part of the ground plane is shown in Figure 4.13. Far upstream of the actuator disk, the pressure gradient (vorticity production rate) is nearly zero. It can be observed that there is a negative pressure gradient on the wall from $X = -6R$ to $X = -2R$ as shown in Figure 4.13. Consequently, the Y -component vorticity is produced. This locally generated vorticity is then diffused into the farther flow field, and finally the vorticity in the whole boundary layer increases as shown in the right hand side of Figure 4.10.

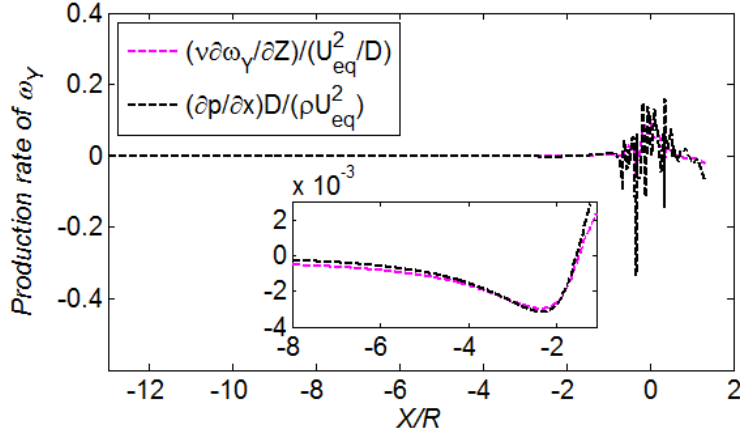


Figure 4.12 Terms of the vorticity-production equation, and the small window is the zoom-in figure. Data are extracted from the intersection line between the meridional plane and the wall.

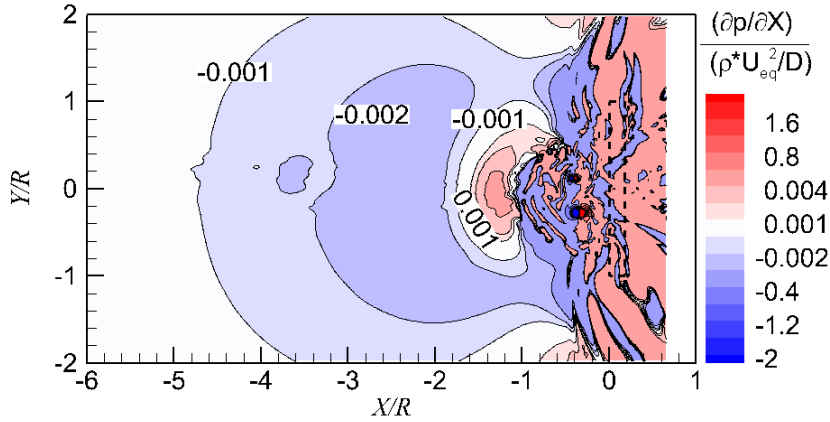


Figure 4.13 Production rate of the Y-component of the vorticity from pressure gradient in the longitudinal component along the wall.

Downstream of the propeller, the pressure gradient is positive. Initially, the vorticity convected from the far field boundary layer still dominates. Due to the positive vorticity gradient induced by the actuator disk, the vorticity on the wall keeps decreasing and finally becomes negative. In other words, due to the low pressure region upstream of the propeller as shown in Figure 4.11, there is a reverse flow downstream of the propeller. Vorticity of negative sign is involved in this reverse flow due to the pressure gradient.

4.2.2 Development of the streamwise-component of the vorticity

Following the same method as above, the flow field in the plane $X = -1.0 R$ (as shown in Figure 4.9) is analysed for the production rate of the X-component of the

vorticity. First, the distribution of the Y-component of the velocity in this plane is plotted in the left hand side of Figure 4.14. In the far sideways positions, i.e. $Y = \pm 10.0 R$, the magnitude of the Y-component of the velocity is approximately zero. At the positions close to the propeller, i.e. $Y = \pm 6R$ and $\pm 3R$, the magnitude of the Y-component of the velocity increases due to the propeller suction effect.

The distributions of the X-component of the vorticity are presented in the right hand side of Figure 4.14. Vorticity is nearly zero in the region far in the sideways distance from the actuator disk model, e.g. at position of $Y = -10R$ and $Y = 10R$. At positions of $Y = -6R$ and $Y = 6R$, the magnitude of vorticity on the wall increases to $\omega_X * D/U_{eq} = 2.5$. At positions of $Y = -3R$ and $Y = 3R$, vorticity magnitude further increases to $\omega_X * D/U_{eq} = 10.0$. The magnitudes of the X-component of the vorticity at the wall at the position $Y = \pm 3R$ are both more than 3 times as large as the magnitude of the Y-component vorticity at the wall in the far field boundary layer, as shown by the black curve in the right hand side of Figure 4.10.

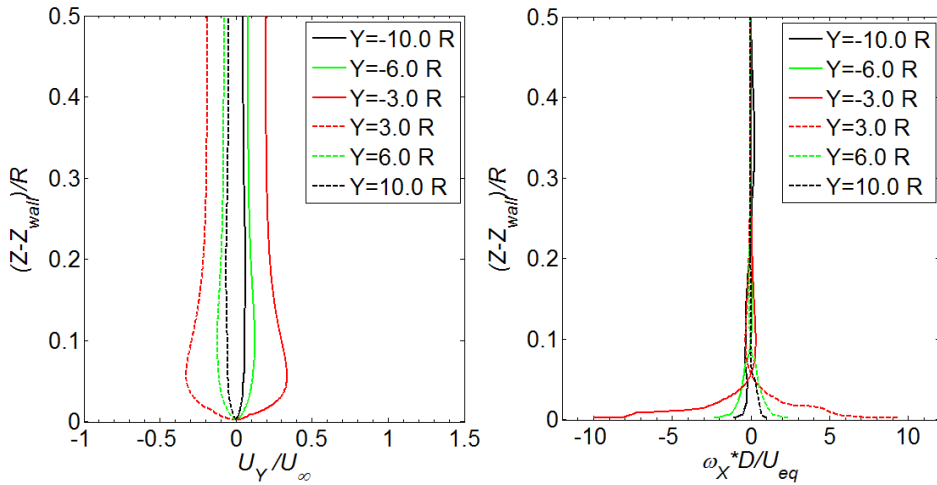


Figure 4.14 Left: profile of the Y-component of the velocity in the boundary layer; right: distribution of the X component of the vorticity in the boundary layer. The data are extracted from the plane of $X = -1R$.

The integration of the X-component of vorticity, in the range from the wall to the position of $0.45 R$ above the wall (boundary layer thickness at the inlet), is evaluated to quantify the locally generated vorticity. At the position of $Y = \pm 3R$, the vorticity integration in the wall-normal direction is $0.73 m/s$, which is 0.3 times the value of the integration of the Y-component vorticity in the far field boundary layer, as shown by the black curve in the right hand side of Figure 4.10. Because the X-component of the vorticity is generated at both sides of the propeller, the integration of the magnitude of the locally generated X-component vorticity in total is 0.6 times as large as the vorticity integration in the far field boundary layer. In addition to the

integration of the locally generated Y -component vorticity as shown in the last section, which is 0.4 times of that in the far field boundary layer, the summation of the locally generated vorticity integration magnitude is 1.0 times the value of that transported from the far field boundary layer. This confirms that the vorticity generated by the pressure suction has a significant contribution to the vorticity source of the ground vortices. Indeed, the vorticity is a vector, but the opposite directions of the vorticity are not necessarily to be cancelled out. They may separately contribute to the wall normal component of the vorticity. The evaluation of the vorticity magnitude of each sign as well as the summation are still meaningful.

The trend found in Figure 4.14 is that vorticity in the boundary layer increases from far field to the region close to the actuator disk. It means that the vorticity production on the wall is low when the wall is far away from the actuator disk, and it increases as the wall is close to the actuator disk. The theory of the vorticity-production rate from the wall established in Chapter 2 is utilized here again. The X -component of the vorticity generated from pressure gradient in the Y component is obtained from Eq. (2.31) as,

$$v \frac{\partial \omega_X}{\partial Z} = (-\partial p / \partial Y) / \rho. \quad \text{Eq.(4.2)}$$

Again, the validity of the calculations is verified against this equation by comparing of the two terms on the left and right hand sides of Eq. (4.2). This is shown in Figure 4.15. The calculated vorticity gradient and the equivalent term due to the pressure gradient agree with each other very well.

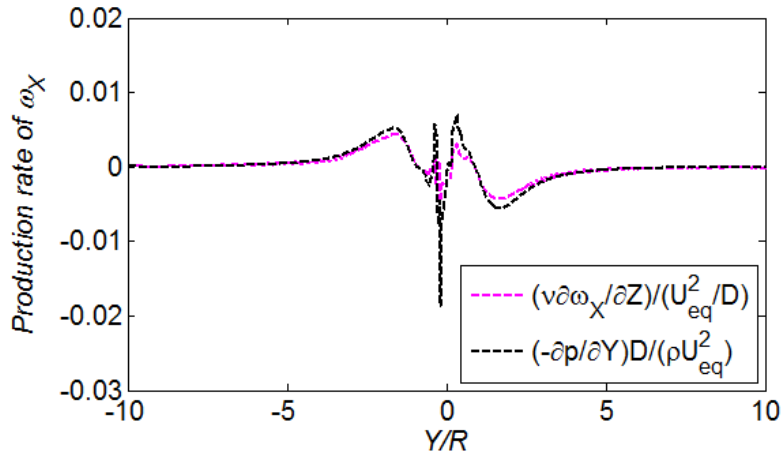


Figure 4.15 Verification of the vorticity production equation. The data is extracted from the intersection line of the plane $X = -1R$ and the wall.

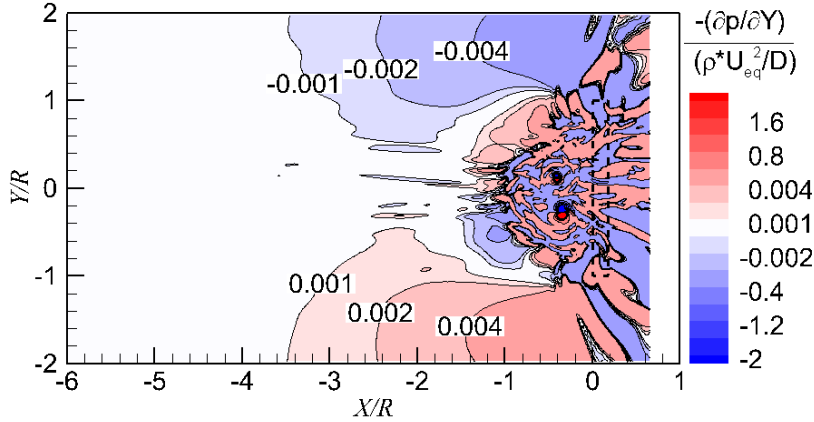


Figure 4.16 X-component of the vorticity generated from pressure gradient in the Y direction on the wall.

Since the vorticity production rate, $v \partial \omega_x / \partial Z$, induced by the pressure gradient is validated on one line located on the wall, the production rate of the X-component of the vorticity on the 2D plane of the wall is shown in Figure 4.16. Far away from the disk, the vorticity production rate is nearly zero, which means no vorticity is produced. It is observed that vorticity production rate is non-zero in a large area close to the actuator disk, which means vorticity is produced in this area.

4.2.3 Development of the wall-normal component of the vorticity

The vorticity production rate in the wall-parallel components was described in the previous sections, and the production rate of the wall-normal component of the vorticity is introduced as follows. As elaborated in Chapter 2, the vorticity production in the wall normal component is due to the divergence of the vorticity on the ground. The equation of the vorticity production rate in the wall-normal component in Eq. (2.32) is shown as below,

$$v \frac{\partial \omega_z}{\partial Z} = -v \left(\frac{\partial \omega_x}{\partial X} + \frac{\partial \omega_y}{\partial Y} \right). \quad \text{Eq.(4.3)}$$

The term on the right hand side of Eq. (4.3) is shown in Figure 4.17. Strong divergence is observed in the vortex core region as represented inside the dashed black circles. These regions with strong divergence coincide with the positions of dominant vortices as shown in the top left of Figure 4.4. This confirms that the formation of the wall normal component of the vorticity is due to the divergence of the vorticity in the wall-parallel components. The earlier proposals were that the wall-normal component of the vorticity was due to the tilting of the vortex line which was originally parallel with the ground [28], which is different from our conclusion. It is also noted that the divergence with non-zero values covers a wide area, which means the wall-normal component of the vortex is distributed.

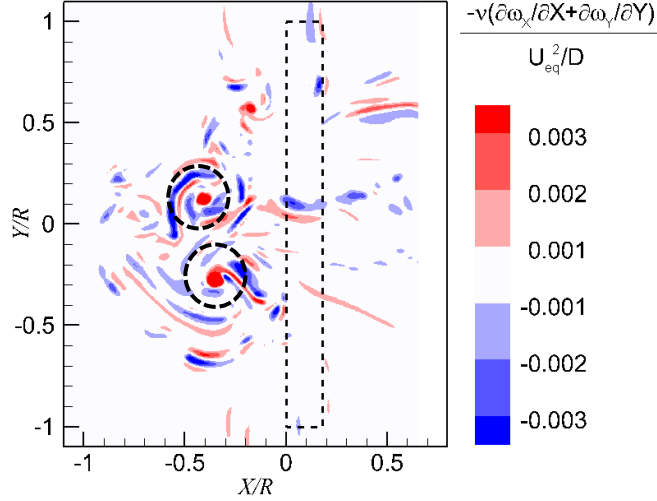


Figure 4.17 Divergence of the wall-parallel components of the vorticity vector on the wall, $-v(\frac{\partial \omega_x}{\partial X} + \frac{\partial \omega_y}{\partial Y})/(U_{eq}^2/D)$.

4.3 Unsteadiness and coherent turbulent structures of ground vortices

As already shown in section 4.1, multiple flow topologies are observed at different instants. It implies that the phenomenon of ground vortices is highly unsteady. In order to resolve this complex phenomenon, the evolution of the flow fields in the time domain, the spectral analysis, and coherent turbulent structures are investigated in this section based on the results that are obtained from the high frequency *PIV* measurements (arrangements 3 and 4 as shown in Figure 3.6).

4.3.1 Time resolved analysis of flow fields

The dynamic evolution of the flow fields captured in the wall parallel plane is shown in Figure 4.18. Let us consider the instantaneous flow fields starting from $t = t_0$, as shown in the top left of Figure 4.18. There is one dominant vortex with positive Z -component vorticity (counter-clockwise rotation direction), which is located upstream of the propeller. In the successive instant, i.e. $t = t_0 + 20 \text{ ms}$, this vortex with the positive Z -component of the vorticity remains and another region with distributed positive Z -component of vorticity occurs at the bottom-right corner of the figure. They interact with each other and finally form a big vortex at the instant $t = t_0 + 60 \text{ ms}$. At the same time, it is also noticed that there is one region with negative vorticity located in the upper side of the figure. This vortex moves to the centre of the flow field at $t = t_0 + 80 \text{ ms}$. As the clockwise vortex (negative Z -component of vorticity) becomes close to the counter-clockwise vortex, they are both weakened and move toward the bottom of the figure due to induced velocities by each other. The time interval for the samples as shown here is explained in Section 4.3.2 by analysing the frequency of the flow.

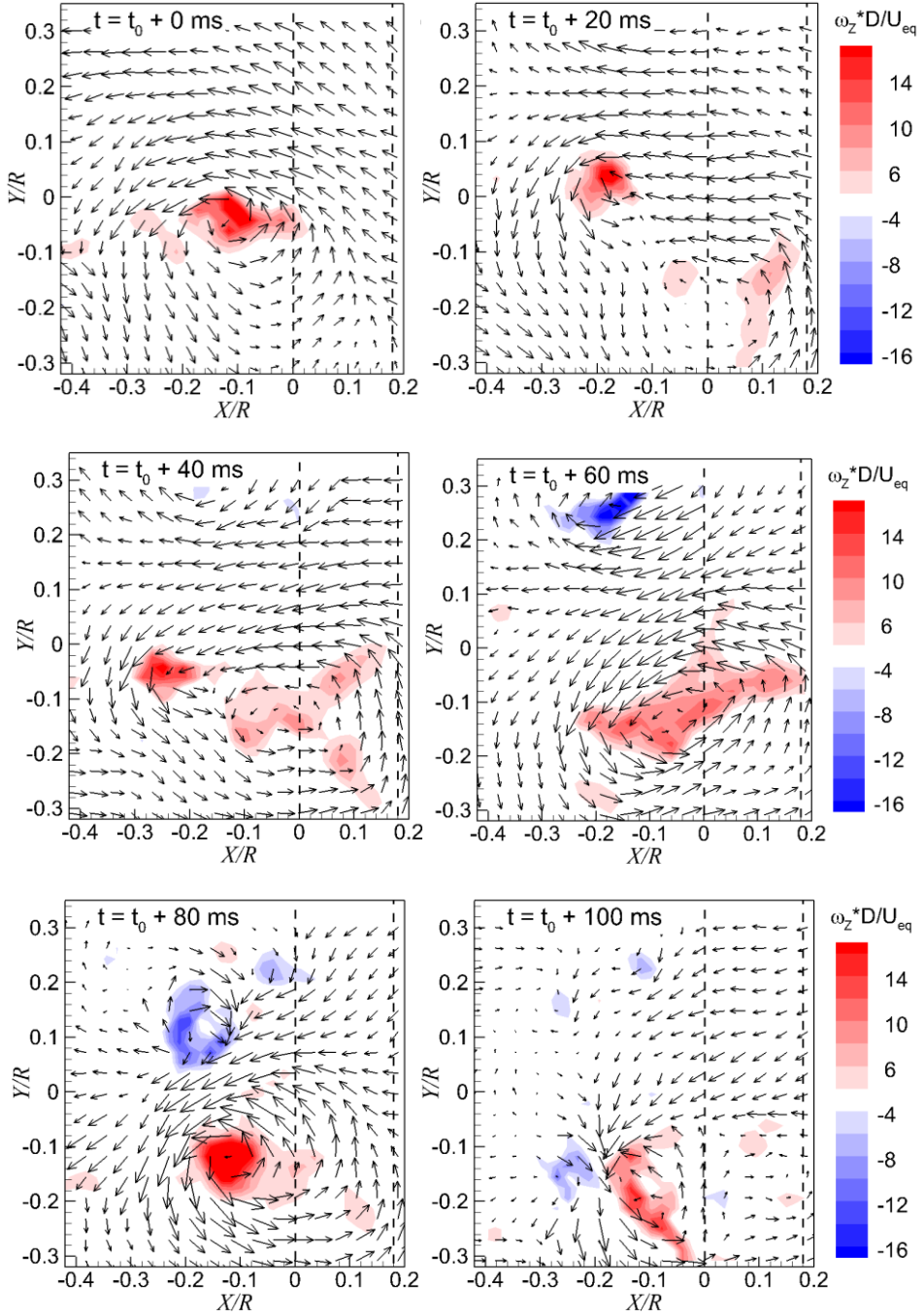


Figure 4.18 Sequence of instantaneous flow fields in the horizontal plane above the ground (PIV arrangement 3). Superimposed are the color-coded magnitudes of the wall-perpendicular component of the vorticity. $T_c = 27.3$. $h/R = 1.46$.

The dynamic evolution of the flow field in the wall perpendicular plane upstream of the propeller, where the vortices go through before entering the propeller disk plane, is shown in Figure 4.19. The instantaneous flow field at $t = t_1$ is shown in the top left of Figure 4.19 (it should be noted that the measurement in the wall-normal plane is not synchronised with that in the wall-parallel plane). One dominant vortex with positive X -component vorticity is observed, as well as distributed negative X -component vorticity in the flow field. These distributed negative X -component vorticity concentrates and forms another two dominant vortices at $t = t_1 + 10 \text{ ms}$. At the subsequent time, i.e. $t = t_1 + 20 \text{ ms}$, the set of vortices move toward the right hand side of the propeller disk plane. At the time $t = t_1 + 30 \text{ ms}$, the dominant vortices in the field of view of the *PIV* measurement plane nearly disappear. The time intervals chosen for presentation in the wall perpendicular plane is 10 ms , whereas that in the wall parallel plane is 20 ms . The criterion for choosing the interval is to follow the movement of the vortices in the measurement plane by a limited number of samples. The detail of the unsteadiness of the ground vortices is going to be discussed in the next section. From that discussion also the justification for the chosen time intervals can be obtained.

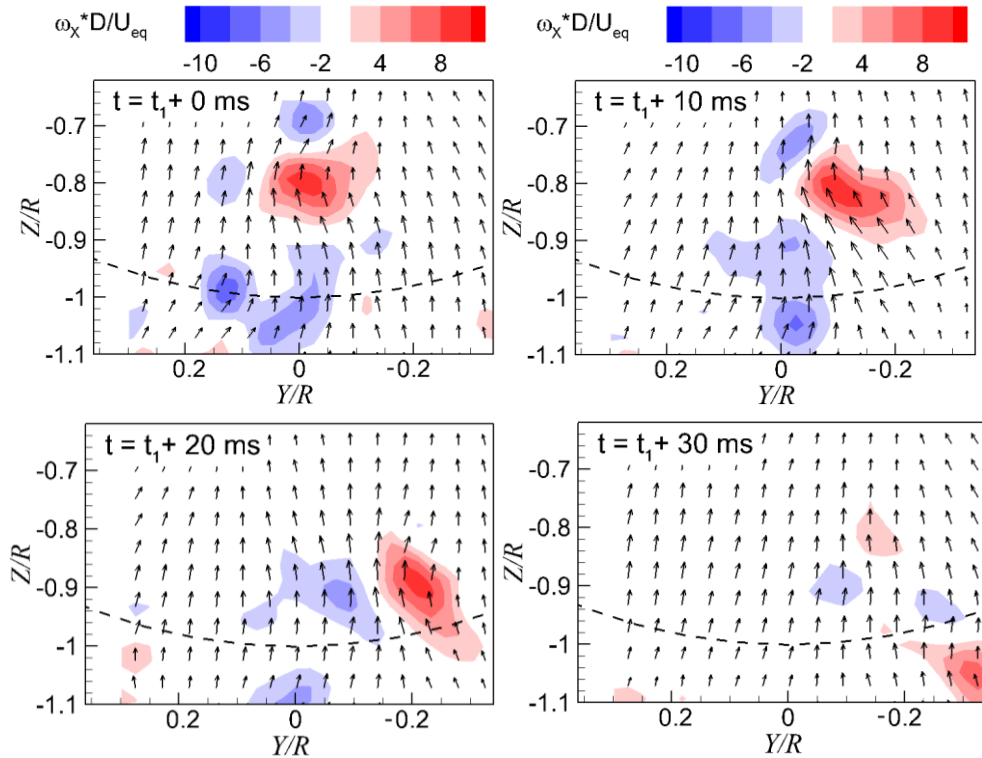


Figure 4.19 Sequence of instantaneous flow fields in the plane upstream of the propeller (*PIV* arrangement 4). Superimposed are the color-coded magnitudes of the X -component of the vorticity. $T_c = 27.3$. $h/R = 1.46$.

The instantaneous flow fields selected for analysis both in the wall-parallel plane and the wall-normal plane capture the main characteristics: the sign of the dominant vortex in the flow fields varies in time; the vortices meander in the measurement plane; the number of dominant vortices is not constant.

4.3.2 Unsteadiness of ground vortices

The time resolved data is also utilized to analyse the energetic frequencies involved in the unsteadiness of ground vortices by means of spectral analysis. In this case the power spectral analysis is performed on the Z -component of the vorticity in the wall-parallel plane (*PIV* arrangement 3). The Z -component of the vorticity is evaluated at three typical regions where ground vortices occur, i.e. $[X/R, Y/R] = [-0.1, 0.0]$, $[-0.1, 0.2]$, $[-0.1, -0.2]$. The value of the Z -component of the vorticity is calculated by the mean value of a spatial kernel of 3×3 points to decrease the error propagated from each point (the scatter of this method is one ninth of an individual point).

The dominant peaks are observed at the frequency range of $f * D/U_{eq} = O(10^{-2}) \sim O(10^{-1})$ for all the locations analysed, e.g. a dominant peak at the frequency of $f * D/U_{eq} = 0.017$ is observed at the position of $[X/R, Y/R] = [-0.1, 0.0]$. This frequency range corresponds to the period of range of 100 ms to 1000 ms; the time intervals of 20 ms and 10 ms as shown in Figure 4.18 and Figure 4.19 respectively are chosen to satisfy the Nyquist sampling rate. This frequency range of the ground vortices is consistent with that observed in [18] for the ground vortices induced by a suction tube model at headwind conditions. This consistence implies that the unsteadiness of ground vortices near the ground is independent of the intermittent flow induced by the blade passing. This is further confirmed by evaluating the power spectrum near the blade passing frequency of $f * D/U_{eq} = 6.598$ during a trial test in our measurements, and no pulse is found near the frequency of the blade passing.

It is also noticed that the frequency content at different locations are different, which implies that the unsteadiness of ground vortices is not only dependent on the movement of the vortices, but also has impacts from other factors, e.g. the turbulence in the boundary layer, and the interaction between vortices.

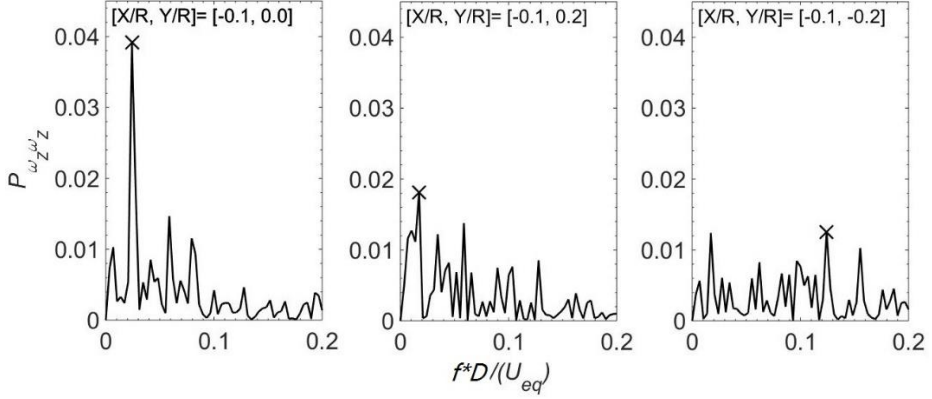


Figure 4.20 Power spectrum analysis of the Z-component of the vorticity at different locations in the wall parallel plane. $T_c = 27.3$. $h/R = 1.46$. The crosses signify the maximum power of the Z-component of the vorticity and their relevant frequencies.

Following the same method as performed in the wall-parallel plane, the spectral analysis of the X-component of the vorticity is conducted in the wall-normal plane (PIV arrangement 4) at $[Y/R, Z/R] = [-0.2, -0.9], [0, -0.9], [0.2, -0.9]$, which are typical positions where ground vortices entering the propeller. An obvious peak value occurs at the frequency of the blade passing, $f^* D / U_{eq} = 6.598$, for all the locations analysed. These peaks are ascribed to the effect of vorticity transportation, by which the vortices are stretched and tilted by the blade-induced velocities; therefore, the X-component of the vorticity varies according to the blade passing.

At the left hand side of the figures, the dominant peak values are also observed at the frequency range of $f^* D / U_{eq} = O(10^{-2}) \sim O(10^{-1})$ as shown in Figure 4.21. The energetic frequencies involved in this range are consistent with that observed in the wall-parallel plane, which implies that they are due to the ground vortices originated from the ground and transported into the propeller plane. It is also noted that the dominant peak values occur at a relatively higher frequency compared with that in the wall-parallel plane, e.g. $f^* D / U_{eq} = 0.135$ at $[Y/R, Z/R] = [0.0, -0.9]$ and the zoom in figure is shown in the right hand side of Figure 4.22. This difference is ascribed to the viscous damping effect: the relatively high frequency in the viscous region near the ground is damped, leaving only the low frequencies over to remain observable.

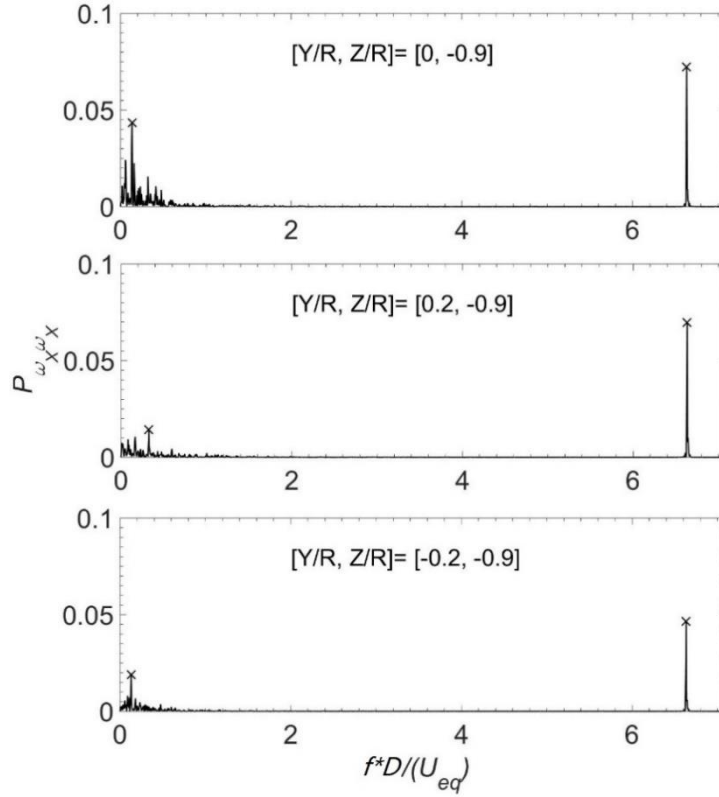


Figure 4.21 Power spectrum analysis of the X-component of the vorticity at different locations in the wall normal plane. $T_c = 27.3$. $h/R = 1.46$.

The spectral analysis of ground vortices in the wall-parallel plane is compared at two different thrust coefficients, $T_c = 27.3$ and $T_c = 48.2$, as shown in the left hand side of Figure 4.22. The energetic frequencies occur at the same range of the two thrust coefficients, which is $f^*D/U_{eq} = O(10^{-2}) \sim O(10^{-1})$. However, as the thrust coefficient increases, the frequency of the dominant peak value decreases. This decrease of the dominant frequency (Strouhal number) as the thrust coefficient increases is consistent with that observed in [33], in which the ground vortices were generated by a suction tube model. It implies that the ground vortices become relatively more stable at a higher thrust coefficient.

The spectral analysis in the wall-normal plane is performed at two different thrust coefficients as well, as shown in the right hand side of Figure 4.22. One noticeable observation is that the frequency corresponding to the blade passing increases as the thrust coefficient increases (the rotating speed of the propeller increases). The energetic frequencies at relatively low values are observed for both thrust coefficients and they are located in the same range; as the thrust coefficient increases, the most energetic frequency in the low frequency domain decreases, which is consistent with that observed in the wall parallel plane.

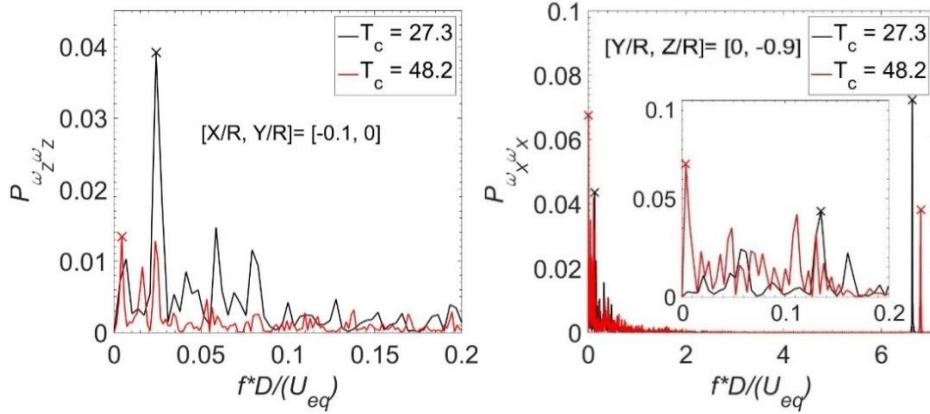


Figure 4.22 Comparison of power spectra at different thrust coefficients. Left: Z-component of the vorticity in the wall-parallel plane; right: X-component of the vorticity in the wall-normal plane, and the small window is the zoom-in figure in the low frequency range.

4.3.3 Proper Orthogonal Decomposition of flow fields in the wall parallel plane

Due to the highly turbulent characteristic of the ground vortices, statistical method of Proper Orthogonal Decomposition (*POD*) is applied to analyse the energetic turbulent flow structures obtained from the *PIV* measurements. *POD* determines a series of orthogonal flow modes basing on the instantaneous flow fields. The mode is ordered in a way that corresponds to the turbulent kinetic energy. The first mode contributes most to the turbulent kinetic energy, and the second mode contributes less than the first mode, and so on. Each instantaneous flow field is a linear combination of the modes superimposed on the time averaged flow field. The detail of the method is described in Appendix C.

The *POD* analysis applied in the flow field of the wall parallel plane is introduced as follows. The operating condition of the propeller is $h/R = 1.46$ and $T_c = 27.3$. The turbulent kinetic energy fraction of each mode on the wall parallel plane is shown in Figure 4.23. The cumulative energy of 88% is attained within the first 50 modes. It is found that 70% of the total amount of the turbulent kinetic energy is captured by the first 10 modes, clearly indicating that the flow fluctuations are dominated by large scale coherent motions.

The time averaged flow field was already shown in the left hand side of Figure 4.5 from the results of low frequency *PIV* measurements, and it is not repeated here. It features two vortices, but the magnitude of the vorticity is low compared with the instantaneous flow field due to the meandering effect of ground vortices.

The first mode represents 25.7% of the total turbulent kinetic energy and its equivalent flow field is shown in the top left of Figure 4.24. One dominant vortex

can be observed below the propeller together with distributed vorticity around it with opposite sign. The 2nd-4th modes represent 11.5%, 9.6%, and 5.9% of the turbulent kinetic energy, and feature a set of vortices. In order to investigate the flow structures corresponding to these modes, the conditional averaging process of the flow fields is conducted (this method was reported in [86], and the idea of this method is to analyse the flow fields which have strong contributions to a specific mode).

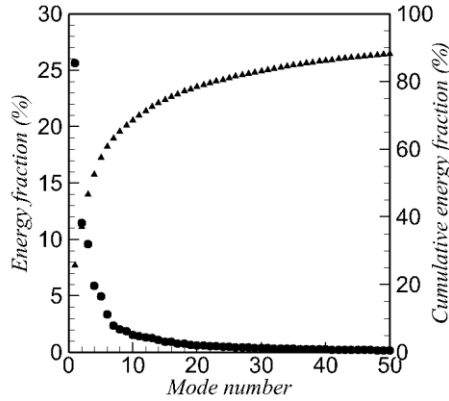


Figure 4.23 Energy distribution of the flow modes in the wall-parallel plane.

$$T_c = 27.3. h/R = 1.46.$$

For mode 1, two data subsets are selected according to the time coefficient of the first mode ($c_1 > 0.035$ and $c_1 < -0.035$, respectively). The value of this specific time coefficient is determined by the number of samples for averaging (at least 20 samples in the current analysis). When $c_1 > 0.035$, there is one dominant vortex in the counter-clockwise direction in the conditionally averaged result (shown in the top left of Figure 4.25). Inversely, when $c_1 < -0.035$, there is one dominant vortex in the clockwise direction (shown in the top right of Figure 4.25). Therefore, the first mode is ascribed to the alternative sign of vortices in the flow field.

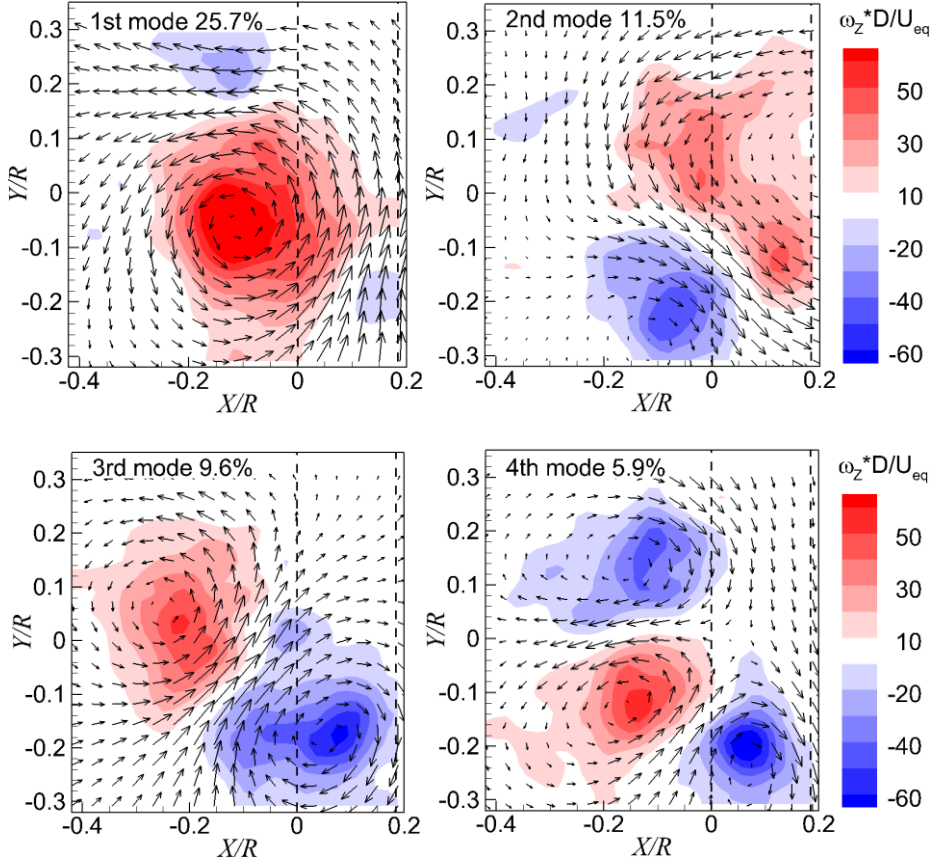


Figure 4.24 The first to the fourth modes in the wall-parallel plane. $T_c = 27.3$. $h/R = 1.46$.

In the same way, the conditionally averaged results on the second mode are shown in the bottom row of Figure 4.25. It is found that the second mode is mainly due to the change of the flow topology near the ground; specifically, the switching of a pair of dominant vortices and one single dominant vortex near the ground. The same methodology can be applied to other modes, and they are not elaborated here.

At different thrust coefficients, the equivalent flow fields corresponding to the first mode in the wall parallel plane are shown in Figure 4.26. The flow structure of the first mode at $T_c = 48.2$ is similar to that at $T_c = 27.3$, which features a dominant vortex upstream of the projection of the propeller on wall; the fractions of the turbulent kinetic energy are close as well. A difference is also noticed that the vortex moves upstream as the thrust coefficient increases, which implies the vortices move upstream by increasing the loading of the propeller.

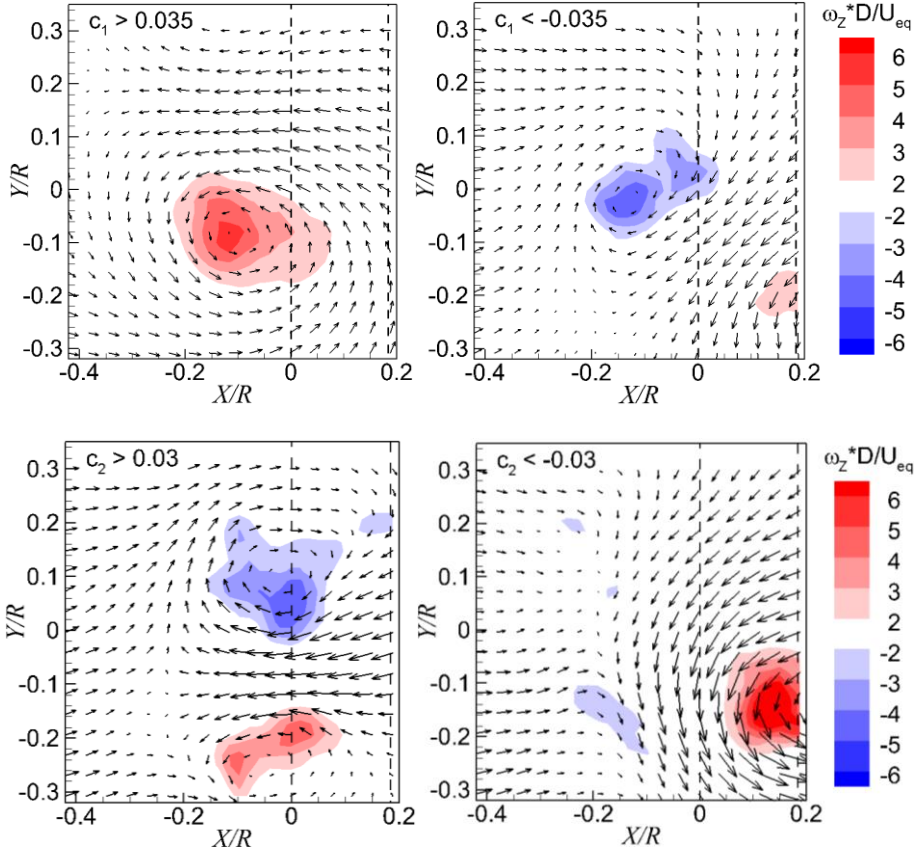


Figure 4.25 Conditionally averaged flow field. Top left: $c_1 > 0.035$; top right: $c_1 < -0.035$; bottom left: $c_2 > 0.03$; bottom right: $c_2 < -0.03$.

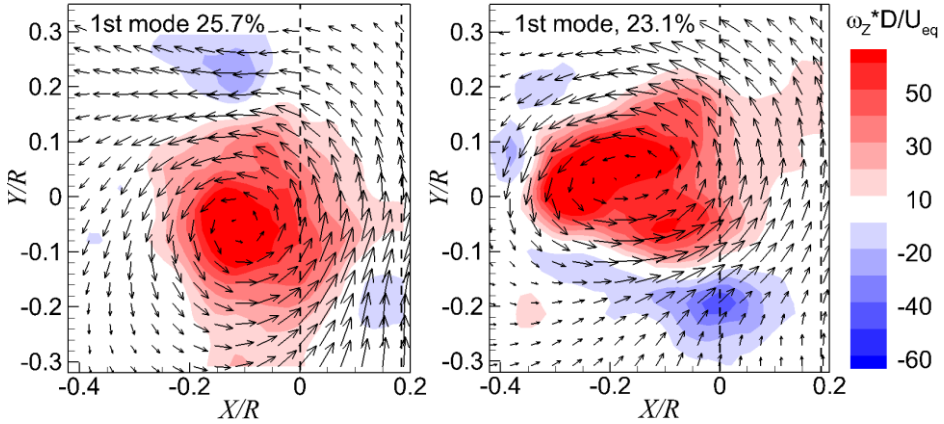


Figure 4.26 Equivalent flow structure of the first mode in the wall-parallel plane at different thrust coefficients. Left: $T_c = 27.3$; right: $T_c = 48.2$.

4.3.4 Proper Orthogonal Decomposition of the flow fields in the plane upstream of the propeller

Following the same method, a *POD* analysis is applied in the plane upstream of the propeller (*PIV* arrangement 4). The fraction of the turbulent kinetic energy and the cumulative energy of the modes are shown in Figure 4.27. The first and second modes capture 14.4% and 12.4% of the total turbulent kinetic energy respectively. The cumulative energy of 73% is attained within the first 50 modes. It is found that 50% of the total amount of turbulent kinetic energy is captured by the first 10 modes. The time averaged flow field of the plane upstream of the propeller was already shown in the right hand side of Figure 4.5 which featured a pair of vortices entering the propeller. The sign of vorticity in the propeller axial direction is opposite on the two sides of the propeller.

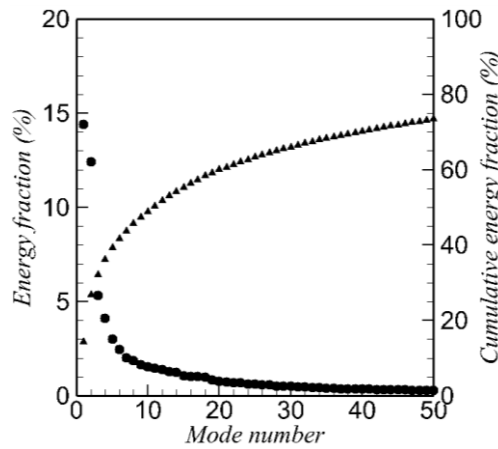


Figure 4.27 Energy distribution of the flow modes in the wall normal plane.

$$T_c = 27.3. h/R = 1.46.$$

The equivalent flow structures of the first and the second modes are represented by contours of the *X*-component of the velocity in Figure 4.28. These two modes feature flow structures with strong contribution from the velocity component in the propeller axial direction. This *X*-component velocity is related to the propeller induced axial velocity upstream of the propeller.

To understand the behaviour of the first two modes, a joint statistical analysis is conducted on the time coefficients of the two modes, c_1 and c_2 . As illustrated by the scatter plot in Figure 4.29, a large correlation between the two modes is retrieved: whenever the first mode has high intensity, the second mode is weaker, and vice versa. The time coefficient plotted in the time domain corresponding to one revolution of the propeller is shown in the right hand side of Figure 4.29. The wave lengths of the time coefficients of the two modes are close, and a 90° phase shift between these two modes is noticed. This observation further confirms that these two modes have strong correlation which is due to the blade passing.

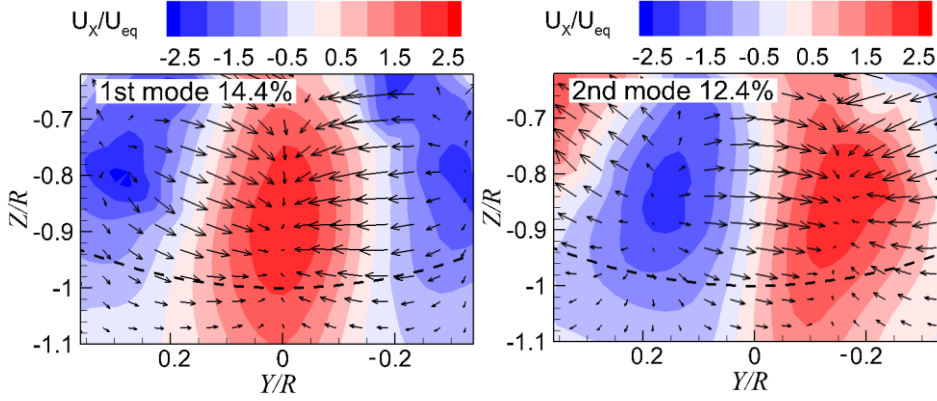


Figure 4.28 Shapes of the first and second *POD* modes in the plane upstream of the propeller color-coded by the axial velocity. $T_c = 27.3$. $h/R = 1.46$.

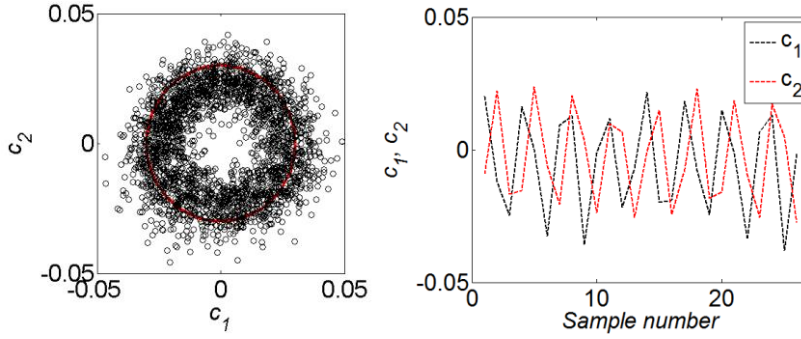


Figure 4.29 Left: scatter plot of the time coefficients of the first and second modes; right: time evolution of the time coefficients corresponding to one revolution of the propeller rotation. $T_c = 27.3$. $h/R = 1.46$.

The third mode exhibits one dominant vortex with the centre located around $[Y/R, Z/R] = [0.08, -0.91]$, of which the vorticity contour is shown in the left hand side of Figure 4.30. The third mode in the wall-normal plane is found to be consistent with the first mode in the wall-parallel plane, which implies that the dominant turbulent flow structures formed near the ground retain after they leave the ground. The fourth mode features a pair of vortices, which are located at the rim of the propeller projection, which is consistent with that observed in the second and third modes in the wall-parallel plane.

Furthermore, the third and fourth modes which are colour contoured by the axial velocity U_x are shown in Figure 4.31. The contour of the axial velocity is consistent with vortex structures as observed in Figure 4.30. Because the vortex has an oblique angle when it enters the disk plane of the propeller, it has induced velocity which is in the axial direction of the propeller. For example, mode 4 has two counter-rotating

vortices, and their induced velocities in the axial direction are consistent with that shown in the right hand side of Figure 4.31.

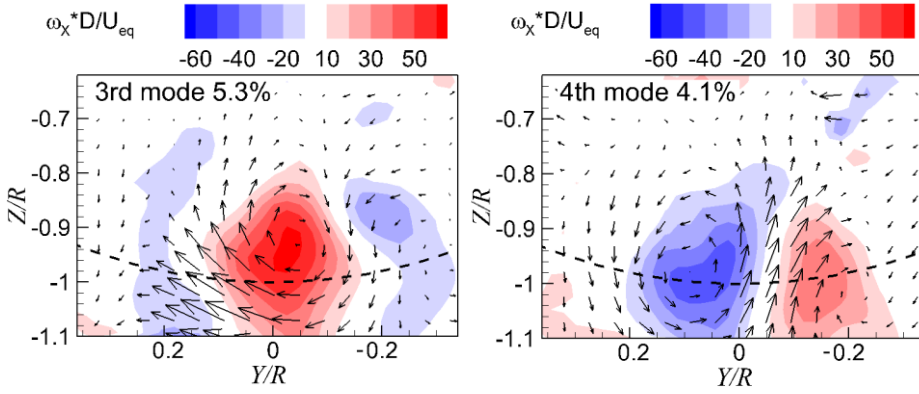


Figure 4.30 Shape of the third mode (left) and fourth mode (right) in the plane upstream of the propeller, colour contoured by the out of plane component of the vorticity. $T_c = 27.3$. $h/R = 1.46$.

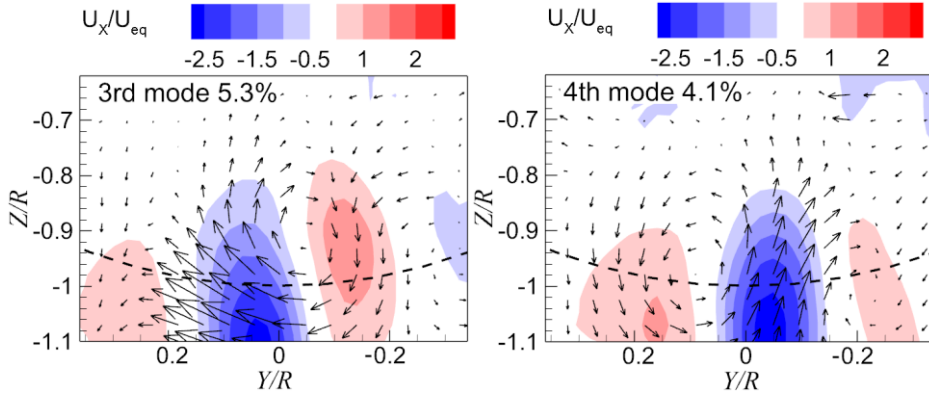


Figure 4.31 Shape of the flow fields of the third mode (left) and fourth mode (right) in the plane upstream of the propeller, colour contoured by the out of plane component of the velocity. $T_c = 27.3$. $h/R = 1.46$.

Conditional averaging is performed on the flow fields which contribute most to the third mode. The conditionally averaged flow fields of $c_3 > 0.022$ is shown in the left hand side of Figure 4.32, and that of $c_3 < -0.022$ is shown in the right hand side of Figure 4.32. These two flow fields generally have two regions of concentrated vorticity (highlighted by the black-dashed circles) and their strengths and positions are different, which contribute to the flow structure of the third mode. The same analysis can be applied to the fourth mode and not elaborated here.

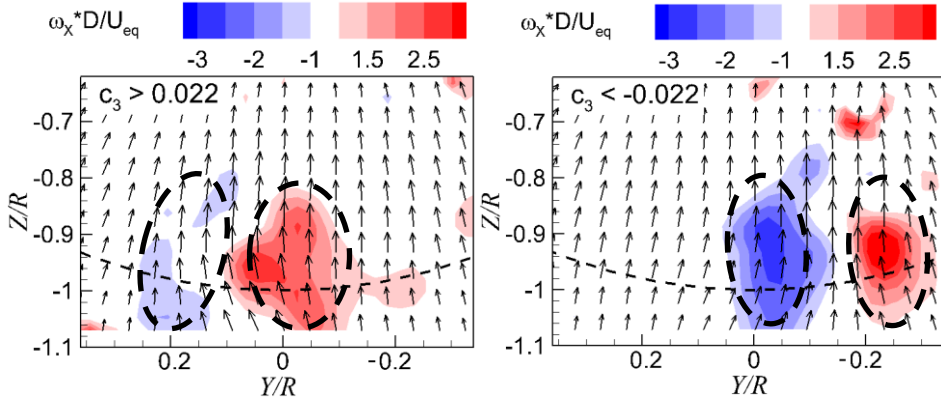


Figure 4.32 Conditionally averaged flow field for $c_3 > 0.022$ (left) and $c_3 < -0.022$ (right).

From the analysis for the four modes in the wall normal plane, it is shown that the first and the second modes are driven by the blade passing induced flow, and the ground vortices have little effect in these two modes. It is also shown that the third and fourth modes are driven by the unsteadiness of ground vortices which are carried from the ground.

At two different thrust coefficients, i.e. $T_c = 27.3$ and $T_c = 48.2$, the flow structures of the third mode in the wall-normal plane are compared and shown in Figure 4.33 (because the first and second modes in the wall normal plane are related to the blade passing, they are obviously similar and not investigated here). The dominant flow structures of the third mode at the two thrust coefficients are generally consistent, which feature a dominant vortex located in the centre of the wall-normal plane and distributed vorticity around it. The main difference is that the area with negative vorticity decreases on the left hand side of the figure as the thrust coefficient increases. As found from the turbulent kinetic energy, the third mode is a relatively less coherent structure than the first and second modes; its structure is sensitive to the structure of the first and the second modes. Although the first two modes are dominated by the blade passing induced flow, there are still structures induced by the ground vortices. As the thrust coefficient increases, the structures in the first two modes would change slightly and consequently the third mode changes slightly accordingly.

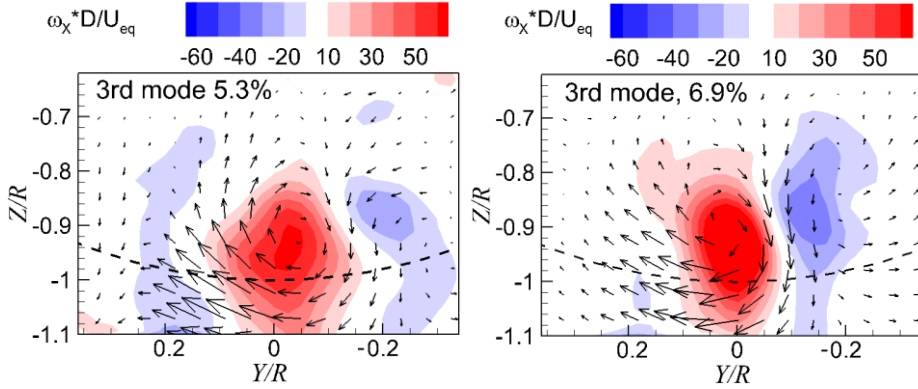


Figure 4.33 Equivalent flow structure of the third mode in the wall-normal plane at different thrust coefficients. Left: $T_c = 27.3$; right: $T_c = 48.2$

4.4 Impact of vortices on the propeller inflow

4.4.1 Non-uniform inflow of propeller due to the impact of ground vortices

As observed in Figure 4.1 and Figure 4.3, there are topologies of one ground vortex, two ground vortices, and multiple ground vortices ascending from the ground and entering the propeller at different instants. For each instant, the inflow of the propeller, which is the vortex-induced flow superimposed on the free stream and the propeller-induced flow, is different. An analysis of the inflow of the propeller at each instant to analyse the impact of the vortex on the propeller is not performed in this part (it will be investigated in the next part with an external vortex impinging onto the propeller); instead, the integral effect of the vortices on the propeller are analysed from the time averaged flow field upstream of the propeller.

The time-averaged flow fields as shown in Figure 4.5, with contour of the out-of-plane component of the vorticity, feature a pair of vortices both in the wall parallel plane and the wall normal plane. A schematic to represent the topology of the time averaged flow fields is drawn in Figure 4.34. The vortices enter the propeller in an oblique angle (this is deduced from the 3D flow topology of the instantaneous flow field as shown in Figure 4.4), the Z-component of the vortices are represented by the red circles, and the X-component of the vortices are represented by the purple circles.

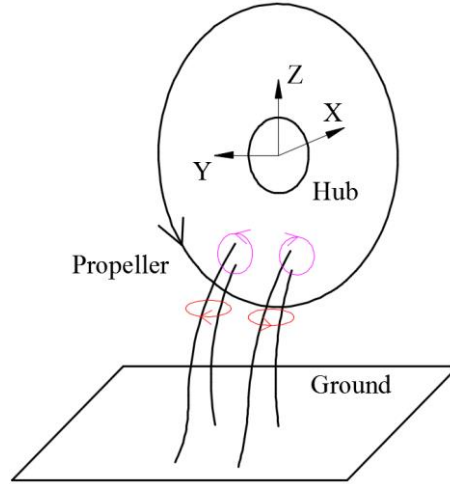


Figure 4.34 Schematic of ground vortices entering the propeller in the time averaged flow field.

The analysis of the impact of vortices on the propeller inflow is performed at the situation of $T_c = 42.1$, and $h/R = 1.46$, which is the case with a strong effect of the vortices on the propeller inflow. The resulting flow fields, due to the interaction between vortices and the propeller, are shown by the distributions of the axial velocity (top left of Figure 4.35), the tangential velocity (top right of Figure 4.35), and the radial velocity (bottom left of Figure 4.35).

The analysis of the flow fields as shown in Figure 4.35 is performed together with analysing the distribution of velocities along the circumferential direction. The radial positions chosen for analysis is $r/R = 0.7, 0.8, 0.9$, and 1.0 , which is inside the region influenced by the ground vortices. The distribution of the axial flow velocity features a region with a dent at the circumferential position around $\Psi = 270^\circ$, and two bulges on the two sides of the dent region, as shown in the top left of Figure 4.36. These bulges and dent of axial velocity are due to the vortex entering the propeller in the wall normal direction (ω_z) which is represented by the red circles as shown in Figure 4.34.

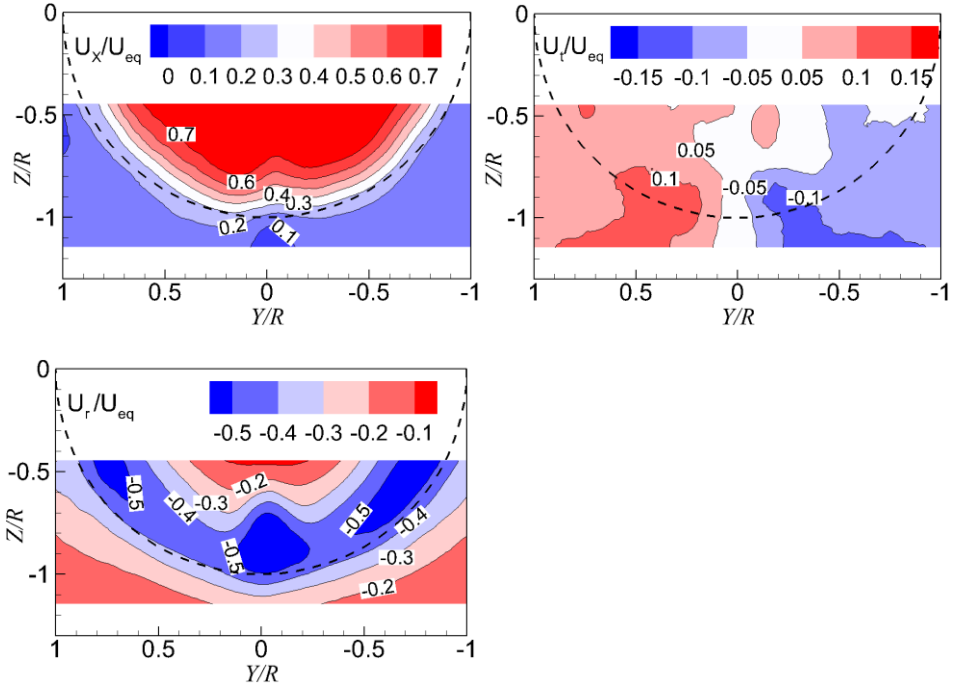


Figure 4.35 Distribution of axial (top left), tangential (top right) and radial (bottom left) flow velocities in the plane upstream of the propeller. $T_c = 42.1$. *PIV* arrangement 2.

The distribution of the tangential velocity is shown in the top right of Figure 4.36, which features half of the field of view with positive tangential velocity and the rest is negative. This is mainly due to the two vortices entering the propeller in the propeller axial direction (purple circle in Figure 4.34). The vortex on the left hand side has the rotating velocity of counter clockwise direction, and vice versa for the vortex on the right hand side. The entering position of the vortex is approximately at radial position of $r/R = 0.75$, so the characteristics of tangential velocity above the impinging position, e.g. $r/R = 0.7$, have the opposite properties of tangential velocity compared with those at $r/R = 0.8, 0.9$, and 1.0 .

The distribution of the radial velocity has a dent in the region around the circumferential position of $\Psi = 270^\circ$, and two bulges on the two sides of the dent. This is mainly due to the induced velocity of a pair of vortices entering the propeller in the axial direction.

The profile of the angle of attack of the blades at the aforementioned radial positions are presented in the bottom right of Figure 4.36. As defined in Chapter 2.1.2, the angle of attack of the blade is determined by the axial velocity and tangential velocity, so the radial velocity does not play a role here. The distribution of the angle of attack can be divided into three sections in the measured domain. The

section on the left hand side (shown inside the red dashed rectangle) has a step with value higher than the right hand side (shown inside the blue dashed rectangle). The section in the middle (shown inside the black dashed rectangle) has the maximum value of angle of attack.

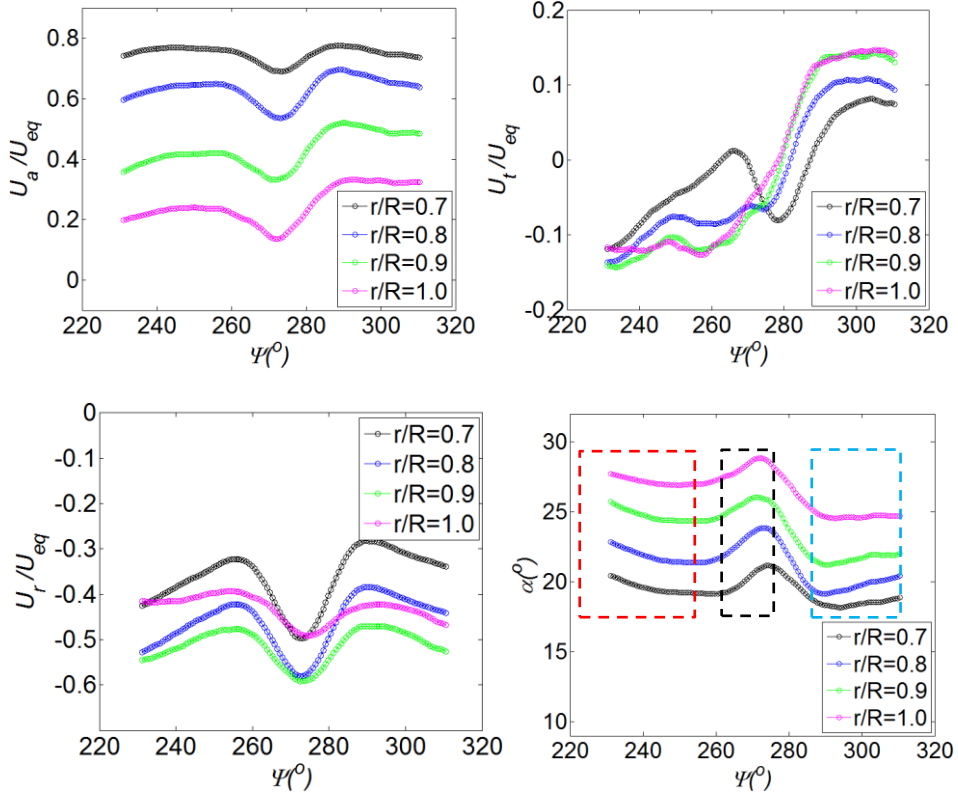


Figure 4.36 Impact of ground vortices on the propeller inflow. Top left: distribution of the axial velocity; top right: distribution of the tangential velocity; bottom left: distribution of the radial velocity; bottom right: distribution of the incidence angle of the blade.

In conclusion of this section, the *PIV* measurement results at the wall perpendicular plane are analysed for a relatively highly loaded propeller with a low height ratio, i.e. $T_c = 42.1$, and $h/R = 1.46$. The velocity components in the polar coordinate system, as well as the angle of attack of the blade are presented. The distributions of the velocity feature a pair of vortices entering the propeller at an oblique angle. The angle of attack is not uniform in the circumferential direction of the propeller due to the impingement of the vortex: near the symmetry line, i.e. $\Psi = 270^\circ$, there is a pulse of angle of attack of the blade; the angle of attack on the left hand side of the measurement domain is also higher than that on the right hand side.

4.4.2 The effect of the thrust coefficient on the non-uniformity of the propeller inflow

Figure 4.37 shows the distribution of angle of attack at four different thrust coefficients. At each thrust coefficient, the angle of attack shows a bulge at the phase angle around $\Psi = 270^\circ$. The ratio of the maximum angle of attack over the minimum ($\alpha_{max}/\alpha_{min}$) increases from 1.03 to 1.23 at the radial position $r/R = 0.9$ as the thrust coefficient increases from $T_c = 5.1$ to $T_c = 42.1$. As explained before, this bulge in the middle is due to the pair of vortices entering the propeller in the radial direction. At $T_c = 11.7$, the angle of attack on the left hand side is slightly higher than that on the right hand side; at $T_c = 42.1$, this step increases. As shown in the top right of Figure 4.36, this step is due to the induced tangential velocity of the vortices which enter the propeller in the propeller axial direction.

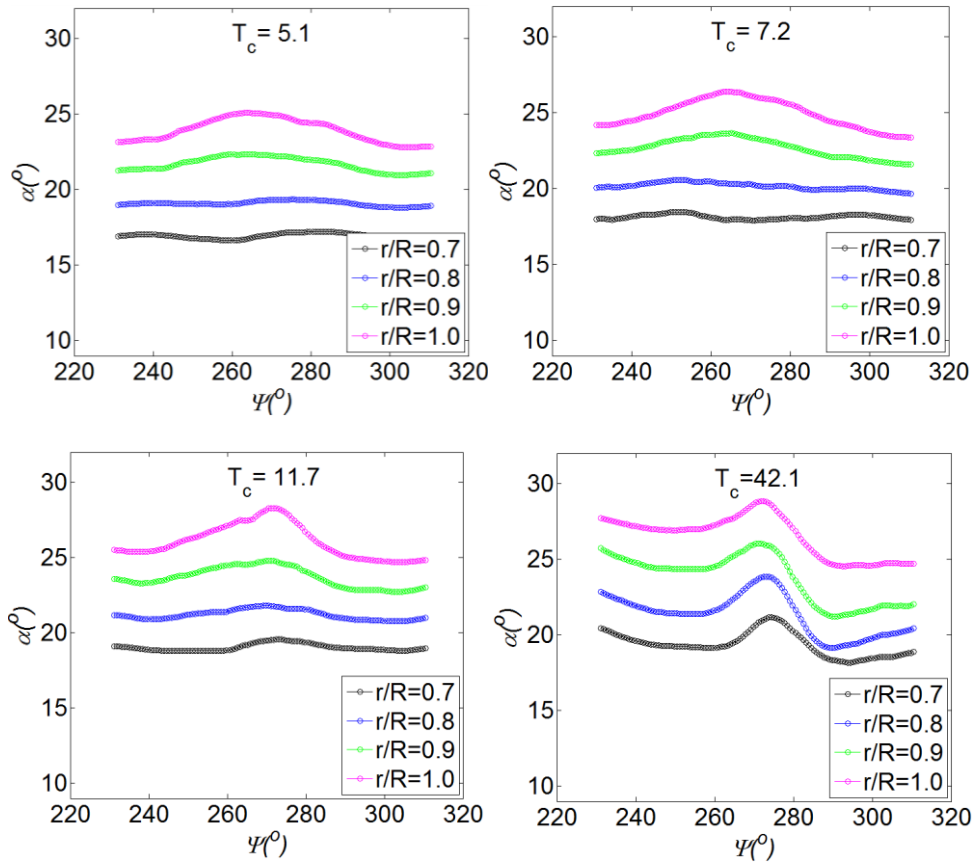


Figure 4.37 The angle of attack of the blade at different thrust coefficients of the propeller.

From the above analysis, it is observed that as the thrust coefficient is low, i.e. $T_c = 5.1, 7.2$, and 11.7 , the flow field is featured by the induced velocity of the Z

component of the vorticity (in the radial direction of the propeller). As the thrust coefficient is high, i.e. $T_c = 42.1$, the flow field is featured by both the X and Z components of the vorticity. This trend is further analysed by investigating the vortex trajectory at different thrust coefficients as below.

From the *POD* analysis, it is found that as the thrust coefficient increases, the vortex foot moves upstream in the wall parallel plane (the same phenomenon was observed in [79]); the entry positions of the ground vortices into the propeller plane have a negligible change. A schematic depicting this trend is shown in Figure 4.38. The vortex trajectory at the *PIV* measurement plane has an oblique angle which is denoted as θ_{imp} , and this angle increases as the thrust coefficient increases. This results in an increase of axial-component of the vorticity.

The foot of the ground vortex moving upstream as the thrust coefficient increases also implies that the occurrence of ground vortices is a local phenomenon. As the thrust coefficient increases, the stagnation point (line), i.e. the intersection point (line) between the stream tube of the propeller and the ground, moves downstream. Therefore, the ground vortices are not originated from these intersection positions which are mainly determined by the thrust coefficient of the propeller. Instead, the ground vortices moving upstream means there are locally formed stagnation points.

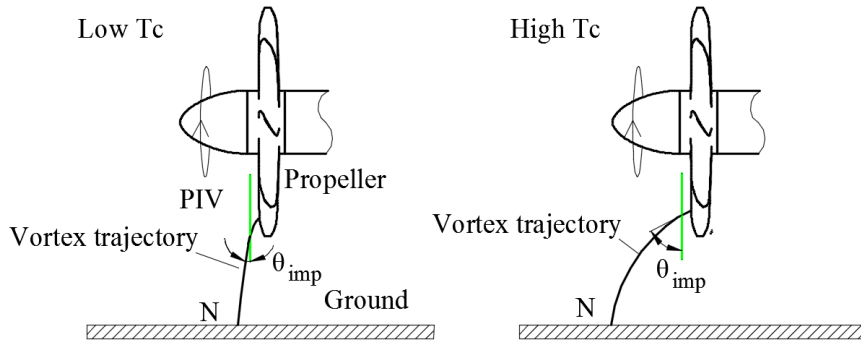


Figure 4.38 Schematic of the vortex trajectory at different loadings of the propeller (side view). ‘N’ is the ascending position of the ground vortex. θ_{imp} is the oblique angle of the trajectory of the impinging vortex relative to the *PIV* measurement plane (green line).

In conclusion for this section, it is shown that as the thrust coefficient of the propeller increases, the amount of vorticity entering the propeller stream tube and the resulted non-uniformity of the flow field increase. It is also deduced that the oblique angle of the vortex trajectory increases as well.

4.4.3 The effect of the height ratio on the non-uniformity of the propeller inflow

The angle of attack of the blade at different height ratios are shown in Figure 4.39. At the height ratio $h/R = 2.0$, the angle of attack ratio $\alpha_{\max}/\alpha_{\min}$ is 1.05 at radial position of $r/R = 0.9$; at height ratio $h/R = 1.7$, the angle of attack ratio $\alpha_{\max}/\alpha_{\min}$ is 1.09. Therefore, as the height ratio decreases, the flow becomes more non-uniform as expected. This result is consistent with the result of a suction tube model which showed the strength of ground vortices increased as the height ratio decreased [30].

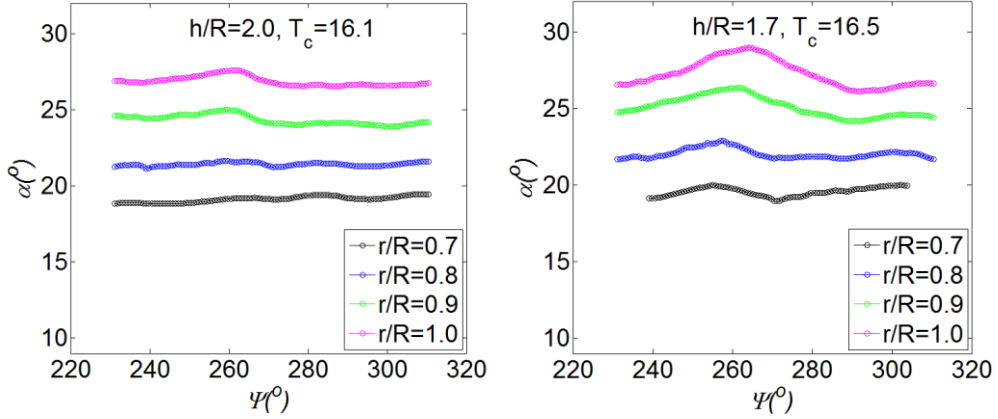


Figure 4.39 The angle of attack of the blade at different height ratios of the propeller.

As found from the analysis in Sections 4.4.1~4.4.3, the angle of attack is not uniform in the circumferential direction due to the ground vortices. Consequently, an unsteady force is generated on the blade at different phase angles, which could induce cyclic stress on the blade and generate tonal noise. This unsteady impact of vortex on the propeller is discussed in the following chapters about the interaction of an external vortex and the propeller. In the next section, the time averaged performance of the propeller is analysed by balance measurements.

4.4.4 Impact of ground vortices on the time averaged performance of propeller

The performances of the propeller at two height ratios are compared, namely, $h/R = 3.0$ and $h/R = 1.46$. The height ratio of $h/R = 3.0$ is the maximum height ratio could be achieved in the setup. It is supposed to be without ground vortices generated at the height ratio of $h/R = 3.0$ when the thrust coefficient is smaller than $T_c = 63$, because the inflow stream tube does not touch the ground based on the analysis of the actuator disk model (as shown in Figure 2.1). The height ratio of $h/R = 1.46$ is the position closest to the ground during our tests, and it induces ground vortices which have the strongest impact on the propeller inflow.

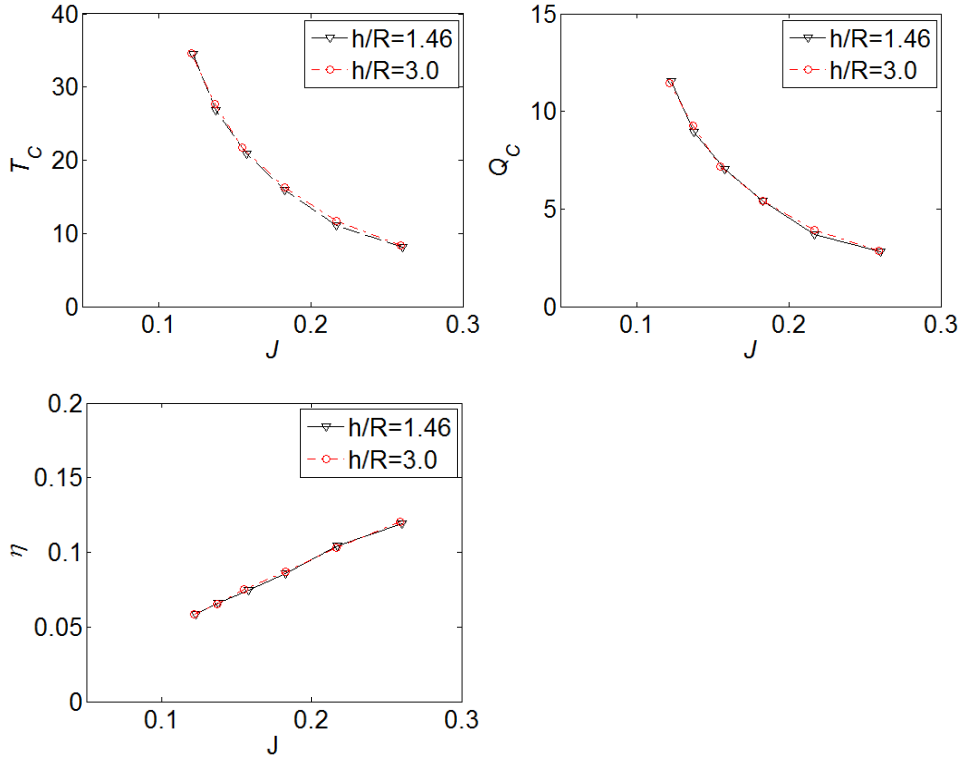


Figure 4.40 Impact of ground vortices upon the time-averaged performance of the propeller. Top left: thrust coefficient; top right: torque coefficient; bottom left: efficiency. Data obtained from experiments.

The difference of the propeller performance between $h/R = 1.46$ and $h/R = 3.0$ is negligible as shown in Figure 4.40, which means that the propeller performance is independent of the ground vortices. Firstly, the effects of the vortices entering the propeller in the propeller axial direction are cancelled out by each other. This hypothesis is confirmed by the tangential velocity distribution as shown in the top right of Figure 4.36. Secondly, although the effect of vortices entering the propeller in the radial direction induces an axial velocity decrease in the propeller inflow (as shown in the top left of Figure 4.36), this influenced region is small compared with the whole disk region of the propeller and its effect is negligible as well.

4.5 Conclusions

The ground vortices induced by a propeller when the propeller operates near the ground is studied both experimentally and numerically. Multiple flow topologies of ground vortices are observed in the instantaneous flow fields, namely, one dominant vortex, two dominant vortices and multiple vortices. A domain boundary of occurrence of ground vortices is built basing on the flow fields near the ground and upstream of the propeller. As the distance between the propeller and the ground

decreases, and as the thrust coefficient of the propeller increases, the occurrence of ground vortices is observed.

From the evaluation of the numerical results, in light of the analytical expressions for the source of vorticity on a solid wall, it is found that the vorticity production rate is consistent with the pressure gradient on the ground in both the lateral and streamwise directions. These results show that the source of the vorticity for the formation of ground vortices is not only from the vorticity in the far field boundary layer, but also has a strong contribution from the locally generated vorticity by the suction effect of the propulsor. The latter source could also be applied to explain the generation of ground vortices under quiescent and take-off conditions of aircraft, which do not involve any far field boundary layer. Furthermore, the production rate of the wall-normal component of the vorticity is found to be due to the solenoidal property of the vorticity.

The spectral analysis performed on the data obtained in the wall parallel plane, shows that the normalized frequencies of order $O(10^{-2}) \sim O(10^{-1})$ dominate the unsteady process. This range of relatively low frequencies is found to be consistent with that observed in the ground vortices induced by a suction tube model. The range of energetic frequencies near the ground is far below the blade passing frequency and this implies that the ground vortices near the ground have a negligible impact from the blade passing. In the wall-normal plane, the spectral analysis of vorticity shows that the energetic frequencies not only occur at the relatively low range as observed near the ground, but there is also a pulse at the blade passing frequency. This pulse is assumed to be due to the extra tilting and stretching of the vortices caused by the change of the pressure field that is associated with the blade passing. This in turn will change the flow field experienced by the propellers.

The flow involving ground vortices is analysed with the help of the *POD* method. The flow fields in the wall-parallel plane feature coherent structures with one vortex (first *POD* mode), two vortices (second and third modes), and multiple vortices (fourth mode). The first and second modes of the flow field upstream of the propeller are dominated by the blade passing; the flow structures in these two modes have the same wave length and a 90° phase angle shift. The modes due to ground vortices can be clearly observed in the third and higher modes in the wall normal plane. The third mode observed in the wall-normal plane is found to be consistent with that observed in the first mode of the wall-parallel plane; the fourth mode in the wall-normal plane is consistent with that of the 2nd-3rd modes of the wall-parallel plane. This consistency means that the turbulent flow structures formed near the ground are transported to the inflow of the propeller without big changes.

The vortices ascending from the ground enter the propeller plane at an oblique angle, where both the radial and axial (with respect to the propeller) components of the vorticity are present. The relative strength of the components is dependent of the propeller thrust setting-the higher the thrust coefficient, the stronger the axial

component of the vorticity. The axial component of the vorticity entering the propeller mainly influences the tangential and radial velocities of the propeller inflow; and the radial component of the vorticity entering the propeller mainly influences the axial velocity of the propeller inflow. Consequently, the blade incidence angle is changed and becomes non-uniform in the circumferential direction. With a higher thrust coefficient and a lower height ratio of the propeller, the non-uniformity of the blade incidence angle becomes severer. The time-averaged performance of the propeller is independent of the ground vortices, because the effects of the vorticity cancel each other and the magnitude of the vorticity is relatively small.

4.6 Discussion

As described in this chapter, there are multiple ground vortices generated on the ground and convected toward the propeller; the number and strength of the individual vortices are not constant. For the interest of understanding the impact of vortical inflow on the propeller, discussing a model with a single vortex with a constant strength impinging on the propeller is helpful. For the benefit of this discussion, following in the next part of this thesis, an external vortex is generated by a lifting surface in the propeller inflow and the interaction between the vortex and the propeller is investigated. On the one hand, this external vortex can be utilized to study the axial component of the vorticity of the one single ground vortex. On the other hand, it gives insights into the interaction between an external vortex and a propeller, which is frequently encountered in aeronautics.

Part III

Interaction between an externally generated vortex and a propeller

Chapter 5 Tools and methods for the investigation of interaction between an externally generated vortex and a propeller

For the study of the interaction of a vortex with a propeller, a pure form of the vortex generated independently of the propeller is chosen. Well-defined conditions can be generated by placing a lifting wing of finite span upstream of a propeller. In the present study, the tip vortex produced by a lifting wing in the presence of a propeller is investigated as well as the effect of the incoming vortex on the propeller. The properties of this vortex are measured with the help of the Particle Image Velocimetry (*PIV*), which yields information about both the location as well as the strength of the vortex. The resultant flow field downstream of the propeller which includes the effects of the vortex interaction is measured using the *PIV* measurement as well. The impact of the vortex on the propeller performance, in terms of the thrust and the torque, is measured by a rotating shaft balance (*RSB*).

Because the flow field is resolved in a limited area at discrete planes by *PIV* measurements, a visualization of the three-dimensional flow topology is helpful for understanding this complex phenomenon in a global way. Furthermore, because only the time averaged performance of the propeller can be measured by the current rotating shaft balance, obtaining the unsteady loading on the propeller is helpful to understand the time dependent impact of the vortex on the propeller. Due to the above reasons, numerical calculations solving the unsteady Reynolds Averaged Navier-Stokes equations (*uRANS*) are performed. For these calculations the boundary conditions are defined in such a way as to represent the experimental cases tested in the wind tunnel.

5.1 Experimental arrangements

5.1.1 Vortex generator

The vortex generator is a truncated 2-dimensional wing with the *DU96-W-180* airfoil, and the profile of the airfoil is shown in Figure 5.1. The airfoil, designed for wind turbines, is used because it was available; there were no specific other considerations related to this choice. The span of the wing is 1 *m*, with the chord length of 0.25 *m* and the maximum thickness of 18%. A vortex was shed from the tip of the lifting surface at a positive incidence angle. The *AOA* of the wing was adjusted by rotating the wing to change the strength of the impinging vortex. In order to adjust the vortex-impinging position on the propeller, the wing can be moved in the lateral and vertical directions, as shown in Figure 5.3.

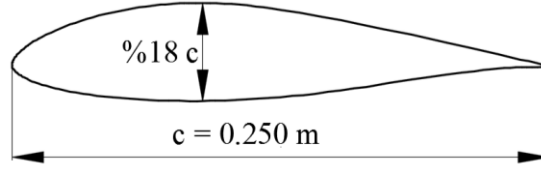


Figure 5.1 Cross section of the vortex generator with the *DU96-W-180* airfoil.

In the present study, the vortex strength is the parameter used to characterise the vortices. The vortex strength is quantified by the circulation, Γ , which was already defined in Eq. (2.21). Herein, the circulation of the vortex is defined in its surface integral form,

$$\Gamma = \iint \omega_X \vec{i} d\vec{S} / (U_\infty * D), \quad \text{Eq.(5.1)}$$

ω_X is the magnitude of the X -component of the vorticity (the unit vector in this direction is denoted as \vec{i}). \vec{S} is the integration area on the *PIV* measurement plane, and the positive direction is defined as the surface normal in the same direction as the X -component. A positive value of the circulation represents a vortex with the opposite rotation direction as the propeller rotation (propeller rotates in the negative X direction), and vice versa for a negative value. The vortex strength divided by D represents the pre-swirl velocity in the propeller inflow, and this pre-swirl velocity divided by U_∞ represents the inflow angle.

5.1.2 Experimental setup

The wind tunnel and propeller model in this part are the same as those used for conducting the study of ground vortices. The equipment was already described in Chapter 3.

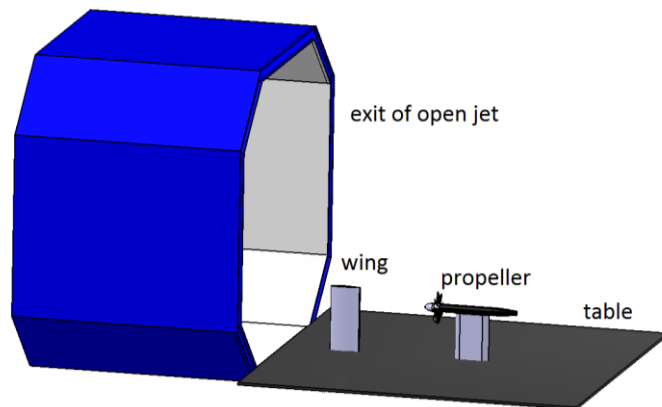


Figure 5.2: Experimental setup of the propeller wing combination in the Open Jet Facility (*OJF*) at Delft University of Technology.

The schematic of the experimental setup for studying the interaction between a vortex and a propeller is shown in Figure 5.2. A horizontal plate is positioned at the bottom of the free jet test section, to avoid interaction with the shear layer of the wind tunnel. The inflow velocity chosen in the experiments is 18.6 m/s which is below the maximum speed (35 m/s) of the wind tunnel, in order to obtain good quality velocimetry data. At higher velocity, the seeding in the vortex became too sparse for good resolution. All the desired advance ratios J and thrust coefficients T_c can be obtained at this wind tunnel setting.

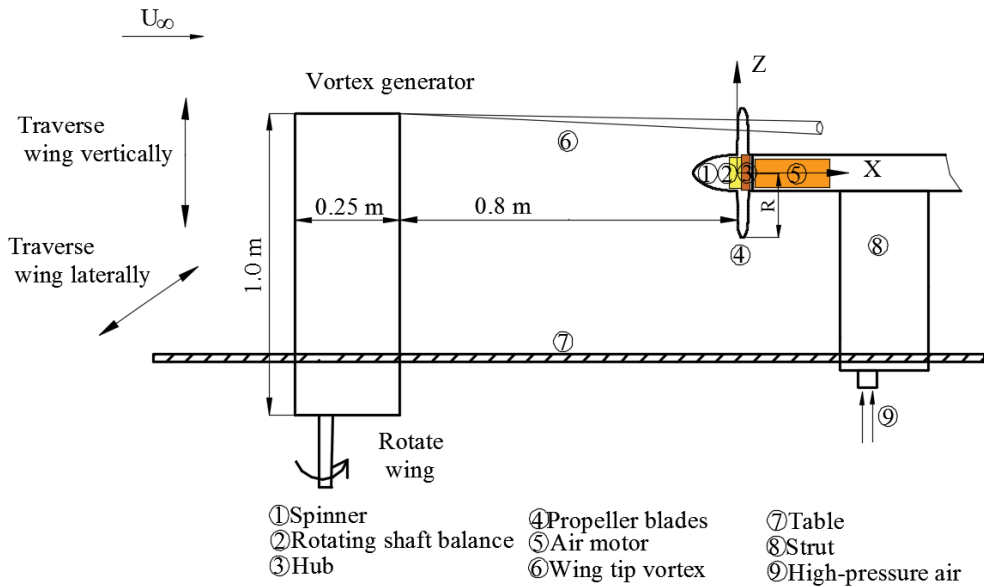


Figure 5.3 Schematic of the experimental setup and dimensions of the model.

A detailed 2D sketch of the experimental setup is shown in Figure 5.3. The vortex is shed from the tip of the wing, and convected downstream by the free stream and the propeller suction-induced flow. The vortex generator (wing) is positioned at a distance sufficiently large (3.2 times of the length of the wing chord) to allow the wing tip vortex to develop and minimize the wing wake in the interaction.

5.1.3 Test matrix

For the investigation of the impact of the propeller on the vortex, the test matrix is determined by applying the methodology of one factor at a time (OFAT). The vortex is maintained at a constant strength by maintaining the setting of the vortex generator. The effect of the propeller on the vortex is investigated at a sweep of advance ratios, $J = 0.5, 0.6, 0.8, 1.1$ and $J = 2.2$ (as shown by the dashed lines as shown in Figure 5.4). It needs to be noted that the zero loading condition of $J = 2.2$ in our measurement is conducted without the propeller being present in the flow. Different advance ratios correspond to different thrust coefficients, the relation of

these two parameters of our propeller model is shown in Figure 5.4. Such an effect (advance ratio or thrust) of the propeller on the vortex is investigated in Chapter 6.

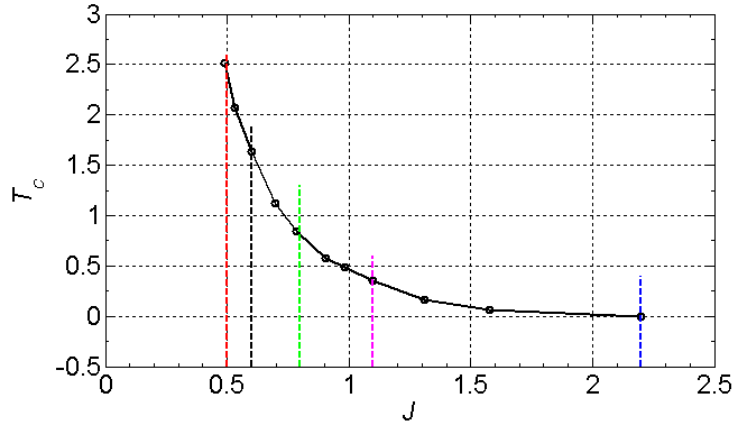


Figure 5.4 Thrust coefficient versus advance ratio of the isolated propeller. The dashed lines show the test points to study the effect of the propeller on the vortex.

For the investigation of the impact of the vortex on the propeller, the test matrix is determined by the *OFAT* method as well. The propeller is maintained at one constant advance ratio by maintaining the free stream velocity and the rotating speed of the propeller, i.e. $J = 1.1$. The effect of the vortex on the propeller is investigated at a sweep of vortex strengths. Due to the impact of the vortex, the propeller loading, e.g. the thrust coefficient as shown in Figure 5.4 is expected to have a change at a given value of the advance ratio, and the relation between the change and the vortex strength is investigated. In addition, the change of the thrust coefficient may have different magnitudes for the same vortex strength but at different advance ratios. Furthermore, as a vortex impinges at different radial positions of the propeller, the propeller response is also analysed. All these studies are presented in Chapter 7.

5.1.4 *PIV* setup

To quantify the position and strength of the impinging vortex and obtain insights into the vortex response to the propeller, velocity measurements were performed in the planes involving the vortex. Because the velocity in the out-of-plane component is in the same order of magnitude as the in-plane components, stereo *PIV* measurements were conducted instead of planar *PIV*, to get rid of the error induced by the velocity of the out-of-plane component.

The devices of cameras, laser, and smoke generator are still the same as those utilized during the study of ground vortices, so they are not repeated here. Only the setup of the *PIV* measurements is described herein. Two planes normal to the propeller axis are investigated. One plane upstream of the propeller was positioned at $X/R = -0.20$, which is on the left-hand side of Figure 5.5; and the other one

downstream of the propeller at $X/R = 0.32$ ($0.13 R$ downstream of the trailing edge of the blade root), which is shown on the right-hand side of Figure 5.5. The processing is conducted with the interrogation window size of $64 \text{ pixels} \times 64 \text{ pixels}$, 50% overlap.

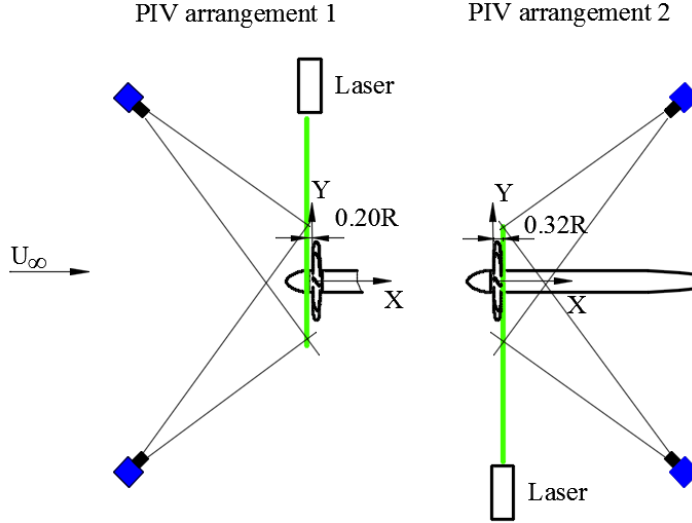


Figure 5.5 Top view of the *PIV* setups in the upstream plane and the downstream plane.

The direction of laser illumination is important to alleviate reflection from the blades. For the *PIV* arrangement 1, the laser sheet is set to illuminate from top to bottom as viewed from the upstream to the downstream position. For the *PIV* arrangement 2, the laser sheet is set to illuminate from bottom to top. The number of samples of the *PIV* measurements of each test condition is 300 in the upstream plane and 500 in the downstream plane.

5.1.5 Bin method for the phase lock analysis

As the impinging vortex is not co-axial with the propeller centre line, the phase angle of the propeller (as defined in Figure 2.4) determines the interaction between the propeller and vortex. In order to investigate the flow field at different phase angles of the blade, an analysis of the flow per given phase angle is necessary.

The phase-lock analysis for the results of the *PIV* measurements is conducted by the bin method. This method matches the sample images of *PIV* measurements with the benchmark images. The benchmark images were acquired by taking images at a sequence of phase angles when the propeller was stationary. These 8 phase angles are $\Psi = 0.5^\circ, 6.0^\circ, 11.5^\circ, 17.0^\circ, 22.5^\circ, 29.0^\circ, 34.5^\circ$, and 40.0° (the interval of 5.5° is chosen by considering the available time in the wind tunnel). For example, the benchmark frame taken at the blade phase angle of $\Psi = 6.0^\circ$ is shown on the left-

hand side of Figure 5.6, and the benchmark frame taken at the phase angle of $\Psi = 34.5^\circ$ is shown on the right-hand side of Figure 5.6. The reflection from the blade causes a high intensity of light in the benchmark image and later during the *PIV* measurements, which has been used to determine the blade position for the matching process.

For each of the aforementioned eight phase angles, 20~30 samples are selected and averaged for the analysis of the phase lock. Other samples of *PIV* measurements are discarded for the phase lock analysis.

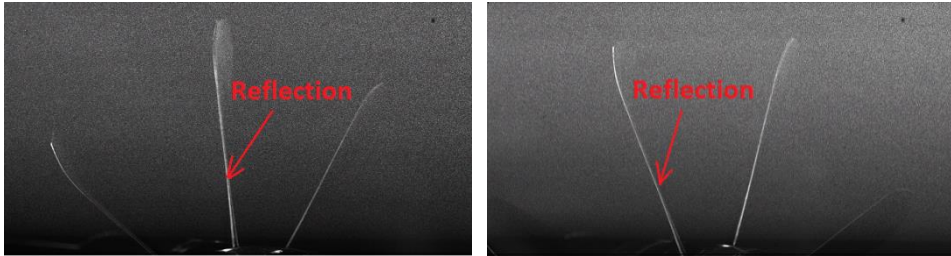


Figure 5.6 Example frames of reflection on the blades, phase angle $\Psi = 6.0^\circ$ (left) and $\Psi = 34.5^\circ$ (right). Viewed from the front.

5.1.6 Error analysis of the experimental measurements

- Error analysis of the *PIV* measurements

The uncertainty of the *PIV* data is estimated by the same method as shown in Section 3.3. In the plane upstream of the propeller, the uncertainty of the instantaneous velocity fields at 95% confidence level is 0.045 *m/s* for the in-plane velocity components and 0.049 *m/s* for the out-of-plane component. The uncertainty of the vorticity in the axial direction at the plane upstream of the propeller is 12.59 *1/s*, in which the vorticity is calculated by the centre-difference method. In the plane downstream the propeller, the uncertainty is 0.064 *m/s* for the in-plane velocity components and 0.089 *m/s* for the out-of-plane velocity component. The uncertainty of the vorticity in the axial direction at the plane downstream of the propeller is 16.45 *1/s*.

- Error analysis of the bin method and *AOA* setting of the vortex generator

The bin method is applied to obtain the phase-angle averaged property of the vortex, e.g. the circulation of the vortex. Therefore, the error analysis of the bin method is performed on analysing the scatter of the circulation in the vortex core. The example selected for error analysis is the case when the propeller operates at the advance ratio of $J = 1.1$, and the vortex generator is set at $AOA = 8^\circ$. The circulation in the vortex core for each sample is denoted as $\Gamma_{c,i}$. The averaged result of the circulation at a specific phase-angle ($\Psi = 6.0^\circ$ in the current analysis) in the vortex core is denoted as $\Gamma_{c,avg}$. The error of the averaged result is evaluated by the

square root of $\Gamma_{c,i} - \Gamma_{c,avg}$. The scatter of the circulation in the vortex core is $0.03 \text{ m}^2/\text{s}$ for the current case and the relative error is 4.2%. It should be mentioned that this value of scatter also has a contribution from the fluctuation of the wing tip vortex, and it is not from the bin method only.

The setting of AOA of the vortex generator is conducted by a rotatable disk with an accuracy of 0.2 degree. The uncertainty propagated to the vortex circulation is considered to be a linear relation, with coefficient of the linear relation determined from the relation of vortex circulation over AOA of the vortex generator (as shown in section 6.2.3). The uncertainty of the vortex circulation determined from the propagation analysis is shown in the relevant figures (Figure 6.12 and Figure 6.19). The error analysis of balance measurements was elaborated in Chapter 3 already.

- Convergence analysis of averaging process

The analysis of the quantities of the vortex, i.e. the circulation, the radius, and the maximum tangential velocity, is performed on the time averaged result. In order to check whether the averaged result converges, the circulation is selected to analyse, and other quantities follow the same trend.

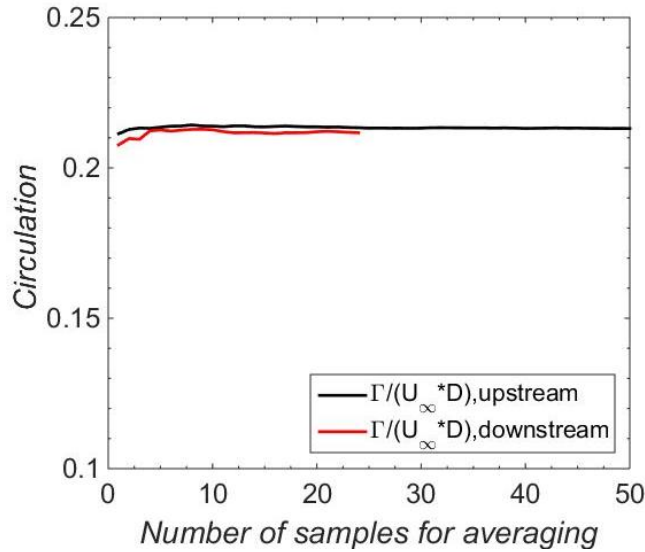


Figure 5.7 Convergence analysis of the circulation during the averaging process.

The convergence analysis of the circulation is shown in Figure 5.7. Upstream of the propeller, the circulation in the disk which is centred at the vortex centre and with the radius of $0.25 R$, R is the radius of the propeller. The circulation converges at the sample number of 3, at which the averaged circulation is already 99.9% of that with sample number of 4. Downstream of the propeller, the circulation (in the disk region with the radius of $0.15 R$, where the circulation has its maximum value)

converges at the sample number of 12. The circulation of 12 samples is 99.9% of that with the sample number of 13. It is noticed that the sample number to achieve convergence is rather small both upstream and downstream of the propeller, because the circulation is an integral quantity of the velocity, which greatly decreases the influence of the fluctuation from each data point.

5.2 Numerical methods

5.2.1 Methodology of the numerical simulation

A numerical simulation is conducted using the same geometry as the experimental model except for two differences. First, there is no strut to support the model; second, there is no exhaust flow at the end of the nacelle, and the nacelle extends to the outlet boundary. The effects from the strut and exhaust jet on the propeller/vortex interaction are assumed to be negligible.

The impingement of the vortex on the blade is an unsteady phenomenon: the vortex response to the propeller and the blade loading are both unsteady. Therefore, the simulation is conducted by solving *uRANS* equations. The technique of sliding mesh [87] is chosen to study this unsteady phenomenon.

The vortex prescribed on the velocity inlet boundary to simulate the impinging vortex is the Lamb-Oseen vortex model, where the axial, tangential, and radial velocity components are respectively given by:

$$U_t = \frac{\Gamma_\infty}{2\pi r_c} \left(\frac{1 - e^{-1.25643\bar{r}^2}}{\bar{r}} \right). \quad \text{Eq.(5.2)}$$

$$U_a = U_\infty. \quad \text{Eq.(5.3)}$$

$$U_r = 0. \quad \text{Eq.(5.4)}$$

Here, the constant of 1.25643 is merely applied to have a peak tangential velocity at the core radius [88] as already elaborated in Section 2.2.5. The Lamb-Oseen vortex model is found to well represent the induced flow field of the wing tip vortex ([68, 69]); and this consistence will be further confirmed in Chapter 6.1.1. The distribution of the tangential velocity is the only parameter defined in the Lamb-Oseen vortex model; the excess or deficit of the vortex axial velocity is excluded; the radial velocity is assumed to be zero. Therefore, by using Lamb-Oseen vortex model, only the effect of the vortex circulation upon the propeller performance is simulated. This simplification by omitting the effect of two other components of velocities are verified to be consistent with experimental result (as shown in Chapter 6 and Chapter 7), because the impact of the vortex upon the propeller is dominated by the tangential velocity of the vortex.

5.2.2 Computational domain and boundary conditions

There are two computation domains which are necessary to conduct a sliding mesh simulation: one is the rotating domain surrounded by the interfaces as shown in Figure 5.8; the rest is the stationary domain. The rotating domain involving the propeller model is a cylinder with the radius of 1.5 times of the propeller radius, and the height of $2.6 R$. The stationary domain is a cylinder with the radius of $10 R$, the height of $10 R$ upstream and $13 R$ downstream of the propeller.

A moving wall boundary with no-slip wall condition is set for the blades, spinner, and hub. The stationary wall with no-slip wall condition is prescribed on the nacelle of the propeller which extends to the far downstream as shown in Figure 5.8. The vortex is added to the flow on the velocity inlet boundary condition. The pressure outlet boundary conditions are prescribed on the outlet and cylindrical surface of the stationary domain.

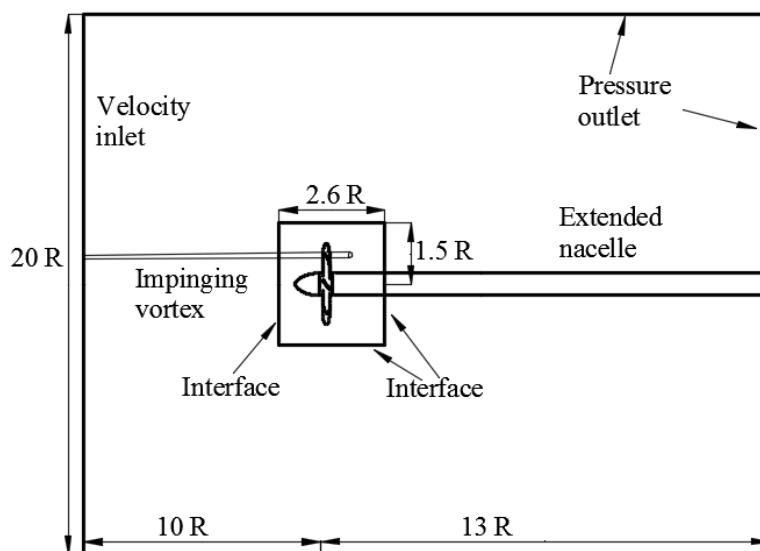


Figure 5.8 Schematic of the computational domains and boundary conditions

5.2.3 Mesh of the model

A hybrid mesh is employed for the computation domain as shown in Figure 5.9. Unstructured mesh is employed for the rotating domain, which involves blades, the spinner, the hub and part of the nacelle, generated by the *ANSYS MESH* module. The mesh near the boundary layer has prism layers, with Y^+ value of 1, and the rest is tetrahedral mesh in the rotating domain. The detail of the mesh on the propeller is shown in Figure 5.10, which has a refinement on the region of the tips, leading edges and trailing edges of the propeller blades to capture high gradients of flow variables.

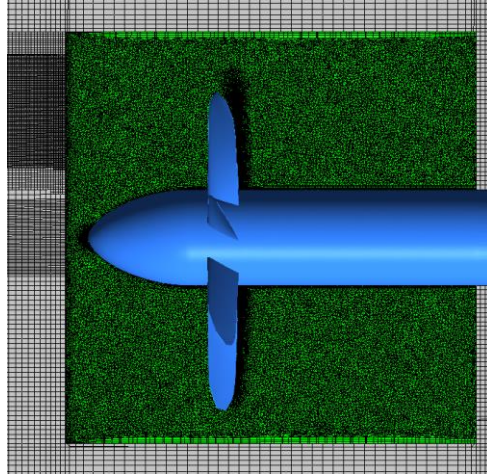


Figure 5.9 Hybrid mesh represented on the cut plane through the propeller centre line. Outer region: hexa-structured mesh; inner domain: unstructured mesh.

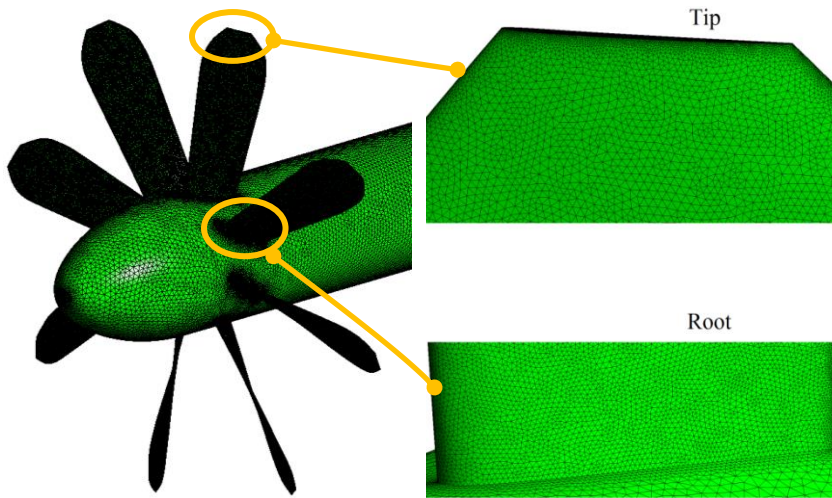


Figure 5.10 Surface mesh on the propeller.

The hexa-structured mesh is generated for the stationary domain. The main reason is that the impinging vortex prescribed on the inlet is convected through this domain and hexa-structured mesh shows a less diffusive character than the unstructured mesh [89]. The region where the core of the impinging vortex goes through is refined to alleviate the diffusion effect as well. The hexa-structured mesh is generated by *ANSYS ICEM* for this domain.

The mesh convergence is studied by checking the thrust coefficient of the isolated propeller at different number of nodes, which is shown in Table 1. The refinement from the coarse mesh to the fine mesh is mainly performed on the

volume mesh of the rotating domain and the surface mesh of the blades. As shown in Table 1, the medium mesh can already be regarded as the converged mesh, in which the thrust coefficient only has a 1.3% increase compared with the coarse mesh. However, in order to well resolve the vortex, the fine mesh is still chosen.

Table 1 Influence of the node number on the thrust coefficient of the propeller, performed on the advance ratio of $J = 1.1$.

Mesh	Nodes number (million)	T_c , thrust coefficient	$\Delta T_c/T_c$ (Δ is relative to the row above)
Coarse	7.6	0.3510	-
Medium	9.7	0.3556	+1.3%
Fine	12	0.3556	0.0%

5.2.4 Turbulence model

The simulation of a propeller by using the $k - \omega$ SST (shear stress transport) model of *uRANS* simulation has been reported to be consistent with experimental results [89] in terms of propeller loadings. In our simulation, not only the performance of the propeller, but also the vortical flow is of interest. The turbulence model is significant in the simulation of a vortex, e.g. the pressure gradient in the radial direction is found to be dependent on the turbulent normal stress in the radial direction [90]. The blade tip vortices and wakes from *uRANS* simulation already give close results to the *DES* (detached eddy simulation) results in two propeller radii downstream [91], in terms of vortex strength. Because the flow field far downstream the propeller is not of interest for this research, the flow field two radii of propeller downstream is enough to understand the interaction between the vortex and vortical structures shed from the propeller. Therefore, the $k - \omega$ SST turbulence model is adopted to guarantee both the accuracy of the propeller performance and properties of the vortex.

5.2.5 Solver

Parallel computation is conducted with the commercial software of *ANSYS FLUENT*. This is run on a cluster of 48 processors. Spatial discretization uses the second order upstream method. Velocity and pressure coupling is achieved by the *SIMPLE* algorithm in *FLUENT*. The temporal discretization of the transient derivatives uses second order implicit schemes. The time-step set at the interval corresponds to the time of propeller rotating by 0.5 degree, e.g. $\Delta t = 0.00002451$ s for the propeller rotating speed of $rpm = 3400$. This selected time step leads to a Courant-Friedrichs-Lewy (*CFL*) number of 0.2 in the rotating domain.

Chapter 6 Results and discussion of the response of an externally generated vortex to a propeller

As the vortex impinges onto the propeller, the propeller is expected to modify the structure of the incoming vortex. By investigating the flow field at the two *PIV* measurement planes, which are upstream and downstream of the propeller respectively, the flow topology of the vortex is analysed. The *CFD* result is validated by the flow fields at these two planes and further analysis builds a three dimensional flow topology that describes the behaviour of the interaction in detail.

Due to the interaction between the vortex and the propeller, the vortex properties, i.e. the vortex meandering, the vortex core radius, the maximum tangential velocity, and the circulation, have the potential to be altered. By investigating these properties of the vortex both upstream and downstream of the propeller, the vortex response to the propeller is studied in a sweep of advance ratios of the propeller, which represents different thrusts generated by the propeller.

6.1 Typical flow fields and three-dimensional vortex topology

6.1.1 Flow fields upstream of the propeller

The flow fields in the plane upstream of the propeller ($0.2 R$ upstream of the leading edge of the blade root) are shown in Figure 6.1 from the *PIV* measurement result (left) and the *CFD* result (right). The propeller is operated at a moderate loading condition $J = 1.1$ for both results ($T_c = 0.35$). The experimental result has a vortex generated at the condition of $AOA = 8^\circ$ (this AOA is chosen because the impact of the vortex on the propeller can be measured with a relatively low relative error by our balance, and at the same time the wing is not stalled [92]). The *CFD* result has a vortex by prescribing a Lamb-Oseen vortex at the velocity inlet with the strength of $\Gamma_{inlet}/(U_\infty * D) = 0.6582$, which is the integrated vorticity in the whole region of the velocity inlet. This case of *CFD* simulation is chosen because the sign and the magnitude of the vortex is close to the experimental case of $AOA = 8^\circ$ (with a 5% difference evaluated at the plane $X = -0.3 R$), hence ensure that the comparison of vortical flow between the two methods is meaningful.

The vectors in Figure 6.1 show the velocity directions in the plane, which feature a contra-rotating vortex with respect to the propeller rotating direction for both the experimental result and the *CFD* result. The colour contour plots show the X -component of the vorticity in the plane, which features a concentrated region of vorticity with the maximum magnitude located at $[Y/R, Z/R] \cong [0, 0.75]$. The experimental result does not feature the wake region of the vortex generator in the

distribution of the vorticity, which means the wake vorticity is relatively small compared with the wing tip vortex in the current experimental set up. The detailed analysis of the impact of the propeller on the vortex upstream of the propeller will be discussed in Section 6.2.

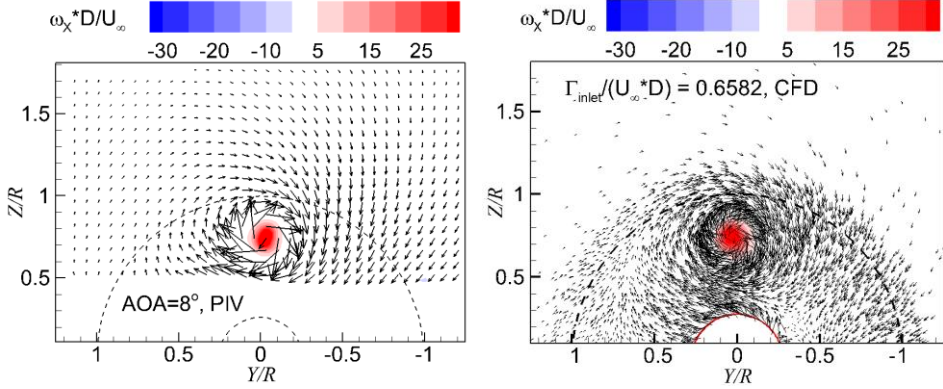


Figure 6.1 Distribution of the X component of the vorticity upstream of the propeller ($X/R = -0.2$). Left: *PIV* measurement with vortex generator set at $AOA = 8^\circ$; right: *CFD* simulation with $\Gamma_{inlet}/(U_\infty * D) = 0.6582$ at the velocity inlet. Moderate loading at $J = 1.1$.

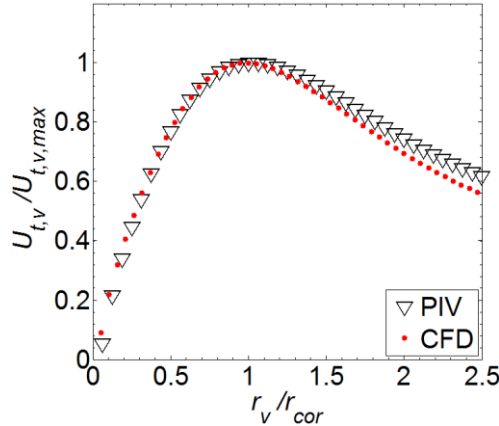


Figure 6.2 Non-dimensional tangential velocity versus non-dimensional radius of the vortex just upstream of the propeller from *PIV* and *CFD* results.

In order to verify that the vortex generated by the *CFD* method represents the wing tip vortex generated in the experiment, the tangential velocity profile of the *CFD* result is compared with that of the experimental result. The tangential velocity in the vortex with respect to the vortex centre is normalized by the vortex maximum tangential velocity. The radial distance from the vortex centre in the vortex is normalized by the vortex core radius. The non-dimensional tangential velocities versus the non-dimensional radii are plotted in Figure 6.2. Inside the vortex core

region, the tangential velocities from the two methods are on top of each other. Outside the vortex core, the tangential velocity of the *CFD* result is slightly lower than the *PIV* result, which is ascribed to the vorticity in the wake region of the vortex generator, but the trends of the results from the two methods are the same. Therefore, their resulting flow fields in the propeller inflow are considered to be the same by the two methods.

The distribution of the axial component of the velocity (U_x) in the plane upstream of the propeller is shown in Figure 6.3. In the region with experimental data, the distributions of U_x of the *CFD* result is generally consistent with the *PIV* measurement result, which are due to the free stream velocity and the induced velocity by the propeller.

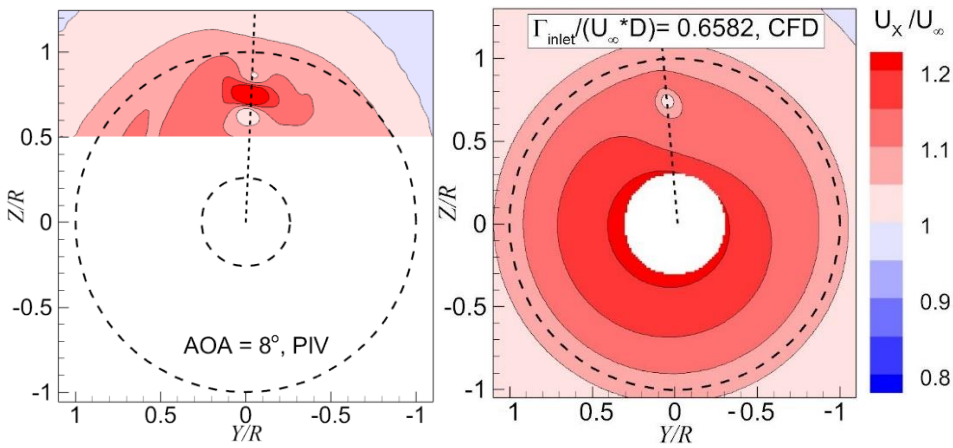


Figure 6.3 Distribution of the X component of the velocity upstream of the propeller ($X/R = -0.2$). Left: *PIV* measurement result; right: *CFD* simulation result. The straight dashed line indicates the line across the vortex centre for interpolation.

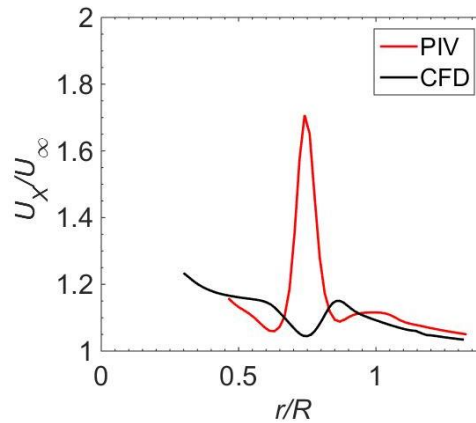


Figure 6.4 Distribution of U_x across the vortex centre.

However, difference is noticed in the vortex core region. The distributions of the axial velocity along radial lines (as show by the straight dashed lines in Figure 6.3) across the vortex core are plotted in Figure 6.4. For the *PIV* measurement result, there is a jet-like region of the axial velocity in the vortex core. This jet-like profile of the wing tip vortex was also reported in [93] for a wing with NACA 0015 airfoil and AOA of 8° . For the *CFD* result, although the axial velocity is prescribed to be the same as the free stream velocity (flat shape) at the velocity inlet, there is still a wake-like shape of the axial velocity in the vortex core. This is because the link between the axial component and the azimuthal component of the velocity [62]. The pressure in the vortex centre is inversely proportional to the square of the tangential velocity (Eq. 2.42). As the vortex goes downstream, the tangential velocity decreases (mainly due to diffusion), so the pressure in the vortex centre increases. Therefore, the axial velocity decreases and it has a wake-like shape.

This difference of the axial velocity in the vortex core region causes a different inflow to the propeller. During the study of the vortex impact on the propeller in the next chapter, this should be taken into consideration. However, as will be found in the next chapter, the propeller inflow (characterised by the angle of attack of the blade) has negligible influence from the axial component of the velocity of the vortex and is dominated by the tangential component of the velocity of the vortex. Therefore, although there is a difference of the axial component of the velocity in the vortex between the *PIV* measurement and the *CFD* results, it has no significant impact on the problem which is going to be investigated.

6.1.2 Flow fields downstream of the propeller

The flow fields downstream of the propeller ($0.13 R$ downstream of the trailing edge of the blade root) for the same settings as the previous section, are shown in Figure 6.5. The phase angle labelled in Figure 6.5 is defined in Chapter 2 (Figure 2.4). The view is from the upstream to the downstream position of the propeller.

The impinging vortex can be recognized by the region with positive value of the X -component of the vorticity located in the centre of the figure. The wing tip vortices are located at the edge of the slipstream close to the dashed curve that shows the boundary of the propeller disk. The blade wakes are extended from the bottom of the figure to the blade tip vortices, with negative values of vorticity in the inner region and positive values of vorticity in the outer region; this is due to the distribution of the circulation in the radial direction of the blade, which is shown in Figure H.0.1 represented by the thrust distribution in the radial direction.

The topology of the impinging vortex is mainly influenced by the wake of the propeller blade and features different topologies at different phase angles. When the wakes of the blades are far from the impinging vortex, the impinging vortex still maintains its axisymmetric shape, e.g. at phase angle of $\Psi = 6.0^\circ$. When the wake approaches and retreats from the impinging vortex, the vortex is deformed due to the

induced velocity of the wake, e.g. at the phase angles of $\Psi = 17.0^\circ$ and 40.0° . When the impinging vortex is located in the wake, the vortex is disrupted by the blade wake, e.g. at the phase angle of $\Psi = 34.5^\circ$. The detail of the impact of the wake of the blade on the incoming vortex will be discussed in Section 6.3.

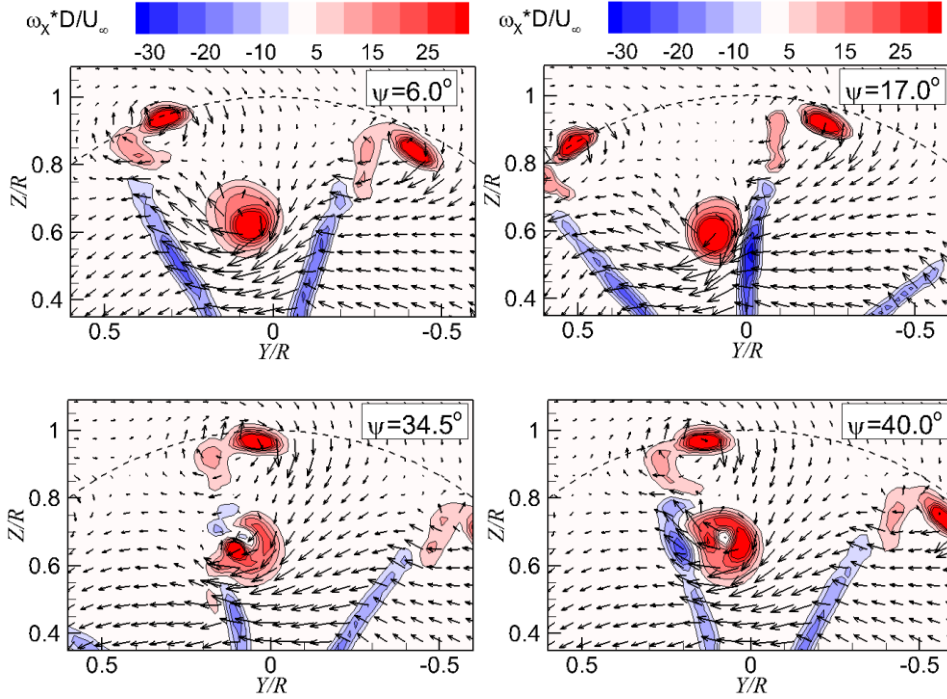


Figure 6.5 Flow fields downstream of the propeller at different phase angles of the blades. *PIV* arrangement 2. The vortex generator is set at $AOA = 8^\circ$.

The flow field downstream of the propeller from the *CFD* simulation, at the same plane as the *PIV* measurement, is shown in Figure 6.6. The vortex topologies at different phase angles of the *CFD* results are found to be consistent with the experimental results. A discrepancy between the *CFD* simulation and the experimental result is found at the phase angle when the vortex is located inside the blade wake, i.e. $\Psi = 34.5^\circ$. This discrepancy is ascribed to the numerical diffusion in the *CFD* simulations, leading to poor resolution of the interaction between the wake and the vortex. This numerical diffusive effect can either be due to the mesh size and the mesh type [89] or the turbulence modelling [90]. Because the qualitative and quantitative trends between the two methods are consistent at most of the phase angles, and because code development was not part of the task here, this issue is not investigated in detail in the current research.

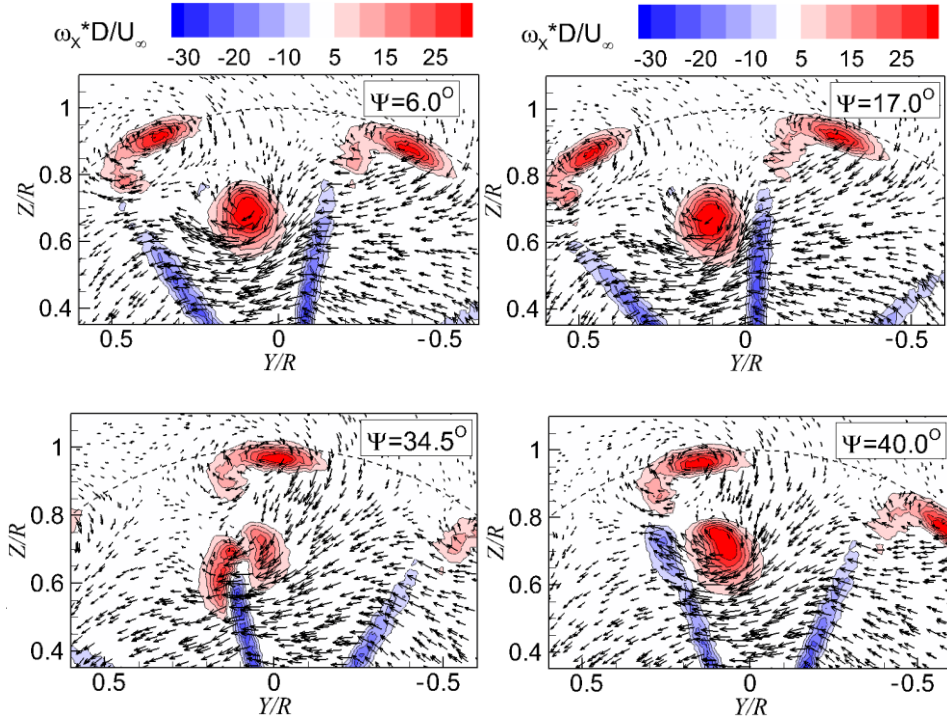


Figure 6.6 Flow fields downstream of the propeller at different phase angles of the blades (*CFD*). $X/R = 0.32$. $\Gamma_{inlet}/(U_{\infty} * D) = 0.6582$.

6.1.3 Three dimensional flow topology

As shown in the flow fields upstream and downstream of the propeller, the *CFD* results show a good consistence with the *PIV* measurement results. Therefore, the methodology of the *CFD* simulation is deemed sufficiently refined to represent the vortex response to the propeller. In order to build a three dimensional flow topology when the vortex impinges into a propeller, the 3D *CFD* result is analysed.

The three dimensional flow represented by iso-surfaces for the vorticity magnitude of $|\omega| * D / U_{\infty} = 13.0$ is shown in Figure 6.7 from the *CFD* result. The impinging vortex upstream of the propeller is represented by ‘*VS1*’. After it goes through the propeller, it is cut into pieces and represented by ‘*VS2~ VS6*’, as shown in the left hand side of Figure 6.7. The tip vortices of the blades are represented by ‘*TVi*’, and the blade wakes are not shown because the vorticity magnitude is less than the chosen value.

As the vortex is at the phase angle with the blade in its trajectory (e.g. $\Psi = 10.0^\circ$ as shown in Figure 6.7), the vortex is penetrated by the blade and chopped into two sections, i.e. *VS1* and *VS2*. A detail illustration of this process is shown in the right hand side of Figure 6.7. During the cutting process, the *VS2* and *VS1* have a

displacement in the chordwise direction. This is due to the velocity on the suction side of the blade which is higher than that at the pressure side, and it is a result of the circulation on the blade cross section.

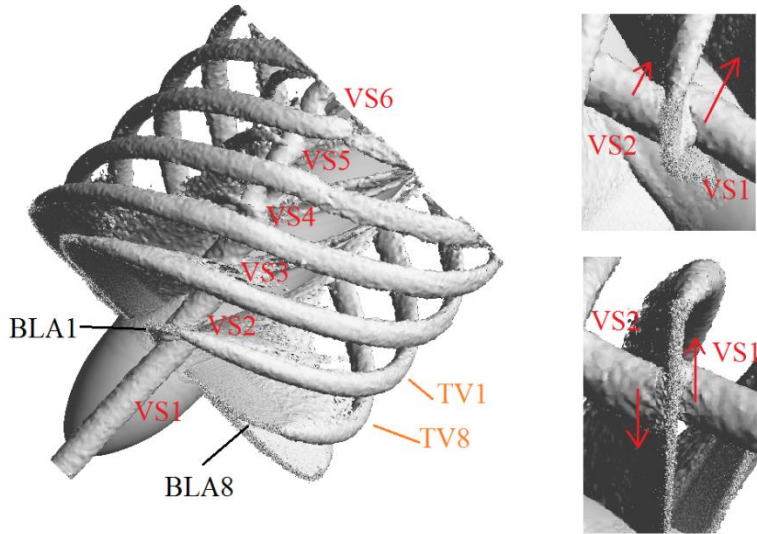


Figure 6.7 The three-dimensional flow topology of the vortex impinging on the propeller. $J = 1.1$, $\Gamma_{inlet}/(U_{\infty} * D) = 0.6582$. The iso-surface shows the vorticity magnitude of $|\omega| * D/U_{\infty} = 13.0$. Left: global view; right top: detail of the cutting process shows the vortex displacement in the chordwise direction; right bottom: detail of the cutting process shows the vortex displacement in the spanwise direction.

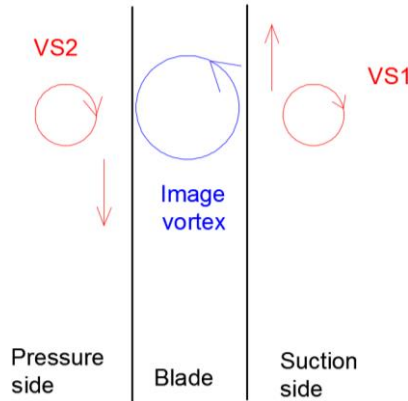


Figure 6.8 Explanation of the displacement of the vortex sections in the spanwise direction of the blade due to the image vortex.

The sections *VS1* and *VS2* also have a spanwise drift. This effect can be explained using the potential flow approximation to describe the effect of the propeller blade as a non-permeable wall (as shown in Figure 6.8). Due to the two

vortex sections, i.e. *VS1* and *VS2* with clockwise rotation direction, a virtual image vortex is utilized to represent the blade surface as a streamline, to ensure that the wall normal component of the velocity remains zero. This image vortex has an induced velocity in the upward direction on the suction side, and the opposite on the pressure side. Consequently, the vortex sections *VS1* and *VS2* have a displacement in the spanwise direction of the blade. The spanwise drift of an impinging vortex on a steady wing (or rudder) was also explained by this method in [46, 94, 95]. In the co-rotating vortex case (as shown in Figure G.0.2), the vortex displacement has the opposite feature due to the image vortex running in a clockwise direction.

6.2 Impact of the propeller on the vortex upstream of the propeller

In the previous section, a general description of the topology of the vortex was conducted for the case when the vortex impinges onto the propeller. This was intended to help build a preliminary understanding of the phenomenon, and validate the *CFD* results in terms of the flow topology. In this section (Section 6.2) and the subsequent section (Section 6.3), the response of the vortex to the propeller is investigated in the planes upstream and downstream of the propeller respectively, in terms of the meandering, the maximum tangential velocity, the core radius, and the circulation of the vortex. These investigations give detailed insights into the behaviour of the vortex under the impact of the propeller.

6.2.1 Impact of the propeller on the vortex meandering upstream of the propeller

The vortex meandering is a normal characteristic of a wing tip vortex, and its meandering magnitude under the influence of the propeller is investigated in this section. The vortex centre is determined by the vorticity weighted averaging method and the detail is introduced in Appendix D. The position of the vortex centre in the instantaneous flow field upstream of the propeller, at the propeller advance-ratio of $J = 0.6$ corresponding to a high thrust case, and the vortex generator with setting of $AOA = 8^\circ$ is shown in Figure 6.9. The X axis represents the recording number of the instantaneous flow fields, and the Y axis shows the displacement of vortex centre relative to the averaged position. The meandering of the vortex in the two directions generally have the same trend. The vortex is located near and on the two sides of the averaging position.

The standard deviation of the vortex position at a sweep of advance ratios of the propeller is shown in Figure 6.10. With the propeller operating at different advance ratios, the vortex meandering magnitude shows differences that are smaller than the measured position error as indicated by the error bars. As found from Figure 6.10, the standard deviation of the vortex meandering is at the order of $O(10^{-3} R)$, which is one order of magnitude lower than that of the vortex core radius ($O(10^{-2} R)$, as shown in Figure 6.11). Therefore, the meandering of the vortices upstream of the propeller is trivial and can be neglected; the vortex impinging on the propeller can be considered to be a constant vortex impingement.

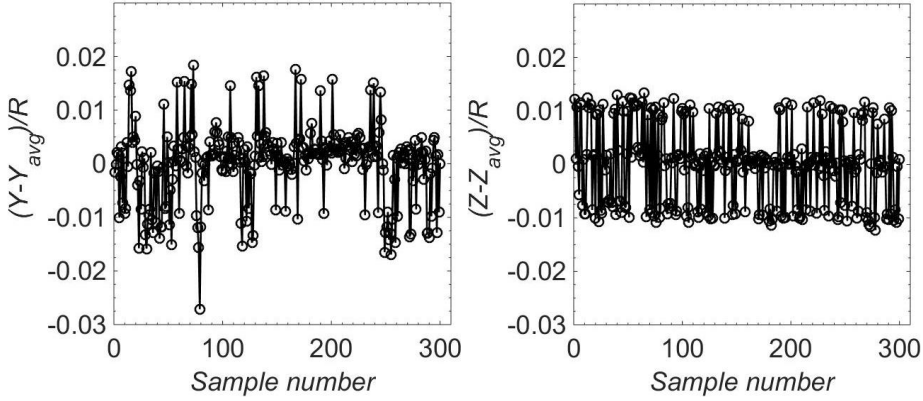


Figure 6.9 Meandering of the vortex centre in the lateral and vertical directions. $AOA = 8^\circ$, $J = 0.6$.

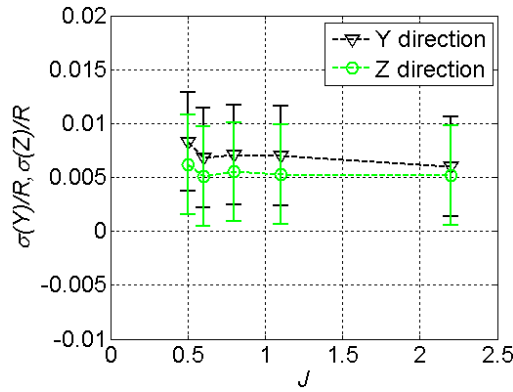


Figure 6.10 Meandering of the vortex centre in the lateral and vertical directions at different advance ratios of the propeller.

6.2.2 Impact of the propeller on the tangential velocity and the radius of the vortex upstream of the propeller

The vortex core is a portion of the vortex, which contains the majority of the vorticity in a vortex (72% for a Lamb-Oseen vortex). In order to gain insight into the interaction, the response of the vortex core to the propeller induced flow is analysed. The vortex core is characterized by a solid-like rotation region, so the maximum tangential velocity and the core radius are two parameters to represent the vortex core.

The core radii of the vortex at a sweep of advance ratios are plotted in the left hand side of Figure 6.11. At relatively high advance ratios, i.e. $J = 0.8, 1.1$ and 2.2 , the vortex core radii do not change significantly at different advance ratios. As the

advance ratio decreases to $J = 0.5$ and 0.6 , the vortex core radius decreases, which is due to the effect of the vortex stretching by the propeller suction effect.

The maximum tangential velocity in the vortex is plotted in the right hand side of Figure 6.11. At relatively high advance ratios, i.e. $J = 0.8, 1.1$ and 2.2 , the maximum tangential velocity has a negligible variation. As the advance ratio decreases to $J = 0.5$ and 0.6 , the maximum tangential velocity increases as the advance ratio decreases, which is due to the strong stretching effect of the propeller suction as well.

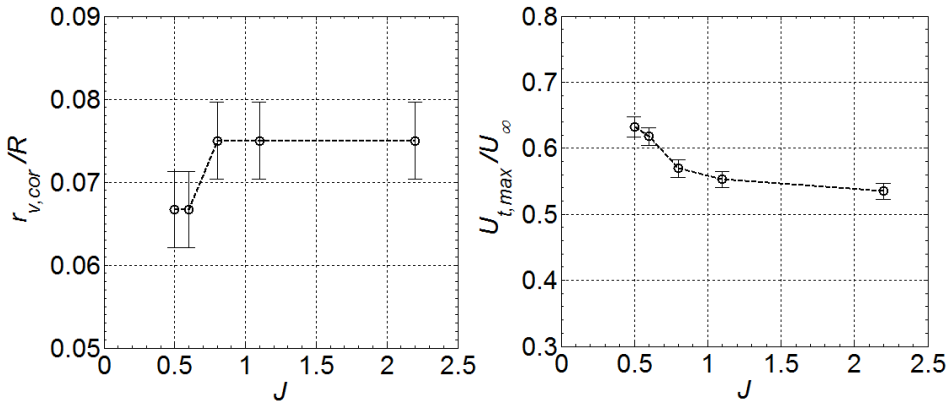


Figure 6.11 Left: vortex-core radius versus the advance ratio; right: maximum tangential velocity of the vortex versus the advance ratio.

6.2.3 Impact of the propeller on the circulation of the vortex upstream of the propeller

As a wing tip vortex is utilized to modify the inflow of a propeller, the circulation of this wing tip vortex (as defined in Eq. (5.1)) due to the impact of the propeller is studied in this section. Although the total circulation of a well-developed wing tip vortex is determined by the lift of the wing solely, the impact of the propeller may change the roll-up process, consequently it may change the distribution of the circulation. The distributions of circulation at a sweep of propeller advance-ratios are shown in Figure 6.12. As the advance ratio of the propeller decreases, the circulation in the inner region of the vortex increases. This trend is consistent with the vortex stretching effect with vorticity transported from the outer region into the inner region of the vortex.

It is noted that the vortex circulation at the radial position $r_v = 0.25 R$ (the maximum range of our analysis) are very close at the five advance ratios. The standard deviation of the circulations of the five advance ratios at $r_v = 0.25 R$ is $\sigma_r/(U_\infty D) = 0.0028$, which is 1% of the circulation at this position of $J = 2.2$. Therefore, the vortex circulation can be assumed to be constant at different propeller advance ratios. This means the wing tip vortex is well developed before it reaches

the measurement plane. Consequently, the circulation of the impinging vortex can be represented by evaluating the circulation of the wing tip vortex (no propeller) inside the radius of $r_V/R = 0.25$, which is denoted as Γ_{imp} .

Based on this, the strength of the impinging vortex, Γ_{imp} , is summarized in Table 2 for different $AOAs$. The quantified strength of the impinging vortex is also utilized to analyse the effect of the vortex on the propeller which will be discussed in Chapter 7.

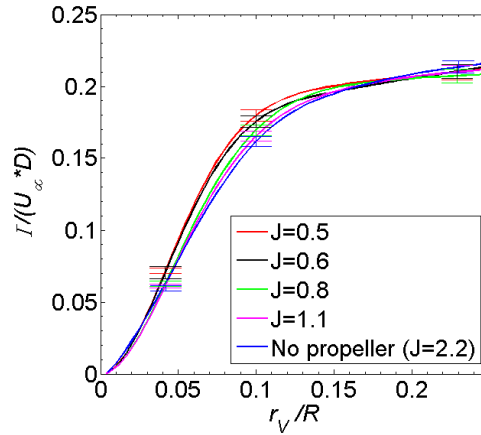


Figure 6.12 Distribution of the circulation in the vortex at a sweep of propeller advance ratios.

Table 2 Vortex strength of the wing tip vortex determined at the plane $X/R = -0.2$, PIV .

$AOA (\alpha^0)$	Vortex strength ($\Gamma_{imp}/(U_\infty D)$)
2.0	0.0989
8.0	0.2161

The circulation in the vortex of the *CFD* simulation is evaluated by the same method (the error bars are determined from the *rms* values). The circulation distribution of the impinging vortex is shown in Figure 6.13. The trend of the circulation dependence on the advance ratio is the same as the *PIV* measurement: as the advance ratio decreases, the vortex is stretched and the circulation increases in the inner region; and the total circulation of the vortex has negligible influence from the propeller, which can be seen in the outer region of the vortex. The *CFD* results have one difference from the experimental results, which is the trend in the outer region of the vortex. For the experimental result, the circulation still has an increasing trend in the outer region. For the *CFD* result, the circulation has a

constant value from the radial position $r_v/R = 0.17$. This difference is ascribed to the additional tangential velocity (or vorticity) in the wing wake, which is not involved in the CFD simulation. The vortex generated in the experiment is a wing tip vortex, which contains wake vorticity in the proximity of it even though it is small. The vortex generated in the *CFD* simulation is an isolated vortex, and the majority of the vorticity is located in the inner region of the vortex.

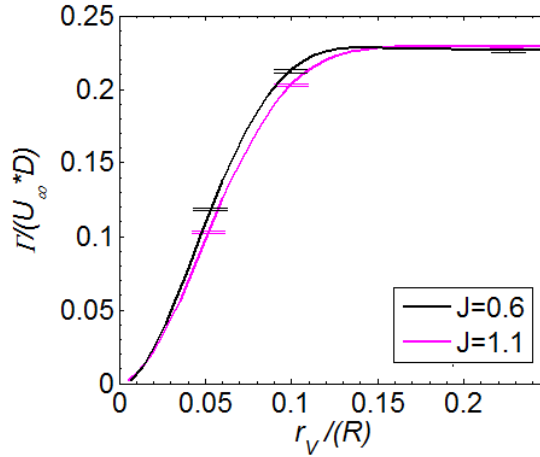


Figure 6.13 Circulation distributions in the vortex at a sweep of propeller advance ratios ($J = 0.6$ and 1.1 , *CFD*).

A summary of the vortex strength at all the *CFD* simulations is shown in Table 3. The first column is the vortex strength prescribed at the velocity inlet, and the second column is the vortex strength evaluated at the plane upstream of the propeller. Compared to experimental conditions as shown in Table 2, the *CFD* simulations include co-rotating vortex (negative value of the circulation), and the flow field at this condition is shown in Appendix G. These vortices with negative values of circulation together with the ones with positive values are utilized to analyse the propeller performance versus the vortex sign in Chapter 7.

Table 3 Vortex strength determined from the *CFD* simulation.

Vortex strength prescribed at the inlet, $\Gamma_{inlet}/(U_{\infty}D)$	Vortex strength at the plane $X = -0.2 R$, $\Gamma_{imp}/(U_{\infty}D)$
0.4388	0.1724
0.6582	0.2260
-0.6582	-0.2255
-0.4388	-0.1728

It is noted that only 30~40% of the circulation is maintained in the vortex as it is transported from the inlet ($X = -10 R$) to the plane $X = -0.2 R$. By investigating the circulation along the streamwise direction, the reason of the decrease is found to be the numerical diffusion of vorticity (especially in the rotating domain with unstructured mesh which was reported to be diffusive in [89]), and the interface between the rotating domain and the stationary domain. This decrease of circulation in the flow field upstream of the propeller has no significant impact for the problem of our investigation, because a well-defined vortex to impinge onto the propeller is our goal and the vortex strength is evaluated at the plane $X = -0.2 R$ downstream of the interface and directly upstream of the blades.

6.3 Impact of the propeller on the vortex downstream of the propeller

The impact of the propeller on the vortex was analysed in the plane upstream of the propeller in the previous section. After the vortex goes through the propeller, the response of the vortex to the propeller is analysed in the downstream plane as well, which is performed in this section. The parameters analysed are mainly the same as before, i.e. the vortex meandering, the vortex core radius, the maximum tangential velocity and the circulation. One more parameter analysed is the vortex shape due to the interaction with the wake of the blade.

6.3.1 Impact of the propeller on the vortex meandering downstream of the propeller

By following the method of determining the location of the centre of the vortex as introduced in Appendix D, the distribution of the vortex positions downstream of the propeller is determined and shown in Figure 6.14 by the black squares. The positions of the vortex upstream of the propeller represented by purple crosses are plotted as a reference. Generally, the positions of the vortex move inward and to the left hand side with respect to the upstream vortex, which are mainly due to radial and tangential velocities induced by the propeller, as well as the cutting process by the blade.

The meandering magnitudes of the vortex downstream of the propeller at a sweep of advance ratios are plotted in Figure 6.15. The vortex meandering in the downstream plane is at the magnitude of $\sigma(Y)/R \cong 0.04$ and $\sigma(Z)/R \cong 0.05$ when the propeller is running ($J = 0.5, 0.6, 0.8, \text{ and } 1.1$), which is higher than that upstream of the propeller. Furthermore, the meandering magnitude in the Z direction is obviously stronger than that in the Y direction, which is ascribed to the interaction between the vortex and blades together with blade wakes (e.g. the spanwise drift could be stronger than the chordwise drift as shown in Figure 6.7). In addition, it is also noticed that the meandering in the Y direction downstream of the propeller has a local minimum at $J = 0.6$ (this local minimum is not obvious for the meandering in the Z direction, although an increasing trend can be found before $J = 0.6$). On the one hand, as the advance ratio decreases, the contraction of the propeller slipstream

increases because the loading of the propeller increases. On the other hand, as the advance ratio decreases, the strength of the wake vortex of the blade increases which would increase the meandering of the vortex. These two factors compete and a local minimum is found at $J = 0.6$ from our results.

When there is no propeller in the flow ($J = 2.2$), the meandering magnitude of the vortex decreases dramatically. This means that the blade cutting process has a strong impact on the vortex meandering. The mechanism of the cutting process was already shown in Figure 6.7 by the visualization of the three dimensional flow.

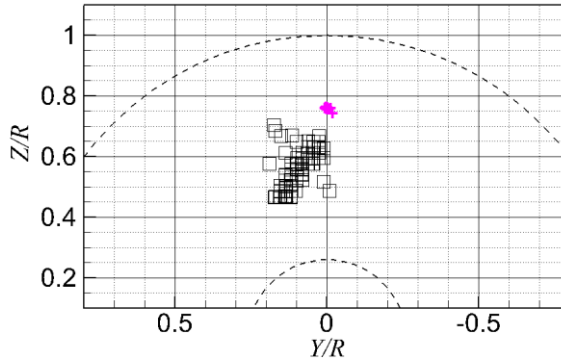


Figure 6.14 Positions of the vortex downstream of the propeller (black squares), and the reference positions of the vortex upstream of the propeller (purple crosses). $AOA = 8^\circ$, $J = 0.6$. Viewed from the upstream to the downstream position.

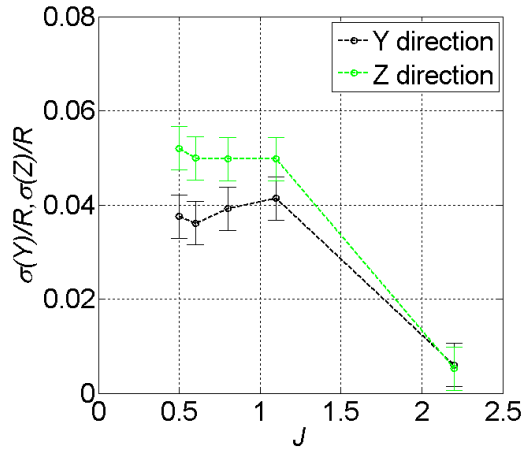


Figure 6.15 Meandering magnitude of the vortex position in the lateral (Y component) and vertical (Z component) directions.

6.3.2 Impact of the propeller on the vortex shape downstream of the propeller

In this section, the topology of the vortex represented by the vortex shape is analysed. The vortex shape is characterised by the iso-curve of the magnitude of the X-component of the vorticity, i.e. $\omega_X * D/U_\infty = 13.0$. The geometric centre (*GC*) of the vortex is determined by the mean value of the coordinates along the iso-curve. The distance between the point on the iso-curve and the *GC* is represented by *d*. An iso-curve extracted from Figure 6.5 at phase angle $\Psi = 6.0^\circ$ is shown in the left hand side of Figure 6.16. The shape factor (*SF*) is defined as the ratio of the maximum value over the minimum value of *d*,

$$SF = \frac{d_{max}}{d_{min}}. \quad \text{Eq. (6.1)}$$

There are cases which the definition of the shape factor have exceptions, when the vortex is strongly disrupted (e.g. V shape and even disrupted into two pieces) and the *GC* is outside the vortex (case *B* in Figure 6.16, corresponding to Figure 6.5 at phase angle $\Psi = 34.5^\circ$, and case *C* in Figure 6.16, corresponding to Figure E.0.1 at phase angle $\Psi = 34.5^\circ$); For such cases, the *SF* is defined as infinity, ∞ , which represents the situation that the vortex is strongly interfered by the blade wake.

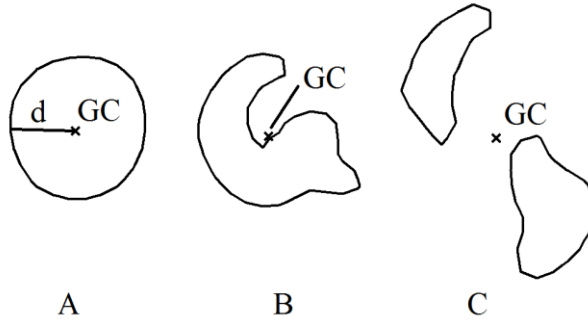


Figure 6.16 Example shapes of the iso-curve of the vortex. $\omega_X * D/U_\infty = 13.0$

As found in Figure 6.5 already, the vortex topology is strongly dependent of the relative distance between the vortex and the wake. Therefore, the position of the vortex is characterized by the angle between the wake and the vortex in the circumferential direction. The angle of the *GC* in the flow field is represented by Ψ_{GC} , and the angle of the wake (the one closest to the vortex *GC*) is represented by Ψ_{wake} . Their distance is defined by the angle between them, $\Psi_{GC} - \Psi_{wake}$.

$$\Psi_{GC-wake} = (\Psi_{GC} - \Psi_{wake})/45^\circ. \quad \text{Eq. (6.2)}$$

As the vortex is on the left hand side of the wake, $\Psi_{GC-wake}$ has a positive value, and vice versa when the vortex is on the right hand side of the wake. The angle difference is normalized by the angle between the two wakes, i.e. 45° .

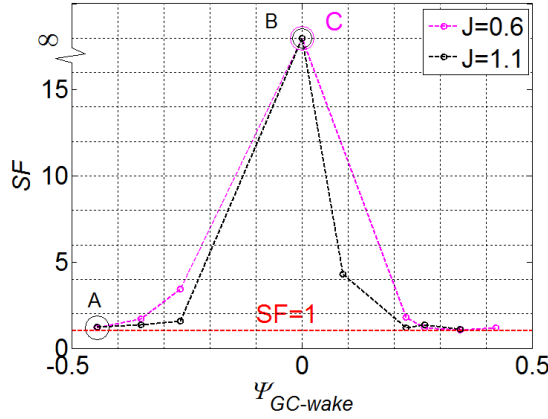


Figure 6.17 Shape factor of the vortex versus the distance between the vortex and the wake of the blade.

The shape factors of the vortex are shown in Figure 6.17 at different distances from the wake. The shape factor generally has a symmetric profile for both advance ratios: the magnitude of SF keeps increasing as the vortex approaches the wake; it reaches its maximum value as the vortex is close to or inside the wake; the SF decreases as the vortex retreats from the wake. The reason for not showing $\Psi_{GC-wake}$ close to ± 0.5 is that the phase-lock samples are only obtained at selected angles, and no phase angle corresponding to $\Psi_{GC-wake} \sim \pm 0.5$ is conducted. As the distance between the vortex and wake is large, the SF values for the two advance ratios are close and approximately equal to one. At the range of $\Psi_{GC-wake}$ approaching zero, the SF values of the vortex at a low advance ratio ($J = 0.6$) are higher than those at a high advance ratio ($J = 1.1$), because the interaction between the vortex and the wakes becomes stronger.

6.3.3 Impact of the propeller on the tangential velocity and radius of the vortex downstream of the propeller

As found from the vortex shape factor, the vortex shape is not always axisymmetric downstream of the propeller. Consequently, the circumferentially averaged tangential velocity and the resulted definition of the vortex core radius based on the axisymmetric assumption are not applicable for all the phase angles. However, these parameters are still significant to characterize the vortex downstream of the propeller. Therefore, the vortex at the vortex-wake distance of $\Psi_{GC-wake} = -0.44$ (*PIV* results) is chosen for analysis, which represents the vortex with approximately axisymmetric shape.

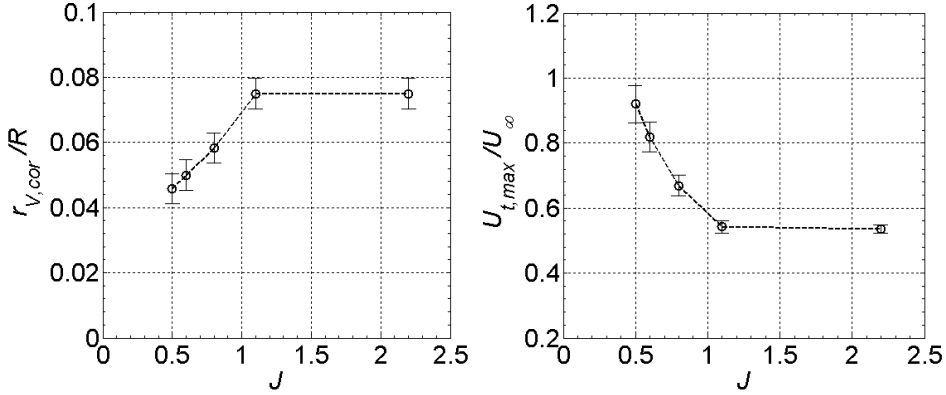


Figure 6.18 Left: vortex-core radius versus the advance ratio; right: maximum tangential-velocity of the vortex versus the advance ratio.

The vortex core radius and the maximum tangential velocity in the vortex are plotted in the left hand and the right hand sides of Figure 6.18 respectively. At the advance ratios of $J = 1.1$ and 2.2 , both the vortex core radius and the maximum tangential velocity of the vortex are approximately the same. This means at the low loading condition of the propeller, the propeller has a negligible effect on the vortex core. As the advance ratio further decreases, i.e. $J = 0.5, 0.6$, and 0.8 , the core radius of the vortex decreases and the maximum tangential velocity increases. This is due to the vortex stretching effect under the impact of the propeller thrust.

Compared with the vortex upstream of the propeller as shown in Figure 6.11, the vortex-core radius downstream of the propeller decreases and the maximum tangential velocity increases at the advance ratio of $J = 0.5, 0.6$, and 0.8 , which is due to the stretching effect of the vortex. For example, at $J = 0.6$, the vortex core radius upstream of the propeller is $0.067 R$ and the maximum tangential velocity is $0.64 U_{\infty}$; and those downstream of the propeller are $0.050 R$ and $0.82 U_{\infty}$ respectively. At the advance ratio of $J = 1.1$ and 2.2 , the vortex-radius and the maximum tangential velocity downstream of the propeller approximately have no change compared with that in the upstream plane. This means the stretching effect is negligible when the propeller loading is low.

6.3.4 Impact of the propeller on the circulation of the vortex downstream of the propeller

The distributions of the circulation in the vortex downstream of the propeller at different advance ratios are shown in Figure 6.19. The error bars shown in the figure are determined from the standard deviations of the circulations from the samples for phase averaging, and the uncertainties of the wing angle of attacks.

The distribution of the circulation in the vortex has two parts which feature different characteristics. One part is from the vortex centre until the radial position

with the maximum circulation, in which the circulation increases as the radius increases; the other part is the outer region in which the circulation decreases as the radius increases. The first part has the same property as found in the upstream plane, and the circulation increases as the advance ratio decreases, which is due to the stretching effect of the vortex.

The second part is different from the upstream plane, which is due to the impact of the blade wake with the opposite sign of vorticity as the impinging vortex. From the definition of the circulation as shown in Eq. (5.1), as the term of vorticity, $\omega_X \vec{l}$, is negative in the region of the blade wake, it has a negative contribution to the circulation. The distribution of the circulation of an isolated propeller operating at $J = 0.6$, is plotted by the dashed black curve to support this observation. The zero radial position of the case of an isolated propeller is set at the same position as the centre of the virtual vortex. It is noted that the circulation of the case of the isolated propeller starts decreasing from the radial position of $r_V/R \approx 0.16$, which is consistent with the case with the impinging vortex (black solid curve). It is also noted that the slope magnitude of the black solid curve is higher than that of the black dashed curve, which implies the impingement of a contra-rotating vortex increases the magnitude of the wake vorticity. This can be readily confirmed by evaluating the induced velocity of the vortex on the blade from Biot-Savart law. Furthermore, the circulation in the outer region decreases more if the advance ratio is lower, because the magnitude of the vorticity in the blade wake increases as the advance ratio decreases.

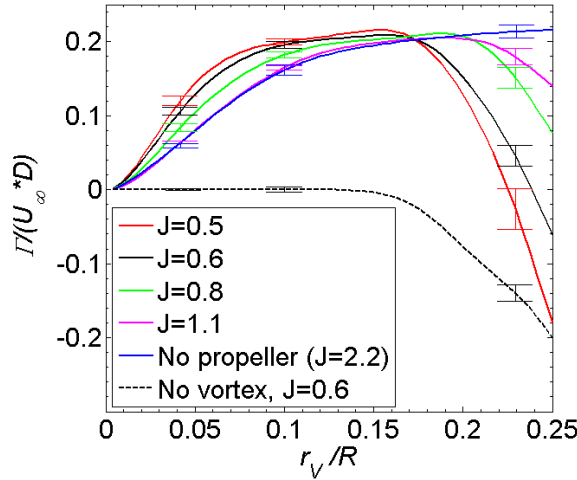


Figure 6.19 Distribution of the circulation in the vortex downstream of the propeller at the situation of the vortex-wake azimuthal angle of $\Psi_{GC-wake} = -0.44$.

The circulation distribution in the vortex from *CFD* simulations is shown in Figure 6.20 for a comparison. The error bars plotted in Figure 6.20 are calculated from the standard deviations of the circulations at these radial positions, and the

contribution of the angle setting is omitted because the vortex is generated by prescribing a constant circulation at the velocity inlet. The *CFD* results are found to be consistent with the experimental results.

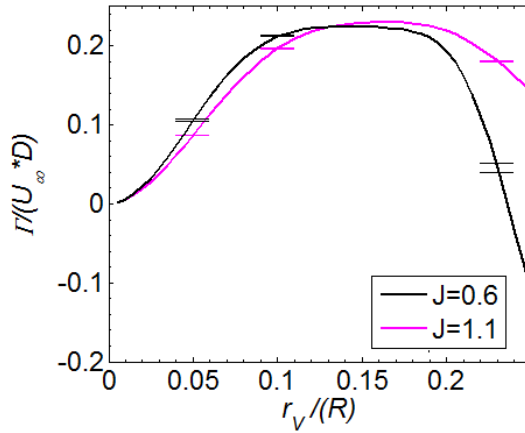


Figure 6.20 Distribution of the circulation in the vortex downstream of the propeller at the vortex-wake azimuthal angle of $\Psi_{GC-wake} = -0.5$. (*CFD*).

Compared with the vortex circulation in the upstream plane as shown in Figure 6.12 and Figure 6.13, it is also found that the maximum circulation in the vortex downstream of the propeller has no noticeable change from that in the upstream plane. For instance of *PIV* measurements, at the advance ratio of $J = 0.6$, the circulation is $\Gamma/(U_\infty * D) = 0.1966$ at the radial position $r_v/R = 0.15$ upstream of the propeller; and that downstream of the propeller is $\Gamma/(U_\infty * D) = 0.2080$. The difference is below the error bar of the measurement and it is assumed to be negligible. This means the vortex after going through the propeller still has the same magnitude of the circulation as that in the upstream plane, at least in the inner region of the vortex (approximately two times of the vortex core radius in the current analysis). This also implies that the vortex after impingement still has the same order of effect on the further downstream parts of the airframe, e.g. the second row of rotors for a contra-rotating propeller.

6.4 Conclusions

By applying a truncated wing upstream of the propeller, a well-defined vortex is generated to impinge on the propeller. The velocities and positions of the vortex upstream of the propeller are quantified by *PIV* measurements. By investigating the vortex properties, i.e. the meandering, the maximum tangential velocity, the core radius, and the circulation, the impact of the propeller on the vortex is analysed. The results show that the propeller induced flow field has an effect of stretching the vortex upstream of the propeller at highly loaded conditions, which results in an increase of the maximum tangential velocity and a decrease of the core radius as the

thrust coefficient increases. The circulation in the vortex core undergoes a redistribution and the circulation in the inner region of the vortex has an increase while the total circulation is not changed. The vortex meandering effect upstream of the propeller is also independent of the propeller advance ratios at the accuracy of our measurements.

After the vortex has passed the propeller, the flow field containing the vortex is measured at the plane $0.13 R$ downstream of the trailing edge of the blade root. The vortex meandering downstream of the propeller becomes larger compared with that upstream of the propeller because of the cutting process by the blade and the induced velocity of the propeller. This causes the vortex to have strong displacements in the lateral and radial directions. The vortex topology is dependent on the relative position between the vortex and the blade wake. As the vortex is located around the middle of the two blade wakes ($\Psi_{GC-wake} \sim 0.5$), the shape of the vortex still features an axisymmetric profile. As the vortex is located close to the blade wake ($\Psi_{GC-wake} \sim 0$), the vortex is disrupted into V shape and even into two pieces. The vortex downstream of the propeller is still characterized by the stretching effect due to the propeller thrust. The circulation shows an increase in the inner region of the vortex because of the stretching effect; the circulation in the outer region of the vortex decreases because of the blade wake with an opposite sign of vorticity for the case with a contra-rotating vortex; the maximum circulation of the vortex downstream of the propeller have a negligible difference from that upstream of the propeller, which means the vortex after the impingement still has a comparable strength with respect to the incoming vortex to influence the further downstream parts of the airframe.

In addition, the impinging vortex implemented by a Lamb-Oseen vortex model at the velocity inlet is applied in the *CFD* simulation. By comparing the vortex upstream and downstream of the propeller, the tangential velocity profile and the vortex topology of the *CFD* results agree with those of the experimental results. This means the methodology in the *CFD* simulation intended to simulate the wing tip vortex is valid to study the propeller-vortex interaction. Based on this, the three dimensional flow topology of the impinging vortex is further analysed by the *CFD* result. During the cutting process, the vortex has a displacement between the suction and pressure sides of the blade; the vortex is chopped into sections which are located between the blade-wakes downstream of the propeller.

Except for the cases studied by an impinging vortex with an opposite rotating direction from the propeller and a constant impinging radial position at $0.75 R$, vortices with the same rotating direction as the propeller and other impinging radial positions are also studied. The measurement results downstream of the propeller together with the 3D *CFD* data of these cases are presented in Appendices E, F and G. The reader can refer to these sections for further information.

6.5 Discussion

As the impact of the propeller on the wing tip vortex was analysed in this section, the next research question is how the externally generated vortex affects the performance of the propeller. Through the method introduced in Chapter 5, the propeller performance with vortex impingement is measured and compared with that without a vortex impingement in the next chapter. The validation of the *CFD* results in Chapter 6 shows that the numerical simulation represents the experimental test well, so it gives confidence for the analysis of the vortex impact on the propeller by the numerical results; the numerical results not only give the integral performance of the propeller, but also the dynamic properties. This enables a thorough understanding of this phenomenon.

Chapter 7 Impact of an externally generated vortex on a propeller

Due to the induced flow generated by the impinging vortex, the propeller experiences changes of velocity of its inflow. The integral effect of this additional velocity on the propeller performance is investigated by determining the time-averaged thrust coefficient, torque coefficient, as well as the efficiency of the propeller. A systematic study on the parameters of the vortex rotation direction, the vortex strength, the vortex impingement radial position, as well as the propeller advance ratio is performed, so as to investigate the dependence of the propeller performance on these parameters. Furthermore, the additional velocity upstream of the propeller has a non-axisymmetric distribution for a non-coaxial impinging vortex, this results in a dynamic loading on the blades. The thrust on one individual blade in one revolution which includes the variation of the blade loading is analysed. In addition, the pressure fluctuation on the blade is evaluated for the prediction of the unsteady pressure field.

7.1 Impact of the vortex on the propeller performance

7.1.1 Effects of the strength and the direction of the rotation of the vortex on the performance of the propeller

Whilst maintaining the advance ratio of the propeller ($J = 1.1$) and the radial position of the impinging vortex ($r_{imp}/R = 0.75$), the impact of the vortex on the propeller is investigated at a sweep of vortex strengths. The propeller performance versus the vortex strength, in terms of the time-averaged thrust coefficient, the torque coefficient and the efficiency, are shown in Figure 7.1.

As the vortex contra-rotates with the propeller (positive value of circulation), both the thrust and torque coefficients increase with respect to the case of no impinging vortex as expected. The opposite is true for the co-rotating vortex (negative value of circulation). The integral results from the experiments and *CFD* simulations show a good agreement, which validate the *CFD* simulations.

Even though the thrust and torque coefficients are both changed due to the imping vortex at the advance ratio of $J = 1.1$, it is found that the efficiency (defined in Eq. (2.17)) of the propeller is independent of the strength of the impinging vortex.

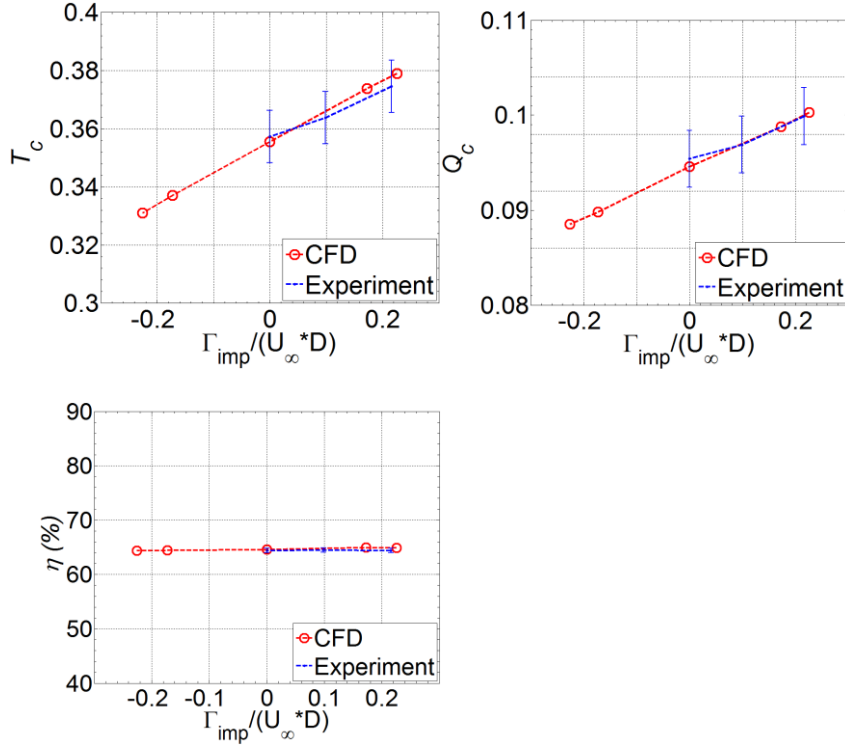


Figure 7.1 Propeller performance versus vortex strength. Top left: thrust coefficient; top right: torque coefficient; bottom: efficiency. $r_{imp}/R = 0.75$, $J = 1.1$. The negative circulation of the impinging vortex represents the co-rotating vortex, and the opposite for the positive value.

The lift-to-drag ratio was reported to have an increase due to the vortex impingement on a steady wing (the impinging vortex contra-rotated with the tip vortex of the wing) [47], which is in disagreement with our results. By investigating the flow as presented in [47], it is found that the wing tip vortex has a downwash effect on the wing. The lift on the wing decreases due to the downwash, so the lift induced drag decreases. The lift induced drag is proportional to the square of the lift coefficient, so the lift to drag ratio increases. However, this does not happen in our case, and the reasons are listed as below. Firstly, the impinging vortex induces both upwash and downwash effects on the blade. Secondly, this is probably because of the relative weakness of the impinging vortex in our case. The lose/gain of the lift or drag of the propeller blades is small, so even the quadratic term can be linearized. Furthermore, even if the impinging vortex may change the efficiency of the blade, but it mainly influences one blade at each instant, the integral effect on the eight blades is small. The unaffected efficiency of our result is also consistent with the results of a propeller operating at an angle of attack: the vertical component of the velocity in the propeller plane had an upwash effect on the down-going blade and

the opposite for the up-going blade, but no obvious change in the propeller efficiency was observed [96].

For the co-rotating and contra-rotating vortices, the fluctuations of loadings on one individual blade in one rotation are compared in terms of the thrust coefficient, as shown by the black and purple curves in Figure 7.2. The definition of the thrust coefficient on one blade is similar to the definition for the whole propeller which is shown in Eq. (2.15), just substituting the thrust of the whole propeller by the thrust of one blade. The reference data without impinging vortex is also plotted by the green line in Figure 7.2. The variation of the thrust coefficient of the blade by a contra-rotating vortex is nearly symmetrical with that by a co-rotating vortex with respect to the green line. For the co-rotating vortex case, the blade loading has its maximum value at the phase angle of $\Psi = 358^\circ$, which is near the position for a contra-rotating vortex with its minimum blade loading ($\Psi = 10^\circ$), and vice versa for a contra-rotating vortex.

In addition, at the phase angles with maximum and minimum values of the blade thrust under the impact of a contra-rotating vortex, the loading distributions in the radial direction of the blade are performed in Appendix H. They show the detail of loading variation on the blade in the radial direction.

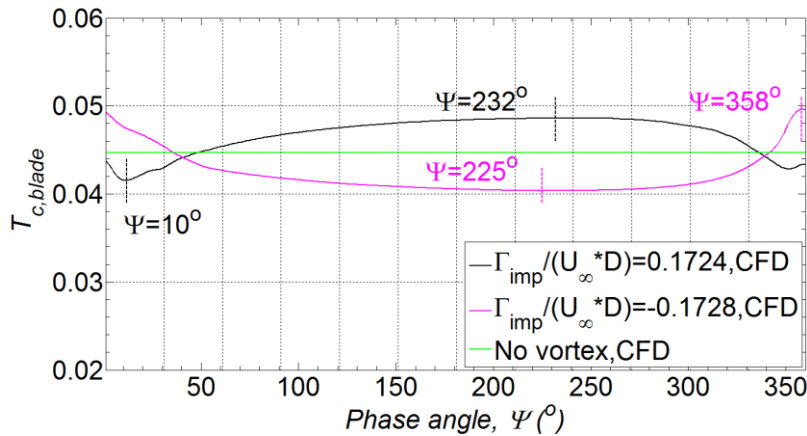


Figure 7.2 Thrust coefficients on one individual blade in one revolution due to different signs of impinging vortices. The circumferential positions with maximum and minimum values of the blade thrust are highlighted by the dashed lines together with the phase angles. *CFD* results.

The reasons for the thrust variation on the blade and hence the change of the time averaged loading of the propeller are investigated by analysing the change of *AOA* on the blade. The definition of the *AOA* of a blade was introduced in Chapter 2 (Figure 2.13). The velocities as shown in Figure 2.13 were extracted from the plane

upstream of the propeller ($X/R = -0.2$), which is close to the blade leading edge and is assumed to represent the characteristic of the propeller inflow.

Without vortex impingement, the blade angle of attack has an axisymmetric distribution, which is shown in the bottom left of Figure 7.3 as reference data. The AOA is in the range of $[3^\circ, 10^\circ]$, with the minimum value at the root of the blade.

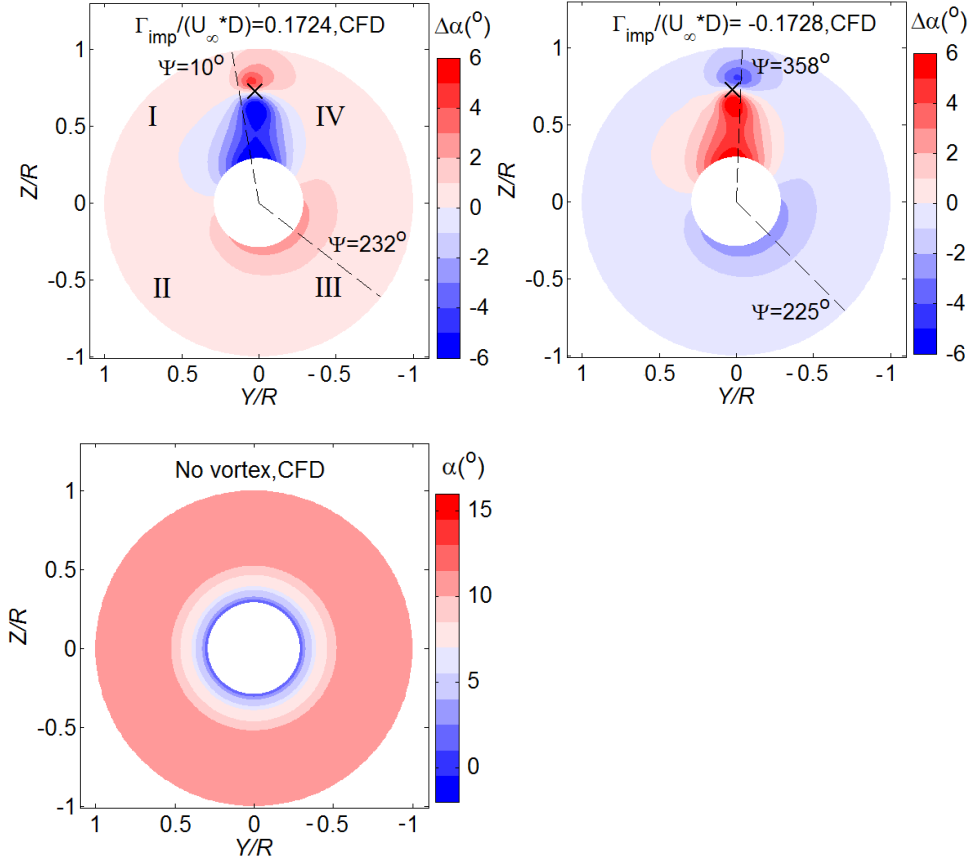


Figure 7.3 Top left: change of AOA for a contra-rotating vortex, $\Gamma_{imp}/(U_{\infty}D) = 0.1724$; top right: change of AOA for a co-rotating vortex, $\Gamma_{imp}/(U_{\infty}D) = -0.1728$; bottom left: AOA for a uniform inflow.

With a contra-rotating vortex, the change of AOA , obtained by subtraction of AOA without vortex impingement is shown in the top left of Figure 7.3. The AOA change noticeably becomes non-uniform in the circumferential direction. In the majority of the angular domain, the propeller experiences an increase of angle of attack; the region between the impinging vortex (symbolised by the cross) and the hub shows a decrease of AOA . This difference is mainly due to the tangential velocity of the vortex (as shown in Figure 7.4): the region with a positive tangential

velocity is consistent with the region with a decreased AOA ; the region with a negative tangential velocity is consistent with the region with an increased angle of attack.

The change of the angle of attack for the co-rotating vortex is shown on the right-hand side of Figure 7.3, and the tangential velocity distribution in the propeller inflow is shown in the right hand side of Figure 7.4 accordingly. Compared with the contra-rotating vortex case, the change of the angle of attack and the tangential velocity distribution are switched. Consequently, the effect of the vortex on the propeller is switched accordingly.

Except for the variation of AOA in the region proximate to the vortex impinging position, another region which shows relatively weak variation of AOA is mainly in the third quadrant (represented by symbol III as shown in top left of Figure 7.3). This non-axisymmetric is probably due to the displacement of the impinging vortex in the chordwise direction by the chopping process of the blade as that shown in Figure 6.7. Therefore, the induced velocity by the vortex system in the propeller slipstream and that by the hub vortex would become non-axisymmetric. The detail of the analysis on this non-axisymmetric is not included in the current research because this is relatively less significant compared with that induced by the impinging vortex directly. The reader can find more information about the induced velocity by the vortex system in the slipstream as reported in [5] and the induced velocity by the hub vortex as reported in [97].

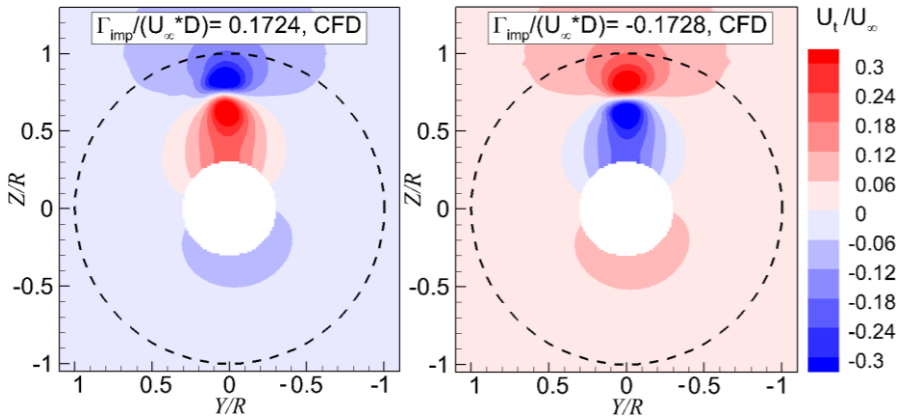


Figure 7.4 Distribution of the tangential velocity in the propeller inflow. Left: contra-rotating vortex; right: co-rotating vortex. Positive tangential velocity is defined in the same direction as the propeller rotation (counter-clockwise).

7.1.2 Effect of the radial position of the impinging vortex on the propeller performance

By maintaining the advance ratio of the propeller ($J = 1.1$) and the vortex strength ($\Gamma_{imp}/(U_\infty D) = 0.1724$), the impact of the radial position of the impinging vortex on the propeller is investigated. The time-averaged performance of the propeller at conditions of different vortex-impinging radial positions is shown in Figure 7.5. As the radial position of the impinging vortex moves outward, e.g. from $r_{imp}/R = 0.6$ to $r_{imp}/R = 0.9$, both the thrust and the torque coefficients display decreases of around 3.5%. The efficiency of the propeller is independent of the impinging radial position.

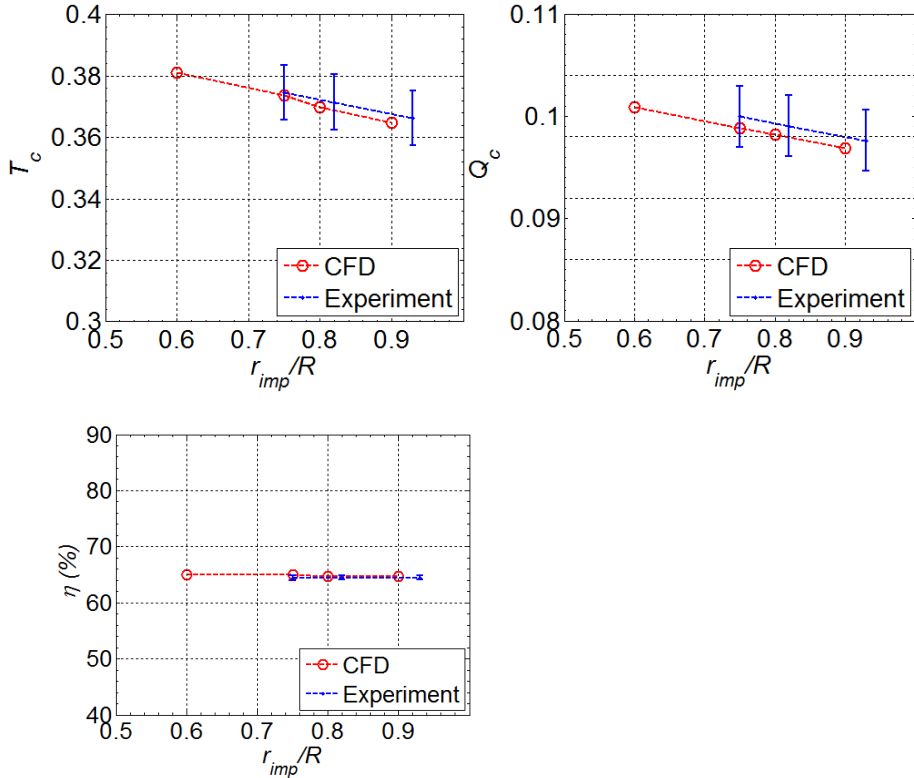


Figure 7.5 Propeller performance versus vortex-impinging radial position. Top left: thrust coefficient; top right: torque coefficient; bottom left: efficiency. $\Gamma_{imp}/(U_\infty D) = 0.1724$.

The fluctuations of the blade loadings are shown in Figure 7.6 for the conditions with different vortex-impinging radial positions, i.e. $r_{imp}/R = 0.75$ and $r_{imp}/R = 0.9$. The blade thrust coefficient fluctuations for the two impinging positions have the same trend. At all phase angles, the blade loading with the vortex impinging at the radial position of $r_{imp}/R = 0.9$ is lower than that at $r_{imp}/R = 0.75$. It is noted

that the blade loading fluctuation (defined by the maximum thrust divided by the minimum value) at $r_{imp}/R = 0.9$ is 1.4. This means that the loading variation needs to be considered when there is a vortex impingement for the structural design of the blade. It is also noticed that this ratio at the impinging radial position of $r_{imp}/R = 0.9$ (1.4) is higher than that at $r_{imp}/R = 0.75$ (1.15). Extrapolations can be deduced at other impinging radial positions: as the impinging position is at the centre of the propeller, there is no blade fluctuation; as the impinging position is at infinity far, the blade fluctuation is negligible. Therefore, it can be concluded that as the impinging vortex moves from the hub centre to infinity, the blade loading fluctuation increases from zero to a maximum value (the maximum value is achieved approximately at $r_{imp}/R = 1.0$), and then starts decreasing to zero again.

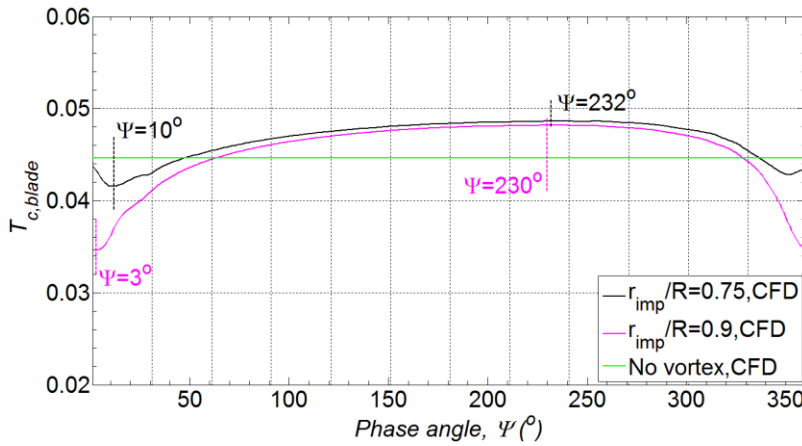


Figure 7.6 Blade thrust coefficients versus phase angle due to impinging vortices at different radial positions.

The reasons for the loading variation on the blade and hence the change of the time averaged loading of the propeller are investigated by analysing the change of AOA on the blade again. The changes of the AOA at two impinging radial positions, i.e. $r_{imp}/R = 0.75$ and $r_{imp}/R = 0.9$, are shown in Figure 7.7. As the vortex moves outward, the noticeable effect is that the area with the angle of attack decrement becomes larger, and vice versa for the area with the angle of attack increment. Consequently, the time-averaged loading of the propeller decreases. In the time domain, the blade loading at $r_{imp}/R = 0.75$ is higher than that of $r_{imp}/R = 0.9$ at all phase angles, because the induced tangential velocity by the vortex decreases as the distance between the point in the disk plane and the vortex centre increases, which can be clearly seen from the contour as shown in Figure 7.7.

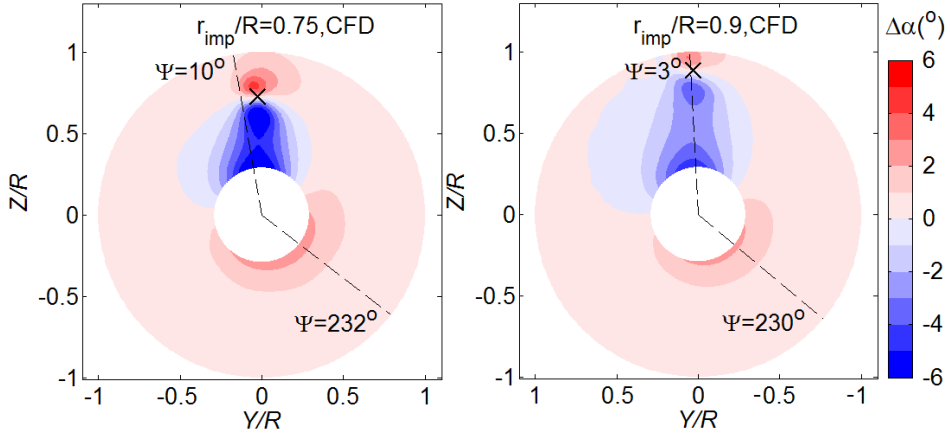


Figure 7.7 Comparison of changes of the angle of attack at different impinging positions. Left: $r_{imp}/R = 0.75$; right: $r_{imp}/R = 0.9$.

7.1.3 Impact of the vortex on the propeller at different advance ratios

By maintaining the strength and the impinging position of the vortex, the impact of the vortex on the propeller performance at a sweep of advance ratios is investigated. The thrust coefficient, torque coefficient and efficiency are shown in Figure 7.8.

The thrust coefficient of the isolated propeller is plotted by the dashed black curve, and that with vortex impingement is plotted by the dashed red curve, as shown in the top left of Figure 7.8. Due to the contra-rotating vortex, the thrust coefficient of the propeller increases with respect to the case of an isolated propeller. The reason of the increase of the thrust coefficient is already given in Section 7.1.1.

It is also noted that as the advance ratio is lower, the absolute value of the thrust coefficient increment is larger, e.g. the increment of the thrust coefficient at $J = 0.6$ is $\Delta T_C = 0.08$ and that at $J = 1.1$ is $\Delta T_C = 0.02$. However, the relative increments are close at different advance ratios, which are 4.9% and 5.6% for $J = 0.6$ and $J = 1.1$, respectively. Because the effect of the vortex on the propeller is dominated by the variation of AOA , the explanation of the advance-ratio effect is conducted by analysing the AOA as well. At higher advance ratio (lower rotating speed of the blade), the AOA of the blade has a higher increment due to a contra-rotating vortex. At the same time, the higher advance ratio means lower local dynamic pressure on the blade. Therefore, these two aspects compete with each other and the combining effect of the vortex on the propeller thrust-coefficient at different advance ratios is small. The torque coefficient follows the same trend as the thrust coefficient. Consequently, the efficiency of the propeller, as shown in the bottom left of Figure 7.8, is independent of the vortex impingement at all tested advance ratios.

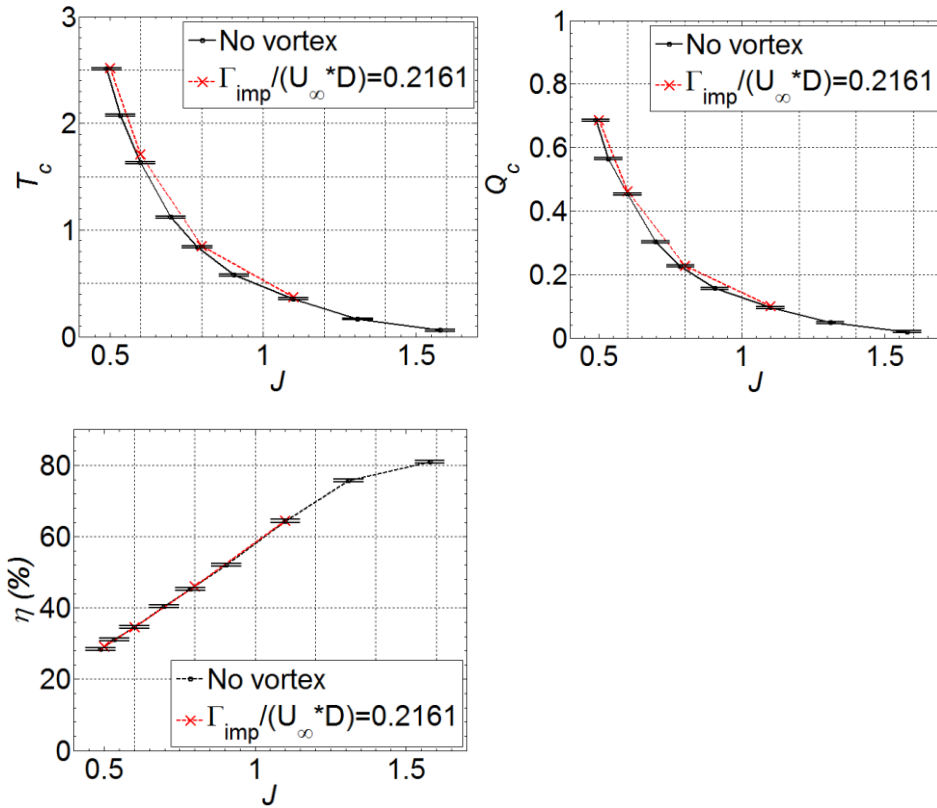


Figure 7.8 Impact of the vortex ($\Gamma_{imp}/(U_{\infty}D) = 0.2161$) on the propeller when the propeller operates at different advance ratios. The data presented are determined from experimental results.

Although the vortex impingement has no detrimental effect on the efficiency of the propeller, it is found that the blade thrust has a high fluctuation in the circumferential direction. For example, the ratio of the maximum thrust over the minimum thrust on the one blade is around 1.4 at the conditions of $\Gamma_{imp}/(U_{\infty}D) = 0.1724$, $r_{imp}/R = 0.9$ (this ratio depends on the strength of the impinging vortex and the radial position of the impingement vortex). This means that, in the structural design of the blade, the loading variation needs to be considered when a vortex impinges on a rotor. As well, the other effect due to the dynamic loading on the blade is the pressure fluctuation on the blade, which is analysed in the section as below.

7.2 Impact of the vortex on the additional fluctuating pressure of the blade

From the comparison of the experimental and numerical results, it shows that the computations are capable of correctly describing the time-averaged performance of the propeller disturbed by an impinging vortex. Therefore, it is assumed that the small scale phenomena obtained from the computations are also representative of the realistic behaviour. Consequently, an evaluation of the fluctuating parameters, required for the prediction of the strength of the unsteady pressure field, is performed from the numerical results.

Before presenting the results, the method to compute the pressure fluctuation on the blade, and that to compute the time-averaged streamlines on the blade are described as follows. The pressure fluctuations at each node of the mesh on the blade are computed from 720 samples which correspond to one revolution of the blade. The geometry chosen for visualization is at the phase angle of $\Psi = 0^\circ$. The streamlines on the blade, at the situation without an impinging vortex, are computed from the time-averaged shear stress on the blade, which is defined in the rotating coordinate system (the same technique of processing was reported in [98]).

For the case without an impinging vortex, contours of the standard deviation of pressure $\sigma(p - p_\infty)/q_\infty$, on the pressure and suction sides of the blade are shown in the left hand side of Figure 7.9 and Figure 7.10 respectively. A barely observable fluctuation of pressure is observed at the leading edge (*LE*) on the suction side of the blade, which ranges from the middle span to the tip. Other regions with observable pressure fluctuation are at the radial position around $r/R = 0.8$ and in a wide range of chordwise positions. The reason for the pressure fluctuation is analysed by the visualization of time-averaged streamlines on the blade, as shown in the right hand side of Figure 7.9 and Figure 7.10.

The figure on the right hand side of Figure 7.9 shows the surface streamlines on the suction side of the blade based on the time averaged shear stress in the rotating coordinate system. A separation region on the blade is approximately at the same region as that displays strong pressure fluctuations, which explains the pressure fluctuation on the blade at a uniform inflow condition. A separation at the leading edge of the blade was also reported in [99] by visualization of oil streamlines via interferometry, which was consistent with the observations as shown in Figure 7.9.

The pressure fluctuation on the pressure side of the blade without a vortex impingement is negligible compared with the suction side, as shown on the left-hand side of Figure 7.10. The streamlines on the pressure side feature attached flow in all the area, which is consistent with the distribution of the pressure fluctuation.

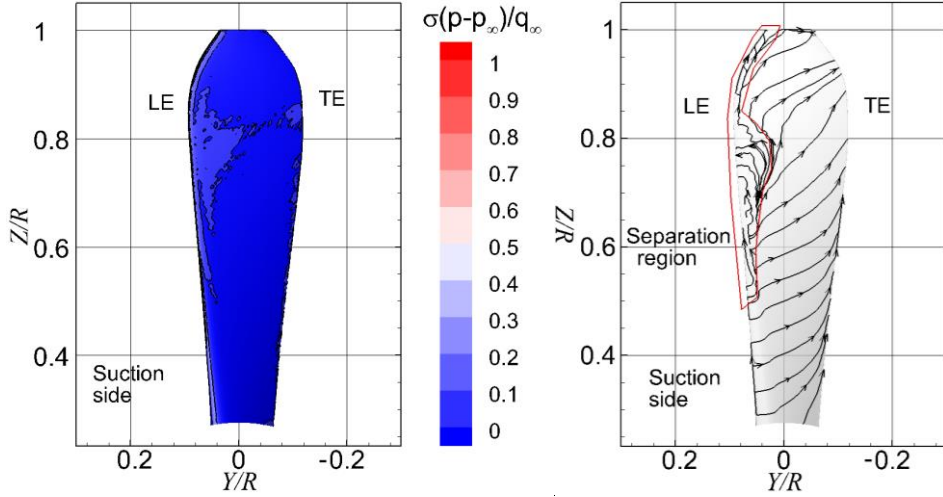


Figure 7.9 Left: standard deviation of pressure on the suction side of the blade; right: time averaged streamlines on the suction side of the blade. Axisymmetric inflow, $J = 1.1$.

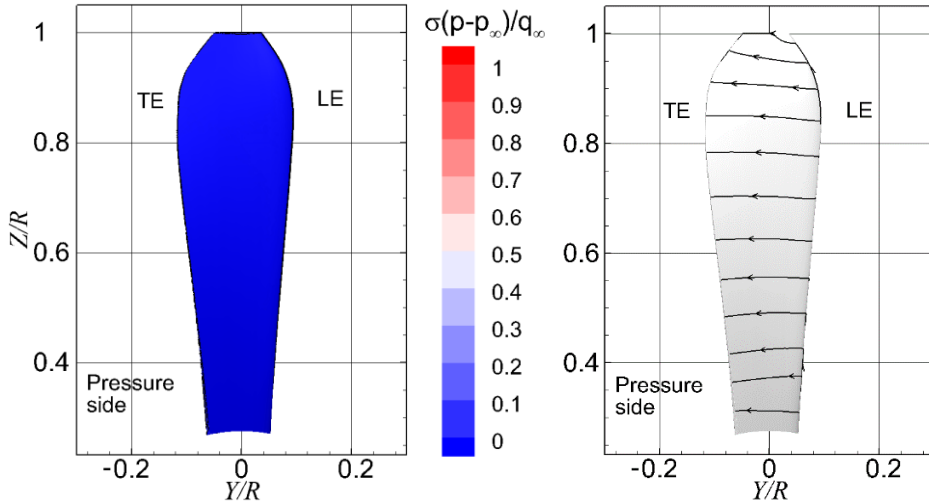


Figure 7.10 Left: standard deviation of pressure on the pressure side of the blade; right: time averaged streamlines on the pressure side of the blade. Axisymmetric inflow, $J = 1.1$.

The pressure fluctuation on the blade with an impinging vortex, $\Gamma_{imp}/(U_\infty D) = 0.1724$, $r_{imp}/R = 0.75$, is shown on the left-hand side of Figure 7.11. Relatively strong pressure fluctuation is observed on the whole leading edge, which extends to the trailing edge at the radial position around $0.9 R$. The increased pressure fluctuation on the blade is ascribed to the variation of the angle of attack on the blade as shown in the top left of Figure 7.3. In the radial range below the impinging

position, the blade experiences an increase and decrease of AOA , consequently the blade loading has an increase and decrease respectively. Illustrations to the phenomenon discussed above are provided in Appendix H. In the radial range above the impinging position, the blade thrust only has increases at all phase angles (as shown at the two phase angles in Figure H.0.1); the magnitude of the loading increase varies in the circumferential direction. This observation of pressure fluctuation on the blade is consistent with the case with a vortex impinging on a still wing, which shows a strong pressure distribution change mostly in the leading 30% airfoil chord [46]. The magnitude of the pressure fluctuation on the suction side of the blade during a vortex impingement is generally in the order of $O(10)$ larger than that without an impinging vortex by comparing Figure 7.9 and Figure 7.11. The pressure fluctuation at the vortex-impinging radial position is relatively smaller than other radial positions, which is due to the small change of angle of attack in this position, as shown in the top left of Figure 7.3.

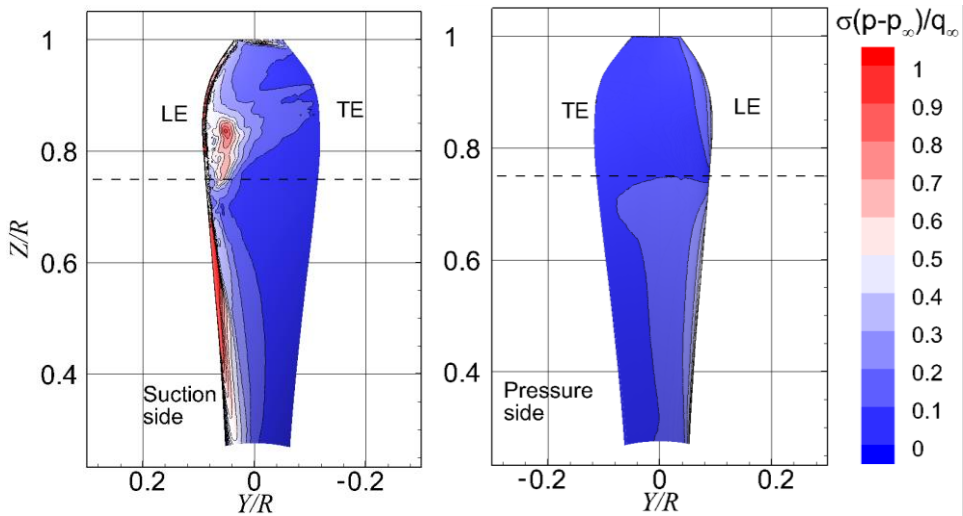


Figure 7.11 Left: standard deviation of pressure on the suction side of the blade; right: standard deviation of pressure on the pressure side of the blade. $\Gamma_{imp}/(U_{\infty}D) = 0.1724$, $J = 1.1$.

On the pressure side, a relatively strong pressure fluctuation is also observed on the leading edge as shown on the right-hand side of Figure 7.11. The maximum pressure fluctuation increases at the order of $O(10)$ times compared to that without an impinging vortex. A similar analysis was conducted in [36] by measuring pressure at the 0.1 chord position, 0.975 R radial position and on the pressure side of the blade, when a vortex impinges on the radial position of 0.9 R . The result showed that the magnitude of the maximum pressure fluctuation due to a vortex impingement increased nearly 6 times compared with the case without an impinging vortex, which is consistent with our results.

7.3 Conclusions

This chapter explains the mechanism of the effect of a vortex upon the performance of a propeller. A change in the angle of attack on the blade causes the blade thrust coefficient to vary in the circumferential direction; the increment of the thrust coefficient dominates the effect of the vortex on the propeller for a contra-rotating vortex. The same mechanism governs the co-rotating vortex but the loading variation is switched with respect to the contra-rotating vortex case. The torque coefficient follows the same trend as the thrust coefficient. As the magnitude of the vortex strength increases, its effect on the thrust and torque coefficients increases. As the impinging radial position moves outward, its effect on the propeller loading decreases. Because the thrust coefficient and torque coefficient change consistently when a vortex impinges onto the propeller, the efficiency of the propeller is independent of the impinging vortex.

The impact of the vortex on the time-averaged loading of the propeller is relatively small, e.g. there is a 5% increase of the thrust coefficient with the impinging vortex strength of $\Gamma_{imp}/(U_\infty D) = 0.1724$ and the imping radial position of $0.9 R$. However, the dynamic loading on the blade has a strong fluctuation, e.g. the maximum thrust coefficient on the blade is 1.4 times of the minimum value for the above case; this cyclic loading has the potential to cause structural damage and it should be taken into account during the blade design. The fluctuation of the blade loading is proportional to the vortex strength; and it is also deduced that the fluctuation strength has its maximum value as the impingement radial position is $1.0 R$.

The blade pressure fluctuation due to an impinging vortex increases in the order of $O(10)$ compared with the case with an axisymmetric inflow, mostly in the leading edge of the blade. The main reason for the pressure fluctuation increment is due to the variation of the angle of attack in the circumferential direction.

Part IV

Conclusions and recommendations

Chapter 8 Conclusions and recommendations

8.1 Conclusions about the interaction between a propeller and its self-induced vortices

As a propeller aircraft is operated near the ground, a system of ground vortices are generated from the ground toward the propeller. By investigating the induced flow field due to the interaction between the highly loaded propeller and the ground, the topology of the ground vortices is studied. By analysing the velocities upstream of the propeller, as well as the loading on the propeller, the impact of ground vortices on the propeller performance is analysed.

For the concern of the vortices ingested into the propeller plane and impinging on the blades, a map of occurrence of vortices is built based on the experimental and numerical results. According to the visualization of the flow field, the flow fields with no vortex, failed vortices and vortices entering the propeller are observed. The criterion for determining the occurrence of ground vortices is the situation with a vortex (vortices) entering the propeller in our study. If the thrust coefficient increases and the elevation of the propeller from the ground decreases, the occurrence of ground vortices is observed.

The vorticity source of ground vortices at headwind conditions is investigated by the numerical study and verified by the analytical method. Both the far field boundary layer and the pressure gradient on the ground are verified to be the available sources of vorticity, which is a deviation from previously offered explanations [27-30] stating that the vorticity source is solely from the far field boundary layer. The production mechanism of the wall-normal component of the vorticity, required for the existence of ground vortices, is found to be the divergence of the wall-parallel components of vorticity on the wall.

The flow field in the region involving ground vortices features a highly unsteady flow. Several flow topologies are encountered at the same thrust setting of the propeller: one dominant vortex, two dominant vortices and multiple vortices are observed. The spectral analysis on the vorticity performed in the plane in close proximity to the ground shows energetic frequencies in the order of $f * D/U_{eq} = O(10^{-2}) \sim O(10^{-1})$. This range of relatively low frequencies is found to be consistent with that observed in the ground vortices induced by a suction tube model [18]. The range of energetic frequencies of the flow near the ground is far below the blade passing frequency and this implies that the ground vortices near the ground have negligible influence from the blade passing.

The complex flow is further analysed with the help of the Proper Orthogonal Decomposition method. The time averaged flow (zero mode) is smeared due to the meandering of the vortices, which features a pair of weak vortices (relative to the strength of the instantaneous vortex) both near the ground and upstream of the propeller. The first mode, in the plane in close proximity and parallel with the ground, features one dominant vortex; the second and the third modes feature a pair of vortices. However, the first and the second modes in the plane upstream of the propeller are dominated by the propeller-suction induced flow; and the third and the fourth modes are dominated by the unsteady ground vortices.

The vortices ascending from the ground enter the propeller and have an impact on the propeller inflow. It is found that the ground vortices enter the propeller in an oblique angle. The axial component of the vorticity mainly influences the tangential and radial velocities of the propeller inflow; and the radial component of the vorticity mainly influences the axial velocity of the propeller inflow. Consequently, the blade incidence angle is changed and becomes non-uniform in the circumferential direction. With a higher thrust coefficient and a lower height ratio of the propeller, the non-uniformity of the blade incidence angle becomes severer. The time averaged performance of the propeller is independent of the vortices. Firstly, this is due to the cancelling effect of vortices with different rotation directions. Secondly, the strength of the vortex is relatively small and its induced velocity is relatively small compared with the propeller inflow. The ground vortices entering the propeller in the radial direction observed in our result were not reported before in the studies on turbofans or suction tube models [26, 28-30, 32, 33], because the shroud directs the inflow of the turbofan to be parallel with the axis of the engine.

8.2 Conclusions about the interaction between a propeller and an externally generated vortex

For the aircraft configuration with propellers installed downstream of the lifting surfaces, e.g. the canard and control surfaces, the vortices from these lifting surfaces can impinge on the propeller. Different from the ground vortices, which are induced by the propeller suction itself, this type of vortex is generated by a separate and independent vortex generator. The research on this externally generated vortex gives insights into the interaction between a streamwise vortex and a propeller; it also helps in analysing the impact of a single ground vortex interacting with the propeller (the axial component of the vorticity of the ground vortex).

In the current investigation of the impact of the propeller on the vortex, the vortex generator is set at one AOA to ensure a constant value of the incoming vortex, and the propeller operates at a sweep of advance ratios from the zero loading to the high loading conditions. The vortex sections both upstream and downstream of the propeller are mainly affected by the stretching effect induced by the propeller thrust when the propeller operates at a highly loaded condition. This results in an increase of the maximum tangential velocity and a decrease of the vortex core radius. Due to

the cutting process by the blade, the meandering of the downstream vortex becomes stronger compared with the upstream vortex section, in both the spanwise and chordwise directions. The circulation of the vortex upstream of the propeller is only redistributed in the radial direction of the vortex, and the total circulation is independent of the propeller settings. For the vortex downstream the propeller, the circulation shows an increase in the inner region of the vortex because of the stretching effect; the circulation in the outer region of the vortex decreases because of the blade wake with an opposite sign of vorticity for the case with a contra-rotating vortex; the maximum circulation of the vortex downstream of the propeller have a negligible difference from that upstream of the propeller, which means the vortex after the impingement still has a comparable strength with respect to the incoming vortex to influence the further downstream airframe.

With respect to the vortex impact on the propeller aerodynamic performance, the results of the time-averaged performance and unsteady loadings are analysed. The vortex induces an additional tangential velocity in the propeller inflow field. The change of the effective angle of attack on the blade causes the blade thrust coefficient to vary in the circumferential direction; its integral effect is dominated by the increase of the thrust coefficient for a contra-rotating vortex. The opposite is true for a co-rotating vortex. The torque coefficient follows the same trend as the thrust coefficient; therefore, the efficiency of the propeller remains independent of the impinging vortex. As the magnitude of the vortex strength increases, its effect on the thrust and torque coefficients increases and approximately has a linear relation. As the impinging radial position moves outward, its effect on the propeller loading decreases. The unchanged efficiency in our results is in disagreement with the results investigated by a vortex impinging on a steady wing [47] which leads to an increase of the lift-to-drag ratio. Our result is found to be consistent with the case of a propeller operating at an angle of attack, where the upwash effect and the downwash effect are cancelled out [96].

The dynamic loading on the blade due to the impinging vortex is strong, and the ratio of the maximum loading over the minimum loading reaches 1.4 for a test case that analysed in this study ($\Gamma_{imp}/(U_{\infty}D) = 0.1724$, $r_{imp}/R = 0.9$); this ratio would increase as the vortex strength increases, and it is also dependent of the impingement radial position. This means that the dynamic loading on the blade needs to be considered for the structural design if there is a vortex in the propeller inflow. This dynamic loading is exactly given by the pressure fluctuation on the blade. The blade pressure fluctuation due to an impinging vortex increases by an order of magnitude compared with the case with an axisymmetric inflow, mostly in the leading edge of the blade. The main reason of the pressure fluctuation increase is due to the variation of the effective angle of attack in the circumferential direction. The fluctuation of the pressure on the blade is found to be consistent with the experimental result of the case with a vortex impinging on the tip of a propeller [46].

8.3 Recommendations

In the present study, the fundamentals of the vortex generation and vortex interaction with a propeller have been analysed and quantified. The understanding of the occurrence of ground vortices entering a propeller can help alleviate the influence of ground vortices upon the propeller by preventing the favourable conditions to form ground vortices. The mechanism found here can be utilized to help design wind tunnel tests on propellers as well, in case a uniform inflow of a propeller is needed and ground vortices have to be prevented. The results of ground vortices induced by a propeller can be also applied to the analysis of the interaction between a propeller and any solid walls, such as the fuselage. The fuselage vortex may be a concern when the propeller is mounted close to the fuselage [19].

The flow field of ground vortices was investigated by temporal analysis in this research. The unsteady features of the ground vortices found in this study are: the number of dominant ground vortices varies in time; the ground vortices meander above the ground; the sign of the dominant vortex switches. The possible reasons of these phenomena are the fluctuation of the free stream, the turbulence in the slip stream of the propeller, as well as the induced velocities of the vortices. Future research on the unsteadiness of propeller-induced ground vortices can be performed by evaluating these three possible factors.

The ground vortices enter the propeller plane in an oblique angle. For the interest of understanding the impact of a vortical inflow on a propeller, a single vortex with a constant strength impinging on the propeller was performed during the study of the interaction between an externally generated vortex and a propeller. However, only the streamwise component of the vorticity was studied, and the impact of the parallel component (in the radial direction of the propeller) of the vorticity on the propeller was not investigated. Further study on this aspect can be conducted by generating a vortex with the vortex axis parallel with the propeller plane.

The vortex impingement is found to have no detrimental effect on the efficiency of the propeller, no matter multiple ground vortices or a single streamwise vortex. However, attention should be paid to the dynamic loading on the blade. This dynamic loading (due to the pressure variation) on the blade would raise the concern of an aero-acoustic noise increase compared with the case of a uniform inflow. In order to quantify this aero-acoustic noise increase in the future study, acoustic measurements are necessary.

The vortex after impinging on the propeller still has a comparable strength with respect to the incoming vortex, which could have influence on the further downstream parts of the airframe, e.g. the second row of rotors of a contra-rotating propeller or a lifting surface. The analysis as shown in the thesis could be applied to the interaction in these cases as well.

Appendix A Particle Image Velocimetry

Particle Image Velocimetry is a technique that measures the instantaneous velocity fields over a field of view of the fluid domain. Herein, a planar *PIV* is introduced to explain its mechanism. The technique measures the motion of small marked region of fluid by observing the locations of the frames of the markers at two times. These methods return to the fundamental definition of the velocity and estimate the local velocity \vec{u} from

$$\vec{u}(\vec{x}, t) = \frac{\Delta \vec{x}(\vec{x}, t)}{(t' - t)}. \quad (\text{A.1})$$

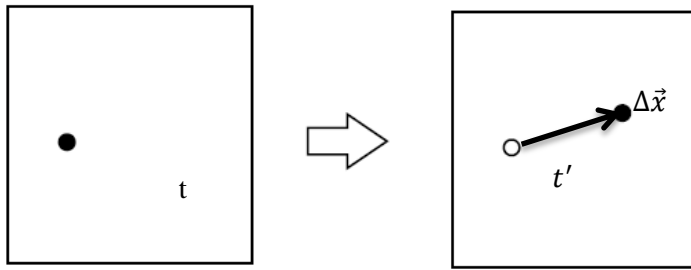


Figure A.0.1 Schematic representation of particle marker movement.

$\Delta \vec{x}$ is the displacement of the marker located at \vec{x} at time t over a short time interval Δt which explained in Figure A.0.1. While the equation is simple in itself, the required equipment and tools for the calculation of the velocity is a complex measurement chain, which is still being improved.

A generic sketch of a *PIV* set up in a wind tunnel is given in Figure A.0.2. It shows the necessary components required to perform a *PIV* measurement, which includes the laser for illumination, optics to adjust the laser beam, particles to trace the fluid motion, camera to record to the images and the computer to store the images. The various steps required in performing a *PIV* measurement are given in Figure A.0.3. The steps in the upper part of this flowchart are practical steps of measuring the flow; the lower ones are the steps related to the analysis of the measurements. The detail of each step is elaborated in [74].

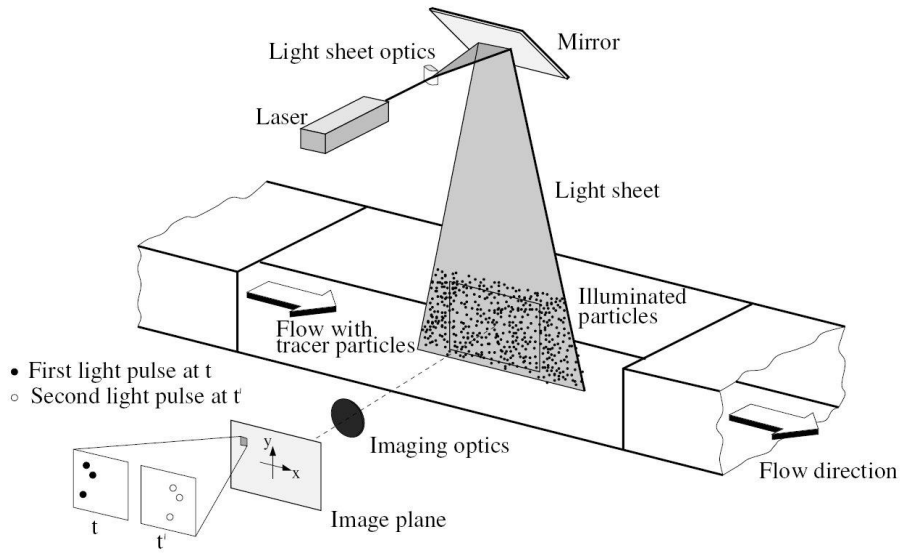


Figure A.0.2 *PIV* set up principle in a wind tunnel [74].

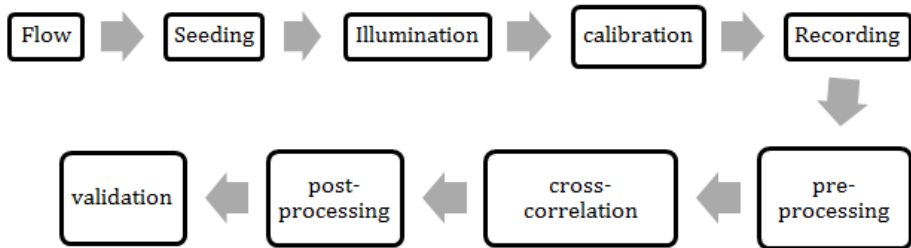


Figure A.0.3 Flowchart of *PIV* steps.

Appendix B Boundary layer profile near the ground table

The measurement of the boundary layer under the propeller was performed to help identify the position of the *PIV* measurement plane (the wall parallel plane as presented in Chapter 4) in the boundary layer. It also supports data for the velocity profile on the velocity inlet of the *CFD* simulations. It should be mentioned that velocity inlet in the *CFD* simulation is 13.1 *R* upstream of the propeller, while the experimental measurement of the boundary layer is under the propeller. This arrangement is utilized mainly because the difficulty to perform the *PIV* measurement at the position 13.1 *R* upstream of the propeller in the wind tunnel, where there is no optical access for the laser or the camera. Furthermore, this difference of boundary layer profile shows no significant influence on the result in terms of flow topology and source of vorticity.

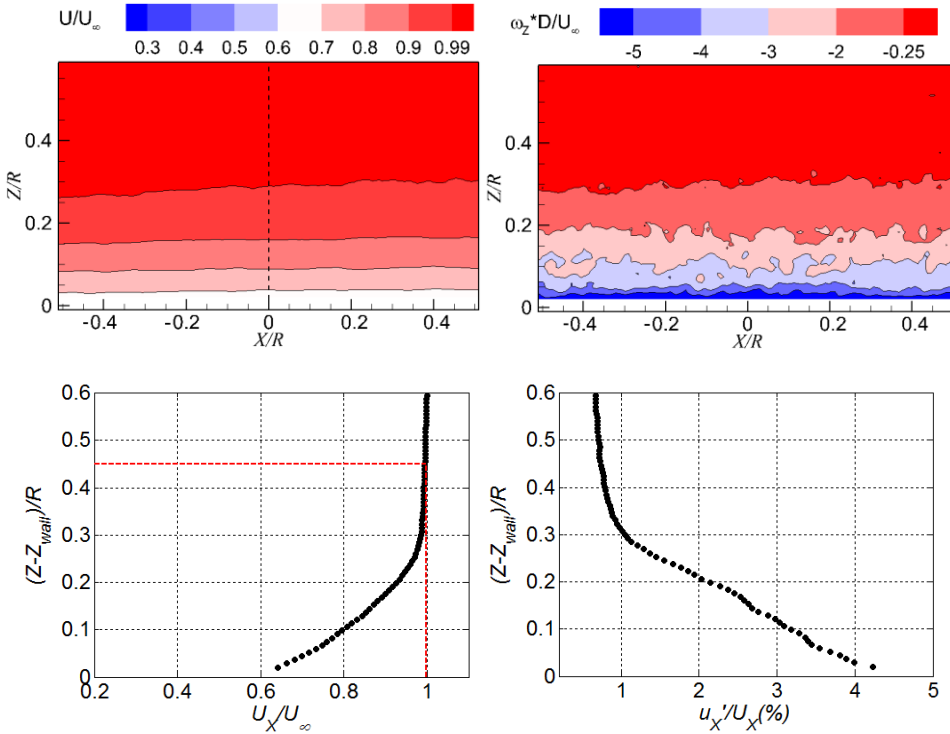


Figure B.0.1 Flow field near the ground wall. Top left: contour of the free stream velocity; top right: contour of the vorticity in the lateral direction; bottom left: profile of the boundary layer at the position $X/R = 0$; bottom right: profile of the turbulent intensity at the position $X/R = 0$;

The measurement of the boundary layer with absence of the propeller model at free stream velocity of 2.7 m/s was conducted, and the results are shown in Figure B.0.1. No detail of the experimental setup is elaborated here. The figure at the top left shows the distribution of velocity in the free stream direction. The figure in the top right shows the distribution of vorticity in the lateral direction (Y component).

The profile of the boundary layer at position $X/R = 0$, where it is aligned with the propeller's leading edge (although propeller is absent during the test), is plotted in the graph at the bottom left of Figure B.0.1. The boundary layer thickness is $0.45 R$. The turbulence intensity of the flow near the wall, represented by u_x'/U_x (u_x' is the root mean square of velocity fluctuation), is plotted in the graph at the bottom right of Figure B.0.1. The maximum value of the turbulence intensity is observed at the position close to the wall, which is around 4.3%. The turbulence intensity outside the boundary layer in our measurement is approximately 0.5%. The turbulence intensity in our measurement does not reach the position from which it starts decreasing as the flow field approaches the wall. This position is normally at the distance of order $O(10^{-3}\delta_{BL})$ for a turbulent boundary layer with zero pressure gradient along the wall as reported in [100].

Appendix C Proper Orthogonal Decomposition

The inspection of coherent structures in complex flows requires detecting and distinguishing them from the less coherent turbulent fluctuations. Proper Orthogonal Decomposition (*POD*) identifies basis functions (i.e. modes) that capture the average energy content from experimental or numerical data [101]. The “method of snapshots” as discussed in [102] is applied in the research. The introduction of this method in this thesis is focused on its application form.

The results of unsteady *PIV* measurement are a set of instantaneous velocities, i.e. three components of velocities ($\vec{U} = [U_X, U_Y, U_Z]$) in a 2D domain ($\vec{X} = [X, Y]$) in our case. The velocities defined in Reynolds decomposition are,

$$\vec{U}(\vec{X}, t) = \bar{U}(\vec{X}, t) + \vec{u}(\vec{X}, t). \quad (C.1)$$

$\vec{U}(\vec{X}, t)$ is the instantaneous velocity, $\bar{U}(\vec{X})$ is the time averaged velocity; and $\vec{u}(\vec{X}, t)$ is the fluctuation part of the velocity.

The proper decomposition is then applied on the autocorrelation matrix C as reported in [103]. The matrix C is defined by

$$C_{i,j} = \frac{1}{N_s} \iint \vec{u}(\vec{X}, t_i) \vec{u}(\vec{X}, t_j) d\vec{X}. \quad (C.2)$$

N_s is the number of snapshots; the integral in our case is a summation for the discrete points of data. The size of C is determined by the number of snapshots and its dimension is $N_s \times N_s$.

The eigenvalues λ_n and the eigenvectors $A_n(\vec{X})$ of autocorrelation matrix satisfy

$$CA_n(\vec{X}) = \lambda_n A_n(\vec{X}). \quad (C.3)$$

The *POD* mode is determined by

$$\vec{\phi}_n(\vec{X}) = \sum_{m=1}^{m=N_s} \vec{u}(\vec{X}, t_m) A_{m,n}(\vec{X}). \quad (C.4)$$

Furthermore, the measurement data contain temporal information that can be retrieved by projecting each snapshot onto the basis functions:

$$c_n(t) = \iint \vec{u}(\vec{X}, t) \vec{\phi}_n(\vec{X}) d\vec{X}. \quad (C.5)$$

The coefficient c_n indicates the correlation between the n th basis *POD* spatial mode and the instantaneous flow field at the time t [101, 102].

Appendix D Determination of the vortex centre

For an axisymmetric vortex, the vortex centre is defined as the maximum magnitude of the vorticity,

$$(x_0, y_0) = (x, y)_{\omega, \max}. \quad (D.1)$$

This method was utilized in [29, 32] to identify the vortex centre during the study of ground vortices induced by a suction tube. In real situations, the vortex is not always axisymmetric, e.g. due to the impact of the vorticity in the blade wake and the interaction among vortices, the method by looking for the maximum vorticity is not robust. Therefore, a weighted averaging method is introduced for the next step. This method follows the formulation which was introduced in [104] about the wake vortex of a helicopter.

After obtaining the location of the maximum vorticity, (x_0, y_0) , a disk with radius r_0 (approximately the same radius as the vortex core radius in our study) which centred at the (x_0, y_0) is built for the next step. The grids of the disk are built for interpolation with resolution in terms of the number of radial direction, m ($m = 80$), and circumferential direction, n ($n = 120$). Second, a new vortex centre (x_1, y_1) is calculated as the weighted average of the position within the disk, where the weighting function is the vorticity $\omega_{m,n}$ at each zone of the disk,

$$(x_1, y_1) = \frac{\sum \omega_{m,n}(x_{m,n}, y_{m,n})}{\sum \omega_{m,n}}, ((x_{m,n} - x_0)^2 + (y_{m,n} - y_0)^2 \leq r_0^2). \quad (D.2)$$

Appendix E Flow fields downstream of the propeller at high loading condition

The flow topologies downstream of the propeller at the advance ratio of $J = 0.6$ (representative of a high loading condition), and $\Gamma_{imp}/(U_{\infty}D) = 0.2161$ are shown in Figure E.0.1 of *PIV* measurements. The trend found at the high loading condition is consistent with that found at the moderate loading condition as shown in Figure 6.5. At the phase angles of $\Psi = 6.0^\circ$, as shown on the left-hand side of Figure E.0.1, there is an approximately axisymmetric vortex located in the centre of the figure. At the phase angle of $\Psi = 34.5^\circ$, the impinging vortex is disrupted into two pieces, which corresponds to the shape factor of infinity. For this disrupted vortex, the vortex centre is considered as the centre of the part with the majority of the vorticity.

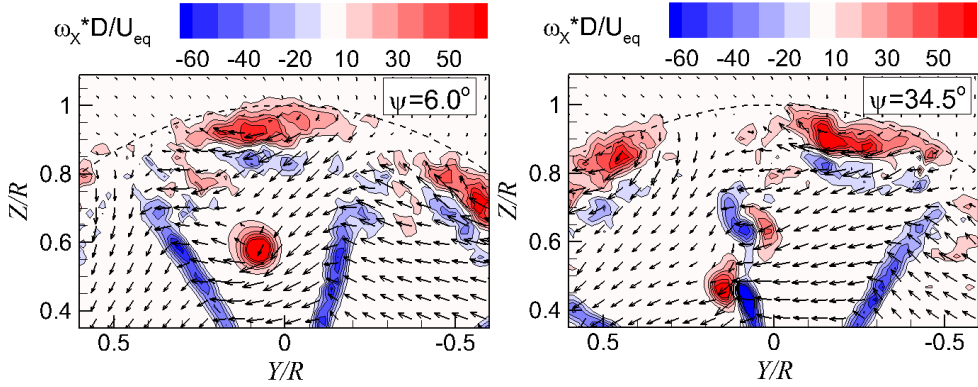


Figure E.0.1 Flow fields downstream of the propeller. $J = 0.6$ (representative of a high loading condition), and $\Gamma_{imp}/(U_{\infty}D) = 0.2161$.

Appendix F Flow fields downstream of the propeller at different impinging radial positions of the vortex

When the vortex enters the propeller at different radial positions, the flow fields downstream of the propeller are presented in this section. The results are compared at radial positions of $r_{imp}/R = 0.82$ and 0.93 , $\Gamma_{imp}/(U_\infty D) = 0.2161$. The profiles of the vortices at different impinging positions are similar and nearly axisymmetric at the phase angle of $\Psi = 6^\circ$, as shown in the figures on the left-hand side of Figure F.0.1.

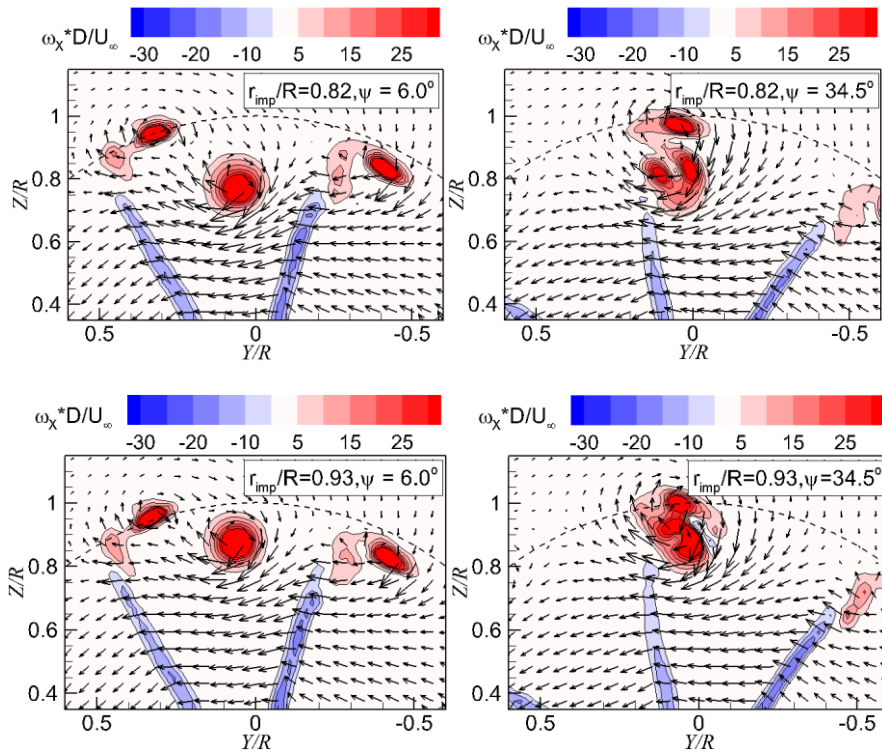


Figure F.0.1 Flow field downstream of the propeller when the vortex impinges at different radial positions. Top: $r_{imp}/R = 0.82$; bottom: $r_{imp}/R = 0.93$.

At the phase angle of $\Psi = 34.5^\circ$, the vortex moves toward the tip vortex as the impinging position moves outward. At the impinging position of $r_{imp}/R = 0.82$, two cores can be observed and they are inter-connected with the tip vortex at the outer region. At the impinging position of $r_{imp}/R = 0.93$, the impinging vortex and

blade-tip vortex are merged in a big clockwise vortex. It is reported in [42] that when the vortex impinges at the tip of a steady wing, the impinging vortex and tip vortex orbit each other downstream of the wing, which is consistent with our observation.

The three dimensional flow represented by iso-surfaces of vorticity magnitude is shown in Figure F.0.2 from the *CFD* result ($\Gamma_{imp}/(U_{\infty}D) = 0.2260$, $r_{imp}/R = 0.90$, $J = 1.1$).

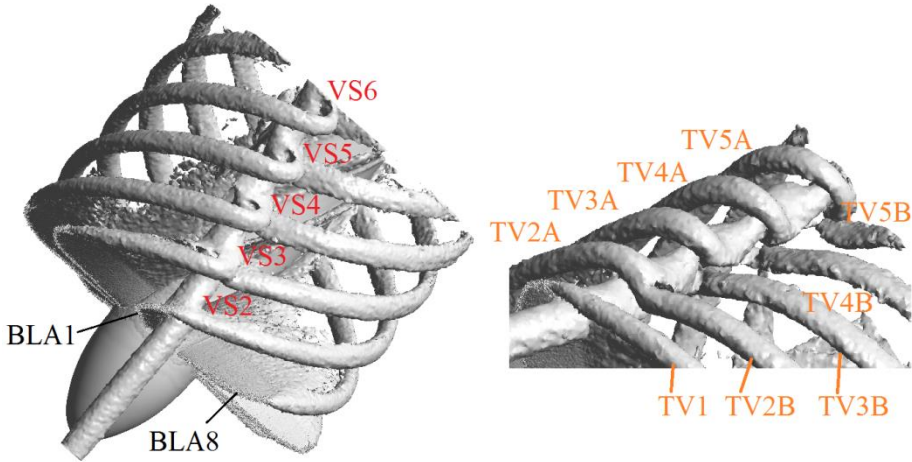


Figure F.0.2 The three-dimensional flow topology of the vortex impinging on the propeller. $J = 1.1$, $\Gamma_{imp}/(U_{\infty}D) = 0.2260$, $r_{imp}/R = 0.90$. Visualized by the iso-surface with vorticity magnitude of $|\omega| * D/(U_{\infty}) = 13.0$.

As the vortex is at the phase angle with blade in its trajectory (e.g. $\Psi = 10.0^\circ$ as shown in Figure F.0.2), the vortex is penetrated by the blade and the cutting process is the same as that with vortex impinging radial position of $r_{imp}/R = 0.75$, as shown in Figure 6.7. One other phenomenon observed here is the interaction between the sections of the impinging vortex and the blade tip vortex, as shown in detail in the right hand side of Figure F.0.2. The tip vortex of the blade 1 (*BLA1*) is represented by *TV1*, and tip vortex of other blades is disrupted into two sections and represented by *TViA* and *TViB*. The tip vortex shed from *BLA1* is not severely influenced by the impinging vortex. The tip vortex shed from *BLA2* orbits around the impinging vortex. As it goes further downstream, e.g. the tip vortex shed from the *BLA3* is disrupted into two sections, and the two sections have a displacement in the radial direction which is due to the induced velocities of the impinging vortex. Both ends of the sections of the tip vortex (*TV3A* and *TV3B*) are connected with the impinging vortex. The tip vortices further downstream shed from other blades follow the same trend as that of the *TV3*.

Appendix G Flow fields downstream of the propeller with different rotating directions of the vortex

The flow topologies downstream of the propeller with different rotating directions of the impinging vortices are shown in Figure G.0.1. Because the flow fields with contra-rotating vortex was already shown in Figure 6.6, herein only the flow fields with co-rotating vortex are shown. The analysis is performed on the propeller setting of the advance ratio of $J = 1.1$, and the impinging vortex with the strength of, $\Gamma_{imp}/(U_\infty D) = -0.2255$. The data are from *CFD* results.

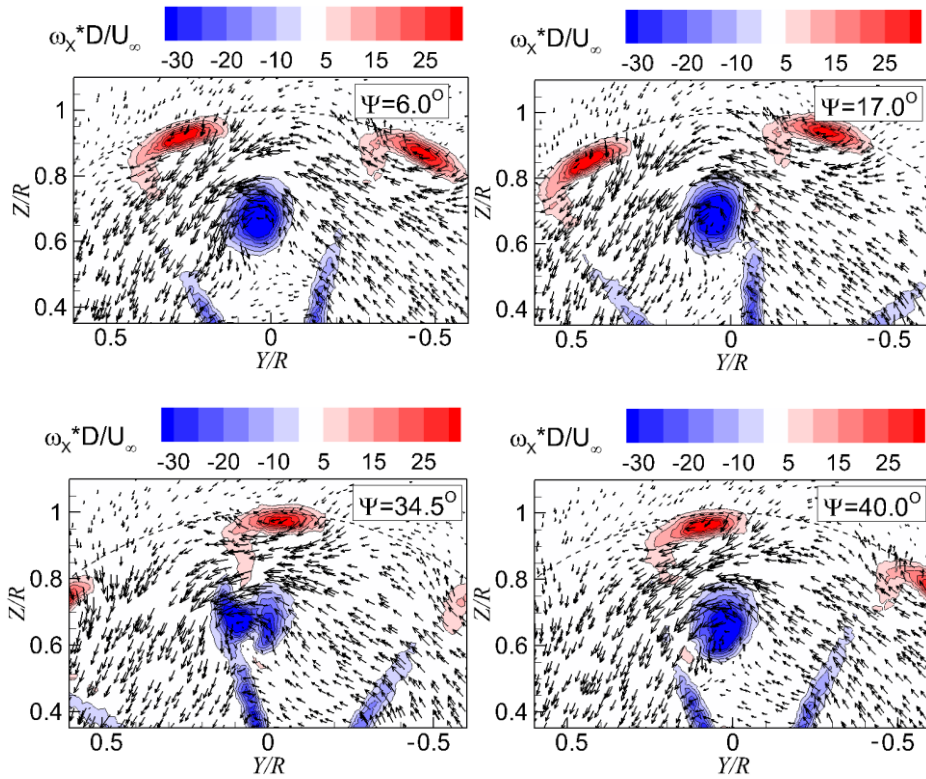


Figure G.0.1 Flow fields downstream of the propeller with a co-rotating impinging vortex (*CFD*). $J = 1.1$, $\Gamma_{imp}/(U_\infty \cdot D) = -0.2255$.

The example flow fields are chosen at the phase angles which are the same as the case of the contra-rotating vortex. Generally, the topologies of the vortex at difference phase angles still follow the same trend as observed for the contra-

rotating vortex. Discrepancies are also found in terms of the disruption of the vortex. For example, at the phase angle of $\Psi = 34.5^\circ$ for the co-rotating vortex, the piece of the impinging vortex located inside the wake is strengthened, and the other piece is relatively weak. For the contra-rotating vortex, the two pieces of the vortex have approximately the same strength. Because both the co-rotating vortex is also dominated by the stretching effect induced by the propeller, the quantities such as the maximum tangential velocity, the core radius and the circulation are supposed to follow the same trend as the contra-rotating vortex at the phase angle with axisymmetric profile (at the phase angle with strong interaction with the wake may be different and it is not considered in this research), and they are not elaborated in detail here.

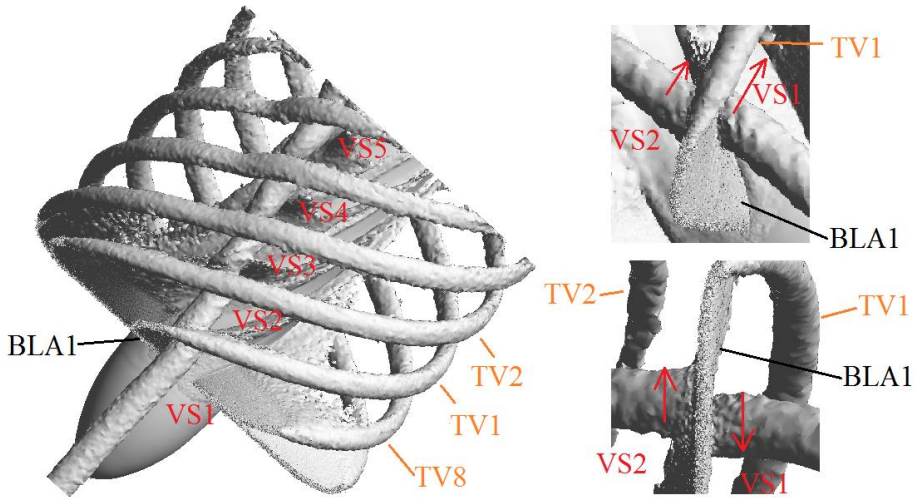


Figure G.0.2 The three-dimensional flow topology of the co-rotating vortex impinging on the propeller. $J = 1.1$, $\Gamma_{imp}/(U_\infty D) = -0.2255$, $r_{imp}/R = 0.75$. Visualized by the iso-surface with the vorticity magnitude of $|\omega| * D/(U_\infty) = 13.0$.

The three dimensional flow topology represented by the iso-surface of the vorticity magnitude of $|\omega| * D/(U_\infty) = 13.0$ is shown in Figure G.0.2 from *CFD* results of co-rotating vortex case. The flow is from the left to the right in the left hand side figure of Figure G.0.2, but it is in the opposite direction in the right hand side figures for a clarity reason. The impinging vortex before and after going through the propeller generally has the same topology as that of the contra-rotating vortex. The cutting process features the vortex displacement in the chordwise and spanwise directions, which is shown in the top right and bottom right of Figure G.0.2 respectively. The vortex displacement in the spanwise direction has the opposite characteristics compared with the contra-rotating vortex, because the image vortex in the blade is opposite.

Appendix H Loading and pressure distribution on the blade

As a contra-rotating vortex impinges at the propeller, $\Gamma_{imp}/(U_{\infty}D) = 0.1724$, $J = 1.1$, the loading distributions in the radial direction of the blade are plotted from CFD results. The phase angles chosen to present correspond to the maximum and minimum loadings of the blade. For the case without an impinging vortex, the distribution of the local thrust along the radial direction is shown in Figure H.0.1 by the triangles. The local thrust increases as the radius increases, and reaches its maximum at the radial position around $r/R = 0.9$.

The distribution of the local thrust on the blade at phase angles of $\Psi = 232^\circ$, which corresponds to the maximum loading, is shown by the crosses in Figure H.0.1. Compared to the case without a vortex impinging on the propeller, the local thrust on the blade increases at all the radial positions.

The distribution of the local thrust of the blade at the phase angle of $\Psi = 10^\circ$, which corresponds to the minimum loading, is shown by the circles in Figure H.0.1. The local thrust at the radial positions from the hub ($r/R = 0.28$) to $r/R = 0.78$ is noticeably lower than the case without an impinging vortex. From the radial position $r/R = 0.95$ to $r/R = 1.0$, the local thrust is slightly higher than the case without an impinging vortex, which is consistent with the distribution of the change of the angle of attack.

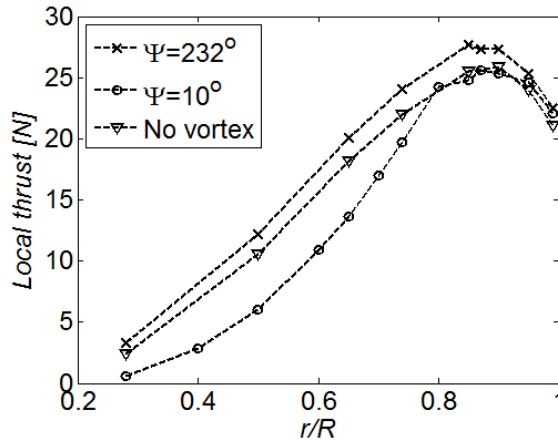


Figure H.0.1 Distribution of the local thrust of the blade along the radial direction ($\Gamma_{imp}/(U_{\infty}D) = 0.1724$). Crosses: $\Psi = 232^\circ$; circles: $\Psi = 10^\circ$; triangles: no vortex. CFD.

The pressure distributions on the blade cross sections are presented at two radial positions, i.e. $r/R = 0.5$ and $r/R = 0.9$, which are at the inward and outward positions relative to the vortex-impinging radial position, as shown in Figure H.0.2 and Figure H.0.3 respectively. The pressure distributions without an impinging vortex are shown by the black dots, which is the reference data. The pressure distributions at the phase angles with maximum and minimum blade thrust coefficients are shown by the blue crosses and red crosses respectively. These example distributions are utilized to calculate the local blade loading as shown in Figure H.0.1, and the characteristics are already mentioned as above.

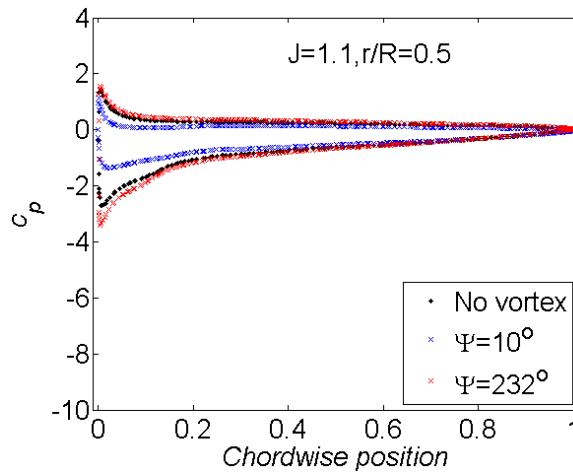


Figure H.0.2 Pressure distributions on the cross sections of the blade. Radial position $r/R = 0.5$. *CFD*.

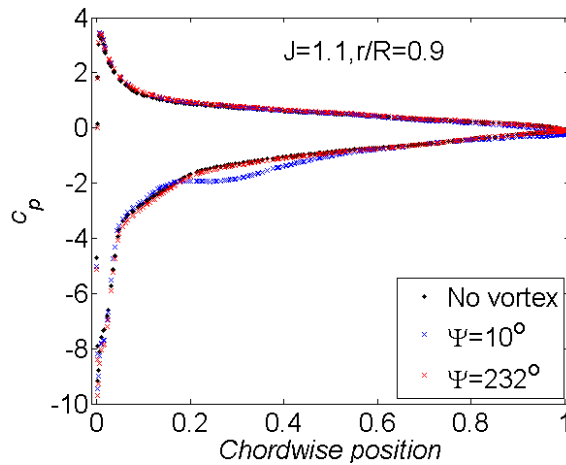


Figure H.0.3 Pressure distributions on the cross sections of the blade. Radial position $r/R = 0.9$. *CFD*.

Bibliography

1. ATR, *Regional turboprops market outlook 2014-2033*. ATR DC/E Marketing, 2014.
2. AeroWeb. *General Aviation Market Data*. 2015; Available from: <http://www.bga-aeroweb.com/General-Aviation.html>.
3. RUAG. *World Air Forces 2015*. 2015; Available from: www.flightglobal.com/insight.
4. Westmoreland, W. S., McDaniel, M. A., and Hall, Z. M., *Time-Accurate Simulations of a Spinning Propeller Using OVERFLOW2*. 32nd AIAA Applied Aerodynamics Conference. 2014. Atlanta.
5. Veldhuis, L., *Propeller wing aerodynamics interference*. PhD Thesis, Delft University of Technology, 2005.
6. Whitlow, J. B. and Sievers, G. K., *NASA advanced turboprop research and concept validation program*. Conference and exposition on future transportation technology. 1988. San Francisco.
7. Janus, J. M., *General Aviation Propeller-Airframe Integration Simulations*. Journal of Aircraft, 2006. **43**(2): p. 390-394.
8. Marretta, R. M. A., *Different Wings Flowfields Interaction on the Wing-Propeller Coupling*. Journal of Aircraft, 1997. **34**(6): p. 740-747.
9. Witkowski, D. P., Lee, A. K. H., and Sullivan, J. P., *Aerodynamic interaction between propellers and wings*. 26th Aerospace Sciences Meeting. 1988. Nevada.
10. Stuermer, A., *Unsteady CFD Simulations of Contra-Rotating Propeller Propulsion Systems*. 44th AIAA/ASME/SAE/ASEE Joint Propulsion Conference & Exhibit. 2008. Hartford.
11. Stuermer, A. and Yin, J., *Aerodynamic and Aeroacoustic Installation Effects for Pusher-Configuration CROR Propulsion Systems*. 28th AIAA Applied Aerodynamics Conference. 2010. Chicago.

12. Yin, J., Stuermer, A., and Aversano, M., *Aerodynamic and Aeroacoustic Analysis of Installed Pusher-Propeller Aircraft Configurations*. Journal of Aircraft, 2012. **49**(5): p. 1423-1433.
13. Aljabri, A. S., Lyman, V., and Parker, R. J., *Evaluation of propeller/nacelle interactions in the PTA program*. AIAA/ASME/SAE/ASEE 22nd Joint propulsion conference. 1986. Huntsville.
14. Stuermer, A. and Yin, J., *DLR-AS CROR & Propeller noise*. 14th CEAS-ASC Workshop. 2010. Warsaw, Poland.
15. Marulo, F., Sollo, A., Aversano, M., Polimeno, U., and Perna, F., *Measurements and Predictions of Community Noise of a Pusher-Propeller General Aviation Aircraft*. 11th AIAA/CEAS Aeroacoustics Conference. 2005. Monterey.
16. Sinnige, T., Lynch, K., Ragni, D., Eitelberg, G., and Veldhuis, L., *Aerodynamic and Aeroacoustic Effects of Pylon Trailing Edge Blowing on Pusher Propeller Installation*. 21st AIAA/CEAS Aeroacoustics Conference. 2015. Dallas.
17. Takallu, M. A. and Block, P. J. W., *Prediction of added noise due to the effect of unsteady flow on pusher propellers*. 25th AIAA Aerospace Sciences Meeting. 1987. Reno.
18. Secareanu, A., Moroianu, D., Karlsson, A., and Fuchs, L., *Experimental and numerical study of ground vortex interaction in an air-intake*. 43rd AIAA Aerospace Sciences Meeting and Exhibit. 2005. Reno.
19. Shmilovich, A. and Yadlin, Y., *Flow control techniques for transport aircraft*. 26th International Congress of the Aeronautical sciences (ICAS). 2008. Alaska.
20. Campbell, J. F. and Chambers, J. R., *Patterns in the sky: natural visualization of aircraft flow fields*. SP-514, NASA, 1994.
21. *Aviation occurrence report: loss of directional control*. A98W0056, Highland helicopters, 1998.
22. *UH-60/VTDP Compound Helicopter Research*. Available from: <http://www.personal.psu.edu>.
23. Rodert, L. A. and Garrett, F. B., *Ingestion of foreign objects into turbine engines by vortices*. NACA TN-3330, Lewis Flight Propulsion Laboratory, 1955.
24. Colehour, J. L. and Farquhar, B. W., *Inlet vortex*. Journal of Aircraft, 1971. **8**(1): p. 39-43.

25. Golesworthy, G. T., *Tests of a blow away jet debris guard applied to a supersonic turbojet intake*. C. P. No. 561, Ministry of Aviation Aeronautical Research Council, 1961.
26. Murphy, J. P., MacManus, D. G., and Sheaf, C. T., *Experimental investigation of intake ground vortices during takeoff*. AIAA Journal, 2010. **48**(3): p. 688-701.
27. Bissinger, N. C. and Braun, G. W., *On the inlet vortex system*. NASA research grant NGL 43-001-086, 1974.
28. De Siervi, F., Viguier, H. C., Greitzer, E. M., and Tan, C. S., *Mechanisms of inlet-vortex formation*. Journal of Fluid Mechanics, 1982. **124**: p. 173-207.
29. Murphy, J. P. and MacManus, D. G., *Inlet ground vortex aerodynamics under headwind conditions*. Aerospace science and technology, 2011. **15**: p. 207-215.
30. Murphy, J. P. and MacManus, D. G., *Intake Ground Vortex Prediction Methods*. Journal of Aircraft, 2011. **48**(1): p. 23-33.
31. Lighthill, M. J., *Introduction. Boundary layer theory*. Laminar Boundary layers, ed. L. Rosenhead. 1963, Oxford University Press.
32. Murphy, J. P. and MacManus, D. G., *Ground vortex aerodynamics under crosswind conditions*. Experiments in Fluids, 2011. **50**(1): p. 109-124.
33. Wang, Z. and Gursul, I., *Unsteady characteristics of inlet vortices*. Experiments in Fluids, 2012. **53**.
34. Rockwell, D., *Vortex-body interactions*. Annual Review of Fluid Mechanics, 1998. **30**(1): p. 199-229.
35. Fletcher, T. M. and Brown, R. E., *Helicopter Tail Rotor Thrust and Main Rotor Wake Coupling in Crosswind Flight*. Journal of Aircraft, 2010. **47**(6): p. 2136-2148.
36. Ahmadi, A. R., Beranek, B., and Newman, I., *An experimental investigation of blade-vortex interaction at normal incidence*. AIAA 23rd Aerospace Sciences Meeting. 1985. Reno.
37. Aboelkassem, Y., *Blade Vortex Interactions: Experimental Measurements of the Near-Flow Field*. Journal of Fluid Science and Technology, 2009. **4**(1): p. 138-155.

38. Garmann, D. J. and Visbal, M. R., *Interaction of a streamwise-oriented vortex with a wing*. AIAA 52nd Aerospace Sciences Meeting, 2014. Maryland.
39. Devenport, W. J., Glegg, S. A. L., Wittmer, K. S., and Rife, M. C., *Perpendicular blade vortex interaction and its implications for helicopter noise prediction*. NASA-CR-193623, NASA, 1993.
40. Ham, N. D., *Some conclusions from an investigation of blade vortex interaction*. Journal of American Helicopter society, 1975. **20**(2): p. 26-30.
41. Khan, F. A. and Mueller, T. J., *Tip vortex/airfoil interaction for a canard/wing configuration at low Reynolds numbers*. 27th Aerospace Sciences Meeting, 1989. Reno.
42. Lee, T. and Adukesem, Y., *Interaction of a Streamwise Vortex with a Blade Tip Vortex*. Journal of Aircraft, 2006. **43**(6): p. 1956-1958.
43. Wang, T., Doolan, C. J., Coton, F. N., and Galbraith, R. A. M., *Experimental Study of the Three Dimensionality of Orthogonal Blade-Vortex Interaction*. AIAA Journal, 2002. **40**(10): p. 2037-2046.
44. Wittmer, K. S., Devenport, W. J., and Glegg, S. A. L., *Effects of Perpendicular Blade-Vortex Interaction, Part 2: Parameter Study*. AIAA Journal, 1999. **37**(7): p. 813-817.
45. Wittmer, K. S. and Devenport, W. J., *Effects of Perpendicular Blade-Vortex Interaction, Part 1: Turbulence Structure and Development*. AIAA Journal, 1999. **37**(7): p. 805-812.
46. Kalkhoran, I. M., Wilson, O. R., and Seath, D. D., *Experimental investigation of the perpendicular rotor blade-vortex interaction at transonic speeds*. AIAA Journal, 1992. **30**(3): p. 747-755.
47. Garmann, D. J. and Visbal, M. R., *Interactions of a streamwise-oriented vortex with a finite wing*. Journal of Fluid Mechanics, 2015. **767**: p. 782-810.
48. Weick, F. E., *Aircraft propeller design*. 1930: McGRAW-HILL BOOK COMPANY.
49. Froude, R. E., *On the part played in propulsion by differences of fluid pressure*. Transactions of the Royal Institution of Naval Architects, 1889. **30**: p. 390-405.
50. Rankine, W. M. J., *On the Mechanical Principles of the Action of the Propellers*. Transactions of the Institute of Naval Architects, 1865. **6**(13): p. 44-70.

51. Froude, W., *On the elementary relation between Pitch, Slip, and Propulsive Efficiency*. Transactions Institutes Naval Architects. Vol. 19. 1878.
52. Gur, O. and Rosen, A., *Comparison between blade-element models of propellers*. The Aeronautical Journal, 2008. **112**(1138).
53. Conway, J. T. and Su, J., *PMAL flow control calculations for the Aurora aircraft using non-axisymmetric propeller actuator disks*. Canadian Aeronautics and Space Journal, 2003. **49**.
54. Xia, Z. and Yang, Y., *Time-accurate versus actuator disk simulations of propeller slipstream flows*. 28th ICAS. 2012. Brisbane.
55. Conway, J. T., *Exact actuator disk solutions for non-uniform heavy loading and slipstream contraction*. Journal of Fluid Mechanics, 1998. **365**: p. 235-267.
56. Conway, J. T., *Analytical solutions for the actuator disk with variable radial distribution of load*. Journal of Fluid Mechanics, 1995. **297**: p. 327-355.
57. van Kuik, G. A. M., *On the limitations of Froude's actuator disk concept*. PhD Thesis, Eindhoven University of Technology, 1991.
58. van den Bosch, F. C. *Vorticity & Circulation*. Available from: http://www.astro.yale.edu/vdbosch/astro320_summary10.pdf.
59. Morton, B. R., *The generation and decay of vorticity*. Geophysical & Astrophysical Fluid Dynamics, 1984. **28**: p. 277-308.
60. Batchelor, G. K., *An introduction to fluid dynamics*. 1967: Cambridge University Press.
61. Zhang, W. and Sarkar, P. P., *Near-ground tornado-like vortex structure resolved by particle image velocimetry (PIV)*. Experiments in Fluids, 2012. **52**(2): p. 479-493.
62. Batchelor, G. K., *Axial flow in trailing line vortices*. Journal of Fluid Mechanics, 1964. **20**(04): p. 645-658.
63. Widnall, S. E., *The Structure and Dynamics of Vortex Filaments*. Annual Review of Fluid Mechanics, 1975. **7**(1): p. 141-165.
64. Vatisstas, G. H., *New Model for Intense Self-Similar Vortices*. Journal of Propulsion and Power, 1998. **14**(4): p. 462-469.

65. Rankine, W. J. M., *A manual of applied mechanics*. 1858: C. Griffen Co. London.
66. Scully, M. P., *Computation of helicopter rotor wake geometry and its influence on rotor harmonic airloads*. PhD Thesis, Massachusetts institute of technology, 1975.
67. Saffman, P. G., *Vortex dynamics*. 1995: Cambridge University Press.
68. Leweke, T. and Williamson, C. H. K., *Cooperative elliptic instability of a vortex pair*. Journal of Fluid Mechanics, 1998. **360**: p. 85-119.
69. van Jaarsveld, J. P. J., Holten, A. P. C., Elsenaar, A., Trieling, R. R., and van Heijst, G. J. F., *An experimental study of the effect of external turbulence on the decay of a single vortex and a vortex pair*. Journal of Fluid Mechanics, 2011. **670**: p. 214-239.
70. Ahmad, N. N., Proctor, F. H., Duparcmeur, F. M. L., and Jacob, D., *Review of idealized aircraft wake vortex models*. AIAA SciTech. 2014. Maryland.
71. Barlow, J. B., William, H., and Pope, A., *Low speed wind tunnel testing*. 1999: Wiley-Interscience.
72. Teng, Z., *Orthogonal vortex propeller interaction-vortex response and impact on the propeller performance*. Master Thesis, Delft University of Technology, 2015.
73. Pratt&Whitney-Canada. *The Green Powerhouse of Regional Airline Turboprops*. 2016; Available from: <http://www.pwc.ca/en/engines/pw100-pw150>.
74. Raffel, M., Willert, C. E., and Kompenhans, J., *Particle Image Velocimetry: A Practical Guide*. 1998: Springer.
75. Yang, Y., Sciacchitano, A., Veldhuis, L., and Eitelberg, G., *Experimental investigation of propeller induced ground vortex under headwind condition*. AIAA Aviation. 2014. Atlanta.
76. Sciacchitano, A., Wieneke, B., and Scarano, F., *PIV uncertainty quantification by image matching*. Measurement Science and Technology, 2013. **24**(4): p. 045302.
77. Pope, B. S., *Turbulent flows*. 2000: Cambridge University Press.

78. Chumakov, S. G., *Subgrid models for large eddy simulation: scalar flux, scalar dissipation and energy dissipation*. PhD Thesis, University of Wisconsin-Madison, 2005.
79. Trapp, L. G. and Girardi, R., *Crosswind Effects on Engine Inlets: The Inlet Vortex*. Journal of Aircraft, 2010. **47**(2): p. 577-590.
80. Mathey, F., Cokljat, D., Bertoglio, J. P., and Sergeant, E., *Assessment of the vortex method for Large Eddy Simulation inlet conditions*. Progress in Computational Fluid Dynamics, 2006. **6**: p. 58-66.
81. ANSYS, *FLUENT 6.3 User's guide*. 2006.
82. Brix, S., Neuwerth, G., and Jacob, D., *The inlet-vortex system of jet engines operating near the ground*. AIAA 18th Applied Aerodynamics Conference. 2000. Denver.
83. Devenport, W. J., Rife, M. C., Liapis, S. I., and Follin, G. J., *The structure and development of a wing-tip vortex*. Journal of Fluid Mechanics, 1996. **312**: p. 67-106.
84. Hegen, S., *DNW-LLF-Upgrade ground simulation*. Symposium on experiments and simulation of aircraft in ground proximity. 2013. Zwolle, Netherlands.
85. Nakayama, A. and Jones, J. R., *Vortex formation in inlet flow near a wall*. AIAA 34th aerospace sciences meeting and exhibit. 1996. Reno.
86. Schrijer, F. F. J., Sciacchitano, A., and Scarano, F., *Spatio-temporal and modal analysis of unsteady fluctuations in a high-subsonic base flow*. Physics of Fluids, 2014. **26**(8): p. 086101.
87. McNaughton, J., Afgan, I., Apsley, D. D., Rolfo, S., Stallard, T., and Stansby, P. K., *A simple sliding-mesh interface procedure and its application to the CFD simulation of a tidal-stream turbine*. International Journal for Numerical Methods in Fluids, 2014. **74**(4): p. 250-269.
88. Liu, C., *Wake vortex encounter analysis with different wake vortex models using vortex lattice method*. Master Thesis, Delft University of Technology, 2007.
89. Morgut, M. and Nobile, E., *Influence of grid type and turbulence model on the numerical prediction of the flow around marine propellers working in uniform inflow*. Ocean Engineering, 2012. **42**: p. 26-34.

90. Dacles-Mariani, J., Kwak, D., and Zilliac, G., *On numerical errors and turbulence modeling in tip vortex flow prediction*. International Journal for Numerical Methods in Fluids, 1999. **30**(1): p. 65-82.
91. Guilmineau, E., Deng, G. B., Leroyer, A., Queutey, P., Visonneau, M., and Wackers, J., *Wake simulation of a marine propeller*. 11th World Congress on Computational Mechanics. 2014. Barcelona, Spain.
92. Timmer, W. A. and van Rooij, R., *Summary of the Delft University wind turbine dedicated airfoils*. Journal of Solar Energy Engineering, 2003. **125**(4): p. 488-496.
93. Anderson, E. A. and Lawton, T. A., *Correlation Between Vortex Strength and Axial Velocity in a Trailing Vortex*. Journal of Aircraft, 2003. **40**(4): p. 699-704.
94. Felli, M. and Falchi, M., *Propeller tip and hub vortex dynamics in the interaction with a rudder*. Experiments in Fluids, 2011. **51**: p. 1385-1402.
95. Kalkhoran, I. M., *An experimental investigation of the perpendicular vortex-airfoil interaction at transonic speeds*. PhD Thesis, The University of Texas at Arlington, 1987.
96. Hughes, C. E. and Gazzaniga, J. A., *Low-speed wind tunnel performance of high-speed counterrotation propellers at angle-of-attack*. AIAA/ASME/SAE/ASEE 25th Joint Propulsion Conference. 1989. Monterey.
97. Wang, M., *Hub effects in propeller design and analysis*. PhD Thesis, Massachusetts Institute of Technology, 1985.
98. Jang, C., Furukawa, M., and Inoue, M., *Analysis of Vortical Flow Field in a Propeller Fan by LDV Measurements and LES—Part II: Unsteady Nature of Vortical Flow Structures Due to Tip Vortex Breakdown*. Journal of Fluids Engineering, 2001. **123**(4): p. 755-761.
99. Schüle, E., Rosemann, H., and Schaber, S., *Transition detection and skin friction measurement on rotating propeller blades*. 28th Aerodynamic measurement technology, ground testing, and flight testing conference. 2012. New Orleans.
100. Klebanoff, P. S., *Characteristics of turbulence in a boundary layer with zero pressure gradient*. NACA-TR-1247, NASA, 1955.
101. Berkooz, G., Holmes, P., and Lumley, J., *The proper orthogonal decomposition in the analysis of turbulent flows*. Annual Review of Fluid Mechanics, 1993. **25**: p. 539-575.

102. Sirovich, L., *Turbulence and the dynamics of coherent structures: Part I: Coherent structures*. Quarterly of Applied Mathematics, 1987. **XLV**: p. 561-571.

103. Kourentis, L. and Konstantinidis, E., *Uncovering large-scale coherent structures in natural and forced turbulent wakes by combining PIV, POD, and FTLE*. Experiments in Fluids, 2012. **52**: p. 749-763.

104. Burley, C. L., Brooks, T. F., van der Wall, B., Richard, H., Raffel, M., and etc., *Rotor wake vortex definition-initial evaluation of 3-C PIV results of the HART-II study*. 28th European rotorcraft forum. 2002. Bristol.

Acknowledgements

This manuscript summarizes the main results during my PhD research at TU Delft. Here I would like to acknowledge all the people that supported and motivated me during the entire PhD, making this thesis possible. I express my thanks to the generous funding from China Scholarship Council (No. 2011629079) which supported me to fulfil the research.

Special thanks to my supervisor and promotor Prof. Georg Eitelberg. You are always ready to give me an answer whenever I have a question. You continuously remind me to make a plan before proceeding, which helps me have a good working habit. You offered me so many opportunities to be a good researcher via teaching assistants, collaborations and projects.

The same thanks to my promotor Prof. Leo Veldhuis for your supervision and motivation. Discussion with you, together with your accurate hand drawings, always help me gain new understandings of the phenomena. I appreciate the guide by you through these years with your enthusiasm, patience and expertise in propeller aerodynamics.

I am grateful to Dr. Andrea Sciacchitano. Your expertise in PIV measurements not only trouble shot the problems in a wind tunnel, but also gave me keys to perform tests independently. I express my gratitude to discussions of *POD* analysis with Dr. Ferry F. J. Schrijer and Dr. Linfeng Chen. I appreciate the suggestions from Prof. Fulvio Scarano during the PhD progress meeting. Many thanks to Teng Zhou, Wei Wang, Tomas Sinnige, Daniele Ragni, and Marios Kotsonis for tests on propellers. I thank Tomas Sinnige, Qingxi Li and Nando van Arnhem during the finalization of the thesis. I am grateful to Sander van Zuijlen for your help of running *CFD* simulations on clusters.

I am grateful to Nana Saaneh, Colette Russo and Bettie Ratuhaling for their efficiency in helping me with any administrative issues. I thank all the technicians for their support: Stefan Bernardy, Henk-Jan Siemer, Nico van Beek, Peter Duyndam, Frits Donker Duyvis, Leo Molenwijk and Eric de Keizer.

I would like to thank the colleagues in the FPP group: Peijian Lv, Feijia Yin, Li Mo, Peijun Wu, Zhaoxu Zhu, Tom Stokkermans, Adam Head, Antonio Rubino, Lucia Azzini, Reinier van Dijk, Salvatore Vitale, Sebastian Bahamonde Noriega, Tiemo Mathijssen, Carlo de Servi, and Matteo Pini. I also would like to thank the colleagues in the Aerodynamic group: Zhengzhong Sun, Shuanghou Deng, Lei Cheng, Qingqing Ye, Vahid Kazemi Kamyab, Stefan Pröbsting, and Jacopo Serpieri. Many thanks to all my friends for all the pleasant moments that we spent together.

I owe special thanks to my parents of Yongdi Yang and Kaifeng Deng, and my sister Fang Yang. You have always helped me in the difficulties and shared the happiness of my success. Finally, I would like to thank my wife, Yanshan Kong, for unconditional support to me. The apart time during my stay in the Netherlands was hard for you, and I appreciate your smile whenever I saw you from the web camera.

Publications

Journal articles

[1] Yang, Y., Sciacchitano, A., Veldhuis, L., and Eitelberg, G., "Spatial-temporal and modal analysis of propeller induced ground vortices by particle image velocimetry," *Physics of Fluids*, Vol. 28, 2016.

[2] Yang, Y., Zhou, T., Sciacchitano, A., Veldhuis, L., and Eitelberg, G., "Propeller and inflow vortex interaction: vortex response and impact on the propeller performance," *CEAS Aeronautical Journal*, Vol.7, No.3, 2016.

[3] Yang, Y., Veldhuis, L., and Eitelberg, G., "Aerodynamic impact of a streamwise vortex on a propeller," *Aerospace Science and Technology*. (in revision)

[4] Yang, Y., Zhou, T., Sciacchitano, A., Veldhuis, L., and Eitelberg, G., "Experimental investigation of the impact of a propeller on a streamwise impinging vortex," *Aerospace Science and Technology*. (under review)

Conference proceedings

[1] Yang, Y., Ragni, D., Veldhuis, L., and Eitelberg, G., "Propeller induced ground vortex," 28th International Congress of the Aeronautical Sciences, Brisbane, Sep. 2012.

[2] Yang, Y., Veldhuis, L., and Eitelberg, G., "Propeller induced ground vortex," AIAA and DNW Ground Simulation Symposium, Zwolle, April, 2013.

[3] Yang, Y., Sciacchitano, A., Veldhuis, L., and Eitelberg, G., "Experimental investigation of propeller induced ground vortex under headwind condition," AIAA Aviation, Atlanta, June, 2014, AIAA 2014-2308.

[4] Yang, Y., Veldhuis, L., and Eitelberg, G., "Propeller induced ground vortex investigation by numerical and experimental methods," AIAA Aviation, Dallas, June, 2015.

[5] Yang, Y., Zhou, T., Sciacchitano, A., Veldhuis, L., and Eitelberg, G., "Propeller and inflow vortex interaction: vortex response and impact on the propeller performance", 5th CEAS Air & Space Conference, Delft, Sep., 2015.

Technical reports and patents

[1] Yang, Y., Veldhuis, L., “Aerodynamic interaction between propeller and wing of MA700”, Project in collaboration with XADRI and DNW, 2016.

[2] Yang, Y., “Design of a propeller for a manned multicopter,” Chinese Patent. (submitted in 2016 and it is under review)

Curriculum Vitae

Yannian Yang was born on July 8th, 1985, in Songzi, Hubei province, China. He started studying Aircraft Design and Engineering in 2005 in the School of Aeronautics, Northwestern Polytechnical University in Xi'an China. He attended the aero sports competition and his team was awarded the champion of China Aeromodelling Design Challenge in 2008. He received his Bachelor degree in 2009.

In 2009, he continued the graduate study in the same school and was supervised by Prof. Yuanming Zhang. His master thesis was about the aerodynamic and flight dynamic analyses of a UAV with a rotatable wing. In 2010, he participated in the project from COMAC about the experimental simulation of the emergency landing of aircraft on water.

In October 2011, He started the PhD study under the supervision of Prof. Georg Eitelberg and Prof. Leo Veldhuis in the faculty of Aerospace Engineering in Delft University of Technology. His research topic is about the aerodynamic interaction between a propeller and a vortex (vortices), involving both propeller self-induced vortices and an external vortex. In 2016, He participated in the project from industry (XADRI) by investigating the interaction between a propeller and a wing for the turboprop aircraft MA700.

From July 2016, he worked as an aerodynamic engineer in the multi-copter company eHANG which focuses on intelligent aerial vehicles. He designs propellers for unmanned and manned multicopters and conducts tests of the propulsors and parachutes.